Search for neutrinos from transient sources with the ANTARES neutrino telescope and optical follow-up observations - Development of hemispheric hybrid photomultipliers for astroparticle experiments

Imen Al Samarai

CPPM-T-2011-11

UNIVERSITÉ DE LA MÉDITERRANÉE AIX-MARSEILLE II
FACULTÉ DES SCIENCES DE LUMINY
163 avenue de Luminy
13288 MARSEILLE Cedex 09

THESE DE DOCTORAT

Spécialité : *Physique et Sciences de la Matière*

Mention : *Astroparticules et Astrophysique*

présentée par

Imen Al Samarai

en vue d'obtenir le grade de docteur de l'Université de la Méditerranée

Search for neutrinos from transient sources with the ANTARES neutrino telescope and optical follow-up observations
-
Development of hemispheric hybrid photomultipliers for astroparticle experiments

soutenue le 06 décembre 2011 devant le jury composé de

Dr.	Stéphane Basa	Jury
Pr.	José Busto	Directeur de thèse
Pr.	Alain Klotz	Rapporteur
Pr.	Marek Kowalski	Rapporteur
Dr.	Thierry Pradier	Jury
Dr.	Gregory Hallewell	Jury
Pr.	Mossadek Talby	Président du jury

Comme tout se meut dans l'univers! Comme tout, l'un dans l'autre, agit et vit de la même existence! Comme les puissances célestes montent et descendent en se passant de mains en mains les seaux d'or! Du ciel à la terre, elles répandent une rosée qui rafraîchit le sol aride, et l'agitation de leurs ailes remplit les espaces sonores d'une ineffable harmonie. Quel spectacle! Mais, hélas! Ce n'est qu'un spectacle! Où te saisir, nature infinie?

Faust
Johann Wolfgang von Gœthe

Remerciements

Je tiens d'abord à remercier le directeur du CPPM, Eric Kajfasz pour m'avoir accueilli au sein d'un laboratoire aussi riche et actif en expériences, d'être proche de chacun et de veiller personnellement sur le bien-être des doctorants. Je remercie les membres du jury d'avoir accepté de participer à cette thèse et pour les commentaires qu'ils ont fourni sur ce manuscrit.

Je remercie mon directeur de thèse José Busto de m'avoir soutenue pendant ces trois années de thèse, tant sur le plan professionnel que moral lorsque j'ai dû interrompre mon activité sur les PMs, et d'avoir veillé à ce que je puisse toujours travailler dans de bonnes conditions. Merci à Gregory Hallewell avec qui j'ai beaucoup apprécié travailler sur les PMs, pour ses nombreuses qualités professionnelles et humaines. Je remercie Stéphane Basa de m'avoir toujours poussé à faire de mon mieux et d'avoir veillé à mon travail depuis le LAM.

Je remercie la société Photonis qui a co-financé cette thèse jusqu'à sa fin. Merci à toute l'équipe d'ingénieurs avec qui j'ai travaillé, Anne-Gaelle Dehaine et Bruno Combettes ainsi que tous les techniciens qui m'ont accompagné pour l'élaboration des prototypes hybrides.

Merci à l'équipe ANTARES où j'ai eu à solliciter chacun de ses membres sur différents sujets au cours de cette thèse. Merci au chef d'équipe Vincent Bertin de m'avoir permis de prendre le large dans deux missions en mer et pour ses nombreux conseils. Je remercie particulièrement Damien Dornic avec qui j'ai travaillé quotidiennement sur le projet TAToO. Merci d'avoir été infailliblement présent et exigent ainsi que de m'avoir donné la responsabilité de la conduite d'analyse d'images dans TAToO, alors que j'étais très novice dans ce domaine. Merci à la petite équipe TAToO, à Michel Ageron sans qui ce projet n'aurait pas avancé aussi efficacement. Un merci tout particulier à Dominique Fouchez d'avoir répondu à mes nombreuses questions sur l'analyse d'images (même celles de 18h00 les vendredis). Je tiens aussi à remercier l'équipe ROTSE de l'université de Michigan; Carl Akerlof et Weikang Zeng.

Merci à tous ceux que j'ai côtoyé pendant cette thèse au CPPM et qui m'ont été d'un grand soutien; Nicolas, Garo, Pierre-Simon, David, Guillaume, Salvo, Manuela, Colas. Merci aussi à mes voisins et amis qui m'ont accompagné dans cette aventure marseillaise et qui contribuent sans le savoir à la diffusion de l'astronomie neutrino en en parlant autour d'eux dans les vernissages et soirées. Merci à mes amis du club de naufragés parisiens à Marseille, Julien et Sourd. Merci Robert d'être un soutien sans faille depuis que l'on se connaît.

Je remercie ma famille; ma mère, ma grand-mère, ma petite soeur et Tom d'avoir supporté mon absence pendant de longues années et de m'avoir donné le courage et l'inspiration dans la vie par le simple fait d'Aimer.

Abstract

Astroparticle experiments are being developed with the aim of resolving the mystery of cosmic rays. Questions like from where cosmic rays originate or how do they get accelerated up to ultra high energies are still unresolved. Cherenkov telescopes like ANTARES detect the Cherenkov light emitted by muons propagating in sea water. Muons are produced by the interaction of cosmic neutrinos (signal) or atmospheric neutrinos (noise) with the Earth nuclei. In order to offer the best detection conditions of Cherenkov light, and subsequently ensure a good reconstruction quality of the muons trajectory, the light sensors i.e the photomultipliers must satisfy various conditions.

The first part of this thesis focuses on the development of photomultipliers using crystals as a preamplifier of the light signal. The advantage of such a method is the possibility to separate individual photo-electrons and to enhance the temporal resolution by applying a high electric field. The design and conception as well as the possibility to produce such devices at large industrial scales is for the first time developed in this thesis.

The second part of the thesis is inspired from the new multi-messenger approach in ANTARES. An optical follow-up with six telescopes spread over the two hemispheres is triggered by the detection of a high energy neutrino or a set of neutrinos coincident in time and direction. Such a system enhances the sensitivity to transient sources such as Gamma Rays Bursts or Core Collapse Supernovae. The neutrino alert system is now fully operational. The system offers good performances; the optical follow-up starts within one minute from the neutrino detection and the median angular accuracy of the reconstructed neutrinos is 0.4°. Upon the reception of an alert, the telescopes point at the neutrino direction and start the acquisition of image series almost each night of the month following the neutrino alert. Image analysis tools have been implemented to search for optical transients and first results on the search of GRB optical counterparts correlated with a neutrino signal are presented.

Key words: *neutrino, Gamma-ray bursts, Core Collapse Supernovae, optical follow-up, astronomical image analysis*

Résumé

L'origine des rayons cosmiques ainsi que les procédés mis en oeuvre dans leur accélération à d'ultra-hautes énergies constituent l'un des sujets les plus débattus en astrophysique de nos jours. Une clé de ce mystère peut se trouver dans la détection de neutrinos cosmiques produits par un panel d'objets astrophysiques candidats à l'émission de rayons cosmiques. Les télescopes à neutrinos tels que ANTARES détectent la lumière Cherenkov issue des muons se propageant dans l'eau de mer. Les muons sont les produits d'interaction de neutrinos cosmiques (signal) ou atmosphériques (bruit) avec les noyaux de la terre. Pour offrir les meilleures conditions de détection de la lumière Cherenkov, et par conséquent bien reconstruire les traces des muons détectés, les détecteurs de lumière i.e les photo-multiplicateurs dont sont équipés les expériences Cherenkov dans la mer ou dans la glace doivent satisfaire plusieurs conditions, telles qu'une bonne résolution temporelle et un bon signal-sur-bruit pour pouvoir séparer les pics photo-électrons.

Le premier volet de cette thèse porte sur le développement de photomultiplicateurs utilisant le cristal comme préamplificateur de signal optique. L'avantage d'un tel procédé est la possibilité de séparer plusieurs pics photo-électrons et d'améliorer la résolution temporelle grâce à l'application d'un fort champ électrique. La conception d'un tel prototype et la possibilité de son industrialisation à grande échelle sont développés pour la première fois dans cette thèse.

Le deuxième volet s'inscrit dans la nouvelle thématique multi-messagers d'ANTARES. Un suivi avec six télescopes optiques répartis sur chaque hémisphère est déclenché lorsque ANTARES détecte un neutrino de haute énergie ou un ensemble de neutrinos coïncidents en temps et en direction. Un tel système permet d'augmenter la sensibilité de détection de neutrinos provenant de sources transitoires tels que les sursauts gamma et les Supernovæ à effondrement de cœur. Un système d'alertes neutrino est maintenant implémenté et fonctionne continument et de manière autonome dans ANTARES. Le système offre de bonnes performances; le suivi optique se déclenche dans la minute suivant la détection neutrino et l'incertitude sur la reconstruction de la trajectoire du neutrino est de 0.4° (valeur médiane). Une fois l'alerte reçue par un des télescopes, celui-ci se repositionne sur la direction du neutrino et entame une série d'observations réparties sur le mois suivant l'alerte. Cette thèse a porté dans un premier temps sur l'aspect neutrino en développant le filtre sélectionnant les évènements haute énergie et multi-neutrinos. Des outils d'analyse d'images optiques ont ensuite été implémentés pour la recherche de sources transitoires. Les premiers résultats de recherche de contreparties optiques de sursauts gamma en corrélation avec un signal neutrino sont présentés.

Mots-clés: *neutrino, sursauts-gamma, Supernovæ à effondrement de cœur, suivi optique, analyse d'images astronomiques*

Contents

List of acronyms

AGN Active Galactic Nuclei

ANTARES Astronomy with a Neutrino Telescope and Abyss environmental RESearch

ARS Analogue Ring Samplers

ASIC Application-Specific Integrated Circuit

BSS Bottom String Socket

CCSN Core Collapse SuperNovae

CR Cosmic Rays

DAQ Data AcQuisition

DSA Diffusive Shock Acceleration

DWDM Dense Wavelength Division Multiplexing board

GRB Gamma Ray Bursts

JB Junction Box

LCM Local Control Module

MEOC Main Electro-Optical Cable

MLCM Master Local Control Module

OM Optical Modules

PMT Photomultiplier Tubes

SCM String Control Module

SPM String Power Module

TATоO Telescopes-Antares Target of Opportunity

TTS Transit Time Spread

Introduction

Astroparticle physics has entered an exciting era with the recent development of experimental techniques which opened new windows of observation of the cosmic radiation in all its components: photons, cosmic rays, but also gravitational waves and high energy neutrinos.

First observations with satellites using concurrent X-ray and UV detection began in the seventies. Many discoveries were reported such as X-binaries or Gamma Ray Bursts (GRB). Accretion processes could be better understood, leading to the basis of our actual understanding of black hole phenomena. Recently, the *Fermi* satellite has allowed a more refined sky cartography involving higher energy bands. Ground-based gamma-ray astronomy was developed later, probing even higher energy ranges by exploiting Cherenkov light issued from the showers induced by the interaction of TeV gamma-rays with the atmosphere. Despite the important advances in terms of detection, constraints due to intrinsic or intergalactic absorption of very high energy gamma-rays can not be avoided.

The acceleration of Cosmic Rays (CR) is believed to take place in a large panel of astrophysical objects. However, it is certainly not an easy task to definitely confirm the sources capable of producing and accelerating CRs to energies reaching 10^{20} eV. The reason is mainly due to the fact that the direction of these particles - mostly composed of protons with some admixture of heavier nuclei - do not point back to their origin as charged particles are deflected by magnetic fields in the Universe. Only the highly energetic CRs are likely to retain any memory of the source direction. A cosmic probe to investigate the mystery of CRs should be electrically neutral, stable and weakly interacting so that it will penetrate regions which are opaque to photons. The best candidate to date is the neutrino. It is clear that sources capable of accelerating protons to such tremendous energies are likely to generate a large associated flux of photo-produced pions, which would decay yielding gamma rays and neutrinos.

Astrophysical sources of high-energy neutrinos have not yet been confirmed. However, there are a number of candidate astrophysical sources. Candidate sources can be identified both within the Galaxy -accreting binaries containing neutron stars or black holes, supernovae and young supernova remnants -and elsewhere, most notably Active Galactic Nuclei (AGN) and GRBs. This represents a rich spectrum of possible sources, both steady and transient.

Since the Earth acts as a shield against all particles except neutrinos, neutrino telescopes use the detection of upward-going muons as a signature of muon neutrino interactions in the matter below the detector. Water or ice are typical detection media through which the muon emits Cherenkov light. Its detection allows the determination of the muon trajectory. ANTARES is a neutrino telescope deployed in the mediterranean sea. About 900 hemispherical standard photomultipliers (light sensors) are distributed over 12 lines anchored at 2500 m depth in complete darkness, in order to avoid the optical background. The technical structure of the detector was optimized for the detection of neutrinos with

energies greater than 100 GeV. The advantageous argument stating that neutrinos are weakly interacting can be thought of as a drawback as they are extremely difficult to detect. ANTARES has an area of about 0.1 km^2 with an active height of $\sim$ 350 meters, it is foreseen to extend it to a km^3 detector. Bigger detector volumes enhance the detection probability. In this sense, Km3NeT will offer a promising platform for neutrino detection thanks to its size, to its expected angular accuracy and to its visible sky covering most of the Galactic plane.

The greatest challenge in neutrino detection is the ability to discern a cosmic neutrino from the background. Atmospheric neutrinos represent an irreducible background. The general method for steady sources search is to look for regions giving a significant excess over the expected neutrino background in the direction of a list of gamma-ray sources. The transient source search relies on the same principle but takes advantage of the temporal information. By searching neutrinos in a limited cone around the bursting source direction and a limited time around the burst duration, most of the neutrino background can be rejected. However, gamma-ray satellites have a limited instantaneous field-of view, which constrains the neutrino search and prevents from detecting sources which can be gamma-hidden but possible neutrino emitters. A neutrino detector has an instant coverage of at least a hemisphere and a high duty cycle, giving the opportunity to use neutrinos to trigger other detections in X-ray or optical. A coincident detection with one single neutrino would allow the identification of the neutrino source by using its X-ray spectrum or its light curve information and give evidence of hadronic processes within the source without ambiguity.

This thesis has three main topics; part one starts with a small review on astrophysics using high energy cosmic rays, high energy gammas and high energy neutrinos. The main debated questions in the community are presented and the general frame within which neutrino astronomy arose as a complementary discipline to other messengers is discussed. In this frame, the ANTARES neutrino detector is presented as well as its expected performances and its target neutrino sources. The second part focuses on the development of new photomultipliers for the Km3NeT detector. These photomultipliers are based on a revised concept of hybrid light sensors which, in contrary to a standard photomultiplier as used in ANTARES, use a pre-amplified light yield issued from a crystal before the electric signal gets amplified. The development program motivations and results are presented.

The third part focuses on the multi-messenger approach using neutrinos to detect transient sources. The physics behind GRBs and Core Collapse SuperNovae (CCSN), which are the most interesting transient candidate sources to emit high energy neutrinos is outlined. An emphasis on the expected neutrino signal and optical counterpart from these sources is done suggesting that both associated instruments can be used in a concurrent way to further enhance the detection sensitivity. An on-line optical follow-up program of selected neutrino events was implemented during this thesis. The events are selected based either on their energy, their multiplicity or their direction to reduce the atmospheric neutrino contamination. An alert is then sent to a network of robotic telescopes triggering a follow-up in the corresponding region over almost a month. Optical data analysis tools based on image subtraction methods were implemented and optimized for the follow-up program in the context of this work. The optical analysis pipeline is presented and first results on early optical observations are presented.

Part I

Neutrino astronomy

Chapter 1

The context of neutrino astronomy

Content

1.1 Cosmic rays

Cosmic rays (CR) were discovered in 1912 by Victor Hess, when he found that an electroscope discharged more rapidly as he ascended in a balloon. He attributed this observation to a source of radiation entering the atmosphere from above, and in 1936, he was awarded the Nobel prize for his discovery. For some time, it was believed that the radiation was electromagnetic in nature (hence the name cosmic "rays"). Later, it was found that cosmic rays must be electrically charged because they are affected by the Earth's magnetic field.

From the 1930s to the 1950s, before man-made particle accelerators reached very high energies, CRs served as a source of particles for high energy physics investigations, and led to the discovery of subatomic particles like the positron or the muon. Although these applications continue, since the dawn of the space age, the main focus of CR research has been directed towards astrophysical investigations of where CRs originate, how they get accelerated to such high velocities, what role they play in the dynamics of the Galaxy, and what their composition tells us about matter from outside the Solar System.

1.1.1 Observation of charged cosmic rays

The origin of primary cosmic rays remains an unresolved problem. The most important clues are revealed by the study of the energy spectrum and the chemical composition of primary cosmic rays, since they reflect the acceleration mechanism and the abundances at the acceleration site.

Composition

The composition of cosmic rays has been measured by several experiments carried out on balloons, on ground or on satellites. Technically, *primary* cosmic rays refer to those particles accelerated at astrophysical sources, and *secondaries* refer to those particles produced by spallation of primaries with interstellar gas. The cosmic radiation incident at the top of the terrestrial atmosphere is composed of all stable charged particles and nuclei. Up to few hundred GeV, cosmic rays are composed of electrons (1%) and nuclei (99%).

- Protons and nuclei :

  Cosmic rays include all of the elements in the periodic table; about 89% Hydrogen (protons), 10% Helium, and about 1% heavier elements. Figure 1.1 shows the relative abundance of different nuclei in cosmic rays compared to the Solar System elements at low energies (less than 270 MeV).

  The common heavier elements (such as Carbon, Oxygen, Magnesium, Silicon, and Iron) are present in about the same relative abundances as in the Solar System, but there are important differences in elemental and isotopic composition that provide information on the origin and history of galactic cosmic rays. For example, there is a significant overabundance of the rare elements Li, Be, and B. These elements are produced when heavier cosmic rays such as Carbon, Nitrogen, and Oxygen fragment into lighter nuclei during collisions with the interstellar gas.

  Up to energies of a few 10^{14} eV, high flying balloons and satellite-borne experiments have provided important information about the origin and transport properties of CRs in the interstellar medium. Two prominent examples are ratios of secondary to primary elements, such as the B/C ratio, which is used to extract the average amount of matter CR particles have traversed from their sources to the Solar System, or the relative abundances of radioactive isotopes, such as ^{10}Be to stable ^{9}Be or ^{26}Al to stable ^{27}Al, which carry information about the average age of CRs.

- Electrons :

  Being charged and light, low energy electrons (less than 10 GeV) are very sensitive to the solar winds and to the magnetic fields in the interstellar medium. The detected electrons are considered to have two origins; primary electrons accelerated in the source and loosing rapidly their energy by interacting via Synchrotron emission and Inverse Compton scattering, and secondary electrons issued from the interaction of nuclei during their propagation through the Galaxy. In the latter case, they are related to the flux of protons and cosmic nuclei.

The anatomy of the Cosmic Ray spectrum

The cosmic ray energy spectrum extends from a few hundreds MeV to above 10^{20} eV. Over this wide range of energies, the intensity drops by more than 30 orders of magnitude. Despite the enormous dynamic range covered, the spectrum appears to have global features and can be well approximated by broken power-laws:

$$\frac{dN}{dE} \propto E^{-\gamma} \tag{1.1}$$

where N is the number of observed events, E the energy of the primary particle and γ being the spectral index ranging from 2.7 to 3.0.

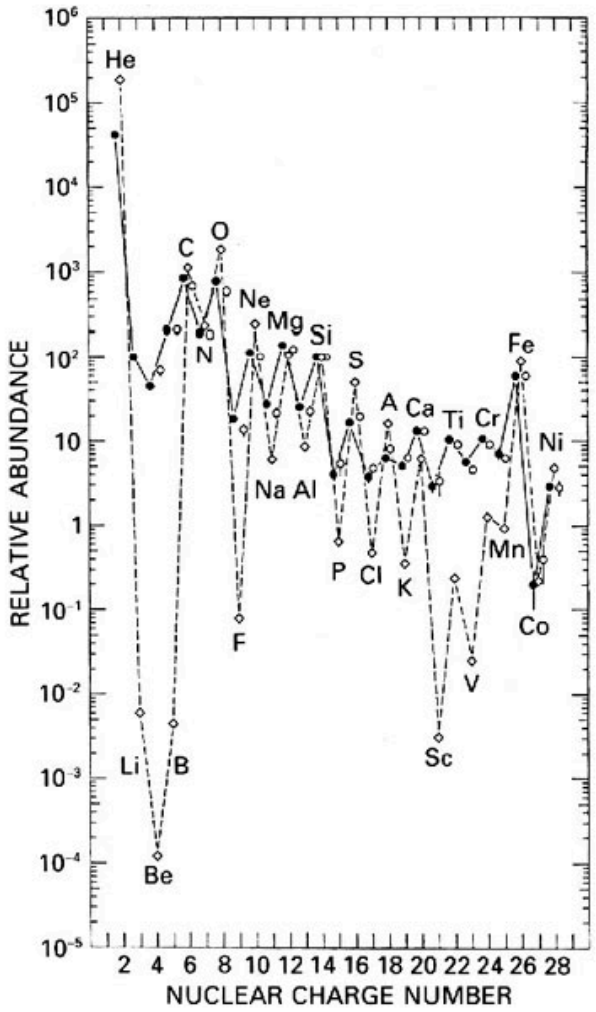

Figure 1.1: Relative abundance of chemical elements present in cosmic rays at the top of the atmosphere (circles and continuous black curve) compared to their abundance in the Solar System (diamond shape and dashed black curve) [110].

- Spectrum at low energies

  For energies between 100 MeV and few GeV, particles issued from outside the Solar System are strongly affected by solar winds. Therefore, the flux arriving at Earth is anti-correlated with the solar activity (11 years solar cycles). This effect is known as *solar modulation*. Moreover, the lower energy cosmic rays are affected by the geomagnetic field, which they must penetrate to reach the top of the atmosphere.

- Spectrum at high energies

  The high energy part of the spectrum (above 10^{13} eV) is shown in figure 1.2 [21]. The flux has been multiplied by $E^{2.7}$ in order to display the features of the steep spectrum. With increasing energy, the flux decreases : at 10^{11} eV, one particle m^{-2} s^{-1} bombards the atmosphere; the flux at 10^{15}eV is only one particle m^{-2} $year^{-1}$. At energies higher than 10^{20} eV, the flux is only one particle km^{-2} $century^{-1}$.

  Different regions can be disentangled clearly based on the variation of the spectral index γ.

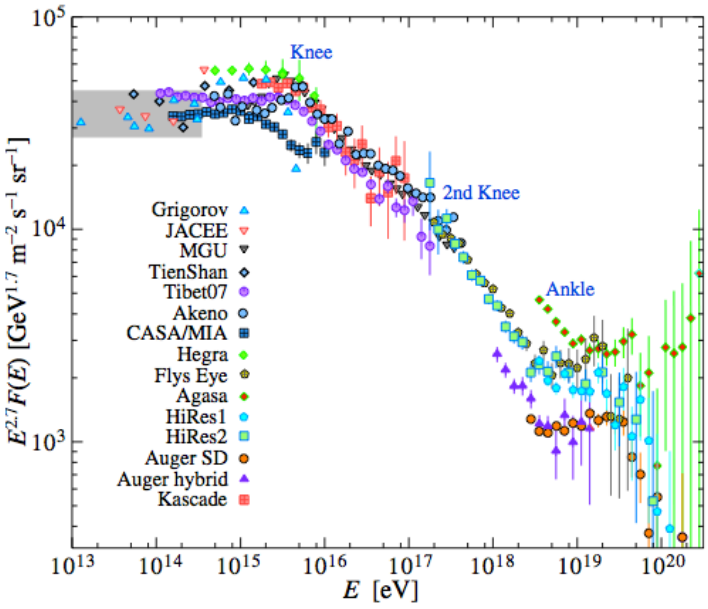

Figure 1.2: The cosmic ray spectrum from air shower measurements [21]. The shaded area shows the range of the direct cosmic ray spectrum measurements mainly provided by satellites.

For energies between 10^{10}eV and 5.10^{15}eV, the spectral index is 2.7. At present, a commonly accepted model of the origin of CRs below 5.10^{15}eV is the model that incorporates the diffusive shock acceleration of interstellar matter around supernova remnants (section 1.1.2). This model can explain the total power budget for the source to supply all the Galactic cosmic rays and predicts a power law spectrum consistent with observational results. These nuclei are produced in the sources with a

spectrum index of 2 and propagate millions of years in the Galaxy where they are confined in magnetic fields. During this period, their spectrum and their abundance are modified by the multiple electromagnetic and hadronic interactions they encounter in the interstellar medium. Hence, at their arrival on Earth, their spectrum index is equivalent to 2.7. This acceleration mechanism, however, meets a difficulty in explaining cosmic rays with much higher energies, because the maximum acceleration energy is limited to about 5.10^{15} eV owing to the decline in the SNR shock waves.

Above a few TeV, the CR flux expected drops to few particles per square meter per year. This excludes any type of direct observation. On the other hand, this energy is large enough so that secondary particle cascades produced in the atmosphere penetrate with a footprint large enough to be detected by an array of detectors on the ground (HESS [63], MILAGRO [3][1]). Such an extensive air shower arrays with typical dimensions of few thousands square kilometers are designed to operate for several years in order to detect fluxes even down to 1 particle per square kilometer per century.

The steepening of the slope from ~ 2.7 to ~ 3.1 at about 3.10^{15}eV is known as the *knee*. The maximum energy produced in the supernova shock acceleration processes is around 5.10^{15} eV [51] for standard galactic supernova remnants but the origin of the knee is still an open question.

The KASKADE results [26] have a crucial implication on the extension of the spectrum due to a galactic origin. Indeed, the galactic spectrum should end at energies of the order of $E_{end} \sim Z_{Fe} \times E^{p}_{Knee}$, where $Z_{Fe} = 26$ is the charge of fully ionized Fe nuclei and $E^{p}_{Knee} \sim 3.10^{15}$ eV is the position of the *knee* in the proton spectrum. This leads to $E_{end} \sim 8.10^{16}$ eV, which conflicts with the standard picture of the transition from Galactic to extra-galactic CRs, as provided by the traditional *ankle* model [62]. Indeed, for energies **above 3.**10^{18} **eV**, the spectral index changes again down to ~ 2.7. Appearing at $\sim 5.10^{18}$ eV is the *ankle* region. The energy spectrum becomes less steep again, the spectral index now being around 2.8. Presently, the most accepted theory about the ankle origin considers it as the transition of cosmic rays from Galactic to extra-galactic origin[125].

Above the ankle, at energies **above 4.10**^{19} **eV**, Ultra High Energy cosmic rays (UHECR) suffer inelastic interactions with the photon gas of the CMB. This effect is called the Greisen-Zatsepin-Kuzim (GZK) cut-off, further discussed in section 1.1.3.

1.1.2 Acceleration process and propagation

To explain the CR spectrum at high energies, models for different sources were suggested. These models are inspired from the connection between non-thermal emission from astrophysical sources and particle acceleration process.
Basically, there exist two different scenarios for the production of charged UHECRs, referred to as the *top-down* and *bottom-up* scenarios. In the former case, UHECRs are due to the decay of super heavy particles with masses ranging from 10^{11} eV up to the GUT scale[2]. Such decays result in protons at the highest energies up to 10^{22} eV. In this scenario, the GZK cut-off is avoided, since the protons are produced in the Earth's vicinity.

[1] Stopped in 2008 after 7 years of operation.
[2] M_{GUT}=10^{24} eV

Furthermore, the proton signal is expected to be accompanied by a large flux of neutrinos and high-energy photons. The absence of such signatures in combination with the CR suppression at highest energies favoring the GZK cut-off support the argument of the particle production and acceleration processes in distant sources, referred to as the *bottom-up* scenario.

Considering the *bottom-up scenario*, there are mainly two kinds of acceleration mechanisms :

- Direct acceleration of charged particles by an electric field.
- Statistical acceleration (Fermi acceleration) in a magnetized plasma.

In the former acceleration mechanism, the electric field in question may originate for example, from a rotating magnetic neutron star (pulsar) or a rotating accretion disk threaded by magnetic fields, etc. For a variety of reasons, the direct acceleration mechanisms are, however, not widely favored as the CR acceleration mechanism. Apart from disagreements among authors about the crucial details of the various models, a major disadvantage of the mechanism, in general, is that it is difficult to obtain the characteristic power-law spectrum of the observed CR. A more detailed description of this mechanism can be found in [36].

In 1949, Fermi suggested the basic idea of the statistical acceleration mechanism that may happen in the CR acceleration process [53]: Even though the average electric field may vanish, there can still be a net transfer of macroscopic kinetic energy of moving magnetized plasma to individual charged particles (test particles) in the medium due to repeated collisionless scatterings (encounters) of the particles either with randomly moving inhomogeneities of the turbulent magnetic field, or with shocks in the medium [40].
In his original paper, Fermi considered the former case, describing particle scattering with randomly moving magnetized "clouds" in the interstellar medium. An average energy gain can be expected in this case after many encounters even when taking into account that the particle may either lose or gain energy at each encounter.
This *original* mechanism is nowadays called *second-order Femi mechanism* because the average energy gain in this case is proportional to $(\frac{u}{c})^2$, where u is the relative velocity of the cloud with respect to the frame in which the CR ensemble is isotropic, and c is the velocity of light.

Because of the dependence on the square of the cloud velocity $(\frac{u}{c})$ <1, the *second-order* Fermi mechanism acceleration process is not efficient. Indeed, for typical interstellar clouds in the Galaxy, the acceleration time scale turns out to be much larger than the typical escape time ($\sim 10^7$ yr) of CR in the Galaxy deduced from observed Be isotopic abundances [110]. Hence, a little number of collisions are expected [1] and consequently, there would be a little hope of gaining significant acceleration from the *original* Fermi mechanism. In addition, although the resulting spectrum of particles happens to be a power law in energy, the power-law index depends on the cloud velocity, and so the superposed spectrum due to many different sources with widely different cloud velocities would not in general have a power-law form.

A more efficient version of Fermi mechanism is realized when one considers encounters of particles with plane shock fronts. In this case, the average energy gain of a particle per

[1] The random velocities of interstellar clouds are very small in comparison with the velocity of light, $\frac{u}{c} < 10^{-4}$. With an estimation of a mean-free path of CR in the interstellar medium of 1 pc, the number of collisions would be roughly one per year.

encounter[1] is of first order in the relative velocity between the shock front and the isotropic CR frame. Currently, the *standard* theory of CR acceleration, the so-called Diffusive Shock Acceleration (DSA) mechanism is based on this *first order* Fermi acceleration mechanism at shocks [69].

Figure 1.3 shows a sketch of the *second* and *first order Fermi acceleration* of a particle with an initial energy E_1 and an exit energy E_2 after multiple encounters.

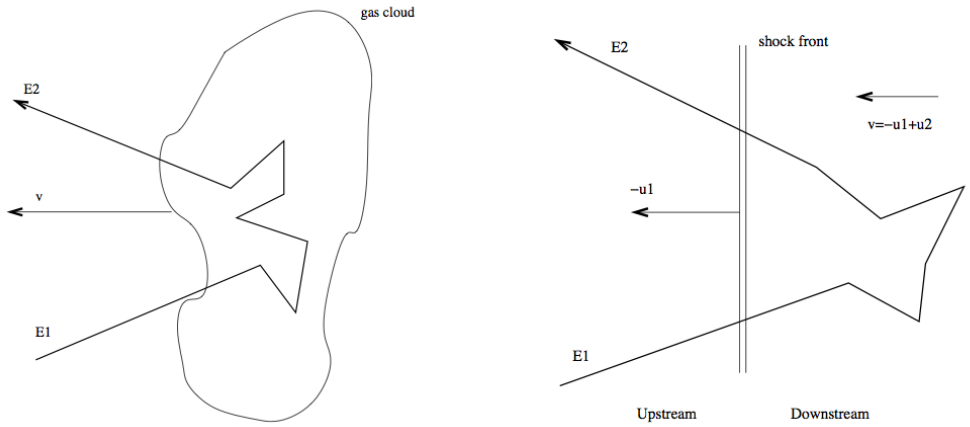

Figure 1.3: Statistical acceleration (Fermi acceleration) in a magnetized plasma. Left : *second* order Fermi acceleration. Right : *first* order Fermi acceleration

An important feature of the DSA mechanism is that particles emerge out of the acceleration site with a characteristic power-law spectrum. The spectrum index depends only on the shock compression ratio, and not on the shock velocity. Shocks are ubiquitous in many astrophysical situations: in supernovae expending shell after explosion or in cosmological situations as in Gamma Ray Bursts (GRBs). The basic ideas of the DSA have received impressive confirmation from in situ observations in the Solar System, in particular from observations of high-energy particles accelerated at the Earth's bow shock generated by collision of the solar wind with the Earth's magnetosphere [31]. We will discuss the DSA again in connection with UHECRs in the next section.

From a theoretical point of view, SNRs are attractive candidates of Galactic CR origin in terms of the maximum achievable CR energy, which is estimated to lie somewhere between 10^{12} and 10^{17} eV. The interactions with the surrounding matter of protons accelerated in SNRs produce neutral pions, and the resulting flux of secondary γ-rays from SNRs has been predicted as well. Nowadays, given the existence of space and ground based γ-ray detecting systems, the SNR acceleration paradigm for Galactic CR origin can also be tested by searching for these secondary γ-rays.

The *first-order* Fermi acceleration in the form of DSA when applied to shocks in supernova remnants can accelerate particles to energies perhaps up to $\sim 10^{17}$eV but probably not much beyond.

[1]Defined as magnetic field irregularities (e.g. Magnetohydrodynamic waves (MHD)) frozen into the plasma reflect particles back and forth across the shock before they are convected eventually away downstream of the shock.

1.1.3 The case of UHECRs

For relativistic nuclei with energy E and electric charge Z×e in a magnetic field B, the gyroradius is given by the Larmor radius $R_L = \frac{E}{Z \times e \times B}$. In the galactic magnetic field, protons with energy up to 10^{18} eV have a Larmor radius which is smaller than the size of the Galaxy and can remain confined. Up to these energies, CRs are therefore thought to have a galactic origin, while at higher energies they can escape from the Galaxy. Heavier nuclei have larger charges and must therefore be accelerated to larger energies to achieve the same Larmor radius than protons. Consequently, the heavier element cutoff lies at higher energies and the composition of CRs for energies above the *knee* shows a domination of heavier nuclei over the protons. At these energies, the gyroradius of the particles in the magnetic fields is greater than the thickness of the Galactic Disk. Hence, the CRs can not be confined within the Galaxy.

Other theories state that the transition from galactic to extra-galactic CRs is produced at lower energies. They explain the shape of the *ankle* region as induced by the electron-positron production when the CRs interact with the Cosmic Microwave Background (CMB) [16] or the Extragalactic Background Light (EBL). In this scenario, the second *knee* could be the result of the disappearance of the heavy nuclei galactic component and the appearance of a proton extra-galactic component [15].

Directional information

If the sources of the most energetic CRs are relatively nearby and not uniformly distributed, then an anisotropic arrival distribution is expected, provided the particles have a sufficiently small charge and a sufficiently high energy for their directions to be minimally perturbed by intervening magnetic fields. The Pierre Auger Observatory recently pointed out an anisotropy in the arrival directions of UHECRs (E > 5.7 10^{19} eV) with 99 % confidence [4]. The result of the correlation study is shown in figure 1.4.

Although recent studies indicate a correlation between the arrival directions of cosmic ray particles of high energy and the positions of nearby Active Galactic Nuclei, the interpretation of this anisotropy is still not verified with the available statistics. For example, an excess was observed in the region of the radiogalaxy Centaurus A but no high energy event pointing back to the Virgo Cluster was noticed. The absence of a significant events clustering may be due to the presence of significant magnetic deflections.

Measuring the composition of CRs above 3.10^{18} eV has an impact on both the physics of acceleration and on hadronic physics. The most recent result comes also from the Pierre Auger Observatory. An evidence for the presence of heavy elements in cosmic rays has been pointed out from the measurement of the maximum longitudinal track length of the electromagnetic showers (Xmax) by the fluorescence telescopes on Auger site [118]. Figure 1.5 shows the X-$<X_{max}>$ shape comparison with hadronic models simulations. At low energy, the shape of the data is compatible with a very light or mixed composition, whereas at high energies, the narrow shape would favor a significant fraction of nuclei. Thus, the composition gets heavier gradually starting from the *ankle* region to become relatively heavy at 3. 10^{19} eV (last point of measure). In fact, a heavy composition would lead to the conclusion that the majority of the sources do not accelerate protons but heavier nuclei up to 10^{20} eV. The measure of the anisotropy effect with high statistics can help to distinguish the two interpretations. Because the detection of a significant event cluster at small scales could point to a light composition, a more diffuse clustering would give more credit to a heavy composition at high energies.

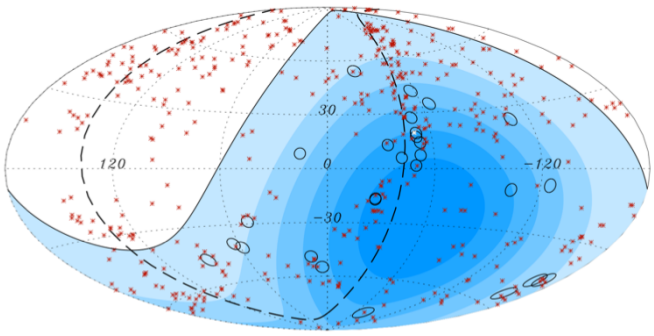

Figure 1.4: Skymap in galactic coordinates of the arrival directions of 27 UHECRs observed by Auger (circles) and the distribution of nearby Active Galactic Nuclei (< 75 Mpc; in red asteriscs). Blue indicates the sky visibility by Auger [4]

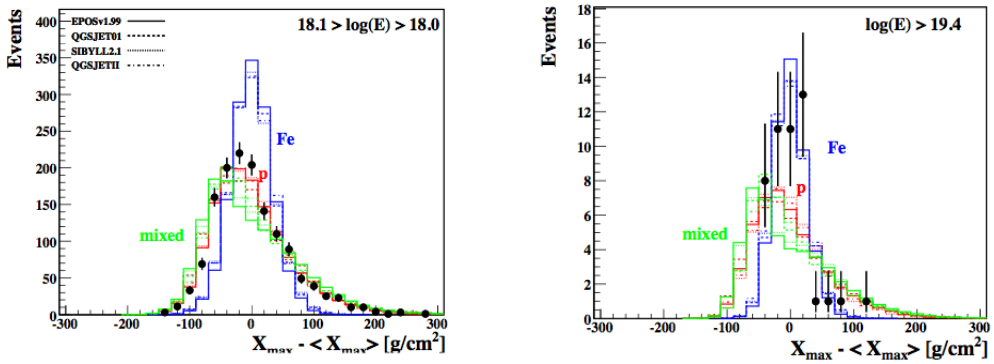

(a) (b)

Figure 1.5: Centered distribution, Xmax - <Xmax>, for the lowest and highest energy bins. Subtraction of the mean allows only for the comparison of the shapes of these distributions with the superimposed MC simulations of light (p) and heavy (Fe) composition scenarios. Mixed is 50% p and Fe.

The GZK cutoff

While the GZK cut-off is not yet firmly confirmed, the Pierre Auger Observatory has detected a flux suppression above 4.10^{19} eV, compatible with the predictions of the GZK cut-off. Figure 1.6 gives an expanded view of the high energy end of the spectrum, showing the results of three of ground-based experiments, AGASA [1], HiRes and Auger.

The interpretation of the flux suppression, if linked with the GZK cut-off, suggests that cosmic rays at highest energies are limited to distances within the local Universe[2] (<100-200 Mpc) due to the attenuation length of cosmic rays (protons and nuclei) with extragalactic photon background (CMB, Infrared) during their propagation.

[1] stopped in 2004

[2] Environment in which measurements should not be affected by the expansion effect

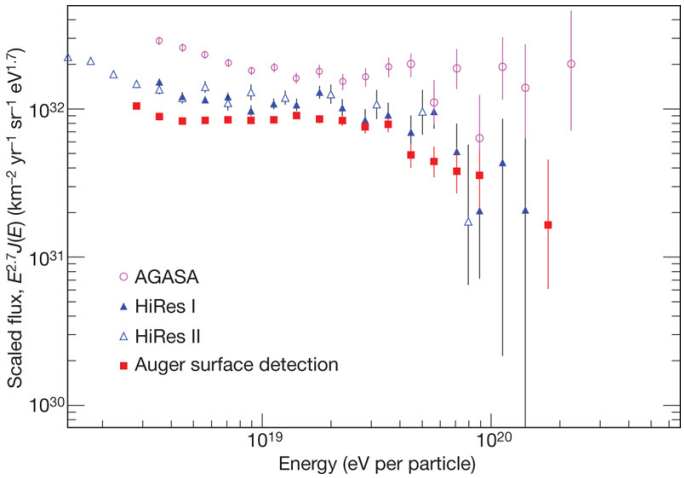

Figure 1.6: Comparison between AGASA (circles), HiRes monocular spectra (open and filled triangles correspond to each HiRes location) and Pierre Auger Southern Observatory. Error bars are 1 σ[34].

Candidate sources for UHECRs

For UHECRs, one has to invoke shocks on large scales, namely extragalactic shocks. Therefore, extragalactic objects such as bright AGNs are possible sites of UHECR acceleration. This relation between the dimensions of an object and the intensity of the magnetic field is reported in the Hillas diagram shown in figure 1.7. This diagram allows one to restrict attention to only a few classes of astrophysical objects as sources capable of accelerating particles to a given energy. Non-exotic acceleration processes require a particle to be confined within a region (of size L) where magnetic field shocks are present (with a field intensity value of B). Once the particle reaches its maximum energy, then the magnetic field is not able to keep the particle confined within the acceleration region and the particle escapes. This gives an approximate value for the maximum achievable energy of Emax $\sim$ ZBL, shown as a solid/dashed line for 10^{20}eV protons/iron nuclei, respectively. Data is shown for a variety of astrophysical objects; only those above the line can accelerate particles to energies into the GZK region [34]. The non -exhaustive list of objects that satisfy the conditions for acceleration up to 10^{20} eV are neutron stars with very strong magnetic fields, jets of AGNs [87], Pulsars [122] [39] and short/long GRBs (section 4.1). However, above such an energy, the candidate sources are very few.

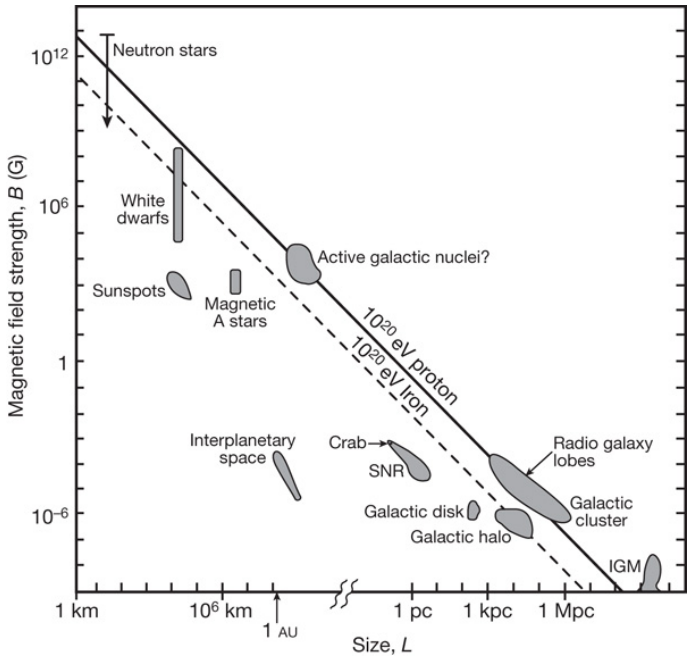

Figure 1.7: The Hillas diagram showing size and magnetic field strengths of possible sites of particle acceleration. Objects below the corresponding diagonal lines cannot accelerate protons (iron nuclei) to 10^{20}eV[34].

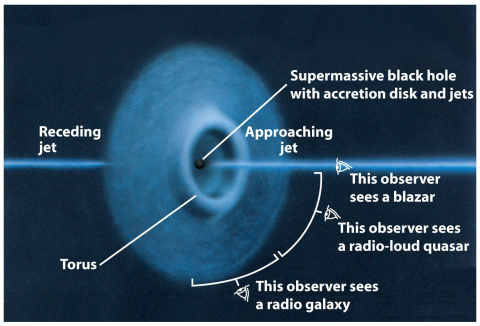

(a) Illustration of the Unified Model of AGNs, according to which the classification of an active galactic nucleus depends on the inclination of its symmetry axis to the line of sight (image credit:http:/ www.physics.ucsb.edu/).

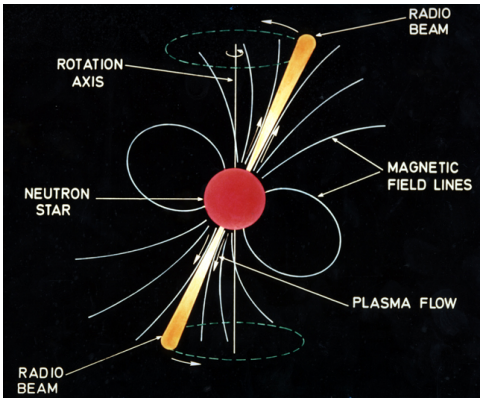

(b) Illustration pulsars properties : a rapidly rotating neutron star and a dipole form magnetic field. Radio telescopes receive a regular train of pulses as the beam repeatedly crosses the earth, making the pulsar appear to be a pulsating radio signal (image credit : http://www.atnf.csiro.au/).

Figure 1.8: Artist view of some UHECR candidate sources

1.2 Cosmic messengers

1.2.1 High energy photons

High energy photon production ($E_\gamma \sim$ GeV-TeV) in astrophysical is mainly explained by two scenarii : leptonic and hadronic. In a leptonic scenario, the HE photons are produced by Inverse Compton of the electron population with the low energy photons. Low energy photons may have two origins: either internal i.e. produced by the synchrotron radiation of the parent electron (Synchrotron Self Compton model: SSC) or from an external source (External Inverse Compton: EIC model). When considering the SSC model, a correlation is expected between the LE photons which spectrum peaks at infrared /X-ray and the HE component. As the electron is much more easy to accelerate, this scenario is preponderant in sources where the magnetic field is low. With this model, HE photons can be produced up to few tens of TeV. A strong energy cut-off in the flux is expected due to a limited acceleration.

The second competitive scenario is based on hadronic interactions of CR with matter in p-p or p-γ interaction scenario. The resulting neutral pions decay into two HE gammas while the decay of charged pions lead to the production of high energy neutrinos.

The question as to whether high-energy photon signals originate from hadronic processes (π^0 decay) or leptonic processes (SSC/EIC) is one of the most important nowadays. As to now, none of these two competing processes is universally favored.

Lately, observations from *Fermi*-LAT has extended the spectrum of the supernova remnant RX J1713.7-3946 as observed by HESS. First, HESS has pointed out a correlation between gamma-ray emission in TeV energies and the SNR molecular cloud region, and compared the expected gamma flux using a hadronic, leptonic and mixed models. No firm conclusion could be drawn from this comparison as the measured points were vaguely agreeing with both scenarii but giving more credit to hadronic processes [85]. In 2011, *Fermi*-LAT has measured the energy spectrum in gamma rays in the GeV-TeV range and thus, extended the spectrum over 5 orders of magnitude combining HESS data (up to $\sim$ 100 TeV). The results are presented in figure 1.9. The results give clearly most credit to a leptonic process occurring in the SNR. However, it does not imply an absence of accelerated protons. Hadronic process may still be undergoing but less efficiently as strongly suggested in *Fermi* paper [2].

Some other hypothesis about the production of high energy photons have been formulated. Some of them have a direct relation with exotic physics. For instance, photons could appear as a result of the annihilation or decay of very massive or energetic objects such as dark matter candidates, very massive particles at unification scales, primordial black holes, etc.

While high energy photons have revealed important insights for many astrophysical phenomena, they are however limited due to their nature. The photon mean free path is considerably reduced due to its interaction with the EBL and the CMB. Therefore, the most energetic sources become opaque at high distances as shown in figure 1.10. For instance, photons with 10 TeV (1 PeV) energy can not probe sources outside the Local Cluster (Galaxy). This reduction vanishes at higher energies ($\sim 10^{20}$ eV) but the fluxes are very low at these energies to be detectable by the current experiments.

Primary photons in the keV-MeV energy range are detected outside the atmosphere by space satellites. At energies greater than few TeV, the only way to detect photons is by collecting the Cherenkov light induced by the charged particles produced when photons interact with the atmosphere. This is the detection principle of the Imaging Atmospheric

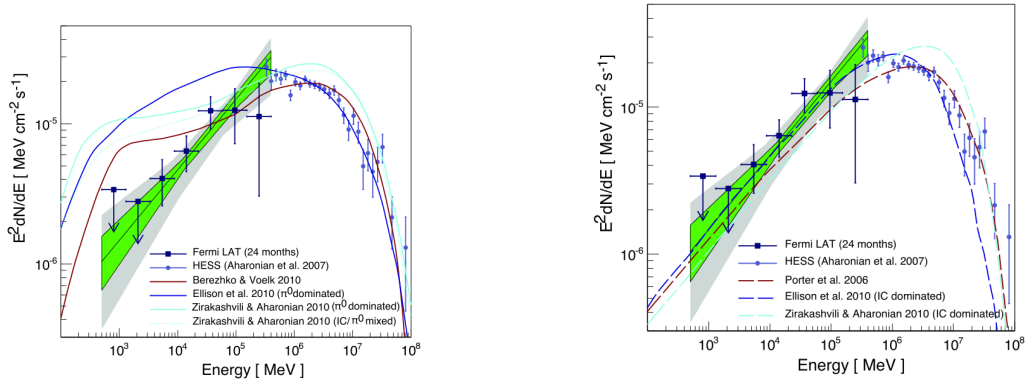

(a) Predictions assuming that the gamma-ray emission predominately originates from the interaction of protons with interstellar gas (hadronic model).

(b) Predictions assuming models where the bulk of the gamma-ray emission arises from interactions of electrons with the interstellar radiation field (leptonic models).

Figure 1.9: Energy spectrum of RX J1713.7-3946 in gamma rays. Shown is the Fermi-LAT detected emission in combination with the energy spectrum detected by H.E.S.S.

Cherenkov Telescopes (IACTs) as H.E.S.S., MAGIC or VERITAS. Other ground-based detectors as MILAGRO, catch the light produced by means of a Water Cherenkov Extensive Air Shower Array (EAS), where the detector takes advantage of the larger density and number of photons created with respect to the IACTs. With these experiments, photons up to ∼100 TeV have been detected.

Satellite-based detectors are limited by their small effective area (~ 1 m^2). The most fruitful experiment was the Compton Gamma Ray Observatory (CGRO), which took data during 9 years (1991-2000) using different photon wavelengths (gamma-rays, X-rays, UV) covering six decades of the electromagnetic spectrum. It completed a full sky map of 271 gamma-ray sources with less than one degree of pointing accuracy for photon energies greater than 1 GeV. However, this accuracy was not enough to correlate 172 of the detected sources with known objects, so they remain still unidentified. Nowadays, the leading satellite project is the Fermi Gamma-ray Space Telescope (former GLAST) which was launched in June 2008. It covers an energy range from 30 MeV to 300 GeV, which includes the energy gap between previous satellites and ground-based detectors. The sky map of the first source catalog with the Large Area Telescope (LAT) on Fermi for eleven months is shown in Figure 1.11. It represents the deeper and better resolved map of the γ-ray sky.

Thousands of sources have been detected and studied bringing out exciting results which have allowed a better understanding of the physical processes at the sources. The proper knowledge of these processes is crucial since the objects producing high-energy gamma-rays are clear candidates for cosmic neutrino emission.

1.2.2 High energy Neutrinos

The detection of MeV neutrinos firstly from the sun has enabled the interpretation of nuclear reactions occurring in its core besides shading the light on fundamental properties of the neutrino particle. Later on, the detection of MeV neutrinos from SN1987A has definitely proved the validity to use neutrinos as a cosmic probe.

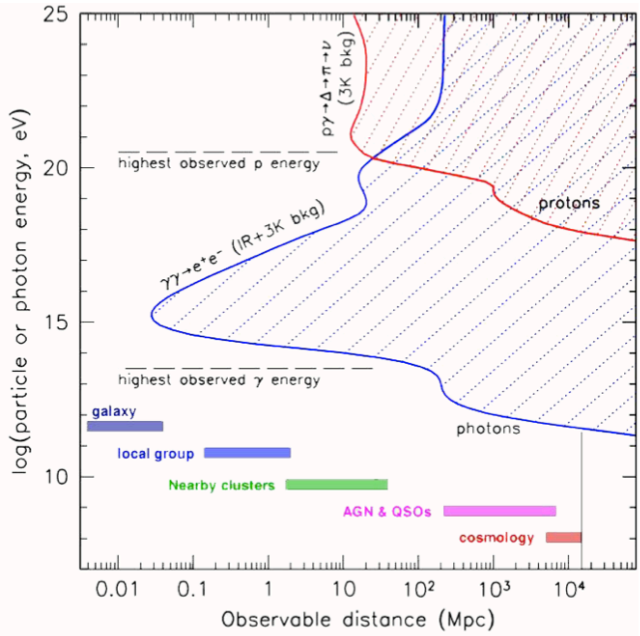

Figure 1.10: Proton and photon mean free path as a function of the energy

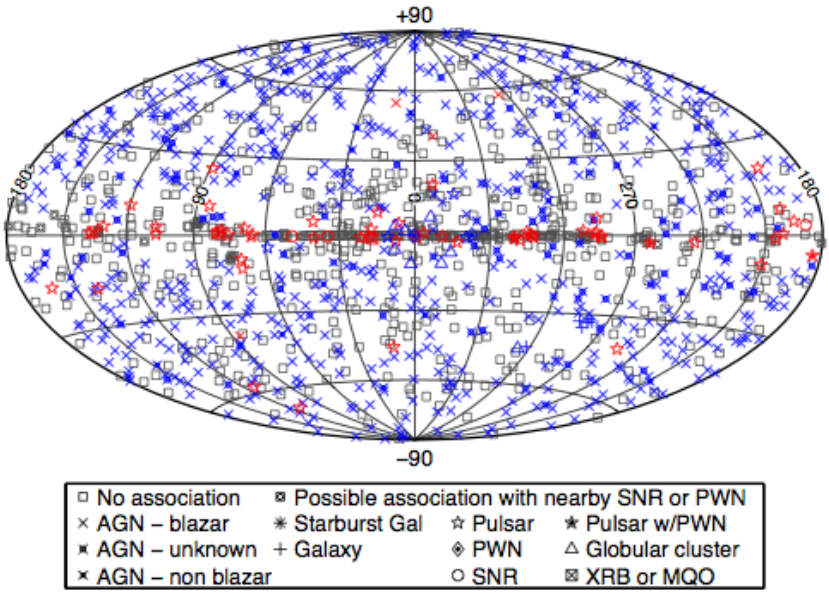

Figure 1.11: The 1451 1FGL catalog sources, showing locations on the sky (in Galactic coordinates with Aitoff projection) and associated source class, coded according to the legend. Gray symbols indicate unassociated sources, blue indicate associated sources, and red symbols firmly identified sources (primarily pulsars) [116].

High energy neutrino production in the frame of the hadronic process

Neutrinos are produced in astrophysical shock-fronts in p-p (or p-nuclei) and/or p-γ interactions via pion productions. Accelerated protons interact with photons in the surrounding of the cosmic ray emitters predominantly via the Δ^+ resonance:

$$p + \gamma \rightarrow \Delta^+ \rightarrow \pi^0 + X \tag{1.2}$$

$$p + \gamma \rightarrow \Delta^+ \rightarrow \pi^{\pm} + X \tag{1.3}$$

Protons can also interact with ambient matter (other protons, neutrons and nuclei), giving rise to the production of charged and neutral mesons:

$$p + p \rightarrow \pi^0 + X \tag{1.4}$$

$$p + p \rightarrow \pi^{\pm} + X \tag{1.5}$$

Neutral pions decay into photons (observed at Earth as γ-rays) with a probability of almost 98.8%:

$$\pi^0 \rightarrow \gamma\gamma \tag{1.6}$$

Charged pions decay into neutrinos with almost 100% probability:

$$\pi^+ \rightarrow \mu^+ + \nu_\mu \tag{1.7}$$

$$\overline{\nu_\mu} + \nu_e + e^+ \tag{1.8}$$

$$\pi^- \rightarrow \mu + \overline{\nu_\mu} \tag{1.9}$$

$$\nu_\mu + \overline{\nu_e} + e^- \tag{1.10}$$

Assuming that neutrino flux is produced by decays of pions and muons with ratio $\pi^+/\pi^- = 1$, the production flavor ratio of neutrinos of the source is ($\nu_e : \nu_\mu : \nu_\tau \sim 1 : 2 : 0$). This implies that tau neutrinos are not produced in the source. However, since neutrinos have non-vanishing mass eigenvalues, they oscillate on their way to Earth.

The fraction of the neutrino flavors at the source is equalized once they arrive at the Earth ($\nu_e : \nu_\mu : \nu_\tau \sim 1 : 1 : 1$) due to neutrino oscillations. Thus, equal numbers of electron, muon and tau neutrinos are expected to be observed at Earth.

Normalization of the spectrum

It is important to realize that at the source, the relation between the neutrino and gamma flux is robust [17]. The $\nu_\mu + \overline{\nu_\mu}$ neutrino flux ($\mathrm{dN}_\nu/\mathrm{dE}_\nu$) produced by the decay of charged pions in the source can be derived from the observed gamma ray flux by imposing energy conservation:

$$\int_{E_\gamma^{min}}^{E_\gamma^{max}} E_\gamma \frac{dN_\gamma}{dE_\gamma} = K \int_{E_\nu^{min}}^{E_\nu^{max}} E_\nu \frac{dN_\nu}{dE_\nu} \tag{1.11}$$

where E_γ^{min} (E_γ^{max}) is the minimum (maximum) energy of the photons that have a hadronic origin. E_ν^{min} and E_ν^{max} are the corresponding minimum and maximum energy of the neutrinos. The factor K depends on whether the neutral pions are of pp or pγ origin. For optically thin sources, in the case of pp interactions, 1/3 of the proton energy goes into each pion flavor and the energy in $\nu_\mu + \overline{\nu_\mu}$ corresponds to the energy in photons, K = 1. This flux has to be reduced by a factor 2 because of oscillations. For pγ interactions, K $\sim$ 1/4. If the source of neutrino emission is optically thick to TeV photons, the TeV signal avalanches to lower energies until it reaches a level at which it can escape the source. Thus, sources of GeV to sub-MeV emission can be sources of neutrino production as well, assuming an optically thick environment.
However, for extra-galactic sources, the degree of the photon absorption within the source itself or with the EBL/CMB when crossing the interstellar medium contributes to the major uncertainties on the prediction of the neutrino energy spectrum at Earth. The actual understanding leads to the conclusion that the same sources which have been described as the potential origin of cosmic rays (section 1.1.3) and which show signs of non-thermal photon emission are selected when discussing neutrino emission.

1.2.3 High-energy neutrino detection methods

Many arguments support neutrinos an excellent cosmic probes : Neutrinos are electrically neutral so that their trajectory is not affected by magnetic fields. They are stable, so that they reach Earth from distant sources, and weakly interacting so that they penetrate regions which are opaque to photons. Taking advantage of these characteristics, it is clear that their use in a complimentary way with high energy protons and high energy photons can give important insight on the hadronic mechanisms occurring in the sources as well as revealing their nature.

Signatures

Neutrinos can interact only via the weak interaction. The reactions that could be produced by a neutrino interacting with quarks in the matter [1] can be divided into two categories:

$$\nu_l(\overline{\nu_l}) + N \rightarrow l^-(l^+) + X \qquad \text{Charged Current(CC)} \tag{1.12}$$

$$\nu_l(\overline{\nu_l}) + N \rightarrow \nu_l(\overline{\nu_l}) + X \qquad \text{Neutral Current(NC)} \tag{1.13}$$

The CC reactions are weak interactions where a $W^\pm$ boson is exchanged and charged particles are created. The Feynmann diagram in the case of a ν_μ interacting via CC with a nucleon is illustrated in figure 1.12. In the case of NC reactions, it is the Z^0 boson which is exchanged to produce neutral particles.

Regarding the CC reactions, events with different topologies can be detected. Muon neutrinos give a μ which is characterized by the long path travelled before being absorbed. This produces long track events which are suitable for a good reconstruction in ice or water Cherenkov telescopes.

Electron neutrinos (ν_e) yield an electron which produces a shower (electromagnetic cascade) producing short-track events. The tau neutrino (ν_τ) interaction produces a τ

[1] Neutrinos can also interact with electrons, however, the smallness of the electron mass makes the interaction cross section negligible comparing to the nuclei. The cross section fractions are of the order of the masses fractions i.e. mN/me $\sim$ 1800.

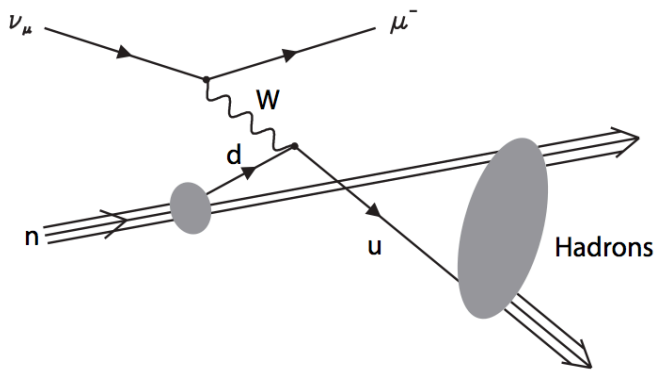

Figure 1.12: Feynman diagram describing the interaction of a muon neutrino ν_μ with the quarks u and d of a nucleon N in a charged current process. The interaction results in a muon and a hadronic shower.

whose behavior is energy dependent. If the energy is lower than about 1 PeV, tau particles decay, producing a track which can not be separated from the subsequent shower. On the contrary, if the τ energy is greater, the τ can travel several meters before decaying giving a second shower (double bang). This cycle of tau particles renders possible signal propagation through the Earth. Therefore, tau neutrino cascades are suitable for investigation of horizontal or Earth skimming neutrino air showers. Cascades are reproduced within the Earth until the shower comes out of the Earth and can be detected by either an Imaging Air Cherenkov Telescope or an air-shower surface array. Regular hadronic or electromagnetic air showers do not traverse the high column density and the neutrino signature is unique. This technique is for instance used by the AUGER experiment in the case of surface arrays and by the MAGIC experiment in the case of IACTs [52]. For illustration, the different neutrino topologies are shown on figure 1.13.

The probability to detect neutrinos raises as a function of the neutrino energy, since the cross section of neutrino-nucleon interactions increases with energy, as shown in figure 1.14.

Detection principle

The detection technique requires discriminating upward going neutrino induced muons against the much higher flux of downward atmospheric muons issued from the interaction of CRs in the atmosphere. As seen in figure 1.15(a), the track number 1 represents the signal neutrino produced outside the Earth atmosphere, while the track number 2 represents the muon produced after the interaction of an atmospheric neutrino with Earth, this latter constitutes an irreducible background. The track number 3 represents a down-going atmospheric muon in the detector referential. To reduce the flux of down-going atmospheric muons, the detector should be installed in a deep site where a layer of water or ice would shield it. Figure 1.15(b) shows the expected flux of atmospheric muons and atmospheric neutrinos in the ANTARES detector situated at $\sim$ 2300 m depth in the Mediterranean sea. Considering down-going events, even at such a depth, the atmospheric muon flux is about 6 orders of magnitude greater than the atmospheric neutrino flux.

In order to correlate the measured muon spectrum with the original neutrino spectrum,

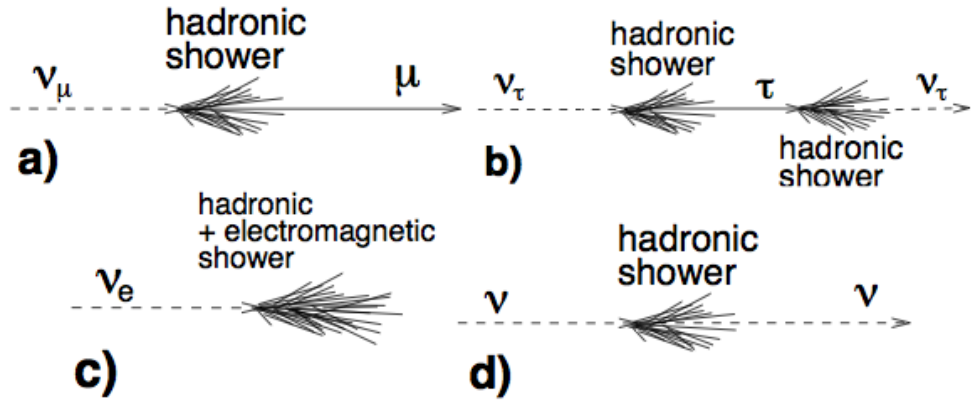

Figure 1.13: Signatures of the event topologies occurring for different types of neutrino interactions [60]. a) Charged current interaction of a ν_μ produces a muon and a hadronic shower; b) Charged current interaction of a ν_τ produces a τ that decays into a ν_τ, tracing the double bang event signature. c) Charged current interaction of ν_e produces both an electromagnetic and a hadronic shower; d) a neutral current interaction produces a hadronic shower.

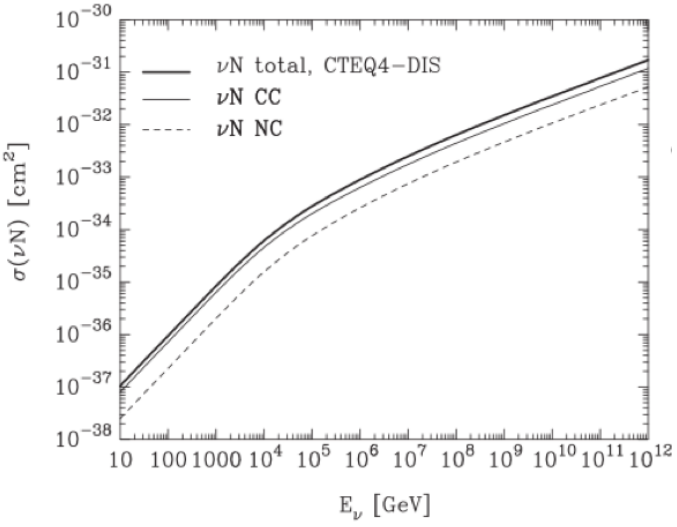

Figure 1.14: Evolution of the interaction cross section of neutrinos with respect to their energy (GeV) [56].

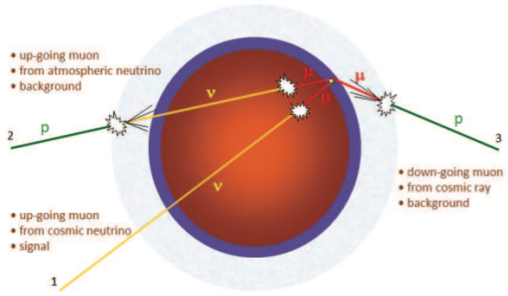

(a) Schematic depiction of signal and background components for a HE neutrino detector. Track 1 is the upward-going signal muon neutrino originating from astrophysical sources. Track 2 is the upward-going muon neutrino originating from the interaction of CRs with the atmosphere. Track 3 is the downward-going atmospheric muon issued from the interaction of CRs in the upper layers of the atmosphere.

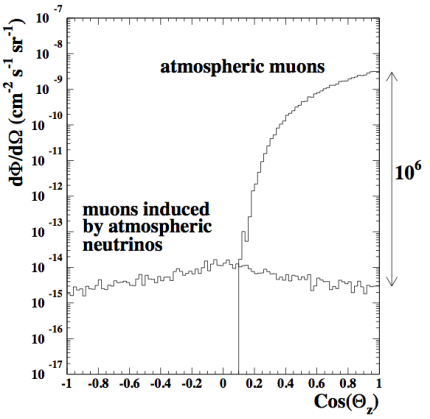

(b) Zenith angular distribution of the muon flux above 1 TeV from atmospheric muons and atmospheric neutrino induced muons at 2300 m water equivalent depth.

Figure 1.15: Signal and background considerations in HE neutrino detection

it is necessary to understand some facts; the opacity of the Earth, the energy loss of muons and the resolution of the detector over a wide range of angles and energies. We will mainly focus on the neutrino detection principle in water.

Several detectors use the properties of the propagating medium to detect indirectly the high energy neutrino via its out-coming charged lepton. The lepton, when propagating with velocity $\beta c > c/n$ in a transparent dielectric medium, with refractive index n, polarize the medium inducing the emission of coherent Cherenkov radiation along the surface of a cone as seen in figure 1.16, whose axis is coincident with the particle direction. Thus, a fraction of the particle energy is emitted as an electromagnetic shock-wave with low intensity [1].

The wave front propagates along a direction which forms a fixed angle, indicated as θ_C, with the direction of the charged lepton. The value of this angle depends on the charged particle velocity β and on the environmental properties:

$$\cos\theta_C = \frac{1}{\beta n} \tag{1.14}$$

The radiation per unit length x and wavelength λ is given by the Franck-Tamm formula [84]:

$$\frac{d^2N_\lambda}{dxd\lambda} = \frac{2\pi\alpha Z^2}{\lambda^2}(1 - \frac{1}{\beta^2 n(\lambda)^2}) \tag{1.15}$$

[1] Energy losses are mainly due to ionization which contribution is 2 or 3 orders of magnitude larger than the energy losses due to Cherenkov emission.

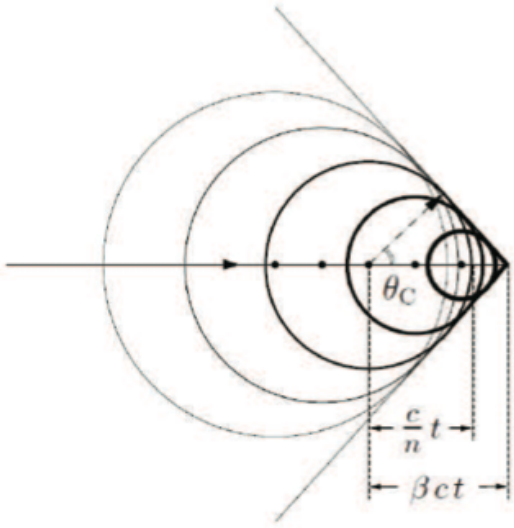

Figure 1.16: The emission of the spherical radiation and the front wave formation around a particle trajectory in a propagating medium.

where Z is the charge of the particle which propagates at superluminal velocity in the medium, and $\alpha = \frac{1}{137}$ is the fine structure constant.

For a detector which is sensitive to neutrinos with energies ranging from ∼100 GeV to ∼10 PeV, the radiation would mostly be in the visible wavelengths. In 300-700 nm wavelength range, the number of radiated photons/cm should be ∼ 200 photons. However, the emitted radiation decreases as a function of the wavelength :

$$\frac{dN}{dx} \propto \lambda^{-2} \tag{1.16}$$

The maximum detection efficiency is possible at frequencies corresponding to blue visible light ($\lambda \sim 440$ nm), where the absorption of light in sea water and ice is minimized. The choice of the Photomultiplier Tubes (PMT) equipping a neutrino detector is firstly based on their detection efficiency in this wavelength range.

The processes of absorption and scattering characterize the transmission of light in water. They are parametrized by the absorption length λ_a, the scattering length λ_s, and the scattering function $\beta(\theta)$ which describes the angular distribution of the scattering [91].

Deep sea water transparency is maximal in the blue, with typical values of 60 m for λ_a and λ_s. Seasonal variations are expected to affect these values, especially the scattering parameters which are governed by the amount of suspended particulate matter.

Detector response

The physical processes involved in neutrino and muon interactions place limits on the angular and energy resolution possible with a neutrino telescope while its location rules out the sky portion to investigate in neutrinos. These limits must be taken into consideration when optimizing the detector design.

The angular response of the detector with respect to the incoming neutrino direction is crucial for the identification of point sources of neutrinos. Three factors determine this response [1]:

- The angle between the neutrino and the muon in the neutrino interaction
- The deviation of the muon direction due to multiple scattering
- The angular resolution of the detector with respect to the muon

The effect of the two first factors is illustrated in figure 1.17. At 1 TeV, the average difference between the ν direction and the μ is about 0.7°. The difference decreases with increasing ν energy.

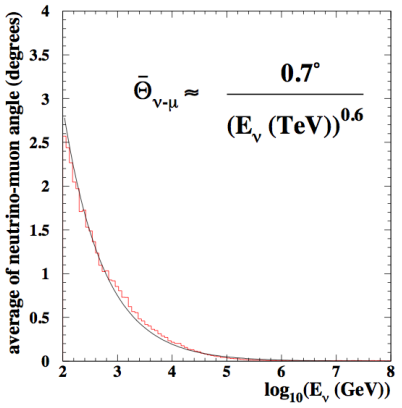

Figure 1.17: Angular difference between the initial neutrino direction and the muon track at the detector; the functional form shown reproduces the observed energy dependence well (solid black curve) [25].

The detector resolution is determined by the alignment quality of the detector components, the time resolution of the photomultipliers, the global timing of the readout system and the quality of the muon reconstruction. The reconstruction is affected by light coming from secondary particles and by scattered light. Monte Carlo studies show that an angular resolution of 0.1° can be achieved with large scale detectors for muons at highest energies. Above 100 TeV, the total angular resolution is dominated by detector effects, whereas below 1 TeV, the resolution is dominated by the angular distribution of the neutrino interactions.

The energy response is determined by the energy fraction transferred to the muon in the neutrino interaction, the energy lost by the muon outside the detector and the energy resolution of the detector. The muon energy determination requires different techniques in different energy ranges.

Below 100 GeV, the muons are close to minimum-ionizing, and the energy of contained events [2] can be determined accurately from the range. The threshold for this method is mostly dependent on the detector configuration. It is about 5-10 GeV for vertical tracks, depending on the vertical distance between groups of photomultipliers, and about 15 GeV for more isotropic events, depending on the horizontal distance between these groups.

[1] The Earth's magnetic field effect on the muon's trajectory is neglected for the scales used in ANTARES experiment

[2] Contained events refer to events with start and end points measured inside the detector.

Above 100 GeV, the range cannot be measured because of the limited size of the detector, but the visible range determines a minimum energy that can be used for the analysis of partially-contained events.

Above 1 TeV, stochastic processes (bremsstrahlung, pair production, γ-rays) are dominant, and the muon energy loss becomes proportional to its energy. The muon range above 1 TeV increases logarithmically with the muon energy. Figure 1.18(a) shows a monte carlo simulation of the mean muon range in rock as a function of the incoming neutrino energy. On the other hand, the detection efficiency increases with energy because of the additional energy loss. The correlation between the measured muon energy and the neutrino energy is shown in figure 1.18(b). Monte Carlo studies have shown that the neutrino energy can be determined within a factor 3 above 1 TeV from the average energy loss.

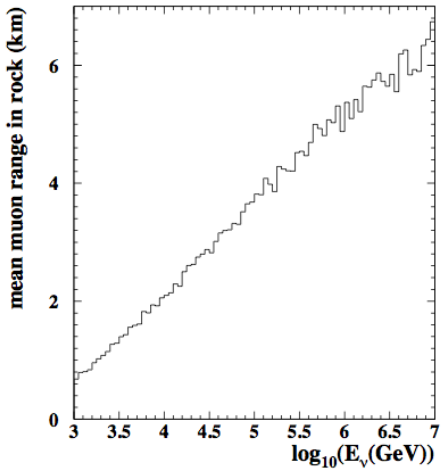

(a) Average range of the muon in standard rock as a function of the initial neutrino energy.

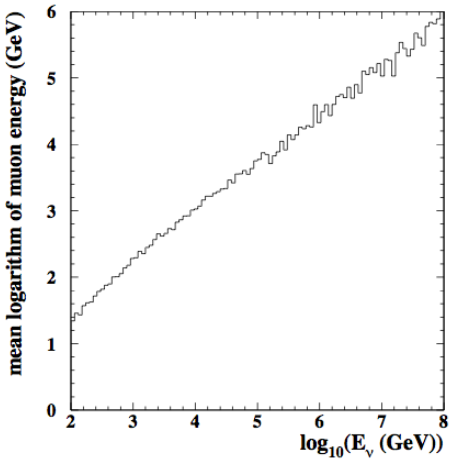

(b) Muon energy at the detector as a function of the parent neutrino energy.

Figure 1.18: Monte Carlo simulations of the muon range and energy as a function of parent the neutrino energy in ANTARES

Above 1 PeV, the Earth becomes opaque to upward-going vertical neutrinos as shown on figure 1.19. However, events with higher energies can still be detected closer to the horizon. Very high-energy tau neutrinos can be observed because the charged tauons produced in ν_τ interactions decay before they getting absorbed, producing ν_τ of lower energy which continue along the original ν_τ flightpath, but with decreasing interaction probability, resulting in an accumulation of events at the highest detectable energies.

The ANTARES neutrino telescope [47] (further described in the next chapter), situated at a latitude of 43° North, can observe upward-going neutrinos from most of the sky (about 3.5π sr), due to the rotation of the Earth. Declinations below -47° are always visible, while those above +47° are never visible. Declinations between -47° and +47° are visible for part of the sidereal day (68%) as shown on figure 1.20. Most of the Galactic plane is visible, and the galactic centre is visible most of the sidereal day. Since the ICE CUBE telescope [58] at the South pole is sensitive to positive declinations, the two detectors will have a reasonable area in common for cross-checks. At energies greater than $\sim$ 40 TeV, the interaction length becomes smaller than the Earth's diameter for ν_μ traversing the dense core of the Earth. Above 10 PeV, only nearly horizontal ν_μ are visible (see figure 1.19). If the field of view can be extended to 10° above the horizon at these energies

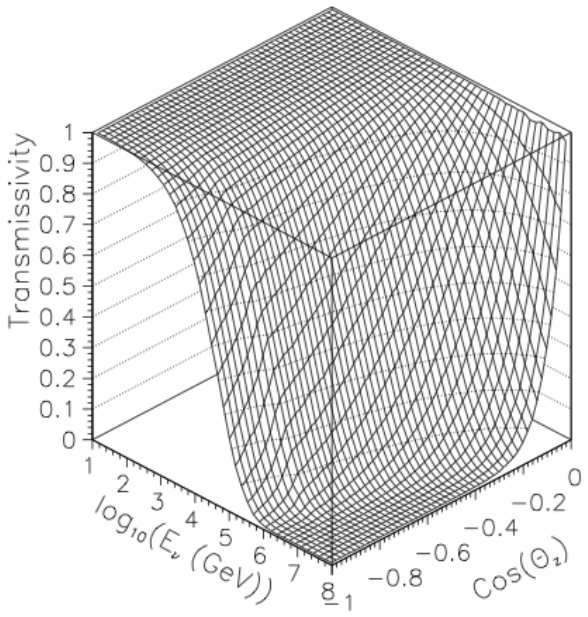

Figure 1.19: Transmittivity of the Earth as a function of incoming neutrino energy and zenith angle.

where the background is greatly diminished, a non-negligible fraction of the sky can be kept observable even at these energies.

While the muon leaves an optical track, cascade events produce a radio and an acoustic signal in addition to the optical emission. Indeed, as it was discussed by Askaryan in [28], the Cherenkov effect is not only present at optical and UV wavelengths. An electromagnetic shower is caused by a neutrino, produced by interactions of the secondary lepton with electrons from molecules in the medium[1]. The Askaryan effect was observed for cascade-like events in sand, salt and also in ice [57].

The need for such detection methods arise from the fact that the expected fluxes are so low at energies $E_\nu > 10^{16}$eV that a cubic-kilometer scale detector would not be enough to collect a sufficient number of events, requiring detectors of unprecedented size: the optical Cherenkov technique is not adequate for such an extension, because the deployment of mechanical structures with PMTs over a volume larger than a cubic-kilometer would imply not affordable costs. On the other hand, if the light sensors distribution is made to be sparse in order to increase the geometric detector size, this would result in poorer performances in angular resolution.

The propagation of radio and acoustic signals in ice, sand or salt, has the fundamental property of a larger attenuation length than for optical signals, of the order of several hundreds of meters. Radio or acoustic detectors could thus be sparser than optical ones, keeping high detection efficiency, covering a much larger area with nearly the same number of sensors, implying an important reduction of costs and resources.

Other ways to explore neutrinos highest energies is exploited by neutrino-induced air showers experiments. As noted before, tau neutrinos are the most promising eg. for the

[1]However, the corresponding signal induced by muons is too faint to be detected in Radio wavelengths.

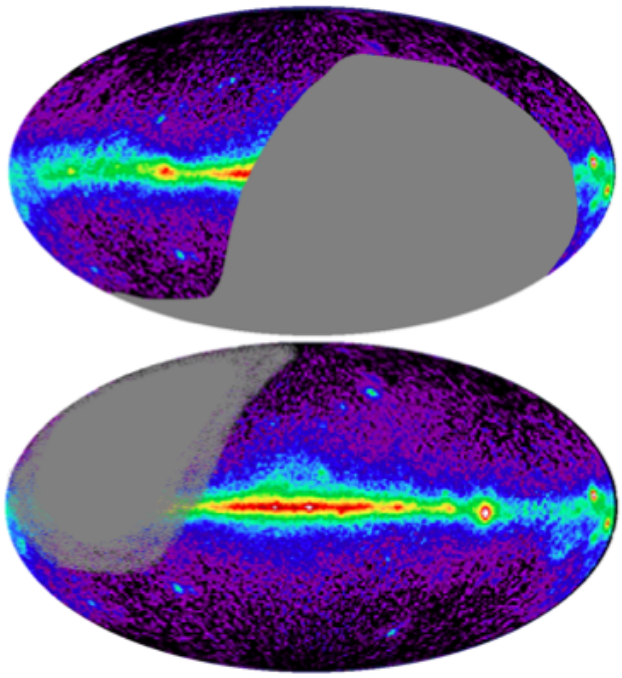

Figure 1.20: Top: Regions of sky observable (Galactic coordinates) by neutrino telescopes at the South Pole (Amanda, IceCube), Bottom: in the Mediterranean Sea (ANTARES at 42° North).

case of AUGER and HiRes. A Cosmic Ray Tau Neutrino Telescope (CRTNT), dedicated to the detection of neutrino-induced air showers is proposed. Cherenkov telescopes with the primary aim of TeV photon showers are also performing neutrino-shower analysis, for example MAGIC. Even higher neutrino energies can be detected when considering radio signals from air showers as planned by the LOFAR experiment. For such an experiment, with a neutrino energy threshold of $\sim 10^{22}$eV, the exploration of neutrinos issued from exotic particle decays, like topological defects is the primary goal since for astrophysical sources like AGNs or GRBs, the maximum neutrino energy lies below $\sim 10^{20}$ eV.

Chapter 2

The ANTARES Neutrino telescope

The ANTARES [1] detector is a deep sea telescope devoted to high energy neutrino detection. It also provides data of interest to a wide field of sciences including biology [11], environmental sciences, geology, geophysics and oceanography thanks to its unique infrastructure and extreme location.
The ANTARES Collaboration contains physicists from 28 institutes in 7 European countries (France, Germany, Holland, Italy, Romania, Russia and Spain).
The detector is situated in the Mediterranean sea, 40 km south of Toulon, at 42°48'N, 6°10'E (Figure 2.1), at a depth of 2475 m.

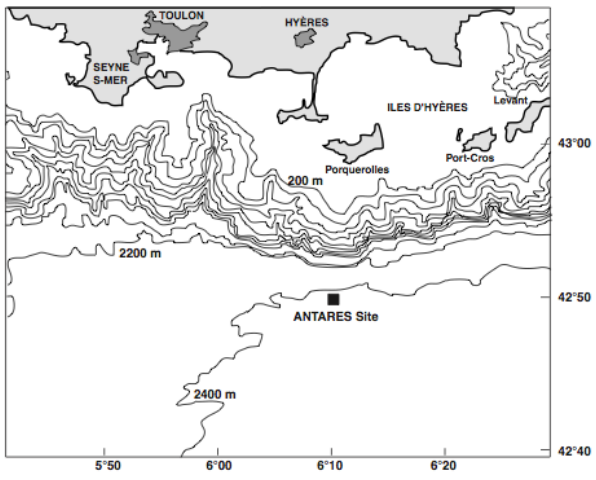

Figure 2.1: ANTARES location

Content

[1] **A**stronomy with a **N**eutrino **T**elescope and **A**byss environmental **RES**earch

2.1 The site properties

As discussed in section 1.2.3, the site where the detector is deployed dictates its achievable performances. In the case of ANTARES, different aspects of the Cherenkov light propagating medium were considered:

- **Water quality**

  The sensitivity of the experiment depends on the water transparency and the light scattering at large angles. Light absorption provides an upper limit to the distance between two sensors, which are used to search for time coincidences due to Cherenkov photons produced by the same muon track. The speed of light in water depends on the refractive index of the medium itself. Absorption of light in water can reduce the efficiency of the detector. The scattering of photons on water molecules or particulates reduces the detector performance and in particular the angular resolution. The knowledge of the dependence of these two parameters as a function of the wavelength is required. During several sea campaigns, the ANTARES collaboration measured these optical properties in the Mediterranean sea [7]. The main setup was an isotropic light source (pulsed LEDs) emitting in two different wavelengths (blue and UV). The absorption length is found to be $\lambda_{abs} \simeq 60$ (26)m and $\lambda_{sct}^{eff} \equiv \frac{\lambda_{sct}}{(1-cos\theta)} \simeq 265$ (122)m. Currently, the optical water properties are measured in situ using the LED Optical Beacon system.

- **Optical background**

  The background caused by the decay of the radioactive isotope ^{40}K diluted in water and the biological activity are the main optical background on the ANTARES site. ^{40}K dissolved in salt water decays, emitting electrons with an energy spectrum up to 1.3 MeV. Each electron produces 5 Cherenkov photons on average in the wavelength sensitivity window of the PMT. This gives rise to a photon flux of about 100 $\mathrm{cm}^{-2}\mathrm{s}^{-1}$ for a 50 m water attenuation length. This light emission is stable, which enables its use for the photomultipliers detection efficiency measurements. On the other hand, bioluminescence (light emitted by a wide range of sea animal species) is time dependent and also site dependent. Bioluminescence in the deep sea is not well known and one should measure the time structure of the emitted light as well as spatial correlations.

  This background can be described by two main components. The first one is a continuous baseline which component has two sources: the Cherenkov light emitted by the electrons produced in the ^{40}K β-decays and the biological activity due to bacteria colonies [1]. The conclusions from the site evaluation were that there is a typical value of $\sim$ 20-30 kHz for this baseline [18]. Measurements with the detector lines over 4 years have shown that the mean rate value is around 60 kHz as shown on the upper panel of figure 2.2. The second component of the optical background is composed by short bursts (generally lasting for hundreds of micro-seconds to seconds) which are simultaneously recorded by nearby Optical Modules (OM) and are observed superimposed on the constant baseline due to their high rates (20% over the baseline). An example can be found in the bottom plot of figure 2.2. These bursts are due to the passage near the detector of light emitting organisms. The modulation of the continuous component is not correlated with periods of high burst

[1] The biological activity is subject to seasonal variations.

activity, so the two effects are probably caused by distinct populations. In order to avoid the aging of the PMTs when high optical background rates are present, a safety threshold is established. If this threshold is exceeded, the PMTs are tuned to low gain mode until a stable low rate is recovered. In the meantime, the rates are monitored by the Instrumentation Line (IL). The burst rates can reach values of few MHz and, therefore, can produce an appreciable dead time in the acquisition system. A rate dependence on the site, season and undersea current velocity has also been observed. The optical background can be rejected by grouping the OMs in triplets since the electrons produced in the ^{40}K decays are low-energy electrons, they travel only few centimeters in water. Therefore, it is quite unlikely that they can produce a simultaneous signal in the three OMs.

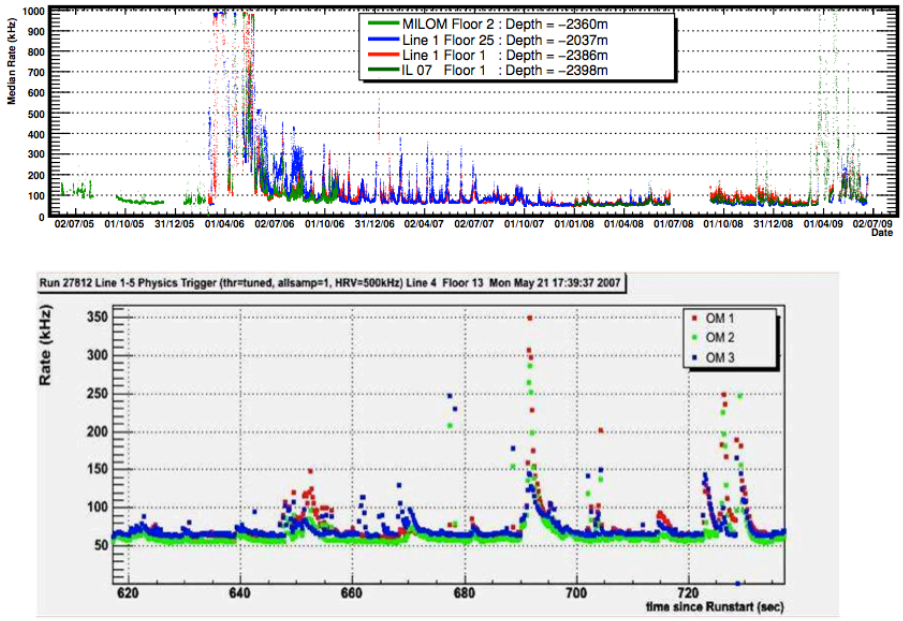

Figure 2.2: Top: Median rate of the optical background recorded over four years in two storeys of the Line 1, one storey of the IL, and one of the MILOM. A period of 3 months of instability in the baseline rate at the beginning of the plot can be seen. Bottom: Baseline rate for a short time period. Some bioluminescence bursts can be seen due to a light-emitting organism crossing the detector.

- **Bio-fouling**

  Deep sea bacteria have a tendency to colonize the surface of immersed objects forming a sticky bio-film which traps sediments. This process is called bio-fouling. The speed of formation of the bio-fouling is site dependent. It may affect the transparency of the optical module in the long term. The rate of accumulation has to be measured at the site and anti-fouling solutions have to be investigated.

  Underwater sedimentation and biofouling are natural processes. The former is caused by the dust accumulation and the latter by the adhesion of microorganisms, mostly bacteria, on external surfaces. Both effects can spoil the OM transparency. As it is seen in figure 2.3, the light transmission in the OM shows a general tendency

to decrease with time. However, some recovery correlated with the water current velocity has been observed, showing that surfaces are fouled by sediments more than by microbial adhesion and growth. Moreover, transmission seems to stabilize after several months. As shown, light transmission is maximum at θ= 90° angle, where only a global loss of $\sim$ 2 % is expected after one year of operation [20].

Average loss sensitivity for the ANTARES OMs is expected to be smaller, since they are downward oriented with an angle of 135°. Therefore, it is foreseen that during the years of ANTARES data taking, fouling will not be a significant problem.

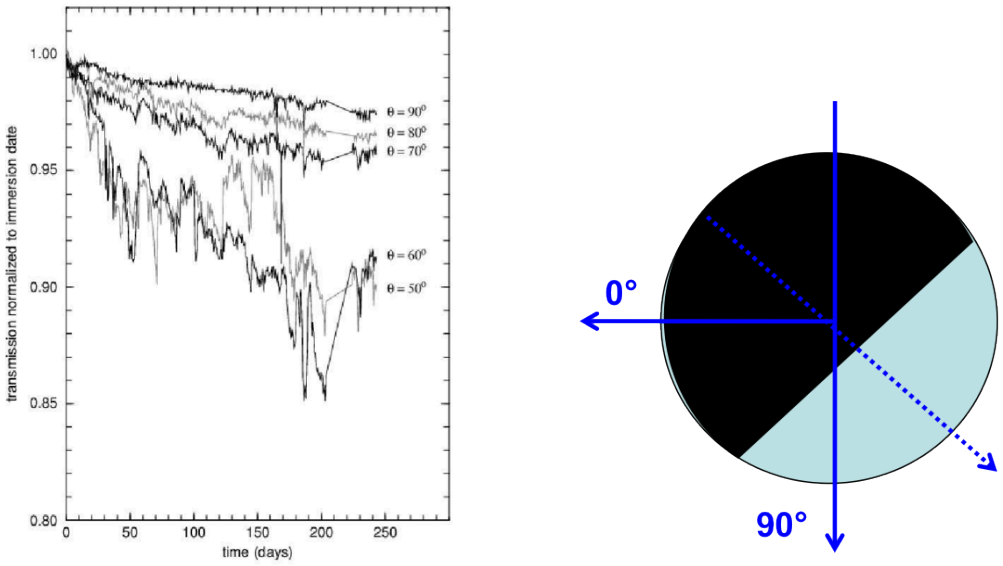

(a) Light transmission decreasing as a function of time. Five zenith angles for OM orientation are considered [20].

(b) Angle convention of the OM. The blue side is visible. The dashed blue line is the ANTARES OM orientation.

Figure 2.3: Light transmission as a function of the OM orientation.

- **Deep sea currents**

  Sea currents have to be taken into account in the mechanical design of the detector. At the ANTARES site, the detector lines sway in the sea current which is typically 5 cm s^{-1} with variations up to a maximum value of 30 cm s^{-1}.

2.2 The detector layout

ANTARES was designed and built with an area of 0.1 km^2. The design parameters were optimized according to the expected performances for high energy neutrino detection. The objective was to define a detector with a good angular resolution, a large effective area and good rejection against cosmic ray muons. The string arrangement is shown in figure 2.4. This arrangement is intended to minimize potential symmetries which could contribute to ambiguities in the reconstruction.

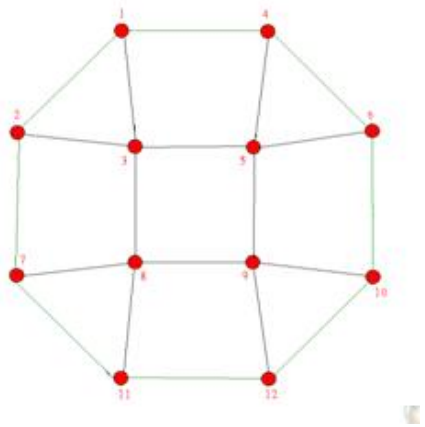

Figure 2.4: ANTARES 12 line configuration. The interline distance is $\sim$ 60 m.

2.2.1 The detector design

The detector is composed of 12 lines, 11 with a nominal configuration of 25 storeys, each of them housing 3 detection units (Optical Modules : OM), the twelfth line being equipped with 20 storeys and completed by devices dedicated to acoustic detection. The total number of OMs in the detector is 885.

The lines are 450 m long, regularly distributed along 350 m. The choice of the horizontal distance between lines depends on the energy range to be optimized. The lines are arranged with a 60-75 m spacing making the detector sensitive to muon energies greater than 100 GeV.

OMs contain the PMT and its electronics. The storeys containing OM triplets are spaced by 14.5 m with OMs oriented 45°, with the axis of the photomultiplier below the horizontal line.

An acoustic positioning system, a time calibration system and a set of devices for the monitoring of site environmental properties are integrated in the detector for complementary measurements. The apparatus also hosts AMADEUS [81], a test set-up devoted to feasibility studies of acoustic neutrino detection.

Each line is connected to a junction box on the sea bed, to be electrically fed and to provide a continuous stream of data to shore. The junction box is connected to the shore station by a 44 km long electro-optical cable as shown in figure 2.5.

2.2.2 The devices

The Optical Module

The Optical Module [19] as shown on figure 2.6 is the basic device of the ANTARES telescope. It contains the PMT enclosed in a borosilicate glass sphere, with 41.7 cm of inner diameter and 15 mm thickness. This sphere is devised to support high pressures about 600 atm at normal operation. Its refractive index is 1.47 in the 300 - 600 nm range, and light transmission is >95 % above 350 nm, so is well fitted for the Cherenkov light detection from muons.

The PMT must satisfy various specifications in order to provide adequate performance for the time resolution. Several PMT prototypes were studied comparing their angular

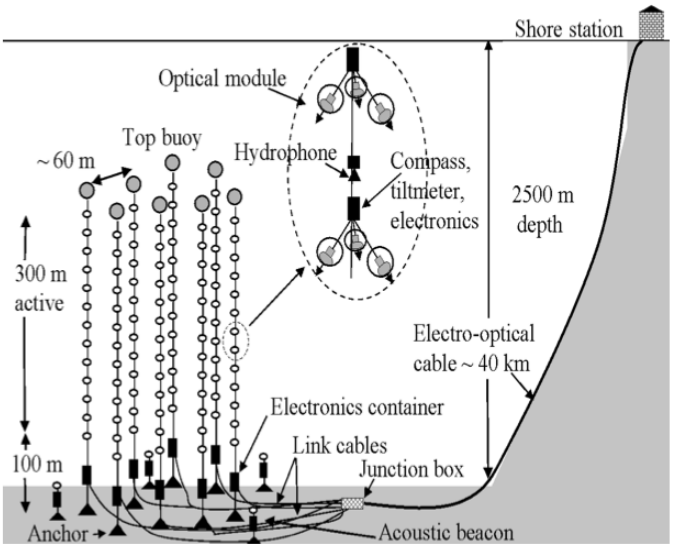

Figure 2.5: Schematic of part of the detector array; the magnified view shows two storeys and a hydrophone.

acceptance, quantum efficiency and time resolution before the final selection of the Hamamatsu R7081- 20 [33]. This model has the following properties :

- A hemispherical 10 inch photocathode diameter : The hemispherical shape insures the best angular acceptance. A 10 inch size is a good compromise between a large angular coverage and still a small contribution in the transit time spread due to the optical entrance.
- A gain $> 5.10^7$ working at high-voltage (< 2000 V)
- A peak to valley ratio > 2 leading to a good separation of the peak of 1 photo-electron (p.e.).
- Transit Time Spread (TTS) < 3 ns (FWHM) [1]: The transit time spread of the PMT has a direct impact on the time resolution i.e on the track reconstruction and hence on the angular resolution of the detector.
- A dark noise rate < 10 kHz for a 0.25 photo-electron (p.e.) threshold.

In order to reduce the influence of the Earth's magnetic field, which can degrade the TTS of the PMT by spreading the trajectories of the low energy photoelectrons in the optical entrance, a μ-metal cage with high magnetic permeability is also included. It also enables to get a uniform response from the 3 PMTs. To fix the μ-metal and the PMT to the glass sphere, the optical coupling between the PMT photocathode and the transparent hemisphere is realized with a silicon gel (refractive index for the three media are: $n_{gel} = 1.40$, $n_{glass} = 1.47$, $n_{water} = 1.35$). This optical coupling reduces photon internal reflection

[1]The TTS is defined as the FWHM of the distribution of the time intervals between the arrival of the photon at the photo-cathode and the detection of the corresponding current pulse at the anode, the PMT being at a fixed high voltage and uniformly illuminated at the level of one photoelectron.

in the glass sphere. Moreover, the opposite hemisphere is painted in black to minimize the reflection as well as insuring little efficiency for downward-going atmospheric muons. Finally, an internal built-in LED placed on the back of the PMT, is used for internal calibration and monitoring of the PMT transit time.

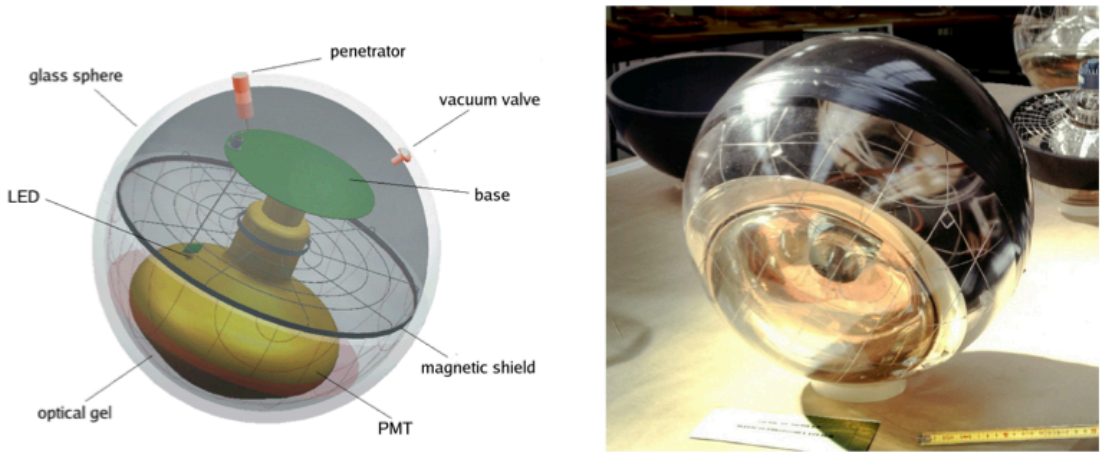

Figure 2.6: Left) Schematic view of the ANTARES Optical Module with its components. Right) Picture of an OM used in ANTARES (right).

The storey

In addition to the OM triplet, each storey contains a titanium box housing the Local Control Module (LCM) preventing the associated electronics from the water pressure. The LCM is placed at the center of the frame, as can be seen in figure 2.7. The LCM contains 2 Analogue Ring Samplers (ARS) per OM. This Application-Specific Integrated Circuit (ASIC) board insures dialogue between the OMs and the off-shore data control. All the electronic commands, the clock signal, the slow control, the HV supply and the readout, arrive at the ARS. Five storeys make up a sector, which is a stand-alone unit for power distribution and Data AcQuisition (DAQ). One out of five storeys has a Master Local Control Module (MLCM). Inside a MLCM is located an Ethernet switch, a bidirectional concentrator and a Dense Wavelength Division Multiplexing board (DWDM) which multiplexes the signal information from each sector (five storeys) onto one optical fiber. The MLCM contains all the electronic boards for all the functionalities at the sector level.

Some storeys have additional instruments: receiving Rx hydrophones (5 per line) devised for the acoustic positioning system, and a LED optical beacon (4 per line) for timing calibration purposes.

The line

Over 450 m of the line length, the lowest ∼100 m are not instrumented in order to avoid the fouling and the mud spread out from the seabed by the marine currents. The lines are anchored to the seabed by the Bottom String Socket (BSS), and held vertically by a buoy at the top of the line. The BSS houses a String Power Module (SPM), which provides the

Figure 2.7: Picture of a storey being deployed. There are 3 /acOMs facing 45° downward, and the LCM in the center housing the readout electronic cards. A LED optical beacon for timing calibration purposes can also be seen in the top part of the storey frame.

power supply to the associated instruments [1] and to all the LCMs in the string. In addition to the SPM, the String Control Module (SCM) contain the electronics required by the slow control system, the clock and the instruments of the BSS and controls of the data traffic from the MLCMs. In addition to the 12 detection lines, an additional instrumentation line is also available to perform detailed oceanographic and water properties measurements.

The Junction Box

Each SCM is connected to the Junction Box (JB) which provides power and control signals and receives the data from the lines. The JB is connected to the shore station through the Main Electro-Optical Cable (MEOC). The internal elements of the JB are protected from water pressure and corrosion by a titanium structure. The JB is equipped with 16 connectors for the 12 lines, the instrumentation line and the spares.

The Main Electro-Optical Cable

This element links the JB to the power hut, located on-shore. The power hut houses the power system and is the first infrastructure on shore reached by the cables. The MEOC contains an internal steel tube and 48 optical fibers. The cable is a standard telecommunication cable and is protected and insulated by a set of external layers of copper and steel, to avoid possible failures and breaking.

[1] The instruments in the BSS are an acoustic transponder RxTx hydrophone, a pressure sensor, and a sound velocimeter. In addition, the BSS of Lines 7 and 8 have a laser beacon for timing calibration.

2.2.3 The construction status

The registration of data started with the connection of the line 1 in March 2006. It was followed by line 2 in September 2006, lines 3, 4, and 5 in January 2007, than lines 6, 7, 8, 9, and 10 December 2007 and finally lines 11 and 12 in May 2008. In addition to the 12 detector lines, the instrumentation line MILOM was installed in ANTARES site to measure and study different parameters. It was operational from March 2005 to June 2007. It was removed, modified, redeployed and renamed IL-07.

Because of cable problems, line 10 was disconnected in Jan. and line 12 in March 2009 and both reconnected in Nov. 2009. Lines 9 and 6 were disconnected in July and oct. 2009 and reconnected end of 2010.

2.3 The data acquisition and filtering

2.3.1 Data acquisition

After the detection of a Cherenkov light signal by the PMT network, the **Data Acquisition system (DAQ)** [9] performs the following steps :

- the PMT signal digitization
- the data transport to the shore
- physics signals filtering from the background
- the storage of the filtered data to disk

The hardware of the DAQ system is a network consisting of hundreds of processors, as shown schematically in figure 2.8. A significant part of this network is located off shore. The off-shore processors are integrated in custom made electronics. The off-shore part of the DAQ system is connected to the on-shore part by the MEOC. The on-shore processors are standard PCs and are located in the shore station.

During data taking, the analogue signals from the PMTs are digitized by the ARS chips, which "read" the timing of each PMT signal and the total charge of the pulse. A voltage threshold of 0.3 photo-electrons (referred to as L0 condition) is set to eliminate small pulses due to the dark current in the PMT. A timing gate is tuned to integrate most of the PMT signal, while limiting the contribution of electronic noise, it is typically set to 35 ns. Each PMT signal above threshold is time stamped using a local clock integrated in the ARS chips. The combined time and charge information of the PMT signal within the integration time is referred to as a single photo-electron hit (SPE). However, an ARS has a dead-time of 200 ns. Thus, the readout of every PMT is made with 2 ARS using a token exchange protocol to reduce this dead-time. After the integration time of the first ARS chip, the second takes over.

The information registered by the LCMs is sent via an optical bidirectional 100 Mb/s link to the MLCM which merges all the data of a sector into a single Gb/s link thanks to an Ethernet switch. Then, the MLCM data goes to the SCM placed at the line anchor. Afterwards, the data from the whole detector (12 lines + instrumentation line) is directed to the JB and subsequently to the shore station located at Institut Michel Pacha at La Seyne- sur-Mer. The data transport between offshore and on-shore is made using the

DWDM technique, with multiple wavelengths to transmit different streams of data [1] along a single fibre. On shore, there is a multiplexer and a demultiplexer for each detector string. The DWDM system is also used for the transmission of the slow control data, and the distribution of initialization and configuration data. The data that are sent from the shore station to the detector are multiplexed on shore, and demultiplexed in the string modules. The on-shore part of the DAQ system is located in the shore station. It consists of a farm of standard PCs, a large Ethernet switch, the DWDM hardware, and the master clock system.

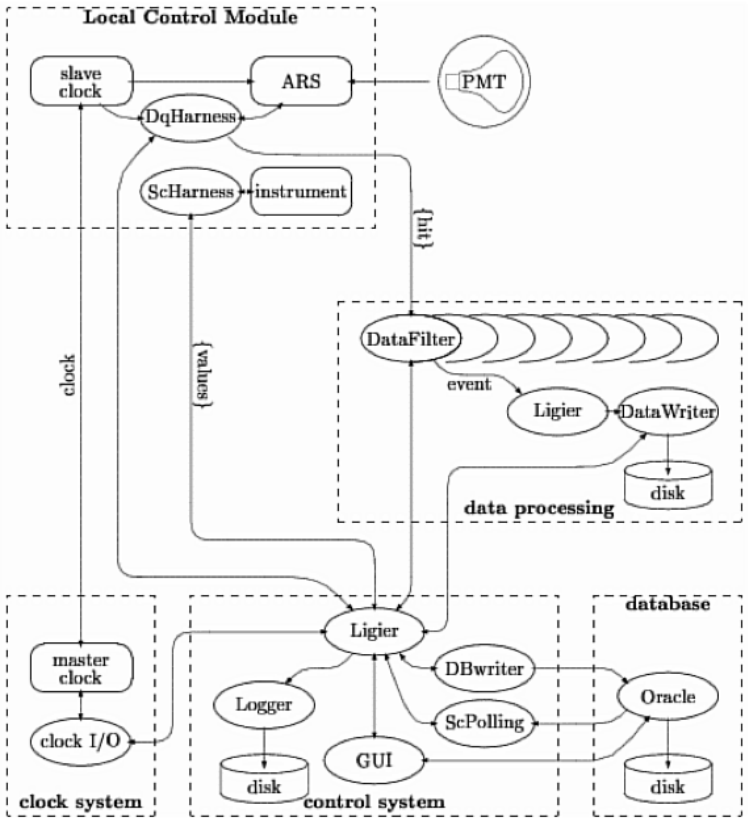

Figure 2.8: Schematic view of the the DAQ hardware. Each storey has its LCM. The information is sent by sectors to the SCM of each line and then to the shore station, at La Seyne-sur-Mer, via the junction box.

2.3.2 Data processing

ANTARES is operated in an all-data-to-shore mode concept, meaning that all signals that are recorded by the PMTs and digitized off shore are transported to shore without any off-shore data selection, giving a volume of raw data of 700 MB/s per line. As a result, all raw data are available on shore where the data processing can be applied. This minimizes the overall loss of physics signal, and allows different processing methods to be applied for

[1] The data flow ranges from a couple of Gb s^{-1} to several tens of Gb s^{-1}, depending on the level of the submarine bioluminescent activity.

specific physics analyses. The on-shore handling of the data is done with the DataFilter processes that run on each PC in the on-shore data processing farm. All data produced by each ARS chip in a certain time window, set to 104.9 ms, is buffered in what is called a frame. The frames from all off-shore DaqHarness processes that belong to the same time window are sent to the same PC in the on-shore data processing system, identified by the IP address.

The collection of frames belonging to the same time window is called a time slice. As a result, a time slice contains all data that were recorded during the same time interval by all ARS chips in the detector. When a sufficient number of correlated single photo-electron (SPE) hits is found to be consistent with a specific physics signal, the data are considered a physics events, and written to disk. The algorithms implemented in the data processing software are designed to find a physical signal by looking for space-time correlations in the data. From the time of the SPE hits, and the position of the PMTs, these algorithms calculate in real-time if hits could originate from light produced by muons traversing the detector, or other kind of interesting physical signatures.

2.3.3 Data filtering and writing

The ANTARES site is characterized by high background rates of the order of 70 KHz in low bio-activity periods, caused by bioluminescence and ^{40}K decays. The data output is processed by the DataFilter software, that run on each processor in the shore station PC farm as illustrated in figure 2.9. The physics signals selected by the DataFilter are passed to the DataWriter, which formats the events and writes them to disk in ROOT format.

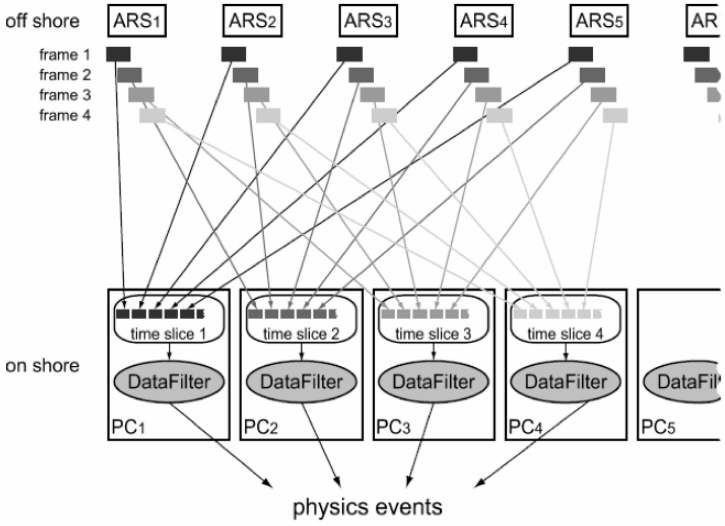

Figure 2.9: Scheme of the data processing based on time slices. All frames belonging to the same time window are sent to a single PC and form a time slice. The DataFilter program running on each PC processes the data in the time slice. All physics events are stored on disk.

Various trigger algorithms are applied to the data and a subset of the data is written to disk. The trigger algorithms rely on three main levels:

- L0: When the electrical signal passes the 0.3 p.e.
- L1: Two types of L1 can be distinguished:
  - When the electrical signal passes the HighThreshold (3 p.e. or 10 p.e. depends from the period of taking the data), the L0 will be L1.
  - The coincidence of at least two L0 from different OMs inside a 20 ns window of time on the same storey. The choice of this time window is such that time delays due to the difference in position of the PMTs and scattering effects are taken into account.
- T3: T3 is a cluster of L1. Two types of T3 can be distinguished:
  - The coincidence of two L1 in 80 ns time window.
  - The coincidence of two L1 in 160 ns time window.

Six trigger algorithms are currently applied:

- 3N : It requires at least 5L1 in time windows corresponding to a muon track.
- T3 (2T3): It requires at least 1 (2) T3.
- GC: The Galactic Center (GC) trigger requires 1 L1 and 4 L0 in the direction of the Galactic Center. It is used to maximize the detection efficiency of neutrinos coming from the Galactic Center.
- Minimum biais: Each second, within the time window is equal to 4 µs, the data is registered without any filter. This is used to monitor the data quality.
- K40: It is used for the in situ calibration. It requires 2 L0 on 2 optical modules of the same storeys within time windows of 50 ns.
- TST: The Transit Sources Trigger is activated when an alert is sent by γ-ray satellites such as *SWIFT* or *Fermi* via the GCN network[1]. In this case, 2 minutes of data around the trigger are saved without any filtering.

The dominant contribution to the triggered data stream is due to atmospheric muons traversing the detector, resulting in rates whose values depend on the particular choice of the trigger logic, between 2 to 10 Hz. At the trigger level, no distinction is made between events due to atmospheric muons, atmospheric neutrinos or cosmic neutrinos.

2.4 The detector calibration

2.4.1 Time calibration

The pointing accuracy of the detector is determined largely by the overall timing accuracy of each event. This is a quadratic sum of terms due to :

- the precision with which the spatial positioning and orientation of the optical modules is known (σ_{geom});

[1] http://gcn.gsfc.nasa.gov/

- the accuracy with which the arrival time of photons at the optical modules is measured (σ_{pmt});
- the precision with which local timing of individual optical module signals can be synchronized with respect to each other (σ_{align})

$$\sigma_t^2 = \sigma_{geom}^2 + \sigma_{pmt}^2 + \sigma_{align}^2 \tag{2.1}$$

Absolute time calibration corresponds to the ability of the detector to measure the time of each event with respect to the universal time (UT). This is done using a master clock on shore. The clock is linked to Universal Time (UT) through the Global Positioning System network which permits to match events to transient astronomical phenomena such as gamma-ray bursts. The required accuracy is of the order of $\sim$ 1 ms.

Furthermore, the clock is tuned to deliver clock signals at 20MHz which are converted to optical signals and distributed to each storey. By measuring the return time of the signal, individual time offsets can be properly assessed and were found to be stable within 0.1 ns. Figure 2.10 shows the round trip time measured for one electronics module. The stability and accuracy of the measurements are at the sub-nanosecond level, as required.

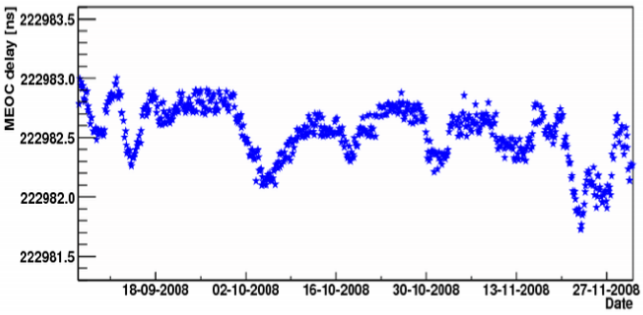

Figure 2.10: Measurement of the round trip time for clock signals between shore and one of the electronics module of the apparatus [109].

The relative time calibration is the ability of measuring the same time for an identical hit, not depending on which OM hit is recorded. In other words, to set a common reference for the whole detector. This is essential to achieve the best angular accuracy which is limited by the muon track reconstruction.

The main uncertainties contributing to the relative time resolution come from the transit time spread (TTS) of the signal in the PMTs which gives $\sim$ 1.3 ns. The calibration results show that the uncertainty of the transit time is less than 0.5 ns. Moreover, the optical properties of the sea water (light scattering and chromatic dispersion) give $\sim$ 1.5 ns for a distance of 40 meters. A contribution of the electronics of the system would spread the timing accuracy, which contributes with less than 0.5 ns to the overall relative time resolution.

Before the deployment of a line, the time offsets of each OM due to its specific PMT transit time and the front-end electronics are measured in a dark room to evaluate the relative time offsets between OMS in a specific line. This measurement is done using a a laser (λ=532 nm) able to send very short (FWHM $\sim$ 0.8 ns) and intense (E$\sim$ 1µJ) pulses of light to the PMTs through a system of optical fibres. Taking a particular ARS of a

specific OM as a reference, the inter-OM time offset can be calculated. Moreover, the ANTARES line is equipped with four Laser Optical Beacons which contain 36 blue LEDs arranged in groups of six on vertical boards forming a hexagonal cylinder. The individual LEDs have been synchronized in the lab to better than 0.1 ns. In situ calibrations are performed regularly, usually once a week, by flashing dedicated configurations of all these light sources. From the comparison between the measured and the expected time of the hits, taking into account the propagation time of the light, one can infer the time offset for each OM.

However, still there is a small inter-line time incertitude. This small offset is corrected in situ with external light sources which will relay the initial calibration and monitor any possible drifts. The proposed system consists of Laser beacons in the number of 2 situated on the BSS of line 7 and 8. They illuminate several strings simultaneously. The time offset between lines is found to be less than 5 ns.

2.4.2 Optical Module efficiency calibration

The optical module efficiency may evolve with time due to modifications of the PMT characteristics (gain, quantum efficiency, etc.), or to a change in the transmission of light from the glass sphere surface to the PMT photocathode(fouling, ageing of gel, etc.). As discussed previously, the ^{40}K present in sea water, is a natural source of single photoelectron signals. The distribution of the collected charge from such events can therefore be used to monitor the gain of the photomultipliers. An in situ measurement of the OM efficiency using an external calibrated light source will be a convolution of three distinct effects: the fouling of the light source itself, variations of the light transmission in sea water, and the OM's intrinsic efficiency, i.e. the change in the response of the OM in units of single photo electrons. A relative calibration is done by comparing the response of several OMs to the high power light sources. The light from these sources will arrive simultaneously at many OMs, allowing an accurate cross-check of the variation in amplitude response of the OMs. In the same way, the LEDs on each storey pointing at the OMs further up the string can be used to measure the change in light transmission.

2.4.3 Positioning

The absolute positioning of the 12 lines has been performed at the time of the deployment, using low frequency long baseline acoustic triangulation from the ship, connected to the GPS satellites. The strings are flexible structures which can bend by deep sea currents. Two positioning systems are integrated in the detector. The acoustic positioning system [27] relies on the measurement of the travel times of acoustic pulses, in the range of 40-60 KHz, emitted by devices located at the BSS of each line. Along each line there are five hydrophones, in order to detect acoustic signals emitted. The transmitters are also able to receive signals. In order to ensure optimal track reconstruction accuracy, it is necessary to monitor the relative positions of all OMs with accuracy better than 20 cm, equivalent to the 1 ns precision of the timing measurements. The reconstruction of the muon trajectory also require the knowledge of the OM orientation with a precision of a few degrees. A set of tiltmeter-compass sensors giving the local tilt angles of each storey with respect to the vertical line (pitch and roll) as well as its orientation with respect to the Earth magnetic north (heading) are used for this purpose. Figure 2.11 shows, as a result of the analysis of the signals received by hydrophones on one ANTARES detection line, the horizontal displacement from the nominal position, of each one of the five hydrophones.

Four additional autonomous transponders are located around the detector to increase the accuracy of the global alignment. In addition to the acoustic positioning system, each LCM is equipped with tilt-meters and compasses, to measure pitch, roll and heading of the whole storey. The positioning system is designed to measure the position of each OM within 10 cm or less.

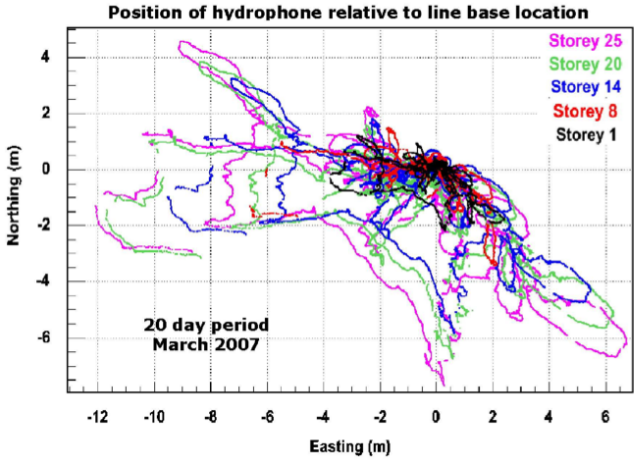

Figure 2.11: Horizontal tracking of the hydrophones of one particular line in a 20-day period. The hydrophones are located at 100, 202, 289, 376 and 448 m from the sea floor. The measurement precision is ∼10 cm [109].

2.5 The performances

2.5.1 Detector operation

The detector is running with 12 lines since the beginning of November 2010. The number of active channels is 773 which represents 87 % of OMs. The number of neutrinos per active 24h is shown in Figure 2.12 for 2009 and 2010. The numbers given are averaged over each month: with 12 lines detector we get about 7 atmospheric neutrinos for 24h of data taking: 5 are reconstructed on more than 1 line and 2 are reconstructed on 1 line.

Figure 2.13 shows the number of effective days of physics runs. During a period of elevated bioluminescence in spring 2010, the PMT gains were reduced by 2, 4 and 8, effectively increasing the thresholds by the same factor (i.e. L0 threshold at $\sim$ 0.7 for Gain/2). This allowed to decrease the single counting rates to match the available data transmission bandwidth, but required specific charge calibrations for each configuration. The G/N runs are included in the numbers shown in figures 2.12 and 2.13, but currently only the Gain/2 is usable for physics in a straight-forward way.

Figure 2.14 shows the rate of down-going muons reconstructed on more than one line in 2009-2010. With 12 lines this rate reaches about 2.5 Hz.

2.5.2 Effective area

The effective area is defined as the equivalent surface, perpendicular to the incident particle beam, which is 100 % efficient. It represents the evolution of the detection efficiency

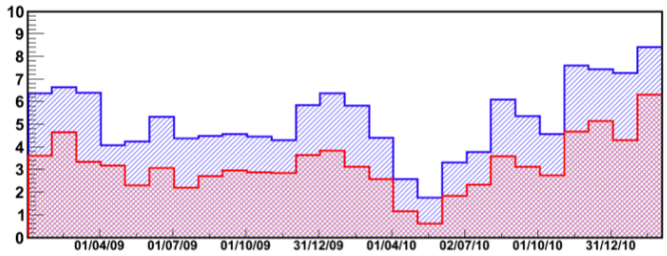

Figure 2.12: Number of reconstructed up-going muons per day (neutrinos): the red part is multi-line neutrinos and the blue part is single-line neutrinos. The blue histogram is added to the red one, so the total number of neutrinos per day is the blue line. The dip observable in spring 2010 is due to the attempt to do data-taking with gain divided by 2, 4 and 8 during high bioluminescence periods. The efficiency of these run setups is lower than in the nominal gain case, but the detector is operating safely and is not blind. In 2009, this strategy was not applied and the high bioluminescence periods are not included.

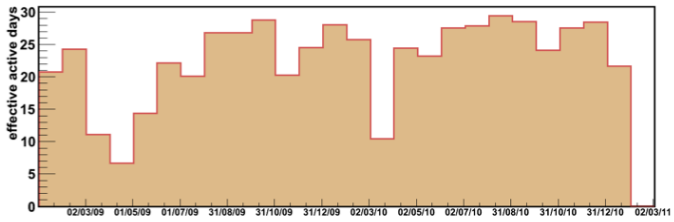

Figure 2.13: Number of active days per month in 2009-2010. *Active* means physics triggers. Are excluded from these numbers the calibration runs, and the runs for which HV has been reduced to get a gain divided by more than 8 (in very high bioluminescence periods). It has to be noticed than in spring 2009 the gain was systematically reduced by a factor 10 (less active days) while in Spring 2010, operation with Gain/2,4,8 was performed, to stay sensitive to physics.

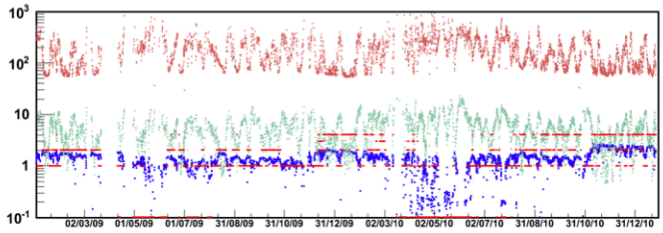

Figure 2.14: in blue: rate (Hz) of down-going muons reconstructed on more than one line. The step in November 2010 corresponds to the reconnection of lines 6 and 9. In brown: single counting rate (kHz). In green: sea current speed (cm/s). In red: code for the type of trigger used: 1 means *standard* causality triggers, 2=1+Galactic Center trigger, 4=2+*low energy* triggers. GC and low energy triggers are used when counting rates are low. Values at 0.1 mean: for 2009 use of causality trigger only (which is the tightest one); for 2010: gains divided by 2,4,8.

(Trigger + reconstruction + quality cuts) as a function of the energy and the direction. The effective area for neutrinos is much smaller than the muon effective area due to the much smaller neutrino cross-section. Since the cross-section increases with the neutrino energy, so the neutrino effective area does, and becomes greater than 1 m^2 for energies above 100 TeV. Above this energy, neutrinos crossing the Earth at a nadir angle of 0° will probably interact during its travel, because of the long path through the Earth. Therefore, an opacity effect appears depending on the angle. Neutrino events with very high energy are thus expected only for angles close to the horizon. The formula giving the effective area of a neutrino telescope depends on the energy of the incoming neutrino (E_ν) and its direction (θ_ν, ϕ_ν), i.e. the altitude and azimuth in horizontal coordinates. It can be written as:

$$A^{\nu}_{eff}(E_\nu, \theta_\nu, \phi_\nu) = \frac{N_{sel}(E_\nu, \theta_\nu, \phi_\nu)}{N_{gen}(E_\nu, \theta_\nu, \phi_\nu)} \times V_{gen} \times (\rho N_A) \times \sigma(E_\nu) \times P_{Earth}(E_\nu, \theta_\nu) \qquad (2.2)$$

where N_{gen} and are N_{sel} respectively the number of events generated and reconstructed (after the corresponding quality cuts), V_{gen} is the generation volume, ρN_A takes into account the nucleon density being N_A the Avogadro's number and ρ the matter density, $\sigma(E_\nu)$ accounts for the cross-section of the neutrino which depends on the energy and finally, P_{Earth} is the probability for a neutrino of energy E_ν and zenith angle θ_ν to cross the Earth up to the interaction point. In Figure 2.15, an example of a neutrino effective area is shown for a particular set of quality cuts. A distinction based on the neutrino nadir angle direction is made.

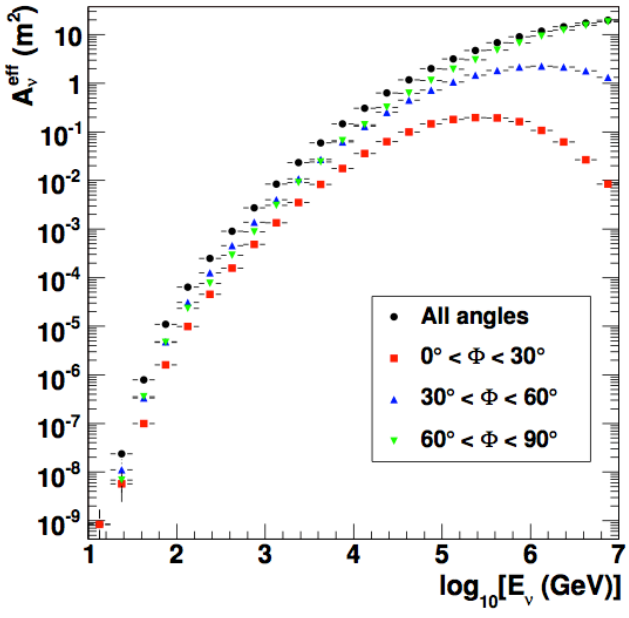

Figure 2.15: Neutrino effective area averaged over several neutrino angle directions as a function of the neutrino energy. Effective areas for different nadir angles (ϕ) are shown. The Earth opacity at high energies can be noticed.

2.5.3 Angular resolution

One of the most important features of a neutrino telescope is its angular resolution. In ANTARES, the muon (neutrino) angular resolution is defined as the median of the distribution of the angle between the true MC neutrino direction and the reconstructed muon direction. The angular resolution is composed of two terms: one dependent on the kinematics and one dependent on the reconstruction. At high energies, the neutrino and the induced muon are essentially aligned. In this case, the pointing accuracy is dominated by errors in the reconstruction of the muon trajectory. The good water properties of the ANTARES site, together with the expected detector resolution (timing calibration, positioning, electronics, etc.), provide an angular resolution better than 0.3° for neutrino events with $E_\nu > 10$ TeV, as can be seen in the Figure 2.16. A good angular resolution is very important in order to point-back to the cosmic neutrino sources.

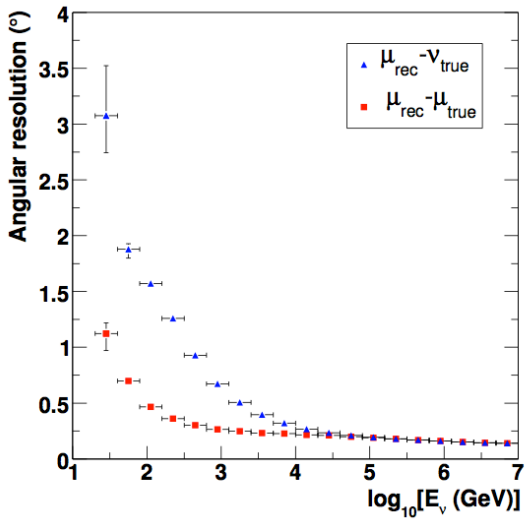

Figure 2.16: Angular resolution of ANTARES according to a detailed simulation of the detector. The points represent the medians of the angular error distribution for muons and neutrinos. Below 10 TeV the angular resolution is dominated by the kinematic angle between the neutrino trajectory and the muon track. Above 10 TeV, it depends on the quality of the reconstruction (calibration, electronics, etc.)

2.6 The multi-messenger approach in ANTARES

Photons, cosmic rays, high-energy neutrinos but also gravitational waves are all different messengers which have in common the same potential astrophysical sources. A strategy based on the detection of such messengers in a temporal and/or directional window have been under investigation in the recent years. The analysis, both at the on- and off-line levels, in ANTARES relies on the extraction of the maximum amount of information from the data and to search for correlations between signals in different components of the cosmic radiation. In addition the optical follow-up of neutrino alerts, which is described in the third part of this manuscript, two other multi-messenger experiments are actually on-going in ANTARES.

2.6.1 Gamma-rays and neutrinos

The search of Gamma-Ray bursts relies on a special data taking procedure. Neutrino data taking for GRBs is triggered by satellites, namely *SWIFT* and *Fermi*.
The left plot on figure 2.17 shows the principle upon which the data taking is done. The DAQ is linked with a socket connection to the GCN. When a GRB alert is received from the GCN, the standard data processing (described in section 2.3) continues, and in parallel to that, the satellite triggered data taking is applied: all raw data covering a preset period (presently 2 minutes) are saved to disk for each GRB alert. There are about 1-2 GRB alerts per day, and half of them correspond to a real GRB. The buffering of the data in the data filter processors is used to store the data up to about one minute before the actual alert. The amount of data that can be kept in memory depends on the background rate in the sea water, the number of data processing PCs, and the size of the RAM. These data not only cover the delay between the detection of the GRB by the satellite and the arrival time of the alert at the ANTARES site, but also include data collected by the ANTARES detector before the GRB occurred. These data therefore include a possible early neutrino signal that is observable before the gamma rays. The right plot on figure 2.17 shows the performance of the satellite-triggered data taking. The dashed line shows the number of GRB alerts from the GCN per month as a function of time, and the solid line shows the number of satellite triggered data taking sessions that were realized. Although data taking with ANTARES is in principle continuous, inefficiencies can occur, for example, when a GRB alert is distributed during a calibration run, or due to power loss. The typical efficiency of the satellite triggered data taking is about 90%.

Presently, two analysis are being done on the standard filtered data. First, one can take advantage of the expected low background relying on positional and timing information in the GCN message while keeping the detection threshold low [41]. The neutrino-induced muon analysis in correlation with GRBs for the 5-line configuration detector has been performed. No events were found from the direction of any of the GRBs in coincidence with their prompt photon emission, allowing a limit to be placed on the flux of neutrinos produced by these GRBs as shown on figure 2.18. Second, a recent analysis exploring the shower channel is complementary to the more commonly used up-going muon channel. Such analyses focus on down-going events and look for a global excess of the muon flux in a direction correlated with the position of the source (and within a given time window, if the source is transient). The corresponding detection volume is smaller, but has the advantage of being sensitive to neutrinos of any flavour[98].

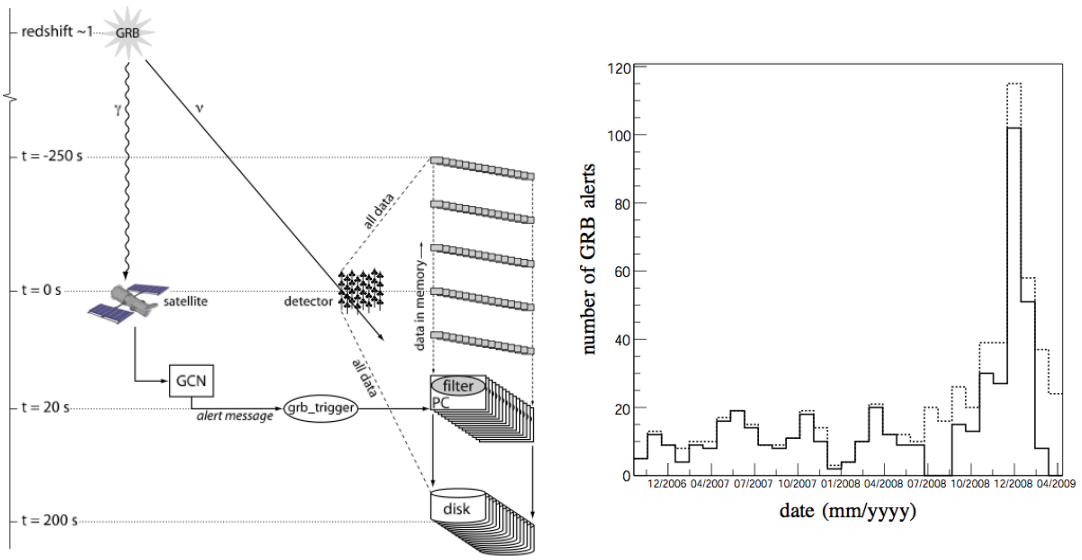

Figure 2.17: a) Time line of the different events during a GRB. When an alert from the GCN is received by ANTARES (GRB trigger program), all raw data covering a few minutes are saved to disk, including all data in memory. Any neutrino signal from the GRB (before, during, and after the photon detection by the satellite) is stored on disk. b) The satellite triggered data taking of ANTARES since the implementation of the satellite triggered data taking system. The dashed line indicates the number of GRB alerts distributed by the GCN per month. The solid line indicates the number of GRB alerts for which the satellite triggered data taking was applied. In November 2008, the GCN started the distribution of alerts from the Fermi satellite.

2.6.2 Gravitational waves and neutrinos

Taking advantage of the concomitant data taking periods for ANTARES and Virgo/LIGO in 2007 and 2009-2010, a GW-HEN program was initiated in 2009 [97]. Several kinds of sources exist for which the simultaneous emission of high energy neutrinos and gravitational waves is expected. The VIRGO/LIGO network monitors a good fraction of the sky in common with ANTARES, as can be seen from figure 2.19. Joint searches are ongoing within a dedicated "GWHEN" working group: preliminary investigations indicate that, even if the constituent observatories provide several triggers a day, the false alarm rate for the combined detector network can be maintained at a very low level, $\sim 1/(600\ \mathrm{yr})$ [121].

2.6.3 Search for point-like sources

A cosmic neutrino point-like source would manifest itself as a localized excess of events on top of the background. To ensure a high signal-to-noise ratio, the event reconstruction and selection are optimized to provide tracks with good angular resolution, in a wide energy range. The event selection was optimized to achieve the best discovery potential for an assumed power-law signal with energy spectrum with spectral index $\gamma = 2$. Figure 2.20.a shows the preliminary sample of selected events: 2040 neutrino candidates have been identified. Simulations indicate that this sample is contaminated by a 40% of misre-

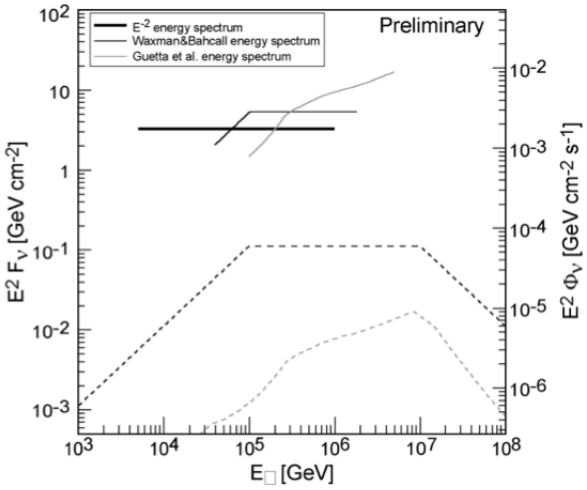

Figure 2.18: The 90% CL upper limits for three different neutrino energy spectra obtained for the Line 1-5 GRBs. The left y-axis indicates the upper limits on the total fluence of the 37 GRBs registered during line 1-5 period, the right y-axis indicates the upper limits on the flux. The limits are shown as a function of the neutrino energy. The thick solid line is the upper limit for an E^{-2} energy spectrum, the thin solid line is the upper limit for the Waxman & Bahcall energy spectrum, the thin grey line is the upper limit for the Guetta et al. energy spectrum. The black dashed line is the expected neutrino fluence for 37 GRBs with the Waxman & Bahcall energy spectrum. The grey dashed line is the sum of the 37 expected individual GRB fluences according to Guetta et al.

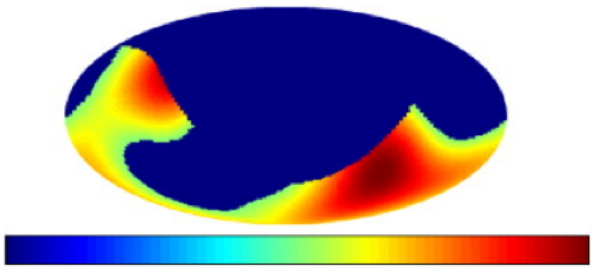

Figure 2.19: Instantaneous common sky coverage for VIRGO+LIGO+ANTARES in geocentric coordinates. This map shows the combined antenna pattern for the gravitational wave detector network (above half-maximum), with the simplifying assumption that ANTARES has 100% visibility in its antipodal hemisphere and 0% elsewhere. The colour scale is from 0% (left, blue) to 100% (right, red)

constructed atmospheric muons. Based on these events, a dedicated search for candidate sources, already known as HE gamma-rays emitters, was performed with a list of 24 astrophysical candidate neutrino sources. It has been found that all observed excesses are compatible with the background hypothesis, a corresponding flux upper limit of 7.5 $\times 10^{-8}$ $(E/GeV)^{-2} GeV^{-1} s^{-1} cm^{-2}$ has been set. The 90% C.L. upper limits for the flux coming from these 24 candidate sources as a function of their declination together with the limits set by other experiments are shown in figure 2.20.b.

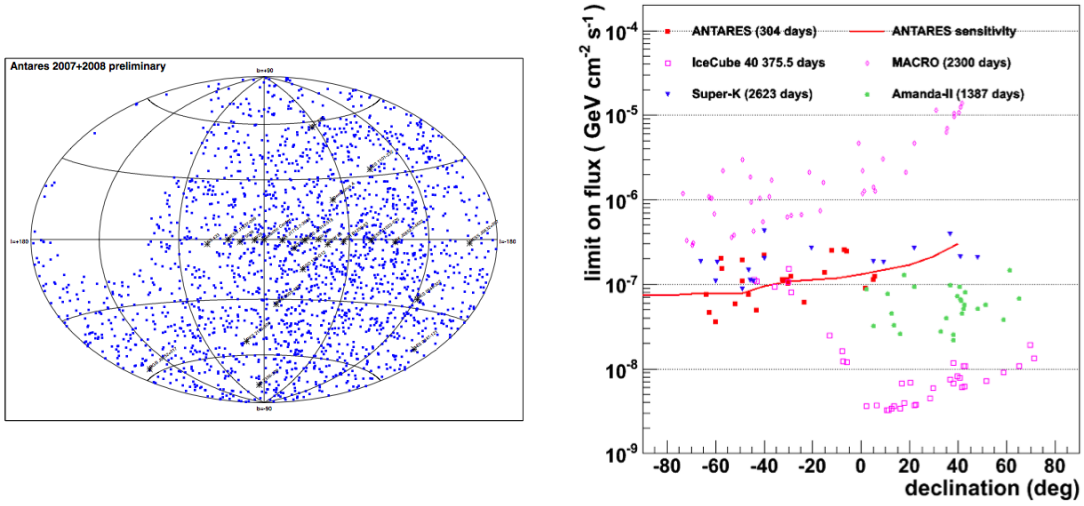

Figure 2.20: a) Skymap of the 2040 neutrino candidates selected for the point source search. Stars indicate the 24 sources of the candidate list. b) 90% C.L upper limit on the flux from 24 candidate point sources as a function of declination (red boxes). The red line is the sensitivity (i.e. the expected median limit). Results from other experiments are also shown.

Part II

Crystal-based hybrid Photomultipliers

Chapter 3

Development of crystal-based hybrid photomultipliers

Because of the low neutrino fluxes expected in the actual mediterranenan neutrino telescopes, an extension to bigger telescope sizes is foreseen. The KM3NeT research infrastructure in the deep Mediterranean Sea will host a multi-cubic-kilometre neutrino telescope. The KM3NeT neutrino telescope will complement the IceCube telescope currently being installed at the South Pole in its field of view. The main challenge in designing the KM3NeT neutrino telescope is to identify and validate technical solutions that are cost-effective, reliable, can be constructed in a reasonably short period and provide the targeted sensitivity. An initial set of design concepts is summarized in the KM3NeT Technical Design Report [1]. The neutrino telescope will be an array of optical modules, attached to vertical structures (detection units, DUs). The DUs are anchored on the sea floor and kept vertical by subtended buoys. They are connected to shore via a sea-bottom network of electro-optical cables and junction boxes. Clusters of PMTs will be used. Although PMT designs are working efficiently in ANTARES, new solutions can be pursued in KM3NeT in order to meet the following objectives: reduction of background due to bioluminescence and 40K decay by excellent separation of single hits from multiple hits; ease of manufacturing and deployment; increased cost effectiveness. In this frame, KM3NeT has investigated optical modules based on hybrid photon detectors (X-HPD) using a large-area spherical photocathode.

In this chapter, the general principle of photomultipliers is presented first. In the second section, crystal-based hybrid photomultipliers are described. Then, as a result of this thesis, the elaboration of a crystal-based hybrid photomultiplier conducted with Photonis is presented and finally the results will be discussed.

Content

[1] `http://www.km3net.org/TDR/TDRKM3NeT.pdf`

3.1 Introduction

The catalogue of photomultiplier application categories is very rich. Apart from being used in most of the high energy physics and astroparticle experiments aiming the detection of light emitting particles, they are also extensively used in medical diagnosis (positron cameras used in tomography based on the coincident detection of gamma-rays accompanying annihilation of a positron and an electron), scintillation counting (the measurement of nuclear radiation by detecting light or single scintillations emitted from a scintillation material receiving nuclear radiation) among many other domains.
However, the photomultiplier industry is still restricted to very few companies : Hamamatsu [1], ET Enterprises [2] and Photonis [3]. Due to the extreme care and the know how needed to construct such devices as well as their relatively high manufacture expense, this industry remains very restrictive.

3.2 The photomultipliers: a short review

The photomultiplier is a very versatile and sensitive detector of radiant energy in the ultraviolet, visible, and near infrared regions of the electromagnetic spectrum. A schematic diagram of a classical photomultiplier tube is given in figure 3.1.
The photocathode is the basic radiation sensor. Located inside a vacuum envelope, it is responsible of the conversion of incident photons into electrons under the application of an electric field. Photoelectrons emitted from the photocathode are directed to an electrode or dynode within the envelope. A number of secondary electrons are emitted at this dynode for each impinging primary photoelectron. These secondary electrons in turn are directed to a second dynode and so on until a final gain of typically 10^6 is achieved. The electrons from the last dynode are collected by an anode which provides the signal current that is read out.

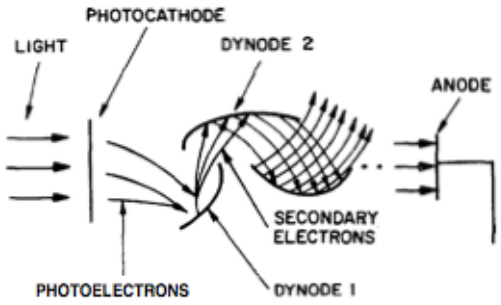

Figure 3.1: Schematic representation of a photomultiplier tube

[1] http://www.hamamatsu.com/
[2] http://www.et-enterprises.com/
[3] http://www.photonis.com/

3.2.1 Early development

The history of the photomultiplier is rooted in early studies of secondary emission. The use of secondary emission as a means for signal amplification was proposed as early as 1919[112] by Austin and Starke. In 1935, Iams and Salzberg[67] of RCA (Radio Corporation of America) reported on a single-stage photomultiplier. The device consisted of a triode photomultiplier tube with a photocathode combined with a single-stage dynode, producing a gain near eight. At that time, the only application reported is the use of the photomultiplier device as a sound pick-up for movies. The first commercially successful photomultiplier tube was the type 931, first described by Zworykin in 1939 [128] and later by Rajchmann and Janes [101]. The PMT consisted of a compact circular array of nine dynodes utilizing electrostatic focusing. The photocathode consisted of Ag-O-Cs but was later replaced with Sb-Cs. The 931 set the industry standard in photomultiplier tube technology.

3.2.2 PMT Fundamentals

The photocathode

The development of more and more efficient photocathodes was essentially motivated by the seek for higher quantum efficiencies. The most valuable feature of a photomultiplier is still the fraction of photons converted to photoelectrons. The conversion of light entering the the photocathode is governed by internal photoelectric effects in which photoelectrons are excited into the conduction band. Illustrated in figure 3.2, incoming photons initially strike the photocathode. The electrons in the valence band absorb the photon energy ($h\nu$) and become excited. These excited electrons diffuse toward the photocathode surface. If the diffused electrons possess enough energy, they overcome the barrier between the valence and conduction bands in the photocathode material and are emitted into the vacuum as photoelectrons. A detailed study of photoelectric effect process can be found in [54]. Here, we give the main features.

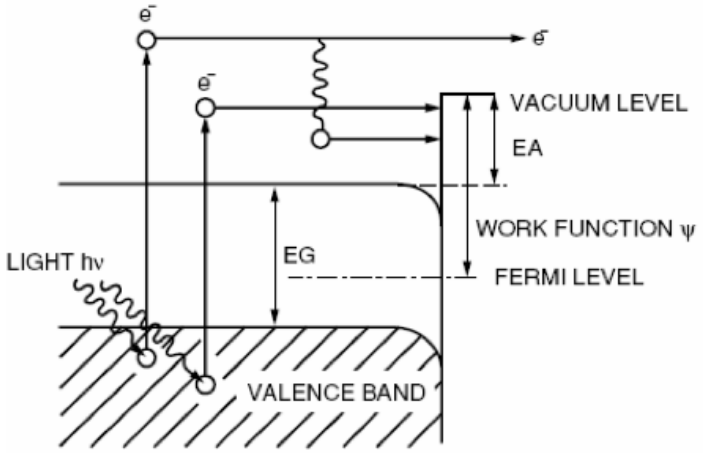

Figure 3.2: Photoelectric effect of a PMT photocathode

The basic photoelectric theory stipulates the following equation for determining the

maximum kinetic energy E of an emitted photoelectron:

$$E = \frac{mv^2}{2} = h\nu - \Phi \tag{3.1}$$

where Φ is the work function which must be given to an electron to allow it to escape the surface of a metal. For each metal, the photoelectric effect is characterized by a value of Φ, usually expressed in electron-volts. The work function is related to the spectral response. Hence, each photocathode material has its own pass band of wavelengths. Figure 3.3 shows spectral response curves for the alkali metals. The curves indicate a regular progression of the wavelength for maximum response with atomic number. The most red-sensitive of these metals is Cesium, which is widely used in the activation of most commercial phototubes.

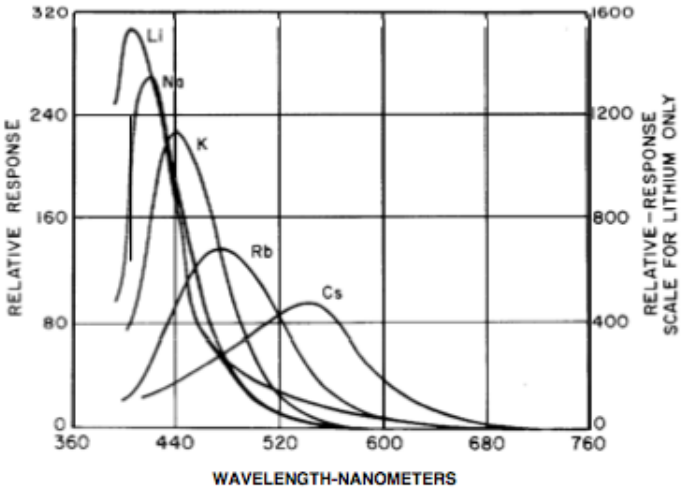

Figure 3.3: Spectral-response characteristics for the alkali metals showing regular progression in the order of the periodic table[129]

To have a qualitative understanding of the variations in quantum efficiency for different materials and for different wavelengths or photon energies, it is useful to consider photoemission as a process involving three steps:

1. absorption of a photon resulting in the transfer of energy from photon to electron.
2. motion of the electron toward the material-vacuum interface.
3. escape of the electron over the potential barrier at the surface into the vacuum.

Energy losses can occur in each of these steps. In the first step, only the absorbed part of the incident light is effective and thus losses by transmission and reflection reduce the quantum efficiency. In the second step, the photoelectrons may lose energy by electron-electron collisions in the material(electron scattering) or with the lattice (phonon scattering). Finally, the potential barrier at the surface prevents the escape of some electrons.

However, the energy losses described are different for each material. A significant difference between metallic and semiconducting materials makes separate consideration of each of these two groups useful. In metals, a large fraction of the incident visible light

is reflected and thus lost to the photoemission process. Further losses occur as the photoelectrons rapidly lose energy in collisions with the large number of free electrons in the metal. As a result, the escape depth (the distance from the surface from which electrons can reach the surface with sufficient energy to overcome the surface barrier) is small, and is typically a few nanometers. Finally, the work function of most metals is greater than 3 eV, so that visible photons which have energies less than 3 eV are prevented from producing electron emission. Only a few metals, particularly the alkali metals, have work function values low enough to make them sensitive to visible light. Because of the large energy losses in the absorption of the photon and in the motion of the photoelectron toward the vacuum (the first and second steps described above), even the alkali metals exhibit very low quantum efficiency in the visible region, usually below 0.1 per cent (one electron per 1000 incident photons). As expected, higher quantum efficiencies are obtained with higher photon energies. For 12 eV photons, quantum yields as high as 10 per cent have been reported.

Semiconductors absorb a much higher fraction of the incident light. In Figure 3.4, one can see that if the incident photon energy exceeds the band-gap energy E_G, electrons from the valence band are raised to the conductive band and photoconductivity is achieved. However, for a successful photoemission, the electron in the conductive band needs to overcome additional forces that bind the photoelectron to the solid. Hence, it must have an energy greater than the electron affinity $E_A$in the material so it can escape as a free electron in the vacuum. Thus, for an incident photon to be converted to a photo-electron, it has to have its energy greater than E_G+E_A. Besides, energy loss by electron-electron scattering is low because very few free electrons are present [1], which results in photoelectrons escaping from a greater distance from the vacuum interface, allowing longer threshold wavelengths than those in a metal.

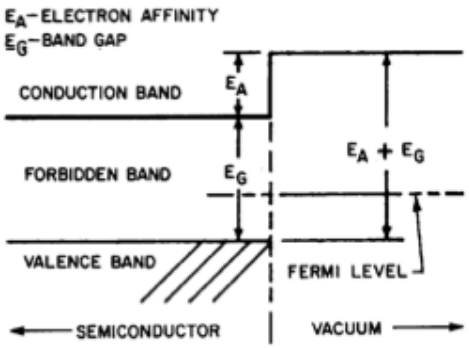

Figure 3.4: Simplified semiconductor energy band model[129]

Research on commercially useful photoemitters has been directed primarily toward developing devices sensitive to visible radiation. The first important commercial photosurface was silver-oxygen-cesium. This surface, is sensitive throughout the entire visible spectrum and into the infrared. The photocathodes most commonly used in photomultipliers are cesium-antimony (Cs_3Sb), multialkali or trialkali (Na_2KSb: Cs)[2], and bialkali (K_2CsSb). Typical spectral response curves for these materials are shown in Figure 3.5.

[1] Thus, energy loss by phonon scattering is the predominant loss mechanism.
[2] The terminology :Cs indicates trace quantities of the element

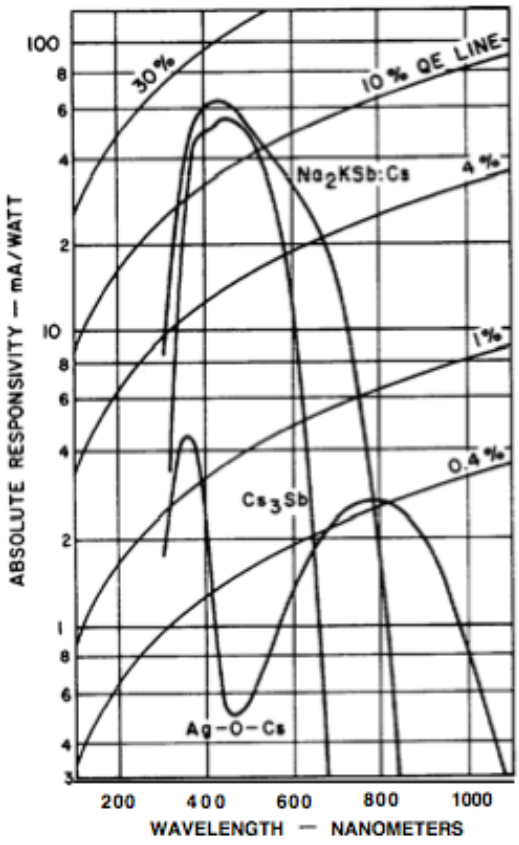

Figure 3.5: Typical spectra-response curves, with 0080 lime-glass window for (a) silver-oxygen-cesium (Ag-O-Cs), (b) cesium- antimony (Cs_3Sb), (c) multialkali or trialkali (Na_2KSb:Cs)

Photocathodes may be classified as opaque or semitransparent. In the opaque photocathode, the light is incident on a thick photoemissive material and the electrons are emitted from the same side as that struck by the radiant energy. In the second type, the semitransparent photocathode, the photoemissive material is deposited on a transparent medium so that the electrons are emitted from the side of the photocathode opposite the incident radiation.

Because of the limited escape depth of photoelectrons, the thickness of the semitransparent photocathode film is critical. If the film is too thick, much of the incident radiant energy is absorbed at a distance from the vacuum interface greater than the escape depth; if the film is too thin, much of the incident radiant energy is lost by transmission. For instance, typical thickness of a Na_2KSb:Cs photocathode is about 0.030μm .Thus, at 400 nm the photocathode absorbs 87% of the flux which is not reflected. The spectral response of semitransparent photocathodes can be controlled to some extent by thickness variation. With increasing thickness in the case of alkali antimonides, blue response decreases as red response increases.

The window materials

Although photocathode spectral response is determined primarily by the nature of the photocathode surface, especially in the visible and long wavelength cut-off regions, the short-wave length cut-off characteristic of all photocathodes is determined by the transmission of the window to the photocathode ie the glass on which the photocathode was evaporated. Ultraviolet cut-off characteristics of a number of glasses or crystals which have been used in photomultiplier fabrication are shown in figure 3.6. Borosilicate glasses are the most widely used in the photomultiplier industry; Its sensitivity ranges from near-infrared to $\sim$ 300 nm.

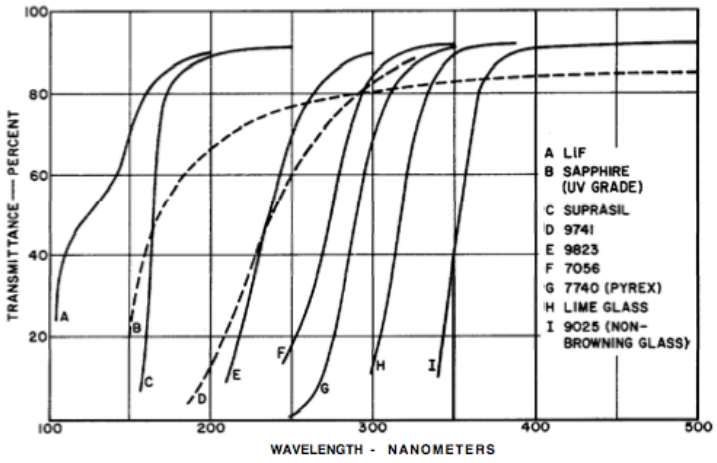

Figure 3.6: Ultraviolet transmittance cut off of various glasses and crystals used in photomultiplier photocathode windows. Data are all for 1 mm thickness.

The amplifying structures

the dynodes The dynodes are the traditional amplifying structure in photomultipliers. Usually, 11-14 dynodes are used in hemispherical 8 inch tubes, leading to a gain of about 10^6. The physical processes involved in secondary emission are in many respects similar to those already described under photoemission. The main difference is that the impact of primary electrons rather than incident photons causes the emission of electrons. The steps involved in secondary emission can be stated briefly as follows:

1. The incident electrons interact with electrons in the material and excite them to higher energy states.

2. Some of these excited electrons move toward the vacuum-solid interface

3. Those electrons which arrive at the surface with energy greater than that represented by the surface barrier are emitted into the vacuum.

The electrons emitted from the photocathode are accelerated toward the first dynode, which is maintained at a positive voltage with respect to the cathode. Each accelerated photoelectron that strikes the dynode surface produces several electrons, that are then accelerated to the second dynode, which is held at a voltage more positive than dynode 1. For conventional dynode materials, such as BeO and MgO, a multiplication factor of 10 can normally be achieved by each dynode stage. By the time this process has been repeated at each of the dynodes, 10^5 to 10^7 electrons have been produced for each incident photon, dependent on the number of dynodes.

However, we will not describe the details of such a classic device [78], and will consider more in depth new amplifying structures in hybrid photomultipliers.

Avalanche diodes Hybrid photomultipliers take advantage of the past 10 years progress on the development of new materials. The hybrid device combines a photomultiplier and semiconductor-photodiode technologies. While its structure is similar to a conventional photomultiplier, the hybrid photodetector (HPD) does have differences.

Like PMTs, the HPD is a vacuum tube with a photocathode that reacts to light, an electron multiplier, and an output terminal. But while PMTs use multiple dynodes as electron multipliers, the HPD uses a silicon avalanche diode (AD) instead. This diode is composed of semiconductor layers: a thin layer of heavily doped p-region that faces the photocathode and is connected to the output terminal, a much thicker silicon substrate in the middle, and a p-n junction connected to a bias terminal. The HPD and PMT have different methods of multiplication. In a PMT, photoelectrons from the photocathode are accelerated by a voltage difference towards the dynodes, where secondary electrons are generated from dynode to dynode, yielding a signal gain of about 10^6. In an HPD, photoelectrons from the photocathode are accelerated toward the AD by a larger voltage difference (about 8 kV). These photoelectrons are then multiplied in the AD in two steps: electron-bombardment gain, followed by avalanche gain.

In electron-bombardment gain, each photoelectron deposits its kinetic energy in the AD and produces many electron-hole pairs in the silicon substrate. The gain generated in this step depends on the voltage applied to the photocathode. A voltage of 8 kV results in an electron-bombardment gain of about 1600 [55]. The electrons then drift toward the p-n junction, and avalanche gain occurs.

In avalanche gain, the electrons collide with the crystal lattice of the silicon and create new electron-hole pairs that create more electron-hole pairs in a series of chain reactions. Depending on the reverse-bias voltage applied to the AD, the avalanche gain can range from 10 to 100. The total gain of the HPD is the product of the electron-bombardment and avalanche gains and can be greater than 10^5. Figure 3.7 shows a component comparison between a classic photomultiplier and an HPD.

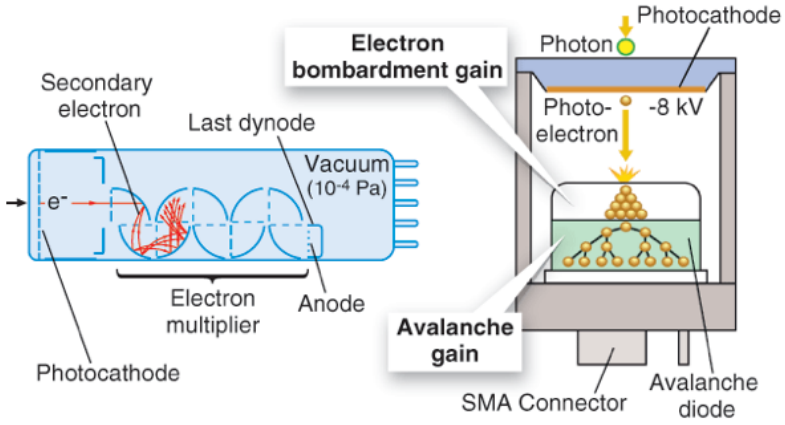

Figure 3.7: A typical PMT (left) uses dynodes as electron multipliers, while an HPD (right) uses an avalanche diode.

3.3 The X-HPD: a crystal-based photomultiplier

Scintillating crystal-based hybrid photon detectors (X-HPDs) have been demonstrated as viable single photon detectors since 1996 in the Lake Baikal neutrino telescope [29]. Prior to this, the Philips XP2600 was developed under the DUMAND program [126], while more recently developments at CERN have demonstrated the advantages of a true concentric geometry with a scintillator at the geometric centre of a spherical photocathode [43]. End of 2008, we started to develop a new series of quasi-spherical 8 inch X-HPDs in partnership with Photonis. The first prototypes were without crystal and first tests on current linearity were undertaken. In parallel, a simulation of the electric field distribution inside different geometries confirmed the results at CERN where a spheric geometry can lead to 100% electrostatic collection efficiency over 3π solid angle coverage.

In contrary to conventional PMTs, crystal-based photomultipliers are composed of two separate structures which together, form the entire detection and amplification process :

- An all-glass electro-optical entrance with a large photocathode. Photons are converted to p.e by the large photocathode. Photo-electrons are accelerated in a high electric field (25-30 kV) towards a first stage amplification consisting of a scintillator. The passage of the accelerated p.e. through the scintillator leads to a photon signal proportional to their deposited energy. This first step is an optical amplification.

- A small high gain photomultiplier tube outside but optically coupled to the electro–optical entrance detects the scintillation light yield, converts it again to p.e and amplify the electric signal through a conventional dynode structure. This second step is an electric amplification.

3.3.1 Motivation for crystal-based photomultipliers for neutrino telescopes

Energy resolution

The high voltage between the photocathode and the anode collimates the p.e trajectories on the anode. The collection efficiency is expected to be ∼100% (in conventional PMTs, the collection efficiency is ∼ 80%). the magnetic field contribution is therefore negligible. A LYSO crystal has a light yield of 25 photons/keV. Thus, 1 p.e from the photocathode leads to 30 p.e in the first stage amplification of the small PMT. Thanks to more statistics, the energy resolution at 1 p.e is 35% (Quasar-370) and 50% for the XP2600, the first prototypes of crystal-based photomultipliers. The first stage gain gives the possibility to distinguish up to 7th the p.e peak, while most photomultipliers can hardly give an angular resolution that enables the detection of the 2nd p.e peak. The time calibration of a neutrino telescope is strongly dependent on an appropriate suppression of the background. This relies on an accurate estimation of the single p.e peak. The charge spectrum of a crystal based hybrid PMT and a classic dynode-structure PMT is shown on figure 3.8.

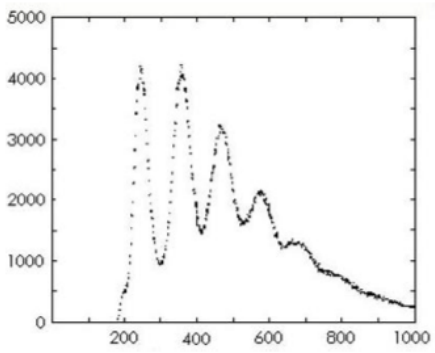

(a) Charge spectrum of the Quasar-370 [29]. The energy resolution enables single peaks distinction up to 7 p.e.

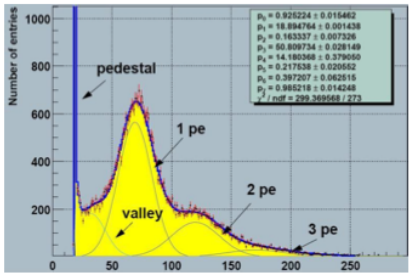

(b) Charge spectrum of the Hamamatsu R 7081-20 [6]. The energy resolution enables single peaks distinction up to 3 p.e.

Figure 3.8

Timing considerations : Transit time spread and after-pulses

The time resolution in hybrid photomultipliers is around 2 ns, similar to classic PMTs. In case of a spherical geometry and under high voltage, the transit time spread is mainly due to the time spread specific to the small PMT as the p.e are multiplied on the dynodes. Residual gases inside a photomultiplier tube can be ionized by collision with electrons. When these ions strike the photocathode or earlier stages of dynodes, secondary electrons may be emitted, thus resulting in relatively large output noise pulses. These noise pulses

are usually observed as afterpulses following the primary signal pulses and may be a problem in detecting light pulses. Small PMTs do not show afterpulses because of the small vacuum volume between the photocathode and the dynodes. Because the small PMT is separated from the electro-optic entrance, even if ionization process are present in the optical entrance, they would be extremely attenuated before reaching the small PMT.

The project

This work was partly funded through the European Union FP6 KM3NeT Design Study Contract 011937 and through the GIS (Groupement Interet Scientifique) signed between Photonis S.A.S. and the Institute National de Physique Nucleaire et Physique des Particules (IN2P3) of the Centre National pour la Recherche Scientifique (CNRS). The thrust of this development study was to investigate the industrialization of the X-HPDs to the point where it represents a significant cost reduction per cubic kilometer of instrumented volume compared to conventional PMTs, thereby allowing for extremely large telescope target volumes.

3.3.2 Crystal-based photomultipliers prototypes

Philips prototype for the DUMAND experiment : XP2600

About 30 prototypes of the crystal-based photomultiplier XP2600[120] were deployed for the DUMAND experiment. Figure 3.9(a) shows a 15 inch (38.1 cm) spherical geometry prototype. As shown in figure 3.9(b), the device was a hybrid glass-metal construction with the almost spherical photocathode dome attached to a central glass insert, equipped with the integral viewing window, via a pair of orbitally welded glass-to-metal seal rings (detail A). The disk- like scintillator geometry used P47 (Y_2SiO_5:Ce) phosphor deposited by sedimentation onto the glass viewing window (detail B). The Aluminum anode electrode (detail C) was deposited on the scintillator and was thin enough (typically 100 nm) that only a few KeV of incident 25KeV photoelectron energy was lost in traversing it. Since the photoelectrons penetrate only a few microns into the scintillator, a thin phosphor was sufficient. Scintillation light from the phosphor could be viewed through the window by a conventional PMT located outside the vacuum space.

Lake Baikal Neutrino experiment PMT : Quasar-370

The QUASAR-370 [29] consists of an electro-optical preamplifier followed by a conventional photomultiplier. Figure 3.10(a) shows the optical module housing the Quasar-370 with its 25 kV voltage supply as well as the small photomultiplier and its electronics. In this hybrid scheme, photoelectrons from a large hemispherical cathode with $>2\pi$ viewing angle are accelerated by 25 kV to a fast, high gain YSO scintillator which is placed near the center of the glass bulb. The light from the scintillator is read out by a small conventional PMT (UGON). One photoelectron emerging from the hemispherical photocathode yields typically 25 photoelectrons in the conventional PMT. This high multiplication factor of the electro-optical preamplifier results in an excellent single electron resolution; important for the detection of low level light pulses and background suppression. Due to the fast acceleration of primary photoelectrons by 25 kV high voltage, the time jitter can be kept under 1 ns, which is twice smaller than PMTs such as in ANTARES experiment. This is most important for accurate track reconstruction. The high electric field inside the tube makes the p.e almost insensitive to the Earth magnetic field.

(a) The Philips XP2600 X-HPD, constructed at the Philips Brive la Gaillard site: now Photonis S.A.S.

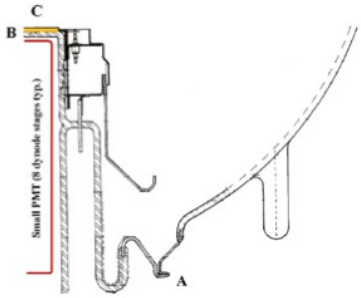

(b) Quadrant view of the anodic section of the XP2600 X-HPD showing the placement of the phosphor, viewing PM, anode electrode and envelope sealing

Figure 3.9: The hybrid XP2600 from Philips [120].

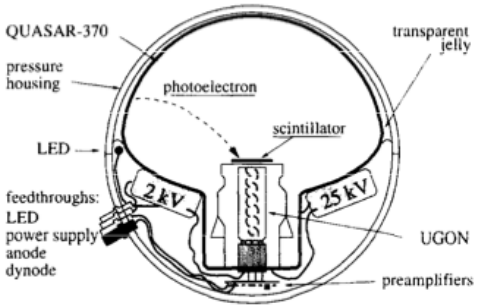

(a) The Optical Module of the Baikal experiment

	QUASAR-370	UGON
Bulb material	Borosilicate glass	Borosilicate glass
Photocathode	K_2CsSb	K_2CsSb
Photocathode diameter	37 cm	2.5 cm
Spectral sensitivity at $\lambda = 410$ nm	60 mA/W	60 mA/W
Number of stages	1	12/13
Gain	25	10^7
1-PE resolution	70%	–
Peak-to-valley ratio (1 PE)	2.5	1.3
TT difference (center-edge)	$\leq$ 1.5 ns	$\leq$ 1 ns
TT jitter for 1 PE point illumination	2 ns	2.2 ns
Noise rate ($\geq$ 0.25 PE, 20°C)	30 kHz	$\leq$ 1 kHz

(b) Performances of the Quasar-370 and the small conventional photomultiplier UGON viewing the scintillator.

Figure 3.10: The hybrid Quasar-370 from the NT-200 Baikal experiment.

The lake Baikal experiment NT-200 was equipped with 200 such PMTs. The main performances of quasar-370 are shown in table 3.10(b). 192 optical modules housing the Quasar-370 were deployed in lake Baikal in 1998.

Since both the Philips XP2600 and the Quasar 370 used a disk-like deposited phosphor scintillator, neither exploited the full advantage of a spherical geometry with a convex shaped scintillator at the geometric centre of the photocathode, demonstrated in recent studies at CERN [42] [44]. Such a geometry offers excellent (sub-ns) isochronicity and close to 100% electrostatic collection efficiency for drifting photoelectrons over 3π solid angle

coverage, a performance significantly exceeding the figure of around 70% of photoelectrons arriving at the first dynode in a typical large hemispherical PMT having a much smaller (typically $3\pi/4$) solid angle coverage.

CERN prototype : X-HPD

This device has a spherical envelope of 208 mm (8 inch) diameter (figure 3.11(a)). Different models were manufactured but the most recent one is based on the use of a LYSO crystal with a "flattened" conic shape as anode (1.2 cm diameter and 1.8 cm height) [42] as shown on figure 3.11(b). The difference of potential between the anode and the cathode is 20-30 kV. The photocathode covers 3π sr offering a half viewing angle of 120°, the anode being placed in the geometric center of the sphere and coated with a 100 nm layer of Aluminum [42] which is deposited directly on the LYSO crystal. The optical transition between the scinitillator and the small PMT is ensured by a light guide to avoid photon loss.

(a) CERN X-HPD prototype

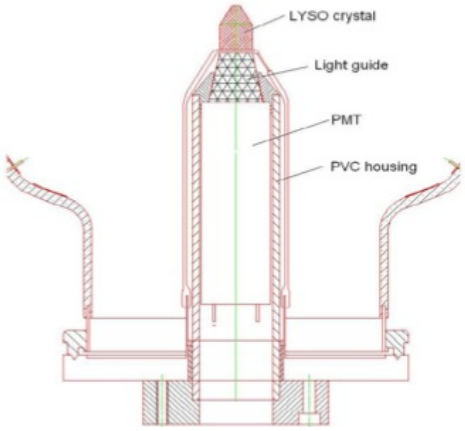

(b) CERN X-HPD prototype sketch showing the crystal shape

Figure 3.11: The X-HPD prototype from CERN [44]

3.3.3 CPPM-Photonis prototype

The device has an ellipsoidal shape of 208 mm diameter. The industrialization of such a bulb shape is easier as most large hemispherical prototypes manufactured at Photonis have an ellipsoidal geometry. The first prototype conceived is shown on figure 3.12(a), it is an all-glass structure with a half-viewing angle of 40°. Figure 3.12(b) shows the complete structure of the device when coupled with a small photomultiplier in the rear of the scintillator. The scintillator is a thin LYSO disk covered with an evaporated Aluminum foil which maintains it at the desired voltage. The scintillator is mounted on a metallic disk which is related to the pins outside the vacuum structure where the high voltage would be applied. The pins in the bottom of the structure are used to apply the voltage on the photocathode and on the metal disk maintaining the scintillator as well as to read the current output from the anode. The other pins are used only in the manufacture process to evaporate the photocathode.

(a) CPPM-Photonis prototype without the rear small photomultiplier.

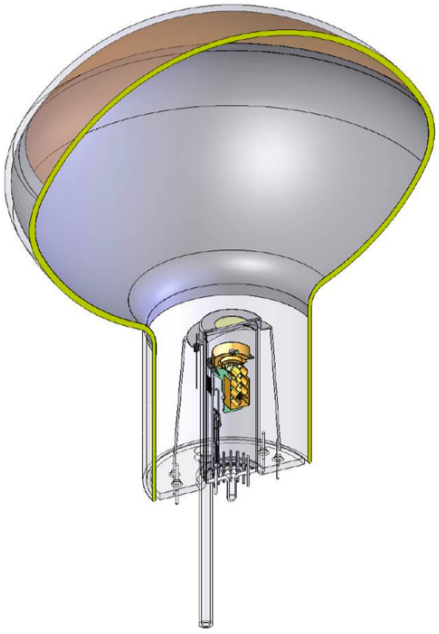

(b) The configuration of the prototype with a small PMT coupled with the all glass structure.

Figure 3.12: The X-HPD prototype from CPPM-Photonis [12][13]

3.4 Simulation of the influence of the entrance window geometry on the electric field distribution

One of the primary design considerations in a photomultiplier tube is the shaping and positioning of the components inside the electron optical entrance. If this step is not well studied, it could result in the loss of electrons and thus in a subsequent gain loss. If all of the emitted photoelectrons are not guided properly to the crystal amplifying structure, the signal-to-noise ratio of the photomultiplier can be degraded leading to poorer pulse-height-resolution characteristics. The complete electron-optical configuration of the photomultiplier must also be such as to avoid regenerative effects. For example, there should not be an open path in the tube through which occasional ions or light could feed back from the amplifier assembly to the photocathode. An electron-optical design for a photomultiplier may be arrived at from computer-developed equipotential lines and electron trajectories plotted on a plan showing the electrode configurations. Collection efficiency and time response may be predicted from an analysis of the electron trajectories. If all the photoelectrons begin their trajectories at the surface of the photocathode with zero velocity, 100% collection would be possible. Because of the finite initial velocities, however, some electrons begin their trajectories with unfavorable angles of launch and are not collected on a useful area.

3.4.1 The simulation tool

SIMION 8 [88] is a software program making charged particle optics simulations. Mainly, it calculates 2D/3D electrostatic field and calculates the trajectories of charged particles

through it. The Laplace equation calculates the potentials inside a volume given certain conditions on the boundary surface. Boundary conditions are typically voltages on the surfaces of electrodes. SIMION solves the Laplace equation using an optimized numerical solution.

SIMION simulations were carried for different configurations with the true dimensions of the optical entrance of the hybrid prototypes described above. In the simulation, we assume the following :

- A pulse of of 100 photons striking the photocathode at different angles
- A bialkali reflective photocathode
- A quantum efficiency of 25%
- Photoelectrons escape the photocathode with directions in a cone of 45° half angle

A standard Bialkali photocathode shows a quantum efficiency of 25% (hence, 25 photoelectrons are released into vacuum) in a range between $\lambda_{min} \sim 350$ nm and $\lambda_{max} \sim 450$ nm. Thus, the incident photon energy $E_{incident} = \frac{hc}{\lambda}$ ranges between 2.75 eV and 3.54 eV. The maximum emission wavelength in bialkali material is 630 nm[54], which corresponds to a minimum emission energy of 1.96 eV. After subtracting the minimum energy of emission from the incident energy, one finds that the equivalent initial photoelectron kinetic energy is situated in a range between 0.8 and 1.6 eV. Thus, 25 electrons will travel the distance separating the photocathode from the anode with initial energy values uniformly distributed between 0.8 and 1.6 eV. The distribution of the equipotentials as well as the electron time of flights will be presented for spherical and hemispherical device configurations.

3.4.2 The electric field distribution and transit time differences

We define the collection efficiency as the fraction of electrons striking the effective volume of detection in respect with the electrons emitted by the photocathode. The effective area of detection is taken to be the whole surface of the crystal as we neglect the effects of reflection on the outside surface of the crystal as well as the reflection inside the crystal bulk. For crystal bulks, we assume the effective detection area to be the entire surface in contact with vacuum. For deposited crystal elements on glass, the effective area would depend on the shape of the support on which the crystal is deposited.

The time resolution of a PMT (Transit Time Spread : TTS) results from the time spread of initial p.e while crossing the optical entrance when the photocathode is entirely illuminated (Transit Time Difference : TTD), the conversion time spread of the crystal (time necessary to convert a p.e to photons), and the transit time spread in the small photomultiplier. The second component is negligible since the p.e path in the crystal is very short comparing to the two other components. The first component can be estimated by an electrostatic field simulation and the latter component is equal to 2 ns for most 2 inches photomultipliers.

Within the optical entrance, the transit time fluctuation has two components :

- Difference in transit times emitted from different points of the photocathode .
- Spread in initial velocities (energy and direction) of the emitted electrons. The tangential initial velocity component shifts the point of impact of the electrons on

the anode by a certain distance but generally the transit time change induced is negligible [54].

The transit time difference is measured by estimating the flight time difference between photoelectrons from the edge of the photocathode and photoelectrons from its center. The optimal optical entrance should offer the largest angle of acceptance independently from its size while keeping a low transit time difference. Figure 3.13 shows the angle convention considered in this study.

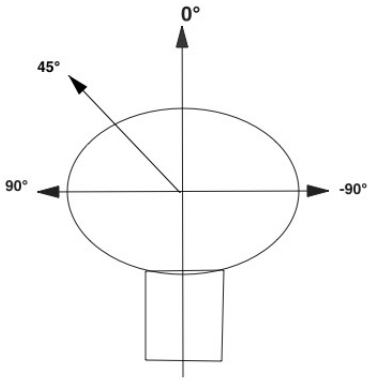

Figure 3.13: Angle convention

The simulation should lead to clues about the optical entrance geometry and the expected contribution of transit time differences in the total transit time spread of the output current pulse.

Ellispsoidal geometry

For the first steps of the development, we decided to test the electro-optical entrance of an ellipsoidal prototype since these glass bulbs are easier to manufacture for this range of 8 inch tubes in Photonis. The crystal is intended to be a thinned LYSO disk of 2 cm radius coated with a 100 nm aluminum layer. Only the inner part of the crystal surface is effective for direct detection (p.e. directly hitting the aluminum), and represents 1.5 cm radius.
Two designs are compared in the simulation. Design 1 has a photocathode coverage of 40° while Design 2 has a photocathode coverage of 60°. The dimensions used in the simulation consider an ellipsoidal volume of major radius 9.6 cm and minor radius of 8 cm.

Figure 3.14(a) shows a 3-dimension simulation of the prototype bulb and the position and shape of its anode. The anode is not situated at the center of the bulb. Figure 3.14(b) shows a lateral cut of the prototype with the distribution of its equipotential lines inside the given geometry in a 25 kV accelerating field. The field is more intense near the anode, while near the photocathode surface, the equipotential distribution less dense. This effect would broaden the arrival time distribution of a single pulse of p.e as the electric field would hardly keep the pulse collimated. This effect is visible on the electron trajectories shown on figure 3.14(c). It is expected in this configuration that p.e. issued from the same

photocathode point would have an arrival time dispersion of $\sim$ 0.1 ns. This component is however still negligible comparing to the TTD i.e arrival time difference between the center and the edge of the photocathode, which is closer to real conditions when the entire photocathode is illuminated. However, even when always smaller than the TTD, in case of a weaker accelerating voltage, its contribution can be more important. Figure 3.14(d) shows a zoom around the arrival positions of the p.e on the anode. The p.e coming from larger angles are strongly deviated and hit the edge of the anode, which is a metallic surface. In the simulation, it is is difficult to predict whether these deviated p.e would excite the scintillator even if not falling directly on it. The junction between the scintillator and the metallic edges of the anode can still channel these p.e to the scintillator. Table 3.1 shows the TTD for Design 1 and Design 2. The enlargement of the photocathode area, while upgrading the angle-of view, degrades the TTD for an ellipsoidal geometry. One can translate this in a figure of merit F = AOV/TTD, where AOV is the angle of view of the detector. Design 1 is 5 times better than Design 2 in an ellipsoidal geometry at high voltage.

Position	Transit time	Transit time difference (RMS)
0°	10.5 ns	
40°	10.2 ns	$\sim$ 0.3 ns (design 1)
60°	8.4 ns	$\sim$ 2.1 ns (design 2)

Table 3.1: Electron mean time of flight for different emission angles and the time of flight difference between the center and the edge of the photocathode.

Figure 3.15 illustrates the transit time difference evolution as a function of the accelerating voltage. The worst case transit time difference for photoelectrons drifting to the anode plate from the pole of the tube and from the polar angle limit of 40° are shown. Above 5 kV the transit time difference is less than 1 ns.

Basic requirements in neutrino telescopes include the effective volume of detection, which is strongly correlated to the photomultipliers angle of acceptance and also the transit time spread which is actually the limitation in neutrino telescopes for an accurate track reconstruction.

The result suggests a concentric geometry around the anode in order to enhance the angle of view and reduce the TTD.

Spherical HPD geometry

The spherical geometry used in the simulation is inspired from the CERN X-HPD[45]. Different crystal shapes are considered inside a sphere radius of 9.6 cm. The difference of potential between the photocathode and the anode is taken to be 25 kV. These models feature a metallic ring at 2 kV to maximize the sphericity of the electric field. A resistive coating whose role is to ensure a smooth electric gradient between the photocathode (25 kV) and the anode (0 V) is applied behind the anode and in the region situated between the ring electrode and the base (from -2kV to 0V). This painting prevents from space charge effects which could disturb the electron trajectories.

- *Cylindric anode*
  In the geometric center of the device, a cylindric anode of 1.8 cm height is considered

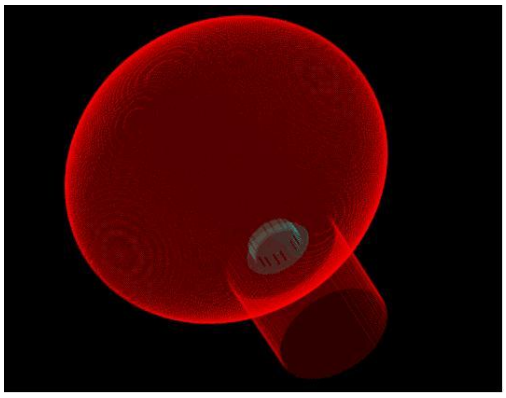

(a) 3-dimensional simulation of the prototype geometry. The simulation considers 2 electrodes : the photocathode and the glass bulb part covered with aluminum foil at 25 kV and the anode at 0 V

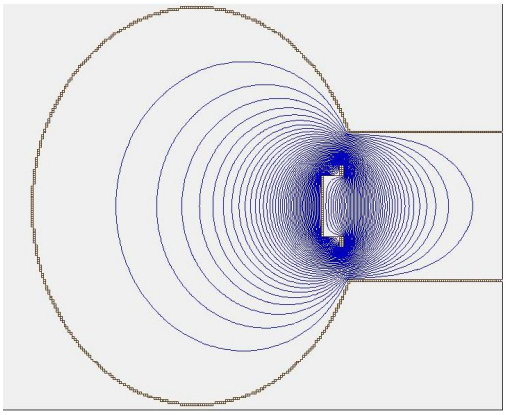

(b) Equipotential lines drawn for 25 kV in an 8 inch ellipsoidal prototype. The potential gradient is very sharp near the anode comparing to the other regions in this design.

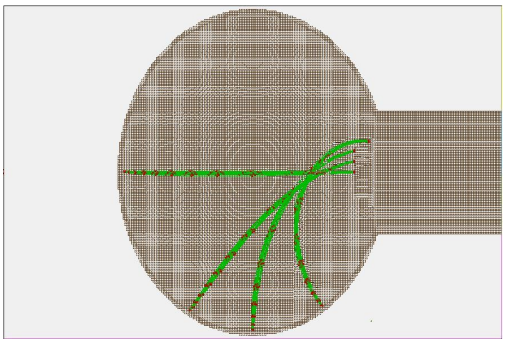

(c) Distribution of equipotentials in an ellipsoidal prototype

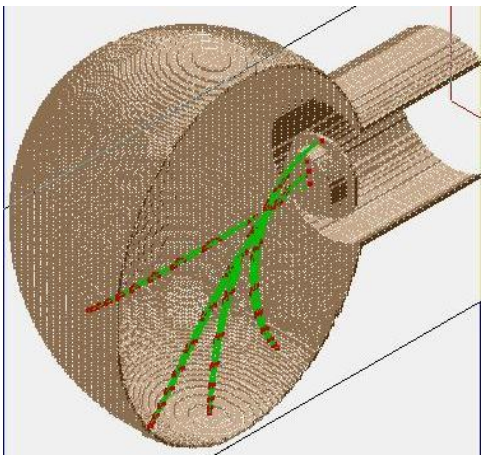

(d) Distribution of equipotentials in an ellipsoidal prototype

Figure 3.14

and 1.2 cm diameter. The simulation results are shown in figure 3.16(a). Table 3.2 shows the p.e. mean time-of-flights for different angles of incident light.

- *Conic anode*
  A conic anode with the same dimensions is placed in the geometric center of the device. The simulation results are shown in figure 3.16(b). The associated time-of-flights are shown on table 3.3.

- *half-spheric anode*

  In the geometric center of the device, a half-spheric anode is placed. Inspired from the Quasar and the XP 2600, a concave glass is used to evaporate a thin layer of phosphor as well as the aluminum layer. The effective surface of the anode is considered to be 180° around the axis of symmetry. The simulation results are shown in figure

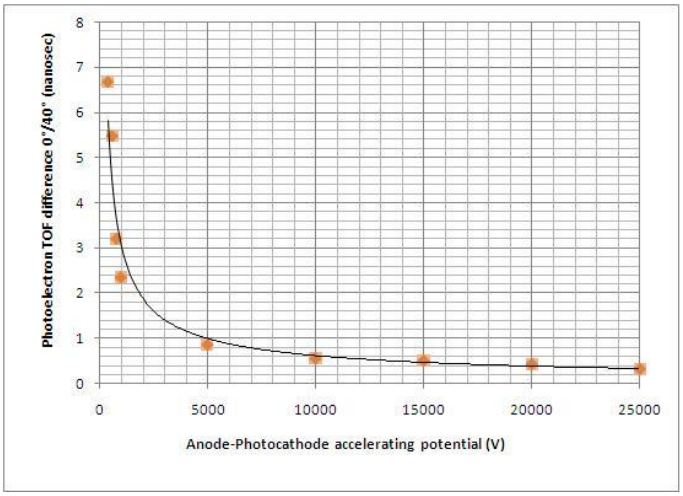

Figure 3.15: Transit time difference (ns) for photoelectrons emitted at polar angles of 0° and 40° using Simion 8.

Position	Transit time (ns)	Transit time difference (RMS)
0°	2.81	∼ 0.4 ns
90°	2.68	
110°	2.90	
120°	3.18	

Table 3.2: Electron mean time of flight for different emission angles and the time of flight difference between the center and the edge of the photocathode .

3.16(c).The associated values are in table 3.4.

Under the hypothesis of a 25 kV potential between the photocathode and the anode, the spherical geometry enables good performances on the mean transit time values. Photoelectrons in a single pulse stay collimated so the time dispersion between electrons in a same pulse is negligible. The collection efficiency is close to 100%. Thanks to the uniformity of the potentials inside the envelope, the electrons are accelerated almost similarly independently from the point of illumination. The conic and half-spheric anode shape give better results as the close-by potential line distribution is more uniform than a cylindric anode shape. Comparing to crystal bulks, an evaporated scintillator is less expensive and gives comparable performances.

The simulations give most credit to the spherical geometries with a concentric anode. First, the large coverage of the photocathode ensures a more efficient light collection. Second, the equipotentials are well distributed and show no charging effects because inter-electrode distances are well distributed . Third, the photoelectron collection efficiency is improved and especially if the anode coats the crystal situated in the geometric centre. Fourth, the transit time spread component due to the time of flight differences is minimized. Conceiving a detector with a spherical shape would have been the next step in the prototype development.

Position	Transit time (ns)	Transit time difference (RMS)
0°	2.9	∼ 0.3 ns
90°	2.71	
110°	2.88	
120°	3.19	

Table 3.3: Electron mean time of flight for different emission angles and the time of flight difference between the center and the edge of the photocathode .

Position	Transit time (ns)	Transit time difference (RMS)
0°	2.5	∼ 0.3 ns
90°	2.38	
110°	2.59	
120°	2.8	

Table 3.4: Electron mean time of flight for different emission angles and the time of flight difference between the center and the edge of the photocathode .

3.5 Development and characterization of the prototypes

In collaboration with Photonis, first ellipsoidal prototypes were manufactured. The first three PMTs are without crystal and without amplifying structure. The aim was to characterize the optical entrance as well as the linearity of the output anode current. The fourth prototype had a LYSO crystal but the current linearity tests proved that this prototype had internal electrostatic repartition problems. Unfortunately, no other hybrid photomultiplier could be manufactured as Photonis closed its PMT branch when it ceased all photomultiplier manufacture in March 2009.

The prototype features are shown in table 3.5

Prototype number	Half-Angle of View (∘)	Anode
Prototype 1	40	Metal
Prototype 2	40	Metal
Prototype 3	60	Metal
Prototype 4	40	LYSO crystal

Table 3.5: Manufactures prototypes characteristcs .

Figures 3.17(a) and 3.17(b) show the 2 designs: prototypes 1 and 2 have 40° (design 1) angle of view and prototype 3 have 60° angle of view (design 2). Photocathode processing on large angles is not an easy task, as it can not be completely controlled. Indeed, there exist two processes to manufacture a photocathode :

- Internal process : Using a small glass tube (visible on figure 3.12(b)), Alcalin metals such as K and Cs are evaporated. A current is applied on some pins which are related to wires with Sb et Mn to evaporate it as a last step. This process is fast and robust, it is actually used by Photonis.

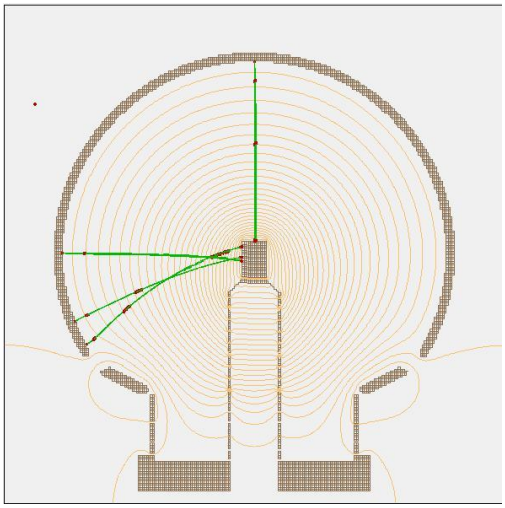

(a) Equipotentials (yellow) and electron trajectories (green) in a spheric shape device with a cylindric anode. Red dots mark the position of the electrons at each nano-second.

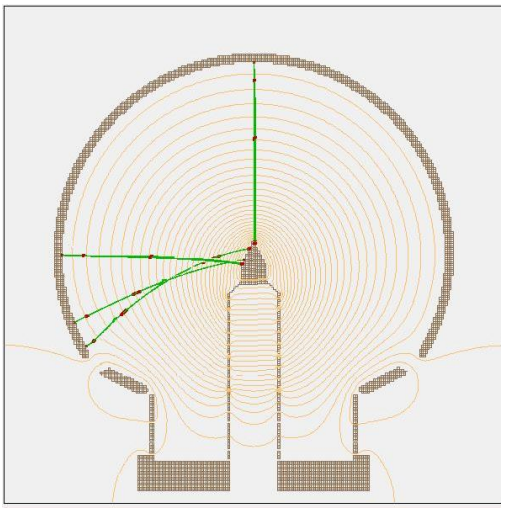

(b) Equipotentials (yellow) and electron trajectories (green) in a spheric shape device with a conic anode. Red dots mark the position of the electrons at each nano-second.

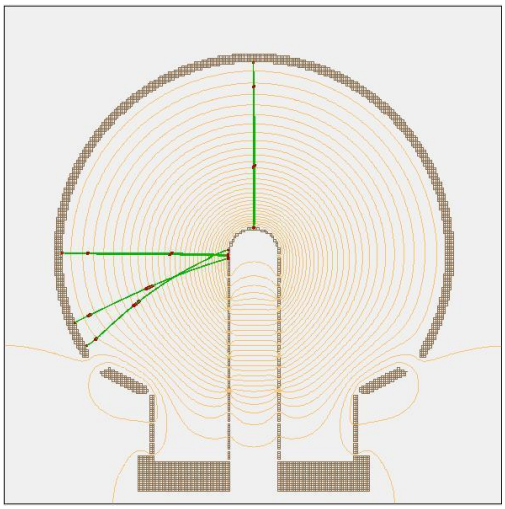

(c) Equipotentials (yellow) and electron trajectories (green) in a spheric shape device with a half-spheric anode. Red dots mark the position of the electrons at each nano-second.

Figure 3.16

- Transfer process: The photocathode evaporation is done under vacuum before the tube is sealed. This process is difficult to industrialize but results generally in more homogeneous photocathodes. This process is used for CERN prototypes.

The standard bi-alkali photocathode of the prototypes is internally processed. The prototypes are not equipped with a scintillating crystal although a 2 cm diameter metal plate anode allows photocurrent measurements of quantum efficiency and also photocathode sensitivity mapping.

All measurements presented in this study have been undertaken in a continuous mode;

(a) Design 1 : 40° photocathode maximum zenith angle for prototypes 1 and 2

(b) Design 2 : 60° photocathode maximum zenith angle for prototype 3

Figure 3.17

The device being exposed to a continuous photon flux using an illuminating LED operating at constant current . It is impossible to work in pulsed mode conditions because no internal amplifying structure is present.

3.5.1 High voltage tests

In order to achieve less than 1 ns TTD, the prototype has to be operated at high voltage($>$ 5 kV) as shown in the last section. However, the PMT device has its own dark current even without any light source in its vicinity. The dark current has basically three components which show respectively as the voltage increses:

- leakage current due to the glass and photocathode conductivity which is dependent on the concentration of alcali metals used.
- thermo-ionic emission due to a spontaneous electron emission from the photocathode under the effect of temperature. For instance, at ambient temperature 50 electrons/cm^2/s are emitted.
- Field emission current due to important local density of the electric field causing a peaking effect which releases photons that can reach the photocathode.

The prototype tubes were operated in air, housed in a black box at cathode voltages up to - few hundreds of Volts (negative polarization) and the anode at ground. Prototypes 1 and 3 showed a significant leakage current (7-8 nA) before reaching 1kV. As can be seen on figure 3.18(a), Prototype 2 ran without significant leakage currents (3 nA at 1.5 kV) before reaching 6nA at 5 kV. The current diverged due to thermo-ionic emission and later field-emission as shown on figure 3.18(b). The field-emission effect is visible on figure 3.18(c). It is particularly present around metallic anode which confirms the electrostatic simulations. Another area leading to such a phenomenon is the spacing around the pins. This suggests

that the pins spacing should be made larger and potential distribution around the anode more uniform to avoid significant dark current at high voltage.

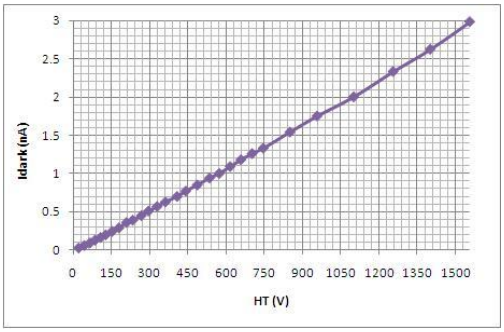

(a) Prototype 2 dark current measurement.

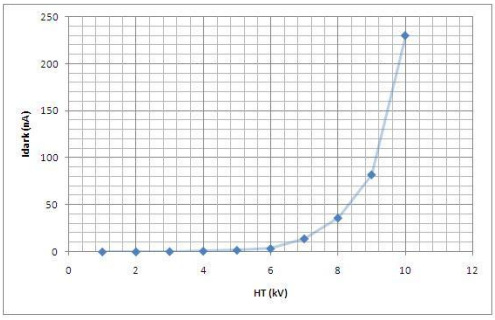

(b) Prototype 2 high voltage test.

(c) Prototype 2 near to 10 kV high voltage. Appearance of the field-emission regime near the pins and around the anode.

Figure 3.18

The opposite powering, i.e. anode at +HV and cathode at ground could not be tested above few tens of Volts, as the anode is supplied by a simple vacuum feedthrough in the base plate which is not HV rated.

Experimental set-up

In order to assess the prototypes optical entrance, a dedicated test bench was mounted in CPPM to perform photocathode uniformity measurements. Figure 3.19(a) illustrates the photocathode mapping test bench. A Keithley 485 picoampermeter is used to read the output anodic current. The light source is a blue (475 nm) LED-fibre optic. The bench allows an accurate positioning of the prototype in space allowing variation in light-source photocathode distance, polar and azimuthal angles. In order to avoid light reflection, all the components are painted in black.

A significant enhancement in the output current is observed at large angles of incidence. Figure 3.19(b) shows the output anodic current for different azimuth and zenith angles normalized by the current value obtained for a vertical (zenith θ=0°) light injection. The azimuthal variation in the sensitivity is due to a non-homogeneity in the photocathode evaporation, this effect lead to a maximum of 30% variation in the output current.

The current variation is however much more sensitive of the zenith angle. The current value when light originates from the edge of the photocathode is $\sim$ 70% more important than a light injection on the topo of the photocathode. It is expected that photons originating from large zenith angles have twice the opportunity to be converted into photoelectrons on the opposite side on the photocathode. Moreover, the photocathode overlays an aluminum layer on the lower hemisphere, which accentuates this reflective mode. This effect influence on the quantum efficiency is thus investigated.

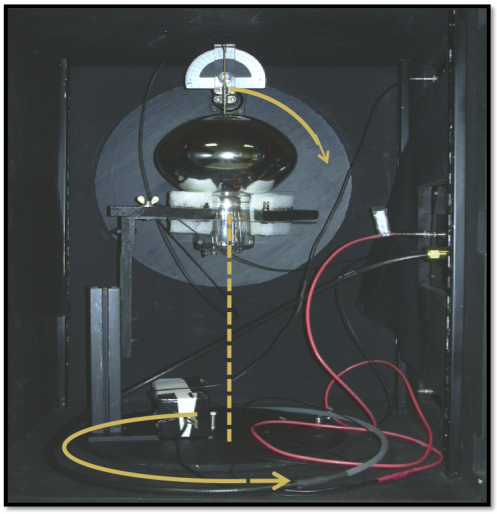

(a) Experimental set-up for sensitivity measurement in CPPM.

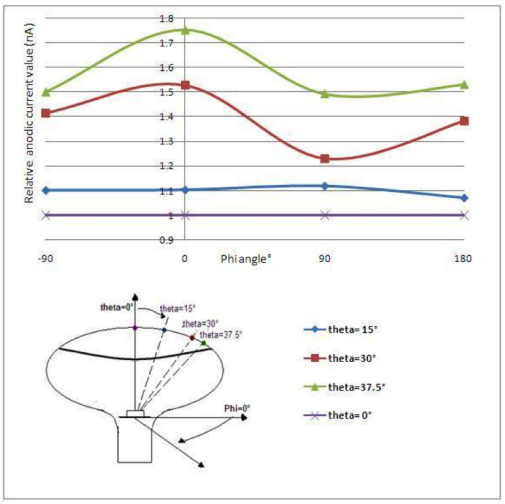

(b) Photocurrent measurement for different zenith and azimuth angles. The current values are normalized to the current value obtained at (θ,ϕ) =(0,0).

Figure 3.19

3.5.2 Quantum efficiency measurements

The quantum efficiency (QE) is one of the main requirements to enhance the sensitivity of an experiment relying on the detection of Cherenkov light.

The double cathode effect

The double cathode effect is an observed phenomenon on hemispherical large photocathodes. Light which is not absorbed by the semitransparent photocathode has a second chance to be detected on the opposite side of the sphere, then in reflective mode. For the same thickness, the QE in reflective cathode is generally higher than in semitransparent mode. Consequently the effective quantum efficiency of the device can be significantly larger than for a conventional PMT design. The price to pay is a contribution of about 1 ns to the transit time for the fraction of the light which is converted only at the second occasion.

The quantum efficiency is measured using a certified calibrated NIST photodiode for which photocurrent values at each wavelength is well measured. A monochromator is placed in front of a tungsten white light lamp. The wavelength is varied from 300 nm to 700 nm and the resulting photocathode current of prototype 2 is recorded. The device was

oriented in different angles comparing to the incident light as it is expected that the QE would be more important in reflective mode. Tests on our prototype were conducted and led to the result shown on figure 3.20(b).

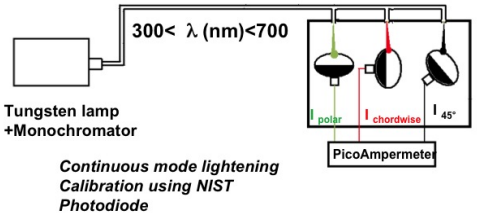

(a) Experimental set-up for QE measurements. The device is placed with different angles comparing to the incident light. In collaboration with O. Kalekin , Erlangen Centre for Astroparticle Physics, Erwin-Rommel-Str. 1, 91058 Erlangen, Germany.

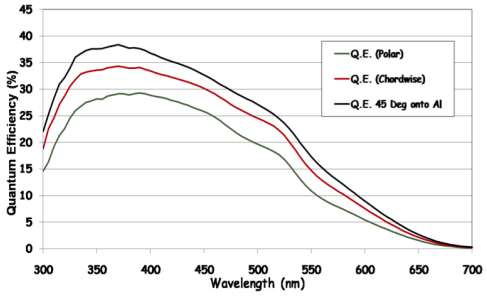

(b) Quantum efficiency measurement for different incidence angles

Figure 3.20

A relative improvement in quantum efficiency compared to the semi-transparent mode (polar direction) of about 35% is noticed for an angle of 45° practically independent of the wavelength. The aluminum foil evaporated on the sides of the device (black in figure 3.20(a)) which role is to take the photocathode at its operating potential is a perfect photon reflector and this acts like a barrier for opposite-side photons escaping the photocathode. The Quasar-370 and the XP2600 show also an enhancement of the quantum efficiency in a reflective mode as can be seen in figure 3.21

For spherical geometries, this effect can lead to a relative improvement in the case of side illumination as found for the CERN prototype of ≈200 % [44].

Comparison with an enhanced photocathode PMT

The same experiment was undertaken on a HAMAMATSU R5912 super-bialkali PMT. tube equipped with an enhanced photocathode. Standard photocathodes have a quantum efficiency of 25%-30%. An enhanced photocathode can reach 35%-40% using an upgraded formula of the chemicals in the photocathode. However, the PMTs equipped with an enhanced photocathode are more expensive. Figure 3.22 shows the result on the QE measurements placing both tubes in a reflective-mode position (chord-wise measurement). The standard photocathode of prototype 2 give similar results as the enhanced photocathode.

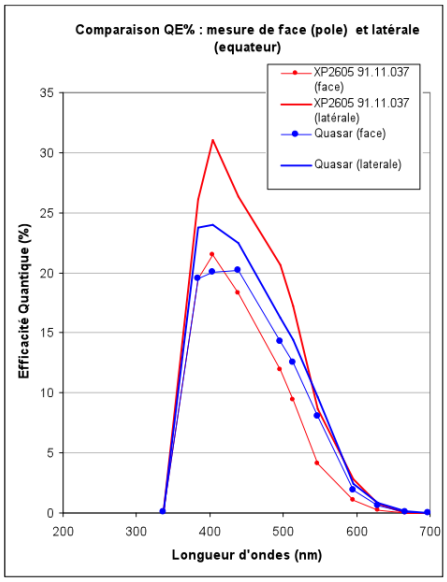

Figure 3.21: Quantum efficiency measurement in a semi-transparent (line) and reflective mode (line with dots) for the Quasar-370 and XP2600.

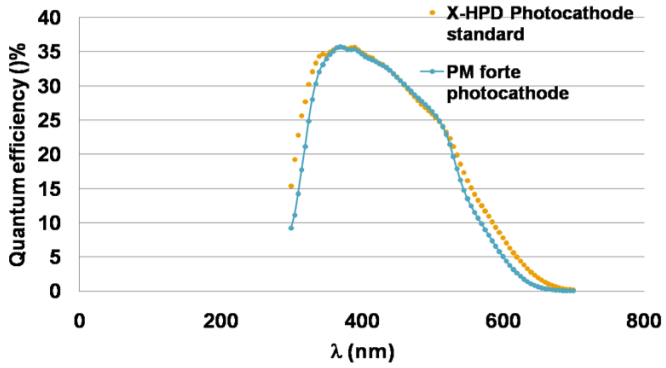

Figure 3.22: Quantum efficiency measurement in a reflective mode of HAMAMATSU R5912 super-bialkali (blue) and prototype 2 standard photocathode.

3.6 The PMT solution for KM3Net

In year 2008-2009, 4 X-HPD prototypes were qualified in collaboration with Photonis. While electrostatic simulations definitely gave credit to a fully spherical geometry regarding the more important photocathode angle of view as well as better timing performance expectations, three prototypes were used to evaluate the electro-optical entrance with an ellipsoidal envelope from the standard Photonis production. The possibility of applying high voltages in the structure and double cathode effect measurements were undertaken. For the best ellipsoidal prototype, the voltage applied was limited to 5000 V before the current diverges due to thermo-ionic effects. However, the X-HPD is intended to handle voltages of 25 kV. Such high voltages are expected to render the device insensitive to the

Earth magnetic field responsible of electron deviation in large standard PMTs.

The double cathode effect is noticed more or less importantly depending on the prototype, the highest effect in quantum efficiency seen is 38% at an angle of incidence of 45°. A comparison with a super-bialkali photocathode in a standard PMT give the same performances on the quantum efficiency in a reflective mode. Because the photocathode deposition is a sensitive process and the reflective material in the photocathode can not be exactly the same from one device to another, this effect may be highly variable and would have necessitated more devices to enhance the statistics on this measure.

However, this work led to the construction of the first ellipsoidal crystal based photon detector with internal processing of the photocathode. A LYSO crystal was used in this prototype but the deposition of 100 nm of aluminum on the crystal did not succeed. Extremely delicate, this operation necessitates the crystal surface to be perfectly smooth, otherwise, electric discharges can cause the photomultiplier output dark current to diverge. For this first hybrid prototype, such effects were noticed and it would have needed to be better controlled for the next steps. However, Photonis stopped its PM activity and the project was consequently terminated. Other independent solutions were envisaged in parallel to the X-HPD photomultipliers :

- **Direction-sensitive optical module:** The standard hemispherical PMT is replaced with a segmented one, together with a mirror system [37]. The check of geometrical compatibility between the reconstructed trajectory and the direction of the detected light allows for reduction of the background and therefore leads to improvement of the muon trajectory reconstruction, mainly at the low energy end of the neutrino energy spectrum for events with a small number of hits. The working principle is summarized in figure 3.23.

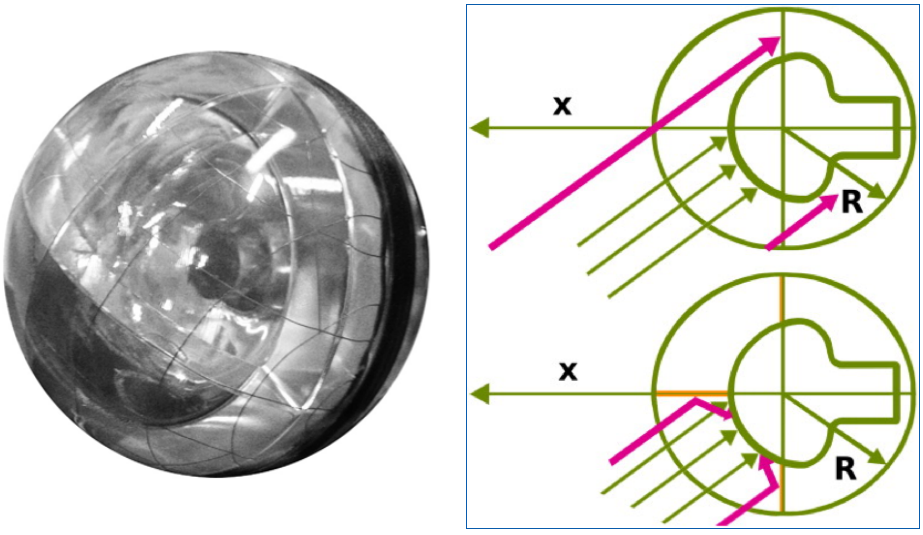

Figure 3.23: a) The complete directional optical module. b) Optical module: the Cherenkov light illuminates the whole photocathode surface (top). The mirrors concentrate the light on a single sector of the photocathode surface (bottom).

- **Optical module containing many small photomultiplier tubes (multi-PMT):** A cost effective way of maximizing photocathode area inside an optical module might be through the use of many small 3-inch PMTs [86]. The installation of up to 31 PMTs is envisaged (figure 3.24). This approach gives several advantages which can be summarized as follows: The photocathode surface of 31 3-inch PMTs is 15% larger than the effective photocathode surface of three 10 in. PMTs. Moreover, it would be combined with an enhanced photocathode giving quantum efficiency up to 45% at 400 nm (figure 3.24[70]). The other advantage is due to the reduced photocathode area compared to a 10 in. PMT, a factor 10 reduction in optical sea background (and charge passed through the dynode structure) is expected in each individual 3 in. PMT, leading to slower PMT aging and reduced degradation of gain over the detector lifetime. Besides, the reliability of the multi-PMT optical module is high, since failure of a single PMT should minimally degrade the performance of the OM. In a prototype the PMTs are suspended in Styrofoam to allow for the compression of the sphere under high pressure. PMTs with glass windows matching the curvature of the sphere are connected to the glass using optical adhesive.The dense packing constrains the space available for power supply and readout.

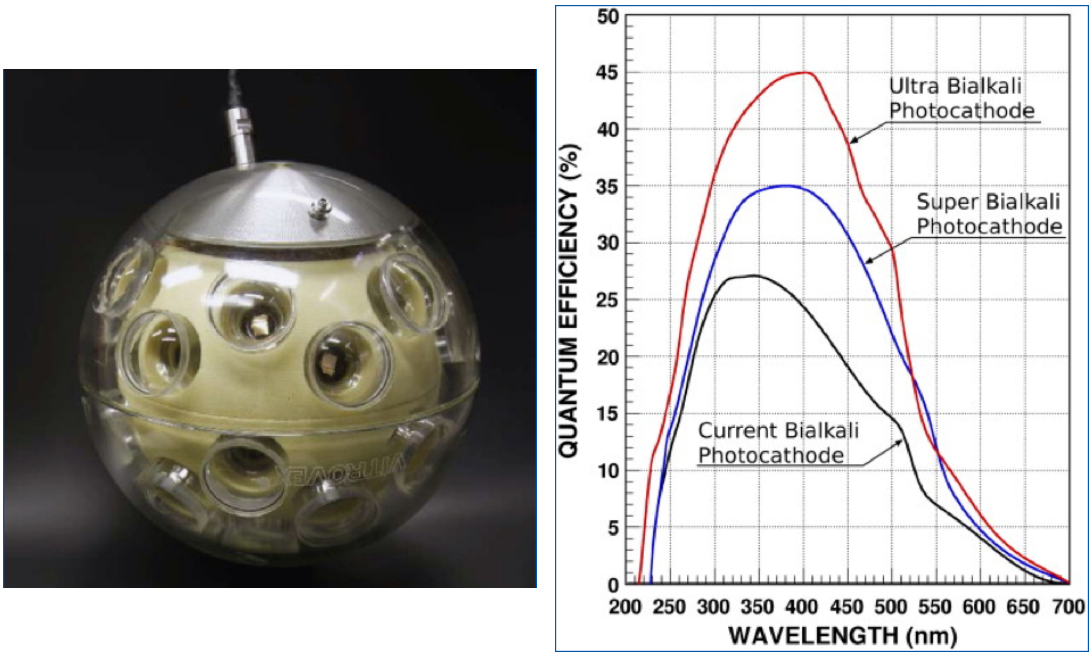

Figure 3.24: Left) Mechanical prototype of the multi-PMT OM with 3-inch PMTs in the Styrofoam support. Right) Quantum efficiency for the new Hamamatsu photocathodes.

This last solution is the one chosen for the KM3Net project, details on the readout electronics as well as the DU structure are detailed in the Technical Design Report [1].

[1] `http://www.km3net.org/TDR/TDRKM3NeT.pdf`

Part III

TAToO

Chapter 4

The context of a follow-up program for transient sources

Given the lack of neutrino positive observations and the expected low signals, observations in coincidence with events seen in other detectors can enhance the significance in respect to fluctuations of the atmospheric neutrino background. This point is strengthening the relationship with telescopes observing other messengers, like photons, protons and gravitational waves (GW) and even between existing neutrino telescopes. Telescopes-Antares Target of Opportunity (TAToO) is a project regrouping ANTARES and a network of robotic optical telescopes and will, in the near future involve other detectors eg. in X-rays or radio-telescopes.

Sources such as Gamma-Ray Bursts (GRBs) and Core Collapses of Supernovae (CCSNe), but also Micro-quasars or Active Galactic Nuclei (AGN) are promising transient neutrino sources which also have an optical counterpart. The light curves of GRBs or Supernovae are characteristic of these sources. Micro-quasars or AGN light curves need more sophisticated approaches for optical signal identification. In this work, we will focus on GRBs and SNe search.

This chapter treats about the main features and observations of GRBs and CCSNe. Then, the expected neutrino flux from these object is calculated using the Waxman-Bahcall model for GRBs and the Ando-Beacom model for CCSNe with mildly relativistic jets.

Content

4.1 Gamma-Ray Bursts

4.1.1 Observations

Gamma-ray bursts were detected accidentally in the late 60's by military satellites monitoring for compliance with the nuclear test ban treaty. Several years later, these observations were made public by the Vela satellites [76]. The extreme energies emitted by these sources intrigued the scientific community which, since then, has carried various research activities dedicated to solve the puzzle of gamma-ray bursts.

In 1991, with the launch of the Compton Gamma-Ray Observatory (CGRO), BATSE recorded 2704 gamma-ray bursts [95], the most striking result of BATSE is that these sources were isotropically distributed in the sky as shown on figure 4.1(a). The population distribution of GRBs is not homogeneous. One mean to evaluate the homogeneity of a distribution is the intensity distribution LogN-LogP with P being the peak flux and N(P) the number of bursts brighter than P. In the case of a homogeneous distribution, considering that the volume V is proportional to r^3 and the flux F is proportional to r^{-2} makes the number of sources N proportional to $F^{-3/2}$, implying that Log(N) = -3/2 log(F)+constant. Thus, the expected slope of log N-log P curve would be -3/2, but a lack of faint sources (P<10) is observed as shown on figure 4.1(b), implying that there exists a greater population of bright GRBs than faint GRBs. However, the dearth of faint events can be due to cosmological effects implying that the photon energy would be reduced by a factor (1+z), z being the burst redshift. This suggests that this result is rather due to the instruments sensitivity to a predefined range of photon energy.

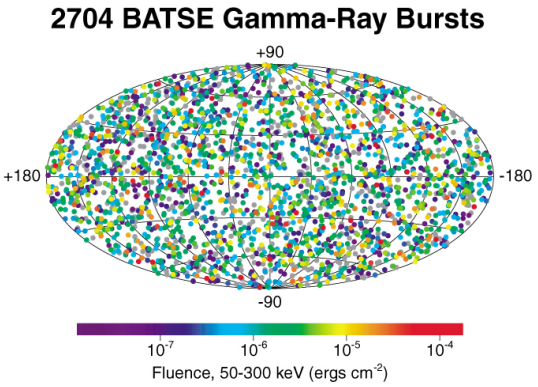

(a) Locations of a total of 2704 GRBs recorded with BATSE onboard CGRO during 9 years of operation: burst spatial distribution is isotropic [95].

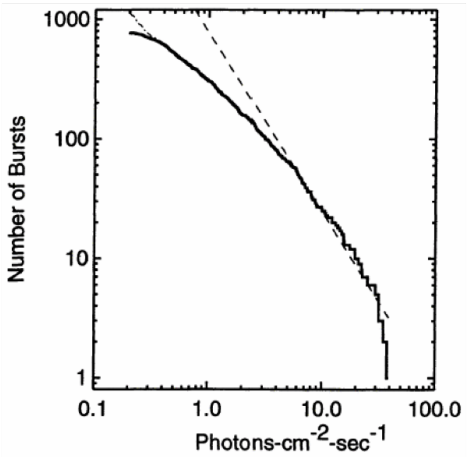

(b) Log N- Log P distribution of 772 bursts in the energy and 50 - 300 keV (continuous line). The dashed line represents a - 3/2 power-law spectrum [89].

Figure 4.1: Isotropy and homogeneity of observed GRB distributions.

Few years after BATSE discovery, Beppo-SAX provided the first high resolution X-ray images of gamma-ray bursts allowing arc-minute position accuracy. Subsequently, optical follow-up of these objects and measurement of their redshift distances [1] were made

[1] As of the end 2010, 915 GRBs were detected, 65% with X-ray afterglows, 43% with optical afterglows, 8% with radio afterglows, 26% only with measured redshifts [119]

possible. Examples of follow-up in X and optical wavelengths are shown on figure 4.2. The results found were inconsistent with any spatial distribution of some known population of galactic objects, ruling out the hypothesis of a galactic origin, which was favored at that time. However, the bursts distribution was found to be consistent with the hypothesis that GRBs are of cosmological origin [1] [89]. GRB 090423 was detected by SWIFT at a redshift of 8.2, making it one of the most distant astronomical objects ever observed [115]. The cosmological origin of GRBs immediately implies that GRB sources are very luminous, this also implies that GRBs are rare events. BATSE observed on average one burst per day. If not accounting for beaming or a cosmic evolution of the rate of GRBs, this corresponds to one burst per million years per galaxy.

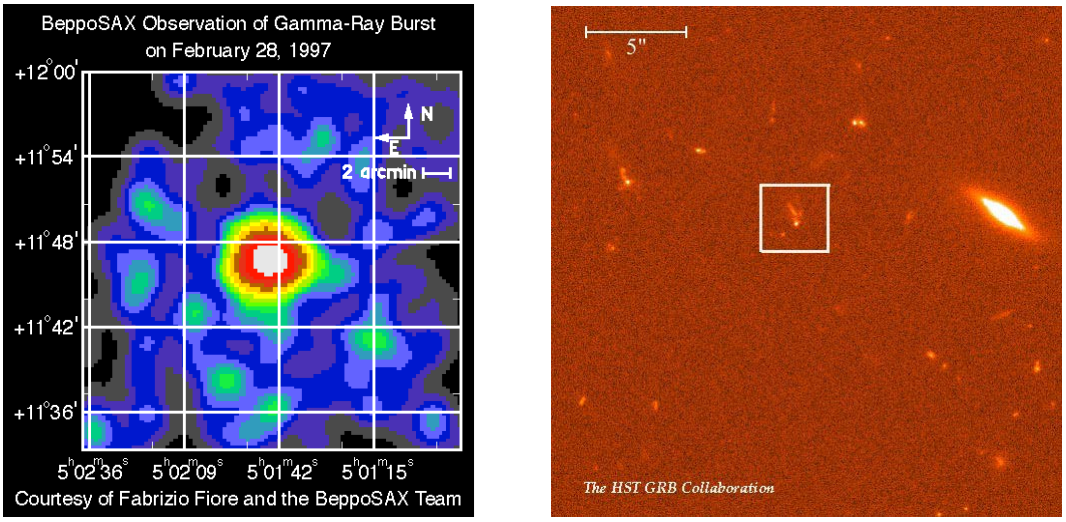

(a) X-Ray Afterglow of GRB970228.

(b) Afterglow and Host Galaxy of GRB990123.

Figure 4.2: Afterglow observations of GRBs in X-ray and optical wavelenghts.

Observed burst durations can vary by six orders of magnitude, from several milliseconds to several thousands of seconds [95]. Figure 4.3(a) shows the T90 BATSE burst distribution, which is the time needed to accumulate 5% to 95% of the total photon counts in the 50-300 keV band. BATSE confirmed earlier hints that the burst duration distribution can be divided into two sub-groups according to T90 : long bursts with T90 $>$ 2 s and short bursts with T90 $<$ 2 s. The ratio of observed long bursts to observed short bursts is around three to one. Apart from the difference in total bursts duration, the bursts have complicated and irregular time profiles, which vary drastically from one burst to another. Several time profiles are shown in figure 4.3(b) [89]. Each burst is composed of a variable number of peaks with a variability down to milliseconds time scales.

Spectral properties measurements mainly relied on BATSE data. The observed spectra are found to be well fitted using two power laws with a smooth transition at the peak energy E_p and a high energy tail. The fitting function is called the *Band function* [30] and

[1] A few GRBs, now called soft gamma repeaters, compose a different phenomenon, are believed to form on galactic neutron stars.

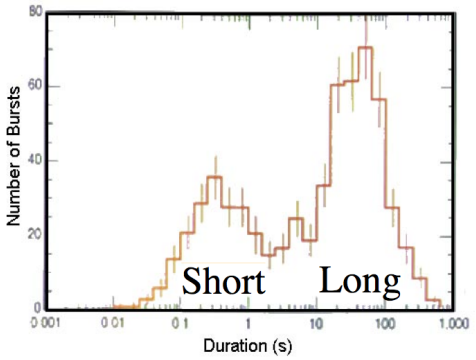

(a) Duration distributions (T90) for bursts in the 4Br catalog [95].

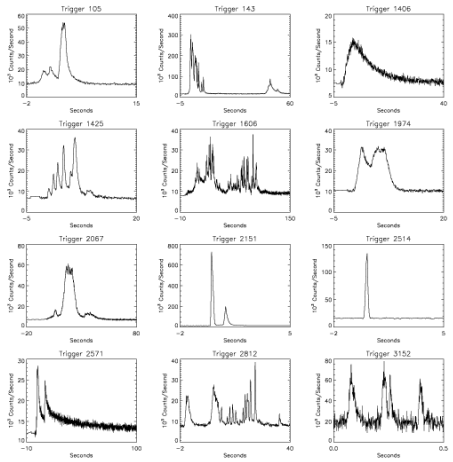

(b) Diversity of GRB time profiles as measured by BATSE [89].

Figure 4.3: Timing considerations related to GRB observations.

is expressed as:

$$N_\gamma(E_\gamma) = A_\gamma \begin{cases} (\frac{E_\gamma}{100keV})^{\alpha_\gamma}.e^{-\frac{E_\gamma}{E_0}} & \text{where } \mathrm{E}_\gamma < \epsilon^b_\gamma \\ (\frac{E_\gamma}{100keV})^{\beta_\gamma}.(\frac{\epsilon^b_\gamma}{100keV})^{\alpha_\gamma-\beta_\gamma}.e^{-(\alpha_\gamma-\beta_\gamma)} & \text{where } \mathrm{E}_\gamma \geq \epsilon^b_\gamma \end{cases} \quad (4.1)$$

Here, $N_\gamma(E_\gamma)$ is in units of photons cm^{-2} s^{-1} keV^{-1}. α_γ and β_γ are the low-energy and high-energy indices respectively. E_0 is called the reference energy, it is related to the energy at the spectral break ϵ^b_γ as $\mathrm{E}_0 = \frac{\epsilon^b_\gamma}{(\alpha_\gamma-\beta_\gamma)}$. The peak energy can be inferred from the fitted spectral break as $\mathrm{E}_p = \mathrm{E}_0\ (2+\alpha)$.

Figure 4.4 shows the model fitted to an average BATSE GRB spectrum. The spectrum is shallow at low energies and steeper toward higher energies. The peak energy E_p is situated at some hundred keV. However, no universal values can be assigned to the spectrum indices nor to the energy at the spectral break E_0, reflecting the peculiarity of each burst phenomenon.

Although it seems hard to find a general behavior among GRBs, a correlation between the Hardness Ratio (HR) [1] and the duration was brought to light, as a result, long GRBs have softer spectra than short GRBs [79]. This suggests that the two classes of GRBs can be ascribed in T90-HR space to the long/soft class, and the short/hard class. Another fact which supports this classification of GRBs population is the confirmation of the detections made by BeppoSAX by HETE2 and Swift of at least some long GRBs associated with core collapses of supernovae Type Ic. Most long GRB host galaxies are found to be dwarf star-forming galaxies. This hints to a connection between long GRBs and death of massive stars. Some short GRBs point towards another type of progenitor, they have host galaxies that are elliptical or early type, with little star formation. The top candidate model for this category is mergers of two compact objects, e.g. two neutron stars (NS-NS) or a neutron

[1] The HR is a measure to indicate the spectral properties, it is defined as the ratio of counts in two different energy bands.

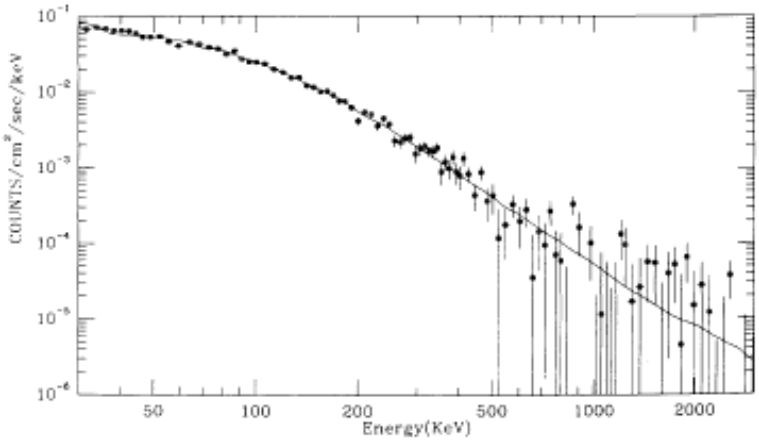

Figure 4.4: Example of a spectral fit. The Band function was fitted to the average spectrum of 1B 911127. The low-energy spectral index is α ∼-1, the high-energy spectral index β ∼ -2.4 and the reference energy E_0 ∼149 keV [30].

star and a black hole (NS-BH). This led to the common idea that long GRB originate from massive star GRB, and short GRB from compact stars. However, certain observation properties do not always refer to certain types of progenitor as 2 nearby long duration GRBs did not have any SN association.

4.1.2 Phenomenology

A generic scheme of a central engine for GRBs has emerged based solely on observational properties:

- The central engine can drive an outflow with extremely high luminosity and energy. If the emission is isotropically distributed in all directions, the required jet luminosity ranges from $L_{iso} \sim 10^{47}$ to 10^{54} erg s^{-1}, and the total gamma-ray energy ranges from $\sim 10^{49}$ to 10^{55}erg.

- The ejecta should have small baryon contamination to achieve a relativistic speed, with Lorentz factor Γ typically greater than 100, some even close to 1000 [123].

- The preferred escape route is along the centrifugally lightened rotation axis, and the stellar pressure tends to collimate the fireball into a jet. The jet needs to be collimated, with a beaming factor $f = \frac{\Delta\Omega}{4\pi}$ ∼1/500 for bright GRBs; the real luminosity and gamma-ray energy would be corrected by the same factor.

- The engine can last long, with progressively less powerful late activities to power X-ray flares and other wavelengths activities.

- The short time scale variabilities (ms) imply that the object must be a compact source out of the order of few stellar masses with a small size($<c.\Delta t$). This leads however to a problem when explaining how photons can be observed at energies greater than 0.5 MeV when photons would hardly avoid pair creation $\gamma\gamma \rightarrow e^+e^-$ under this hypothesis.

The leading model, namely the *fireball model* suggests that a fraction of the gravitational potential energy is initially converted into thermal energy, forming a hot fireball of photons, electron/positron pairs and a small number of baryons. The fireball expands under its own thermal pressure, and converts thermal energy to the bulk kinetic energy of the ejecta. This model efficiently avoided the compactness problem. In the fireball scenario, the radius of the source would be proportional to the Lorentz factor Γ and the variability time scale ΔT:

$$R \sim \Gamma^2 c \Delta T \tag{4.2}$$

The kinetic energy can be converted into particle energy and then into radiation in shocks. The internal collisions within an unsteady matter-dominated wind injected from the central engine give rise to internal shocks. The relative Lorentz factor between the two colliding shells can range from mildly relativistic ($\Gamma \geq 1$) to relativistic ($\Gamma \sim$ a few to tens). After the collisions, it is assumed that shells merge. The leading fast shell interacts with the circumburst medium and drives an "external" forward shock into the medium as sketched in figure 4.5. A reverse shock propagates into the ejecta until crossing it. The shocked materials between the forward and the reverse shocks form a "blast wave". The forward shock is initially relativistic. The reverse shock is mildly relativistic if the central engine duration is not long, but could be highly relativistic if the central engine duration is long enough.

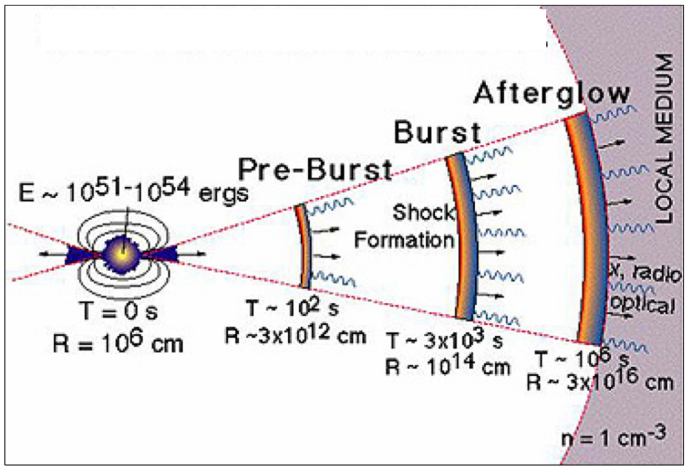

Figure 4.5: A sketch of the fireball model for GRBs.

Baryons and leptons are believed to be accelerated in shocks by *first-order Fermi acceleration*. γ-rays are produced by synchrotron or inverse Compton radiation from Fermi accelerated electrons in optically thin shocks.
The internal shocks time structure is reflected by the time variability of the peaks in the GRB light curve, δt « T, with δt being the duration of a typical pulse and T the overall duration of the burst [107].
The afterglow is produced via external shocks with the circumburst medium. The optical afterglow light curve typically invoke a highly collimated relativistic jet, which is beamed toward the Earth. The light curve is expected initially to decay as a low power of t (flux $\propto \sim t^{-1.1}$) and then break to a steeper slope (flux $\propto \sim t^{-2.4}$) at late times. A number of GRB afterglows show evidence for just this behavior, this has led to conclude that the

GRB emission is collimated into opening angles of $\sim 4^\circ$ as an average.
One important implication of the jet model of GRBs is that the vast majority of GRBs are beamed in directions away from Earth and therefore not observed in gamma-rays. However, the afterglow emission, occurring at much later times and at longer wavelengths, should be beamed into a larger fraction of the sky because of the decay of the jet Lorentz factor with time. There should therefore be afterglows that are observable when the associated GRB is not, namely, "Orphan Afterglows". Schematic depiction of the emission geometry is shown in figure 4.6(a). The ejecta are collimated into an angle θ_{jet}, corresponding to solid angle $\Omega_{jet} \sim \frac{1}{2}\theta_{jet}^2$. The emission from each element of the jet face is relativistically beamed into an angle $\sim \gamma^{-1}$, giving a total solid angle Ω_{opt}. As time progresses, the Lorentz factor γ and flux both decay, the relativistic beaming angle γ^{-1} then exceeds the jet opening angle θ_{jet} at t_{break} until reaching a certain time t_{max} after which the flux is too faint to be detected. As an illustration, figure 4.6(b) shows a power-law fit to a GRB light curve [59]. Because of the beaming effect, off-axis light curves are different from on-axis light curves, the former class being governed by relativistic effects, as well as the lateral spreading and internal structure of the jet.

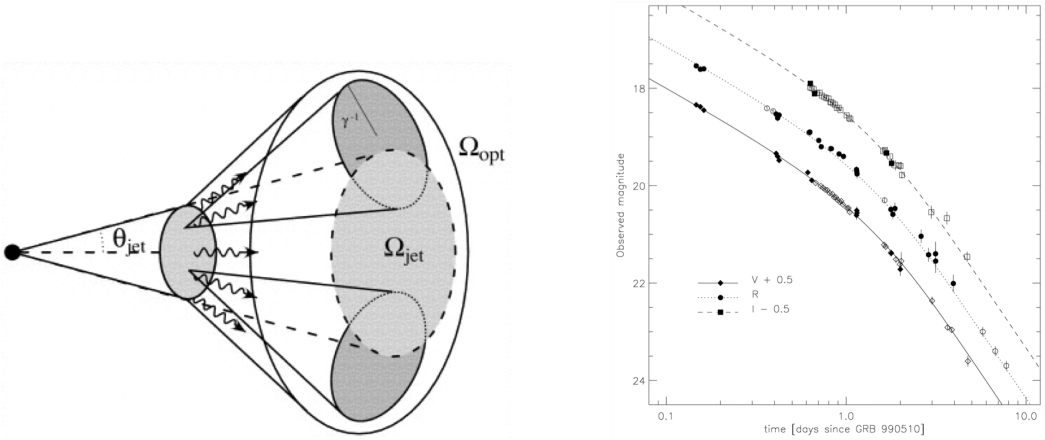

(a) Schematic depiction of the afterglow emission geometry [49].

(b) Optical light curves of the transient afterglow of GRB 990510.

Figure 4.6: Jet collimation principle and relation with afterglow light curves.

GRB optical emission has a wide range in apparent brightness, ranging from 5th magnitude for the prompt optical emission associated with GRB 080319B, down to the limiting magnitude R $\sim$ 23-24 of follow-up searches for afterglows. Figure 4.7 shows measured optical GRB light curves, the fast decay of the afterglow emission makes the afterglow detection very challenging and requires a fast response to gamma-ray telescopes triggers or neutrino triggers as in the context of this work.

4.1.3 GRB rates

According to the results obtained so far, the predicted rate of GRBs in the Universe seems to be between unity (or less) GRB and several hundreds per Gpc^3 and per year. These results seem to be related to the nature of the bursts under study, i.e. (1) "classical GRBs" also called "high-luminosity GRBs" (HL-GRBs) and/or (2) "sub-luminous" (low-luminosity) GRBs (LL-GRBs). For the HL-GRB rate, the rate is close to 1 Gpc^{-3} yr^{-1}.

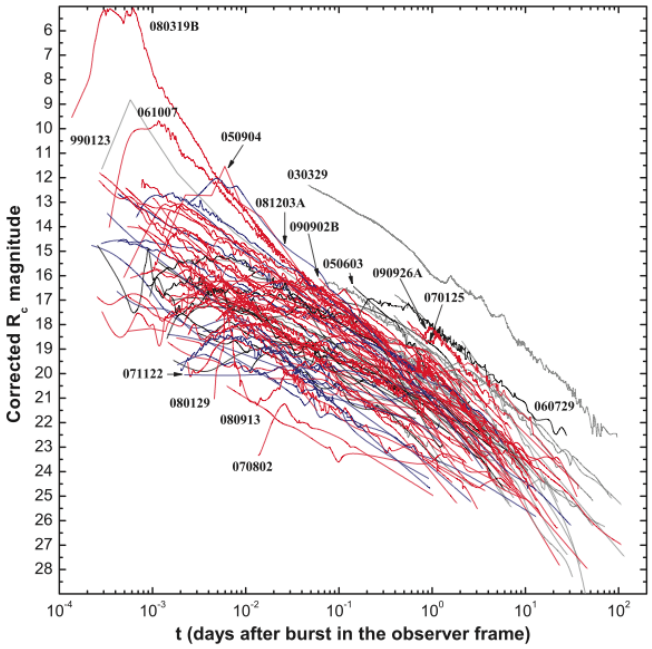

Figure 4.7: Optical light curves of GRBs in the R-band [72]

The method used is generally based on the determination of the luminosity function [1] (LF) by fitting a phenomenological model to the log(N)- log(P) relation of well known GRB catalogs. Assuming that GRBs trace the star formation rate (SFR), a model of the SFR is adopted for it and the rate of GRBs is determined.

Concerning LL-GRBs such as GRB 980425 and GRB 980425 which are the two closest GRBs, imply a local rate of low-luminosity GRBs (LL-GRBs) of $\sim$ 800 Gpc^{-3} yr-1. However, instruments sensitivity limitations and the lack of statistics makes the true rate of GRB still uncertain.

The fact that GRBs are detected up to very high redshifts makes it tempting to try and use them as standard candles that could be used to constrain the cosmological parameters, similar to SNe Ia. However, GRBs have a broad dispersion in peak luminosity (by a factor 1000 at least), which prevents using them as standard candles in contrary to supernovae of type Ia. This topic is still very challenging nowadays. The present limited sample of bursts and the lack of low redshift events, necessary to calibrate the correlations used to standardize GRBs energetics in a cosmology-independent way, prevent from establishing a sustainable cosmological rate evolution.

Since it is believed that GRBs are tightly connected with type Ib/c SNe, the rate of GRBs could be inferred from the SN rate. However, a low ratio of GRBs to SNIb/c is found, which highlights the fact that not all the type Ib/c SNe produce GRBs. The main explanation invokes a mildly relativistic jet, which is the source of the GRB, but that does not appear in all SNe Ib/c. Moreover, if the optical luminosities of GRBs and SNe can be considered to be similar, optical spectroscopy reveals broad absorption lines in SNe spectra associated with GRBs, indicative of fast ejecta. These peculiar highly energetic

[1]The luminosity function gives the number of stars or galaxies per luminosity interval. Luminosity functions are used to study the properties of large groups or classes of astronomical objects.

SNe, often designed Hypernovae (HNe) would not represent more than 3% of the SNe Ib/c, as obtained by studies based on the comparison of radio luminosities of GRB afterglows and SNe Ib/c.

4.1.4 High energy neutrinos from GRBs

The shocks producing the γ-rays must occur after the fireball has emerged from the stellar envelope. The shocks should also lead to Fermi accelerated relativistic protons with energies up to 10^{20}eV. Furthermore, the spectrum and flux of ultra-high energy cosmic rays (above 10^{19}eV) are consistent with those expected from Fermi acceleration of protons in cosmological GRBs [123].

Internal shocks within the jet lead to synchrotron radiation of electrons responsible of the observed prompt emission of γ-rays. The observed break in the photon spectrum around $\sim$ 250 keV and the steepening of the spectrum by one power could be due to one of these reasons; either the cooling of the electrons at high energy or the inverse Compton scattering process. When fitted with the Band function described in 4.1, an average GRB would have spectral breaks of $\alpha \sim$ -1 and $\beta \sim$ -2. By assuming that the proton spectrum follows the electron spectrum, and that electron losses are negligible, the neutrino spectrum $\frac{dN_\nu}{dE_\nu}$ would follow the proton spectrum as a first order approximation.

Protons interaction with the source photon field would lead to neutrinos via the Δ^+ resonance (see section 1.2.2 for further details). The neutrino energy is equivalent to 0.05 times the proton energy $\mathrm{E}_\nu = \frac{E_p}{20}$, while this latter value is constant when multiplied by the photon energy $\mathrm{E}_p \times \mathrm{E}_\gamma = \text{const}$. This results in the fact that the neutrino energy is inversely proportional to the photon energy $\mathrm{E}_\nu \propto \mathrm{E}_\gamma^{-1}$. Thus, from the Band function describing the photons spectrum, the nutrino flux is given as:

$$E_\nu^2 \frac{dN_\nu}{dE_\nu} = A_\nu \begin{cases} (\frac{E_\nu}{\epsilon_\nu^b})^{\alpha_\nu} & \text{if } \mathrm{E}_\nu < \epsilon_\nu^b \\ (\frac{E_\nu}{\epsilon_\nu^b})^{\beta_\nu} & \text{if } \epsilon_\nu^b < \mathrm{E}_\nu \leq \epsilon_\nu^s \\ (\frac{E_\nu}{\epsilon_\nu^b})^{\beta_\nu} (\frac{E_\nu}{\epsilon_\nu^s})^{-2} & \text{if } \mathrm{E}_\nu \geq \epsilon_\nu^s \end{cases} \tag{4.3}$$

Where $\alpha_\nu = 1 + \beta_\gamma$ and $\beta_\nu = 1 + \alpha_\gamma$ are the neutrino spectrum indices derived from the photons spectrum. ϵ_ν^b is the first break in the spectrum derived from a fit to the Band function. The second break denoted as ϵ_ν^s is caused by the fact that high energy pions would suffer synchrotron radiation before decaying into neutrinos. Hence, the spectrum is further steepened by one power for energies above ϵ_ν^s .

As already discussed in section 1.2.2, the spectrum is normalized to the γ-ray fluence F_γ. For the specific case of GRBs, we get:

$$x.F_\gamma = \int_{E_{min}}^{E_{max}} dE_\nu \frac{dN_\nu}{dE_\nu} \sim \ln(10).A_\nu \tag{4.4}$$

With $x = \mathrm{f}_\pi \times \frac{1}{8} \times \frac{1}{f_e}$.

Where f_π is the energy fraction the energy transferred to the pions, a factor 1/8 since half of the photo-hadronic interactions result in four neutrinos and a factor $\frac{1}{f_e}$ to account for the fraction of total energy in electrons compared to protons in the jet.

The normalization constant is then equal to:

$$A_\nu = \frac{1}{8} \frac{1}{f_e} \frac{F_\gamma}{\ln(10)} f_\pi \tag{4.5}$$

It is interesting to explicit how the break energies are obtained. Note that in this description, primed quantities are related to the comoving volume, others are expressed in the observer frame. The first break in neutrino energy ϵ_ν^b is determined through the minimum energy necessary to produce a Δ resonance in the GRB jet.

$$E'_p \geq \frac{m_\Delta^2 - m_p^2}{4E'_\gamma} \tag{4.6}$$

In the observer referential, this energy would be equivalent to $E_p \geq \mathrm{E'}_p\, \Gamma^2$ with Γ being the Lorentz factor. By assuming that the pion energy is equitably shared by its four final products, the neutrino would have a quarter of the pion energy. Moreover, because this phenomenon is cosmological, one has to account for an energy correction by taking into account the redshift z. Thus, the neutrino energy would be:

$$E_\nu = \frac{1}{4(1+z)^2} < x_{p\to\pi} > E_p \tag{4.7}$$

where $< x_{p\to\pi} >$ is the mean fraction of energy transmitted to the pion by the original proton during the Δ-resonance process (equivalent to 0.2). The redshift dependance is quadratic since both the proton energy and the photon energies are shifted by a factor (1+z).

Therefore, the final expression for the first break in neutrino energy can be expressed as:

$$\epsilon_\nu^b = \frac{1}{4(1+z)^2} < x_{p\to\pi} > \Gamma^2 \frac{(m_\Delta^2 - m_p^2)}{\epsilon_\gamma^b} = 7\times 10^5 \frac{1}{(1+z)^2} \frac{\Gamma_{2.5}^2}{\epsilon_{\gamma,MeV}^b} GeV \tag{4.8}$$

where $\Gamma_{2.5}^2 = \frac{\Gamma}{10^{2.5}}$ and $\epsilon_{\gamma,MeV}^b = \epsilon_\gamma^b / 1MeV$.

The second break results from the fact that high energy pions lose some energy via synchrotron emission before decaying. The effect becomes important when the pion lifetime becomes comparable to the synchrotron loss time.

$$\epsilon_\nu^s = \frac{10^8}{1+z} \sqrt{\frac{\epsilon_e}{\epsilon_B L_{\gamma,52}}} \Gamma_{2.5}^4 t_{v,-2} GeV \tag{4.9}$$

Here, ϵ_e is the fraction of internal energy converted to electrons, it is introduced because it is assumed that the wind luminosity carried by the internal plasma energy L_{int} is related to the observed γ-ray luminosity though $\mathrm{L}_{int} = \frac{L_\gamma}{\epsilon_e}$ *i.e* electrons must lose all their energy radiatively. ϵ_B is the fraction of all the internal energy carried by the magnetic field. $\mathrm{t}_{v,-2}$ = $\mathrm{t}_v/100$ s is the time scale of fluctuations in the GRB light curve, while $\mathrm{L}_{\gamma,52} = \mathrm{L}_\gamma$ / 10^{52} erg/s is the γ-ray luminosity of the GRB.

Figure 4.8 shows the neutrino spectrum for an individual GRB from the model described above. The parameters of an average spectrum were taken from [124]:

These values lead to the following values of the energy breaks in the neutrino spectrum:

- $\epsilon_\nu^b \sim 10^5$ GeV
- $\epsilon_\nu^s \sim 10^7$ GeV

The normalization constant using a typical γ fluence $\mathrm{F}_\gamma = 10^{-5}$ erg/cm^{-2}, gives $\mathrm{A}_\nu \sim 7.10^{-4}$ GeV.cm^{-2}.

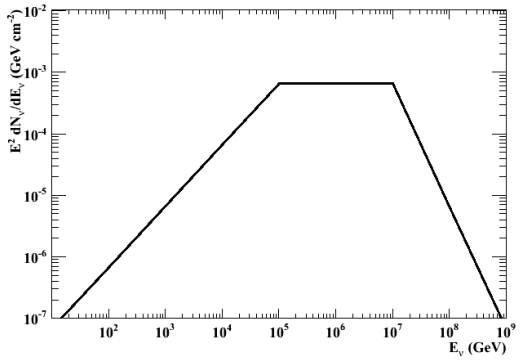

Figure 4.8: Neutrino spectrum shape of an individual typical GRB with values from [124].

4.2 Core collapses of SNe

Several GRBs have been observed in coincidence with core-collapses of supernovae [64] [113]. The jet signature, but more mildly relativistic, may be common to supernovae, which are much more frequent than GRBs, even correcting for the effects of jet opening angle on observability. If a significant fraction of core-collapse supernovae are accompanied by jets with $\Gamma_b \sim$3, perhaps $\sim$ 1%, then TeV neutrinos could be the only prompt signature of these hidden sources. In addition to being more frequent, mildly relativistic jets are expected to be much more baryon-rich (a "dirty fireball"). Ando and Beacom [23] developed a model of high-energy (TeV) neutrino emission from jets with $\Gamma_b \sim$3 based on the model of Razzaque, Mészáros, and Waxman [104] but including the kaon contribution which offers more interesting detection prospects, since compared to pions, kaons undergo less energy loss before decaying into neutrinos due to their larger mass and shorter lifetime. The relatively larger energy transferred to the daughter neutrinos, means that the neutrino spectrum from kaons is harder and more detectable than that from pions.

The mildly relativistic jet model assumes the collapse of a massive star M $>$ 8 Solar masses with subsequent formation of a neutron star or black hole. The rotation of the merger powers jets with bulk Lorentz factors of $\Gamma_b \sim$ 1-10 and opening angles $\theta_j \sim 1/\Gamma_b =$ 5°-50°. Moreover, due to the low Lorentz factor and to the high baryon density, collisions among accelerated protons(pp) occur efficiently. The associated jets are however too weak to penetrate the stellar envelope. Thus, it would not be observable in the electromagnetic spectrum. The core collapse is assumed to deposit E $_j \sim 3 \times 10^{51}$ erg of kinetic energy in the material ejected in the jets, which is common to standard GRBs. Protons are Fermi accelerated to a E^{-2} spectrum and produce efficiently muon neutrinos through the decay of charged pions and kaons formed in proton-proton collisions. The mesons are produced with 20% of the parent proton energy, so that they follow the original spectrum of accelerated protons with power-law index -2. They cool, however, by radiative (synchrotron radiation and inverse Compton scattering off thermal photons) and hadronic (πp and Kp) processes. If mesons decay faster than they cool, then the daughter neutrinos maintain the E^{-2}spectrum shape, otherwise, the spectrum becomes steeper. The steepening mark the beginning of each cooling process. The time scale of hadonic cooling t'_{hc} is energy independent while for radiative process, $t'_{rc} \propto E^{-1}$ where E is the meson (π or K) energy. The total cooling time is given as for $t'^{-1}_{c} = t'^{-1}_{rc} + t'^{-1}_{hc}$. For default parameters used in

Ando and Beacom model [23], this suggests that at low energies, the hadronic process is dominant so the first energy break is due to this latter process, and the second is due to radiative cooling.

The energy breaks for pions and kaons are given here along with their dependency on the jet parameters:

$$\pi \begin{cases} E_{cb}^{(1)} = 30\text{GeV} \times (\frac{E_j}{E_{jo}})^{-1} \times (\frac{\Gamma_b}{\Gamma_{bo}})^5 \times (\frac{t_j}{t_{jo}})^2 \\ E_{cb}^{(2)} = 100\text{GeV} \times \frac{\Gamma_b}{\Gamma_{bo}} \end{cases}$$

$$K \begin{cases} E_{cb}^{(1)} = 200\text{GeV} \times (\frac{E_j}{E_{jo}})^{-1} \times (\frac{\Gamma_b}{\Gamma_{bo}})^5 \times (\frac{t_j}{t_{jo}})^2 \\ E_{cb}^{(2)} = 2 \cdot 10^4\text{GeV} \times \frac{\Gamma_b}{\Gamma_{bo}} \end{cases}$$

The first energy break is strongly dependent on the jet boost factor, this means that for high values of Γ ($\Gamma > 3$), radiative cooling of mesons has to be set in at lower energies than hadronic cooling.

The spectrum can be normalized at 1 GeV energy value as follows:

$$F_{\nu,1GeV}^{i} = \frac{\langle n_i \rangle \ B_{\nu,i}}{8} \frac{E_j}{2\pi \ \theta_j^2 \ d^2 \ \ln(E'_{p,max}/E'_{p,min})} \frac{1}{(1GeV)^2} \text{GeV}^{-1} \ cm^{-2} \quad (4.10)$$

Where d is the source distance, $\langle n_i \rangle$ is the meson multiplicity (1 for pions and 0.1 for kaons), $B_{\nu,i}$ is the branching ratio of the decay into neutrino mode (1 for pions and 0.6 for kaons), and the factor $\ln(E'_{p,max}/E'_{p,min})$ normalizes the proton spectrum to the jet energy. This leads to:

$$F_{\nu,1GeV}^{\pi} = 44.3 \ \frac{E_j}{E_{jo}} \ (\frac{\Gamma_b}{\Gamma_{bo}})^2 \ (\frac{d}{d_o})^{-2} \ GeV^{-1} cm^{-2} \quad (4.11)$$

$$F_{\nu,1GeV}^{K} = 0.26 \ \frac{E_j}{E_{jo}} \ (\frac{\Gamma_b}{\Gamma_{bo}})^2 \ (\frac{d}{d_o})^{-2} \ GeV^{-1} cm^{-2} \quad (4.12)$$

The expected neutrino spectrum from pion and kaon contributions can be expressed as:

$$E^2 \frac{dN}{dE} = \sum_{i=\pi,K} F_{\nu,1GeV}^{i} \times \begin{cases} E_\nu^0 & \text{E}_{p,min} \leq \text{E}_\nu < \text{E}_{\nu,cb}^{i(1)} \\ E_{\nu,cb}^{i(1)} \ E_\nu^{-1} & \text{E}_{\nu,cb}^{i(1)} \leq \text{E}_\nu < \text{E}_{\nu,cb}^{i(2)} \\ E_{\nu,cb}^{i(1)} \ E_{\nu,cb}^{i(2)} \ E_\nu^{-2} & \text{E}_{\nu,cb}^{i(2)} \leq \text{E}_\nu \leq \text{E}_{\nu,max}^{i} \end{cases}$$

Where

$$E_{\nu,max}^{K} = (\frac{\Gamma_b}{\Gamma_{bo}}) \frac{E'_{K,max}}{2} = \frac{0.2 \ E'_{p,max}}{2} = 21 \cdot 10^3 GeV \quad (4.13)$$

$$E_{\nu,max}^{\pi} = (\frac{\Gamma_b}{\Gamma_{bo}}) \frac{E'_{\pi,max}}{4} = \frac{0.2 \ E'_{p,max}}{4} = 10.5 \cdot 10^3 GeV \quad (4.14)$$

The left column of figures 4.9 illustrates the expected neutrino spectrum from pions, kaons and both kaons and pions when varying the jet boost factor for a SN at 10 Mpc with a jet energy of $3{\cdot}10^{51}$ erg. The right column show the effect of varying the jet energy of a SN with a jet boost factor of 3.

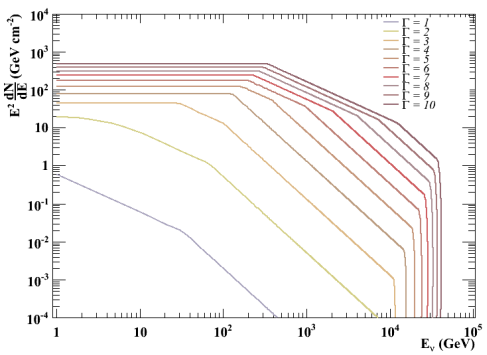

(a) Neutrino spectrum from Pions for several boost factors values.

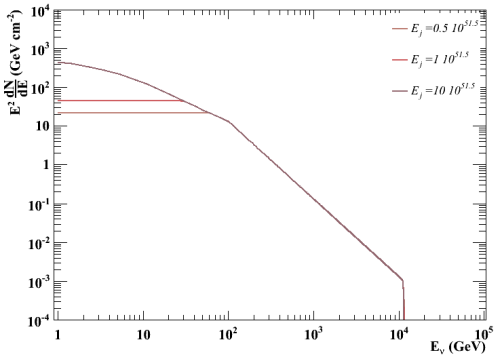

(b) Neutrino spectrum from Pions for several jet energies values.

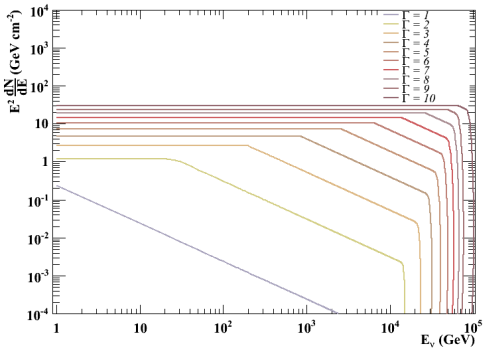

(c) Neutrino spectrum from Kaons for several boost factors values.

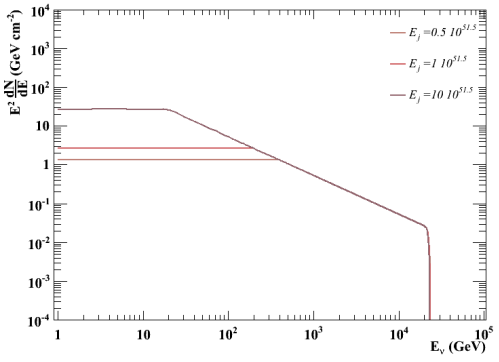

(d) Neutrino spectrum from Kaons for several jet energies values.

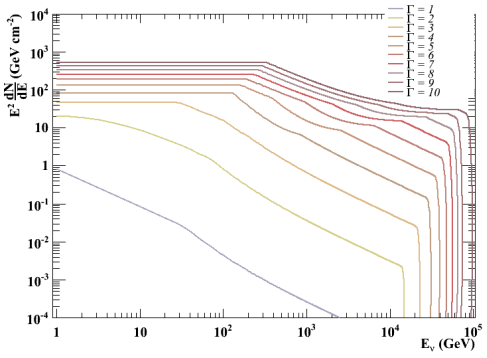

(e) Neutrino spectrum from Pions and Kaons for several boost factors values.

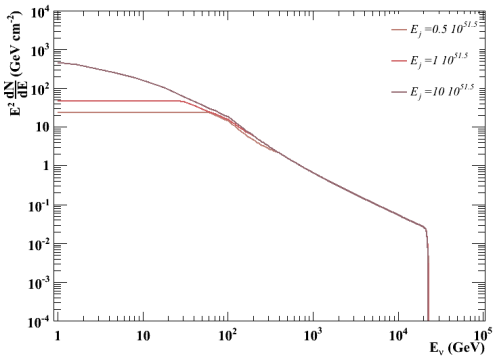

(f) Neutrino spectrum from Pions and Kaons for several jet energies values.

Figure 4.9: CCSN spectra with varying boost factors and jet kinetic energies.

For greater values of Γ_b, the neutrino spectrum is governed by the meson decay mode, the meson cooling energy break is then shifted at higher energies. ANTARES is sensitive to energies greater than 100 GeV, implying that more neutrinos are expected to be detected

from jets of high boost factors. The kaon contribution extends the energy range, meaning that most of the neutrinos that ANTARES could be sensitive to would originate from the kaon decay. For higher Γ_b, the spectrum of neutrinos from kaons is expected to follow a perfect E^{-2} spectrum with no subsequent cooling but a sharp cut-off related to the maximum proton energy achievable before $p\gamma$ interactions. The influence of the jet energy is seen on the first break offset, since it should not have any impact on the second break neither on the maximum neutrino energy. Above 100 GeV, for low boost factor values, the expected neutrino spectrum is almost insensitive to the jet energy. For higher boost factors, as the first break is shifted towards greater energy values, the influence of the jet kinetic energy on the spectrum when $E_\nu >$ 100 GeV is stronger.

Chapter 5

The neutrino alert system and optical-follow-up

In order to improve the sensitivity to transient sources such as gamma-ray bursts (section 4.1), as well as Core Collapse Supernovae (section 4.2), a follow-up scheme of high energy neutrino events was proposed in [73] [80]. Triggered by selected events from a neutrino detector, a network of small optical telescopes is meant to point at the neutrino direction in search for a correlation with an optical counterpart from a SN or a GRB. Based on this idea, an on-line optical follow-up program named TAToO [1] is operating efficiently in ANTARES since end of 2009 [5]. TAToO is based on an alert system which is activated in case of the detection of *multiplet*-neutrinos *i.e* 2 neutrinos or more coming within a predefined temporal and directional window, or the detection of a single high energy neutrino. A sketch of the program principle is shown in figure 5.1(a). The optical network covers both hemispheres and englobes 6 robotic telescopes composed of 4 ROTSE[10] telescopes and 2 TAROT[77] telescopes which location is shown on figure 5.1(b).

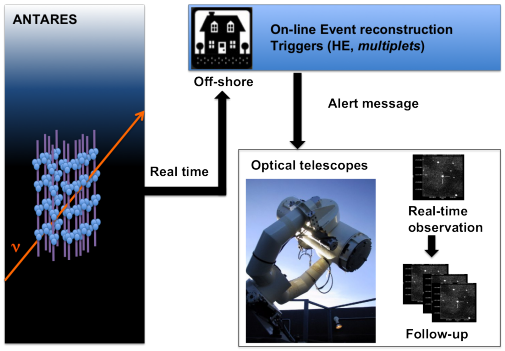

(a) TAToO principle : An ANTARES event is reconstructed on-line and its direction is sent to the network of optical telescopes if it passes the trigger conditions.

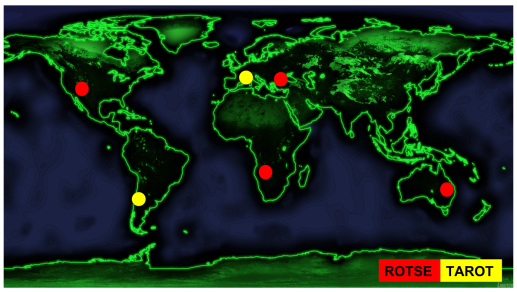

(b) World map of the robotic telescopes network composed of 4 ROTSE telescopes and 2 TAROT telescopes covering both hemispheres.

Figure 5.1: The TAToO system

This program is now capable to achieve a high performance timing ($\sim$ 1 mn delay between the neutrino detection and the alert reception by the telescopes), which is essential for the search of rapidly fading optical counterparts such as GRBs. Moreover, to achieve the

[1] **T**elescope- **A**NTARES **T**arget **o**f **O**pportunity

basic requirement that the neutrino direction should be reconstructed within the telescopes $2^\circ \times 2^\circ$ field-of-view, TAToO is capable to reconstruct an event with $\sim 0.45^\circ$ angular resolution during the on-line process. This value can be reduced down to 0.3° using an alternative off-line reconstruction giving a refined position available within $\sim$ 15mn-1h.

In this chapter, the on-line event filtering and reconstruction are described. The selection of the highest energy events as well as multiplet events capable of triggering neutrino alerts will be presented. The technical monitoring of the entire system (neutrino telescope+optical telescope) is described in the last section.

Content

5.1 The on-line event reconstruction

The reconstruction algorithm `BBfit` [8] is integrated in a fully dedicated TAToO program called `BBAlert`[1] running in a loop mode. This program is running on a dedicated TAToO machine and is connected to the ANTARES data stream after the data filters (section 2.9) before writing the data to disk.

Originally designed for the on-line monitoring of ANTARES data taking, the `BBfit` algorithm is fast, taking $\sim$ 5 to 10 ms to reconstruct an event. Nonetheless, being based on a very strict hit selection, it gives robustness with respect to the optical background as well as a good up-down track separation.

In the following paragraphs, its main features will be described for completeness, although we address the reader to [46] for an exhaustive description of the algorithm.

5.1.1 Hit treatment and hit selection

As a first step of the track reconstruction, time and charge calibrations are applied on the hits passing the low-threshold amplitude of 0.3 pe (L0 condition, see section 2.3). The geometry of the three optical modules on a storey is ignored in `BBfit`. A storey is considered as a space point centered on the detector line. All hits from the same storey are time ordered, regardless from which optical module they originate. Moreover, hits within 20 ns in a storey are merged, keeping the first hit time as information. If the merged hits originate from different optical modules, the merged hit obtains a bonus charge of 1.5 photoelectrons and is kept for the next steps. If the hit comes from a single OM and is already energetic enough to pass a threshold of 2.5 p.e, it is also kept for the next steps (L1 condition).

Further hit selection is undertaken to avoid from accounting random photons issued from the optical background or scattered late hits. For this purpose, timing conditions between adjacent and next-to-adjacent floors are set to 80 ns and 150 ns respectively to prevent from random background hits (T3 condition). Only lines having at least one T3 are thus considered and all hits which contribute to a T3 cluster are selected. New hits (even at L0 level) are searched for within a narrow time window around the T3 times by calculating the expected hit times in each adjacent floor [2] and added to the final list of selected hits.

5.1.2 Fitting procedures

To ensure a non-degenerate 5-parameter track fit, a preliminary cut on the number of selected hits is done before any fitting attempt. `BBfit` can handle two fitting procedures, a single-line fit if the hits are all issued from the same line or a multi-line fit. Events triggered on a single line do not allow to reconstruct the muon direction. For TAToO, only the multi-line fit is used.

Fitting a particle track

The fitting of a muon track lies on the determination of a certain amount of parameters given a set of measured physical quantities : the time, position and hit amplitude.

[1] Besides the event filtering and reconstruction, `BBalert` includes the event selection and the creation of the alert message in GCN format.

[2] assuming the hits arrive from a plane wave front, i.e. linearly in the z-t plane.

Assuming a particle moving with the speed of light c, its track assumed straight in space can be expressed as :

$$\vec{p}(t) = \vec{q}(t_0) + c(t - t_0).\vec{u} \tag{5.1}$$

The particle is at position $\vec{q}$ at time t_0 and moves in the direction $\vec{u}$. Therefore, the track is defined by a total of 5 parameters : three values to fix the position $\vec{q}$ for a given time which can be shifted, and two angles to define the direction $\vec{u}$, which can be expressed as a function of the the azimuth Φ and zenith angle θ.

Fo each line, the track can be parametrized based on geometrical considerations in terms of z_c, t_c, d_c and the two angles which define $\vec{u}$. As shown on figure 5.2, z_c is the z-component of the point of closest approach to a detector line, strictly vertical in space. At this point, the particle passes at time t_c at a distance d_c.

The arrangement of a track and a single detector line is invariant against rotation around the z-axis. The track can be conveniently reparametrized in terms of z_c, t_c, d_c and u_z (the latter being nothing other than the cosine of its zenith angle). This means that the track is now fully defined by only 4 parameters [1]. To build a fitting function, it is necessary to know : (a) the arrival time t_γ of a Cherenkov photon at the detector line position (0, 0, z), (b) its corresponding travel path d_γ and (c) its inclination with respect to the detector line $\cos(\theta_\gamma)$. All three values can be derived from the parameters of the track closest approach as well as from the propagating medium refraction index n which is related to the Cherenkov angle θ_c by $1/n = \cos(\theta_c)$. n= 1.38 is used in the code.

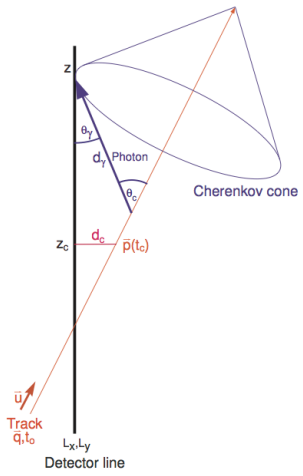

Figure 5.2: Illustration of the variables used to describe a track and its corresponding Cherenkov cone with respect to a vertical line [8].

At this step, `BBfit` does not handle an input parametrization of the detector geometry. Instead, it uses a *nominal* detector geometry based on the measured BSS positions from acoustic triangulation (see section 2.4.3). An important simplification with respect to a full geometry derived from acoustics and compass data is that the detector lines are perfectly vertical and line distortions due to sea currents are ignored.

[1] The multi-line arrangement breaks rotational symmetry, therefore all parameters (5 in total) are needed to determine the track.

A further fit based on an M-Estimator maximisation has been added in order to improve the precision of the reconstruction. This fit is applied only to those events where `BBfit` has reconstructed a track using more than one line and uses this track as a reference for both the hit selection and the fit. In the M-Estimator fit, a new hit selection is applied based on a time residual cut of 30 ns with respect to the `BBfit` multi-line track coming out from the track fit described above. While using a nominal detector geometry, no merging is applied to the hits and all the OMs are taken with their own position.

Fitting a point-like source (the bright point fit)

The bright point fit considers a point-like source emitting an isotropic single flash at a given moment. It can describe artificial light sources such as LED and laser beacons used during calibration runs or charge sparks (as have been observed in some optical modules) but also the light from hadronic and electromagnetic showers which extent should be smaller than the detector lines distances. Since it is a point in space, a bright point is defined by 4 parameters; its position $\vec{q}$ and its time t_0.

Track fit function and minimization procedure

The fitting function relies on time residuals information, defined as the time difference between the hit times t_i and the expected arrival time t_γ of the photons from the track or the bright point. Besides this standard χ^2 fit, an additional term accounting for the measured hit charge a_i and the calculated photon distances d_γ is considered:

$$Q = \sum_{i=1}^{N_{hit}} [\frac{(t_\gamma - t_i)^2}{\sigma_i^2} + \frac{A(a_i)D(d_\gamma)}{\langle a \rangle d_0}] \tag{5.2}$$

σ_i accounts for the time uncertainty[1]; it is set to 10 ns for a_i>2.5 p.e and to 20 ns otherwise.

The second term gives a penalty for high amplitudes and large distances combinations. The product is divided by the average charge[2] of hits selected in the fit $\langle a \rangle$. This would compensate for the fact that more energetic tracks or showers will produce more light at the same distance. d_0 balances the weight between the two terms. It is chosen to be 50 m. At this distance, a typical signal output of 1 p.e is expected from PMTs which point straight into the Cherenkov light front.

The MIGRAD function of the MINUIT package [68] is used to determine the minimum of the quality function Q. The value of Q divided by the number of degrees of freedom is the associated reduced fit quality and will be used for further selections.

For the M-estimator fit, the track fit is performed by choosing the track parameters that maximize the value of the M-Estimator :

$$M = \sum_{i=1}^{N_{hit}} [2 - 2 \cdot \sqrt{1 + \frac{r_i^2}{2}}] \tag{5.3}$$

[1]The PMT transit time spread (1.3 ns) is significantly smaller than the time uncertainty considered above. The timing uncertainty take into account an additional smearing due to the applied geometrical approximations and due to the occasional presence of late hits from small angle scattering or from electromagnetic processes which passed the hit selection.

[2]The charges are corrected for the angular acceptance of the storey.

where r_i is the time residual of the considered hit. The prefit is taken from the previous `BBfit` multi-line track fit.

The M-estimator fit is not used in the cut optimization described in this section but instead, the track fit defined in equation 5.2 is used and the resulting prefitted events are then fitted by the M-estimator.

5.2 The selection of the triggers

Two distinct filters are implemented in the follow-up program. These filters are optimized to efficiently reject the atmospheric muon background. However, the other background component *i.e.* atmospheric neutrinos, represent an irreducible background source. Cosmic neutrinos are assumed to have an energy spectrum proportional to E^{-2}, where E is the neutrino energy. It is expected that the atmospheric neutrino contribution is reduced at high energies since their spectrum is steeper. One triggering condition is therefore the selection of the highest energy events in ANTARES in order to enhance the probability to select neutrinos of cosmic origin. Another condition is to require time and direction coincidences between two neutrinos or more. The expected background rate from multiplets is very low (see section 5.2.4), the high energy trigger is thus tuned to send neutrino alerts to the telescopes. High energy events are selected keeping in mind two fundamental conditions :

- The alert rate should be around 25 per year. This stands as an agreement between ANTARES and the telescope network.
- The triggering events should be well reconstructed and the direction error box should be smaller than 1° radius. Due to the limited telescopes field-of-view (fov), this is the minimum condition to allow an appropriate optical counterpart search within the neutrino direction error.

The triggering events selection is optimized using Monte Carlo (MC) simulations and a subset of 2008 data taken with the full detector configuration from September to December 2008 representing 70.3 active days. The selection procedure described in this section consists of removing the background associated to atmospheric muons and to tune cuts on different parameters in order to fulfill the basic requirements on the alert rate and the angular resolution.
During TAToO operation in 2009-2011, the detector has faced periods with 9 lines, 10 lines and 12 lines configurations. The cuts were tuned accordingly based on the appropriate MC. The optimization with 12 line MC will be presented here, as for the other configurations, the principle remains the same.

5.2.1 Monte Carlo simulations

To simulate the atmospheric muon background, a signal from down going atmospheric muons is simulated with Corsika [61]. The primary flux composition, weighted by the Horandel flux [65] and the QGSJET hadronic model[71], is used in the shower development.

Upward going neutrinos are simulated with genhen [94]. The events are weighted with the parameterization of Bartol for the atmospheric ν_μ flux [32]. Both productions have been processed through km3 and geasim to propagate the Cherenkov light in sea water. Light absorption and diffusion in sea water is simulated according to [96] with a maximal

absorption length of 55 m. The angular acceptance of optical modules is taken from a fit to water tank measurements made by a group from the ANTARES collaboration [24].

Then, TriggerEfficiency [50] is used to simulate the ARS electronics response and merges the optical background to the MC. An optical noise from a typical data run has been added from the 12 line configuration of 2008 data. The simulation takes into account dead optical modules by using a "mask", i.e. physics hits are suppressed when they happen to occur on a faulty module.

Finally, Trigger Efficiency processes the MC through the ANTARES software trigger : any of the trigger algorithms which are used in the DAQ system presented in 2.9 can be applied to the MC. In the 12 line configuration, the T3 trigger was applied.

5.2.2 Preliminary cuts

Before any selection cut is undertaken, preliminary cuts are applied based on considerations due to the reconstruction conditions:

- $|cos(zenith)| < 0.9998$ to exclude events for which the fit stopped at the boundary condition for the elevation angle.
- Number of hits used in the fit (nhit) > 5 to ensure a non-degenerate 5-parameter track fit. The cut reduces the data sample by 2.5%.
- Number of lines used in the fit (nline) > 1 to have the information about the track direction, *i.e* the azimuth direction.

Figure 5.3 shows all reconstructed MC and data events zenith distribution after preliminary cuts. A scale factor of 1.8 was applied on the muons to match the data, this has no impact on the selection efficiency as the subsequent cuts, would aim at the elimination of the atmospheric muons [1].

Atmospheric muons represent the main background but this contribution can be significantly reduced by selecting only upward-going tracks as illustrated by the vertical black line on figure 5.3.

5.2.3 High energy filter

The high energy filter is the usual trigger used to send neutrino alerts to the telescopes. In this section, the cuts used for this trigger are developed and the performance on the angular resolution as well as on the efficiency of the filter are presented.

Cut on the number of lines

For all up-going events and preliminary cuts, figure 5.4 shows the angular resolution, defined as the median of the space angular difference between the incoming neutrino and the reconstructed neutrino-induced muon, as a function of energy for different number of lines involved in the fit. The angular resolution is enhanced if more lines are considered in the fit. In order to obtain a good angular resolution while keeping a sufficient number of data events, only events fitted strictly on more than 2 lines are considered. This is the first condition applied in the HE filter development.

[1] The discrepancy between the data and the MC atmospheric muons can be due the fact that the simulation does not handle efficiently atmospheric muons arriving in bundles from electromagnetic showers.

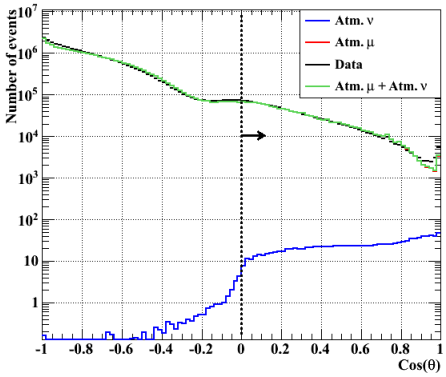

Figure 5.3: Distribution if the cosine of zenith angles for MC and data events after preliminary cuts. The vertical line shows the boundary between up-going and down-going reconstructed events.

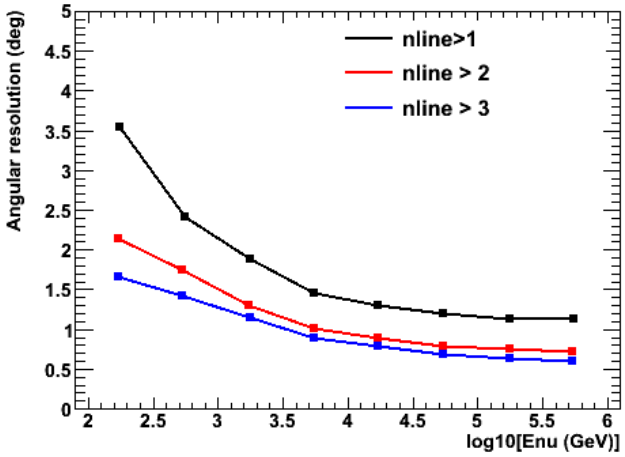

Figure 5.4: Angular resolution as a function of the neutrino energy for all up-going events after preliminary cuts with tracks reconstructed using different number of lines.

Atmospheric muon rejection

As can be seen on figure 5.3, even after requesting only upward-going events, still a significant part of atmospheric muons are reconstructed as up-going. A cut on the track fit quality Q would efficiently reduce this background if one requests the best reconstructed events. During TAToO operation, the cut sets on the fit quality have been improved to achieve better performances on the angular resolution as well as on the estimated average energy of the triggering events. Three main sets of cuts on Q were developed. Namely, the standard on-line track fit quality cut used in ANTARES [1] was applied in 2009, the line-dependent track fit quality cut was used in 2010 and the last optimized cut; the hit-dependent cut applied since January 2011. In this section, they are presented and their performances are compared.

[1] This cut is used in the on-line monitoring of the neutrino telescope.

Standard ANTARES on-line cut: In the first months of TAToO (Jan.2009-Apr.2009), the standard cut used to filter the atmospheric muons in the ANTARES on-line event selection was used. It consists of selecting upward-going events fitted on at least 2 lines achieving the condition Q $<$ 1.4, as suggested in figure 5.5. To further enhance the purity [1] of the so selected sample, the bright point fit quality χ^2_b is considered. Events from electromagnetic or hadronic showers usually have a good χ^2_b. In principle, they can be excluded by requesting that Q is always better than χ^2_b. Table 5.1 shows the number of events after applying the successive cut steps on the MC and the data of 2008 with the 12 line configuration. This cut shows good performances in selecting a pure neutrino sample by significantly reducing the atmospheric muon contribution.

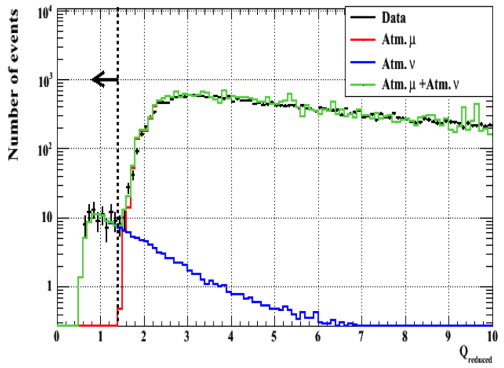

Figure 5.5: Distribution of the reduced quality fit Q for upward-going events reconstructed on more than 2 lines.

Cuts	Atmospheric ν	Atmospheric μ	Data
All reconstructed events	1569.1	$3.1{\cdot}10^7$	$3.8{\cdot}10^7$
Preliminary cuts +nline $>$ 2	176.1	$3.8{\cdot}10^6$	$4.1{\cdot}10^6$
$\cos(\theta) > 0$	173.7	$5.8{\cdot}10^4$	$6.2{\cdot}10^4$
Q$<$1.4	72.7	0.1	81
Q $< \chi^2_b$	72.7	0.1	81

Table 5.1: Expected number of atmospheric neutrinos, atmospheric muons and 12 line configuration data from 2008 at each cut step for 70.3 active days.

However, equation 5.2 shows that the track fit quality function is dependent on the amplitude and on the number of hits used in the fit. Figures 5.6(a) and 5.6(b) show that the amplitude and the number of hits are correlated to the energy of the neutrino as more energetic neutrino induced muons emit more Cherenkov light in a first order approximation. Subsequently, the quantity Q would be related to the neutrino energy. Inevitably, when applying a sharp cut on Q, an influence on the number of storeys and the amplitude, and subsequently on the energy of the selected events will be propagated. This effect is illustrated in figure 5.7(a) where the MC neutrino event distribution as a function of their track fit quality and their energy is plotted. A fraction of the high energy events

[1] The purity P is defined as : $P = \frac{\nu_{atm}}{\nu_{atm}+\mu_{atm}}$

lie at greater values of Q. The pink line shows the cut at Q < 1.4. If this standard cut is used in TAToO, it would reject these HE events. Figure 5.7(b) shows the fraction of the pure neutrino sample i.e passing the cut Q < 1.4 to the number of all up-going events fitted on more than 2 lines as a function of the neutrino energy. The cut efficiency drops dramatically at high energies. Despite its good purity performances, this cut was quickly abandoned because of its inefficiency at high energies.

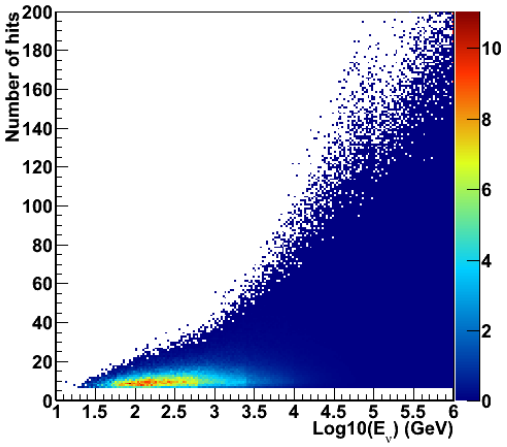

(a) Distribution of the number of storeys used in the fit as a function of the MC neutrino energy.

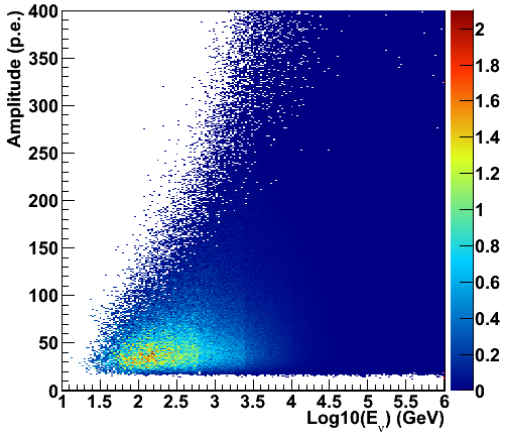

(b) Distribution of the hit amplitudes used in the fit as a function of the MC neutrino energy.

Figure 5.6: Energy correlation with the number of storeys and the amplitude used in the fit.

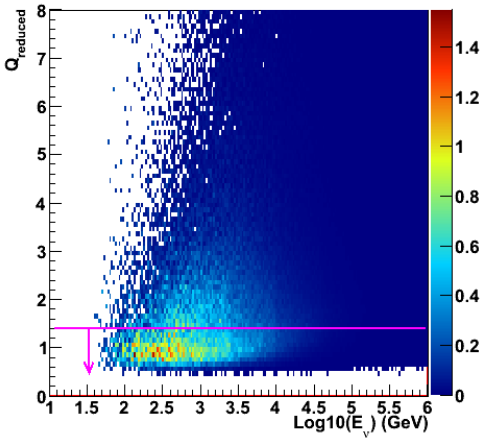

(a) Distribution of the events fit quality as a function of the MC neutrino energy. The pink line represents the sharp cut Q < 1.4.

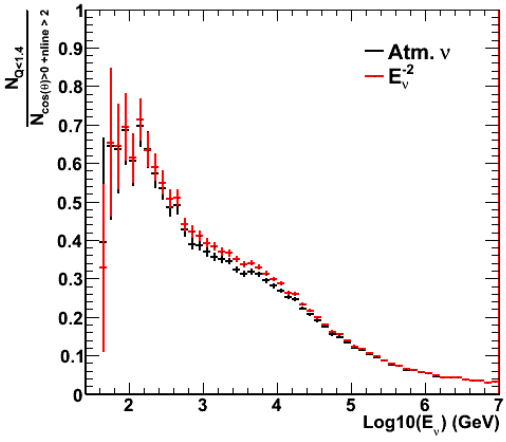

(b) Q < 1.4 filter efficiency as a function of the neutrino energy.

Figure 5.7: Impact of Q < 1.4 cut on the HE event selection

Line-dependent cut: In order to improve the performances at high energies, the events sample is split into three subsets: events which are reconstructed on only 3 detector lines are separated from those seen on 4 lines, or 5 line and more. The probability to reconstruct down-going tracks as upward-going should be smaller if more detector lines are involved in the reconstruction. This in turn might allow to apply looser cuts when selecting neutrinos and especially, those of interest, i.e. the highest energy ones lying at higher Q values.

Figure 5.8 shows the fit quality distribution for upward-going events fitted on at least 3 lines, 4 lines and 5 lines or more respectively. The optimum cut to discard atmospheric muons may be expressed as a function of the lines involved in the track fit. The cuts used are marked by the vertical green line in the figures. The general cut on Q was optimized to reach a purity better than 90% using the conditions shown on table 5.2 related by an OR statement :

Number of lines used in the fit	Cut on Q value
3 lines	$Q < 1.5$
4 lines	$Q < 1.8$
5 lines and more	$Q < 2.1$

Table 5.2: Line-dependent fit quality cuts

Table 5.3 shows the number of events in the 12 line configuration along with the corresponding data in 2008 for 70.3 active days obtained after the presented selection cuts.

Cuts	Atmospheric ν	Atmospheric μ	Data
All reconstructed events	1569.1	$3.1{\cdot}10^7$	$3.8{\cdot}10^7$
Preliminary cuts	176.1	$3.8{\cdot}10^6$	$4.1{\cdot}10^6$
$\cos(\theta) > 0$	173.7	$5.8{\cdot}10^4$	$6.2{\cdot}10^4$
Line dependent quality cut	84.0	0.3	95
$Q < \chi^2_b$	83.9	0.3	95

Table 5.3: Expected number of atmospheric neutrinos, atmospheric muons and 12 line configuration data from 2008 at each cut step for 70.3 active days.

Hit dependent fit quality cut: Along with a new version of `BBfit`, a dynamic cut on the track fit quality is implemented. $Q < 1.3 + (0.04\times \text{ NDF })^2$ as suggested in [8]. NDF is equal to N_{hits} - 5 and is used as a simple energy estimator. This cut replaced the line-dependent cut and is running since January 2011.

To avoid accounting for sparking OMs [1], which record high N_{hits} values, a condition $Q < 10$ is added. Table 5.4 shows the expected rate of atmospheric neutrinos and muons for 70.3 days of data taking in 2008 with the 12 line configuration after each step of this cut.

[1] PMTs which record an intense light flash because of ionized gas particles inside the PMT.

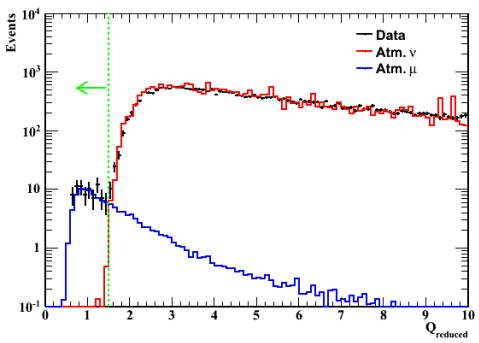

(a) Quality fit distribution of upward-going events reconstructed on at least 3 lines.

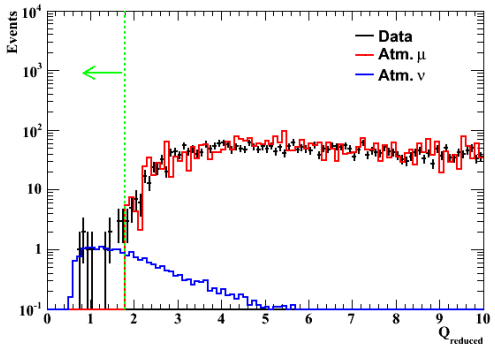

(b) Quality fit distribution of upward-going events reconstructed on at least 4 lines.

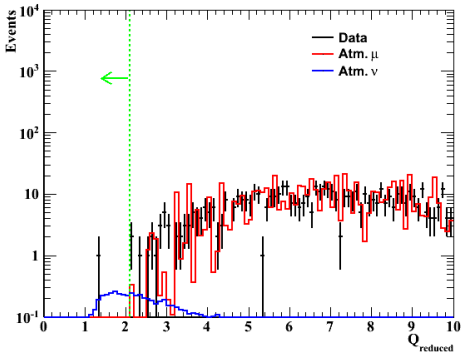

(c) Quality fit distribution of upward-going events reconstructed on 5 lines or more.

Figure 5.8: Fit quality distributions for events fitted on 3, 4 and more than 5 lines. The vertical line shows the adopted cut on the fit quality.

Cuts	Atmospheric ν	Atmospheric μ	Data
All reconstructed events	1569.1	$3.1{\cdot}10^7$	$3.8{\cdot}10^7$
Preliminary cuts + nline > 2	176.1	$3.8{\cdot}10^6$	$4.1{\cdot}10^6$
$\cos(\theta) > 0$	173.7	$5.4{\cdot}10^4$	$6.2{\cdot}10^4$
Q $<$ 1.3 + (0.04$\times$ NDF)^2	84.4	1.3	97
Q $< \chi^2_b$ + Q $<$10	84.0	0.2	97

Table 5.4: Expected number of atmospheric neutrinos, atmospheric muons and 12 line configuration data from 2008 at each cut step for 70.3 active days.

Quality cuts efficiency and induced purity

Figure 5.9 illustrate the neutrino selection efficiency [1] of the track fit quality cuts described above as a function of the energy. The standard and the line-dependent track fit quality cuts

[1] The efficiency of a particular filter is defined as the ratio of the number of events passing the filter to the number of events before the filter is applied.

show poor performances in selecting high energy events. The energy dependence using the hit-dependent quality cut is reduced and a stable selection of events with energies greater than ∼1 TeV is expected.

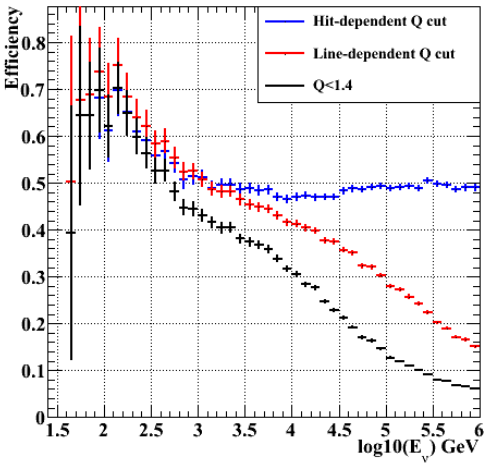

Figure 5.9: Neutrino selection efficiency as a function of the neutrino energy for the three sets of fit quality cuts applied in TAToO.

In order to assess the purity of the neutrino selection using the fit quality cut, figures 5.10(a) and figure 5.10(b) show the event zenith distribution respectively before and after the hit-dependent cut as an example. A good separation between the atmospheric muon contribution and the atmospheric neutrinos is obtained. As shown on table 5.5, the three distinct cut sets on the fit quality have comparable purity performances [1]. The number of atmospheric neutrinos left per year after quality cuts is also shown.

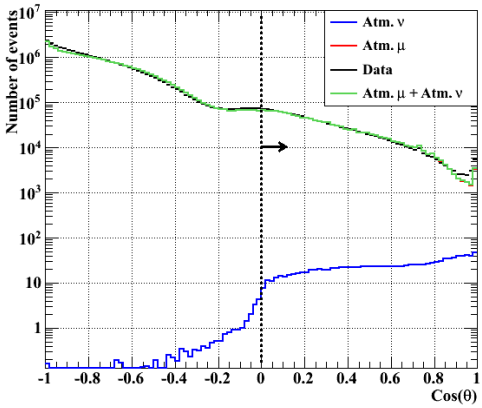

(a) Zenith distribution of events before the fit quality cut.

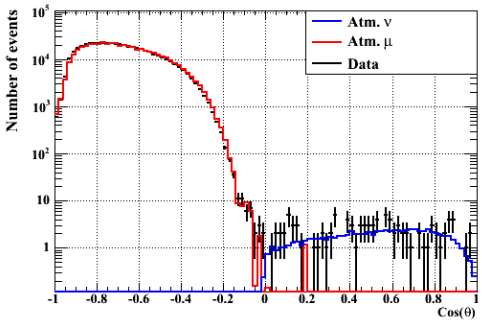

(b) Zenith distribution of events after the hit-dependent fit quality cut.

Figure 5.10: Zenith distributions of the events selected after fit quality cuts.

[1] Due to the statistic uncertainty on the number of atmospheric neutrinos and atmospheric muons, it is more conservative to state that in general, a purity better than 90% is achieved for the three cut sets.

Cuts	Atm. ν (/year)	Purity
nline >2 + Q < 1.4 + χ^2_b > Q	420.9	99.8%
Line-dependent cut on Q + χ^2_b > Q	435.9	99.5%
nline >2 +Hit-dependent cut on Q + χ^2_b> Q + Q < 10	436.4	99.7%

Table 5.5: The number atmospheric neutrino MC events after atmospheric muon rejection.

For each quality cut used in TAToO, the rate of atmospheric neutrinos left was tuned to send 25 HE alerts to the telescope network. As the last optimized quality cut is the hit-dependent one, it is chosen here for the development of the next event selection steps.

High energy alert rate tuning

More energetic events should hit more storeys, they are also expected to give signals of higher amplitudes. Thus, the number of hits and the amplitude can be used as simple energy estimators. Since the neutrino energy spectrum for signal events is expected to be harder than that for atmospheric neutrinos, a cut on these two parameters should reduce the atmospheric neutrino background while most of the astrophysics signal events is kept. The hits and amplitude distribution of events after the hit-dependent cut weighted with an E^{-2} spectrum and atmospheric neutrino spectrum shapes can be compared on figure 5.11.

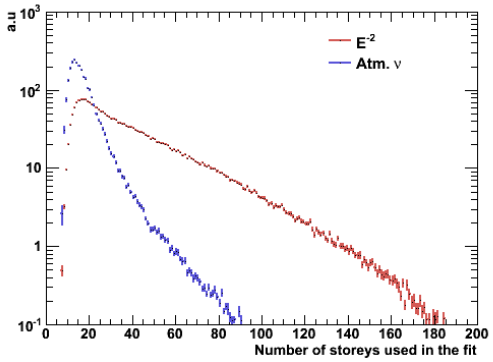

(a) Number of hits distribution for events passing nline >2 and the hit dependent quality cut.

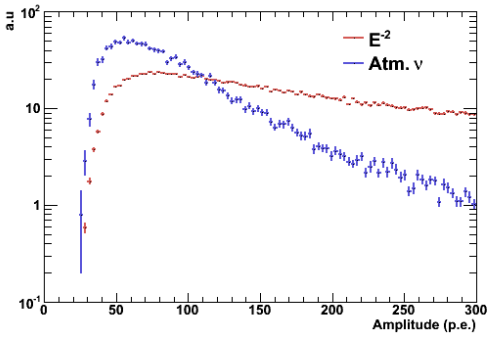

(b) Amplitude distribution for events passing nline >2 and the hit dependent quality cut.

Figure 5.11: Distribution of the number of hits used in the fit after quality cuts for an E^{-2} spectrum and atmospheric neutrinos.

Cuts on the number of hits and amplitude are tuned in order to give the predefined alert rate accounting for the number of active days. As we are not aiming at the detection of one source in particular, the selection is only constrained by the fact that the triggering events should be among the most energetic and best reconstructed in ANTARES. Different combinations of (nhit, amp) are checked to get the appropriate alert rate after applying the hit-dependent fit quality cut [1]. The optimized values for the 12 line configuration are (nhit,amp) = (20,180). The expected alert rate with this set of cuts is 40 alerts / yr, if

[1]The same selection process was used during the operation of the standard and line-dependent quality cuts, not shown here for simplification purposes.

one accounts for the detector active time per year ($\sim$ 60%) taken from figure 2.13, the obtained rate is equivalent to $\sim$ 25 alerts / yr.

Figures 5.12(a) and 5.12(b) show the MC and data events distribution of the number of hits and on the amplitude respectively, along with 2008 12-line configuration data.

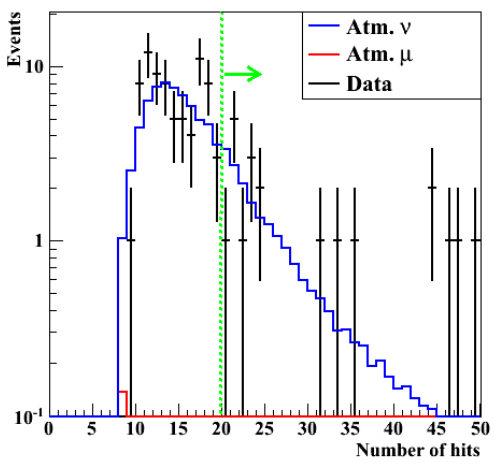

(a) Distribution of number of storeys having at least 5 hits used in the reconstruction, for data and Monte Carlo up-going events reconstructed on at least three lines. The vertical line indicates the alert selection criterium.

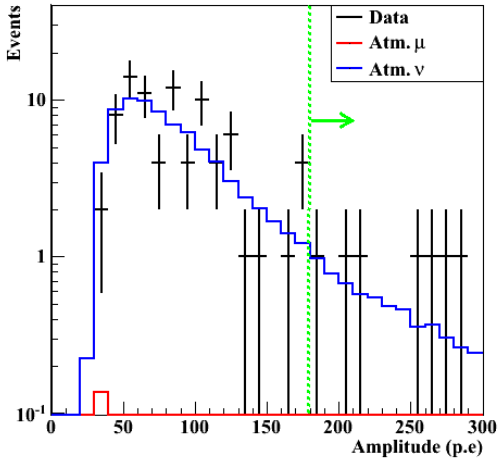

(b) Total amplitude distribution in photoelectrons (pe) for data and Monte Carlo up-going events reconstructed on at least three lines. The vertical line indicates the alert selection criterium.

Figure 5.12: MC event and data distribution of the number of storeys and amplitude used in the fit for the 12 line configuration from 2008.

High energy selection performances

Figure 5.13(a) and 5.13(b) illustrate the MC energy distribution after the cut (nhit,amp) = (20,180) using atmospheric neutrinos and events weighted with an E^{-2} spectrum respectively. The line-dependent and Q $<$ 1.4 fit quality cuts are shown for comparison.

The effective area and the median angular resolution distribution are shown on figures 5.14(a) and 5.14(b). The hit-dependent cut selects more HE events and gives a better angular resolution. The median angular resolution is expected to be $\sim 0.6°$ for the standard and line-dependent cut. It is reduced down to 0.45° with the last optimized track fit quality cut. On-line events passing the hit-dependent cut, are further fitted by the M-estimator fit before sending the alert coordinates to the telescopes, the angular resolution value is expected to be enhanced down to 0.4° for events passing the HE filter.

The bi-dimensional point spread function for single HE neutrino events with an E^{-2} spectrum is shown in figure 5.15. $\sim$91% of the events are reconstructed within the field of view (FOV) of the TAROT or ROTSE telescopes.

The summary of the final cuts after optimization for high energy events are shown on table 5.6, the condition HE is shown for different number of lines active in the detector.

Tables A.1, A.2 and A.3, give the list of alerts sent in years 2009, 2010 and 2011 respectively. 15 alerts were sent in 2009, 12 in 2010 and 13 in 2011 (not complete). The fact that the alert rate is about the half of the expected rate with MC is partly due to the

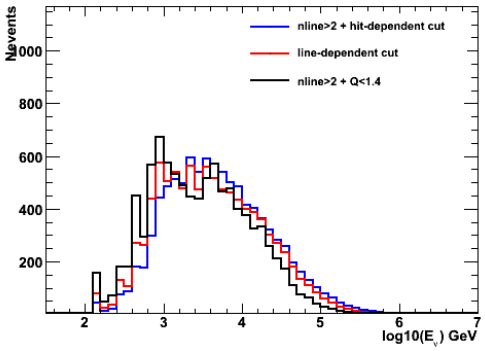

(a) Energy spectrum of atmospheric neutrino events after (nhit,amp) = (20,180) cut, for each quality cut used in TAToO.

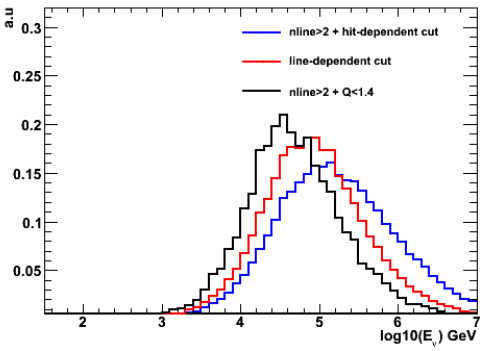

(b) Energy spectrum of events weighted by E^{-2} spectrum after (nhit,amp) = (20,180) cut, for each quality cut used in TAToO.

Figure 5.13: High energy filter expected performance on energy for atmospheric and E^{-2} events.

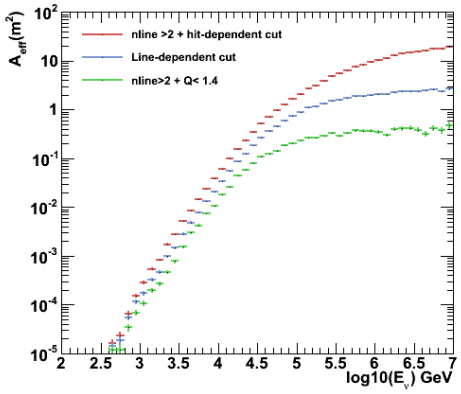

(a) Effective area after applying HE neutrino cuts.

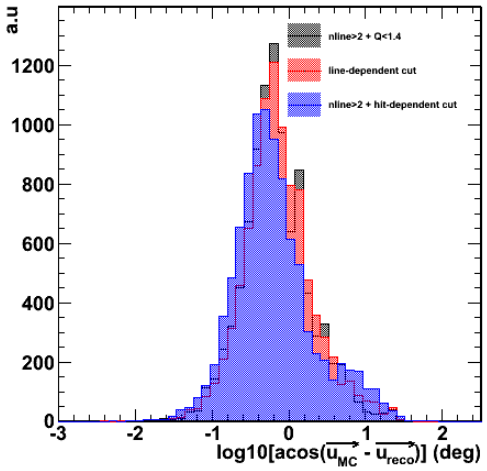

(b) Median angular resolution distribution for atmospheric neutrinos.

Figure 5.14: Performance on the effective surface and angular resolution after HE selection. The performance using the line-dependent and standard on-line quality cuts are shown for comparison.

test phase in early 2009. In the MC study, the detector efficiency could be overestimated. The different detector operations and periods with reduced HV gain, which are difficult to guess *a priori* were not taken into account while optimizing the cuts with the MC. In this study, 60% detector efficiency (periods with physics runs) was assumed. Alerts with a number of hits and amplitude lower than the thresholds specified in table 5.6 correspond to periods where the detector was running with reduced HV gain. The cuts on (nhit,amp) were thus relaxed to keep a stable alert rate.

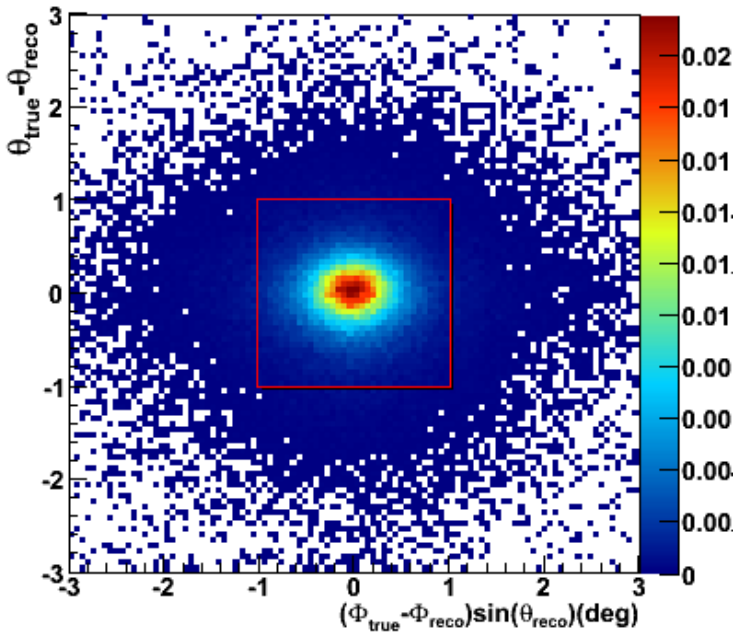

Figure 5.15: Bi-dimensional point spread function. The red solid-line square corresponds to the telescope field of view ($\sim 2° \times 2°$). The z-axis is in arbitrary units.

Cuts	Expression	Formulation
C1	Muon rejection cut at level 1	tcosth $>$ 0 & nhit$>$5 & nline$>$2
C2	Muon rejection cut at level 2	Q $<$ (1.3 + (0.04*(nhit-5))^2) & $\chi^2_b >$ Q & Q$<$10
HE-12 lines	High energy selection	nhit $>$ 20 & amp$>$ 180
HE-10 lines	High energy selection	nhit $>$ 20 & amp$>$ 150
HE-9 lines	High energy selection	nhit $>$ 17 & amp$>$ 120

Table 5.6: The selection cuts for the high energy trigger

5.2.4 Multiplet filter

The detection of two coincident neutrinos or more corresponding to a neutrino burst from transient sources should be defined within a time and direction window. When expecting n-multiplets, the angular resolution is normalized by a factor $\sqrt{n}$. Thus, the condition on the number of lines used in the fit is relaxed comparing to the singlet HE filter, by requesting events fitted on at least 1 line instead of 2. The neutrino selection in the multiplet filter is common with the HE filter as it is based on the hit-dependent cut. Table 5.7 shows the expected event rate of neutrinos after these cuts.

The time window is set to 15 minutes, it represents the maximum T90 GRB duration from the BATSE catalog. The angular window corresponds to the maximum angular difference so that neutrino directions fall into the telescope Field-Of-View (FOV). Being $2° \times 2°$, the maximum angular difference should be set to $2\times\sqrt{2} \sim 3°$.

An estimation of the number of expected multiplets in ANTARES can be calculated approximately. The background rate from n coincident, uncorrelated, upward-going atmo-

Cuts	Atmospheric ν	Atmospheric μ	Data
All reconstructed events	1569.1	$3.1{\cdot}10^7$	$3.8{\cdot}10^7$
Preliminary cuts + nline > 1	759.6	$1.6{\cdot}10^7$	$1.9{\cdot}10^7$
$\cos(\theta) > 0$	744.4	$3.1 \cdot 10^5$	$3.6{\cdot}10^5$
Q $<$ 1.3 + (0.04$\times$ NDF)^2	300.7	32.6	329
Q $< \chi_b^2$ + Q $<$10	300.2	31.2	329

Table 5.7: Expected number of atmospheric neutrinos, atmospheric muons and 12 line configuration data from 2008 at each cut step for 70.3 active days.

spheric neutrinos can be calculated using the following expression:

$$R^{atmo}_{n-multiplets} \sim n!(\frac{\Delta\Omega}{2\pi}\Delta T)^{n-1}.(R^{atmo}_{singlet})^n \tag{5.4}$$

With $\Delta\Omega = 2° \times 2°$ and ΔT = 900 s. $R^{atmo}_{singlet}$ is the rate of atmospheric neutrinos per year after quality cuts. It can be retrieved from table 5.7 and converted to a rate per year, which gives $\sim$ 1600 events per year. One doublet in 25 years is expected. Up to now, no doublet alert has been recorded in TAToO. Due to their rarity in ANTARES, this trigger is not the one optimized to maintain TAToO operational. Hence, we will focus on the high energy trigger in this work.

5.2.5 Expected efficiency for GRB neutrino and CCSN neutrino detection

Using the cuts expressed in table 5.6 for the 12 line configuration, the expected neutrino events from a GRB and a CCSN can be calculated. Figure 5.16(a) shows the expected neutrino event energy distribution for a CCSN with Ando and Beacom parametrization (Γ = 3, $E_j = 3.10^{51}$ erg) and figure 5.16(b) shows the expected event distribution for a GRB using an average spectrum parametrization after HE cuts.

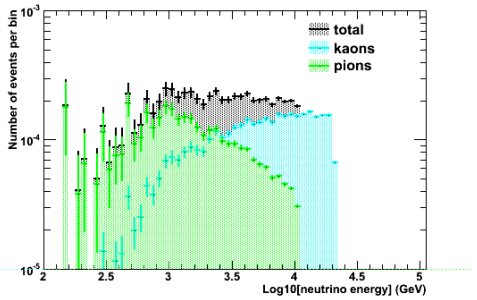

(a) Energy distribution of the expected events from a CCSN at 10 Mpc, with a jet duration of 10s, a jet kinetic energy of 3.10^{51} erg and a boost factor of 3 passing the HE filter.

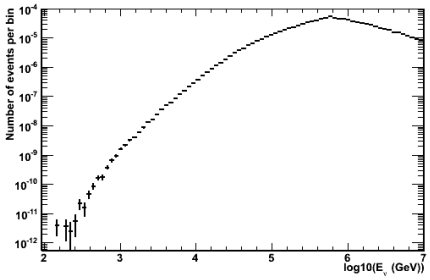

(b) Energy distribution of the expected events from a GRB at z=2, with a jet duration of 10s, a jet kinetic energy of 3.10^{52} erg and a boost factor of 100 passing the HE filter.

Figure 5.16: Energy distribution of neutrino events from a CCSN with soft jet model from Ando and Beacom and from an average GRB as described in chapter 4.

Table 5.8 shows the total signal events and background (atmospheric neutrinos) expected within 10 s using the high energy filter and the multiplet filter. The expected signal

from a CCSN situated at 10 Mpc, with a jet duration of 10 s is also quoted in the table for two different values of the jet boost factor and 3.10^{51} erg jet kinetic energy.

Cuts	Atm. ν (10s)	GRB	CCSN		
			$\Gamma = 3$	$\Gamma = 5$	$\Gamma = 8$
C1	$2.8 \cdot 10^{-4}$	$2.8 \cdot 10^{-3}$	0.3	10.2	90.0
C2	$1.4 \cdot 10^{-4}$	$1.1 \cdot 10^{-3}$	0.2	5.4	43.7
HE-12 lines	$1.2 \cdot 10^{-5}$	$1.0 \cdot 10^{-3}$	$1.0 \cdot 10^{-2}$	0.3	6.0

Table 5.8: The number of expected events for both atmospheric neutrinos and signal events from a CCSN and a GRB with canonical parameters.

Figure 5.17 shows the HE filter efficiency per energy bin defined as the ratio of neutrino events passing the HE cuts (HE-12 lines in table 5.6) to the number of events at the neutrino level (C2 in table 5.6). The events considered are weighted with a GRB and a CCSN spectrum. The HE filter favors the GRB detection comparing to CCSNe with mild jets (here $\Gamma = 3$) as these latter sources have a energy cut-off around $2{\cdot}10^4$ GeV. From table 5.8, one can retrieve the overall HE filter efficiency for each source. These values are noted in table 5.9.

Cuts	GRB	CCSN		
		$\Gamma = 3$	$\Gamma = 5$	$\Gamma = 8$
HE filter	91%	0.05%	5%	14%

Table 5.9: Overall filter efficiencies

Figure 5.18 shows the performance on the angular resolution by the representation of the point spread function of the reconstructed events relatively to their true direction, 83% to 92% of the events are reconstructed into the telescope field-of-view for a CCSN and a GRB spectrum respectively.

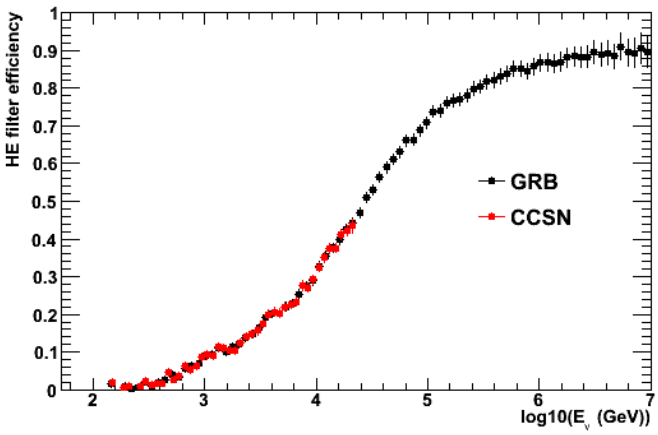

Figure 5.17: HE neutrino filter efficiency as a function of energy.

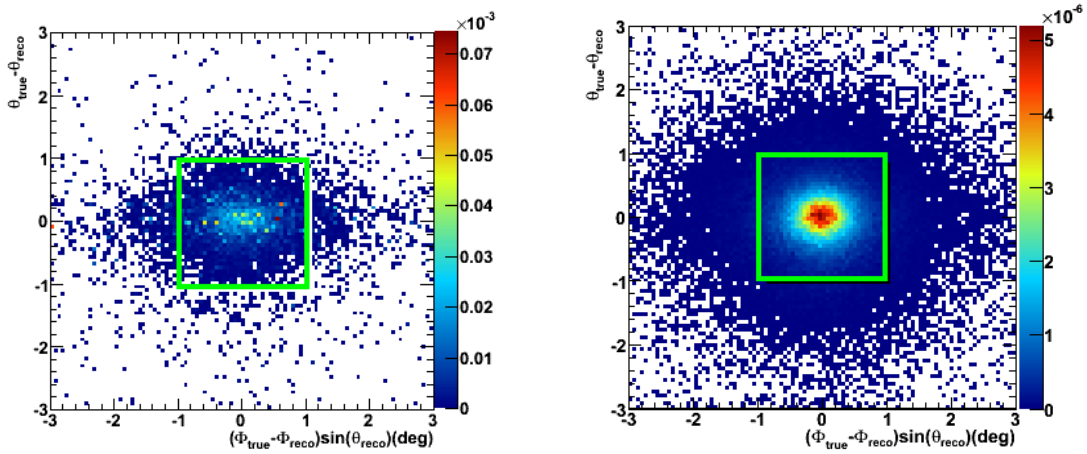

(a) PSF for events weighted with a CCSN spectrum.

(b) PSF for events weighted with a GRB spectrum.

Figure 5.18: Bi-dimensional point spread function.

5.2.6 Towards a new trigger logic

The high energy filter is more suitable for GRB detection than soft jet core collapses. In order to enhance the detection prospects of softer jets sources, a third trigger is being developed; the directional trigger. It basically consists of considerably relaxing the hit and amplitude cuts while still keeping a pure neutrino sample. Direction windows are defined pointing at known nearby galaxies as SNe core collapses are more likely to happen in galaxies. The rate of alerts is tuned based on the cone aperture considered in the search. The galaxies coordinates were retrieved from Karachentsev catalog [74] and Tully catalog [117]. Figure 5.19(a) shows the cumulative distribution of the galaxies from each catalogue within a distance of 20 Mpc. Figure 5.19(b) shows the ANTARES sky visibility. The distribution of galaxies visible by ANTARES is plotted on figure 5.19(c). The visibility being represented by the shaded grey area. A total of 517 galaxies are always visible by ANTARES.

With this new trigger, it is expected that the efficiency for CCSNe detection would be multiplied by a factor ∼100 comparing to the HE trigger while the number of atmospheric neutrinos and atmospheric muons passing the cuts would be multiplied by a factor ∼10. The alert rate is still to be fixed. A preliminary study shows that the number of data events associated with the galaxies considering a cone aperture of 1 deg would give a rate of 0.7 alerts per month.

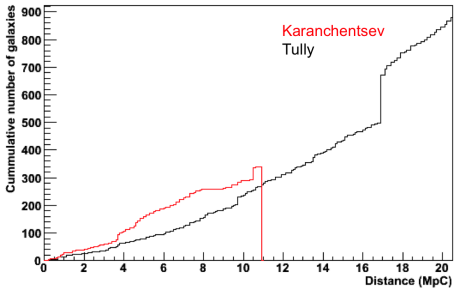

(a) Cumulative distribution of nearby galaxies retrieved from [74] and [117] within a distance of 20 Mpc.

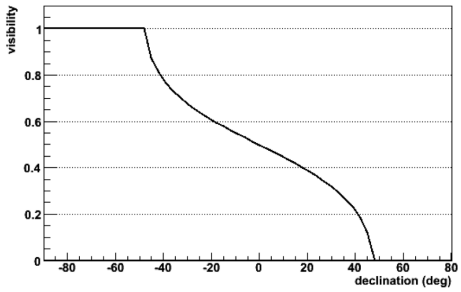

(b) ANTARES detector visibility

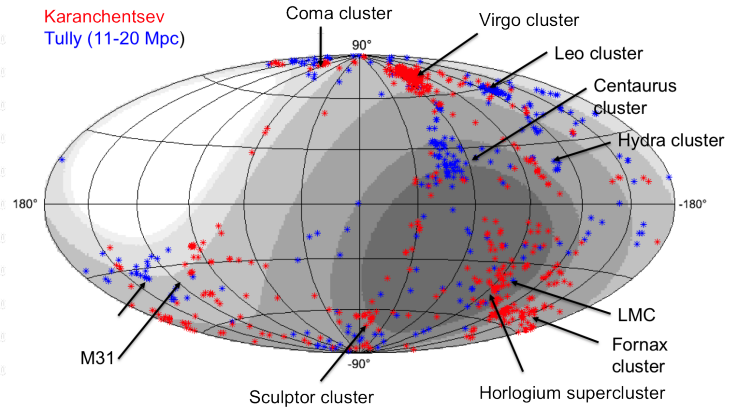

(c) Distribution of local galaxies in galactic coordinates considered in the trigger study. The shaded area represents the detector visibility.

Figure 5.19: Study of the implementation of a new trigger logic; the directional trigger.

5.3 Background associated to CCSNe and GRB detections

In the case where a positive detection is found using the neutrino-optical information, it is important to assess its associated background. In this section, the rate of random neutrino-optical coincidences in the case of CCSNe with mild jets is evaluated as an exemple.

The sensitivity horizon of the telescopes involved in TAToO network can be assessed in terms of the limiting magnitude. The limiting magnitude is not a straight forward concept, it is not only dependent on the telescope performance but also on atmospheric conditions, light pollution, exposure time, etc. However, in this calculation, we will use $m_R \approx 17.0$ as a value for typical 60 s exposure image and allow for a Poissonian fluctuation around this value of about 1 sigma.

In the case of SNe type Ib/c, we used the absolute peak magnitude M_p in the R-band inferred from [105] taken to be -18.5 with 1.34 sigma fluctuation. To calculate the probability to identify an optical SN, a rising signal is expected before the peak. During the days before the maximum(at $\sim$ 20 days after explosion), the absolute magnitude rises by 4 magnitudes before reaching the maximum. In this calculation, the observation time for a single SN is randomly distributed between 0 and 20 days and the associated magnitude is noted. At each distance step, 1000 SNe each at a different observation epoch before

maximum are simulated. If the associated magnitude is brighter than the telescope limiting magnitude, it is considered as a detection. Figure 5.20(a) shows the probability to detect a single SN before its maximum brightness as a function of its distance.

The number of expected neutrinos from a SN at whatever distance is obtained by scaling the number of neutrinos from a CCSN at 10 Mpc passing the HE cuts : N(d) = N_{10Mpc} $\times$ $(\frac{d}{10Mpc})^{-2}$. Figure 5.20(b) shows the probability to detect 1 or more HE neutrinos from a SN as a function of its distance. At large distances, the number of expected events is very low but one can still expect some events by virtue of Poisson law. Hence, this was included in the calculation.

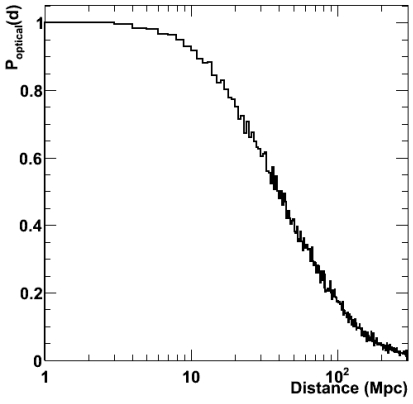

(a) Probability of detecting a SNIb/c type SN before maximum brightness using a telescope with a limiting magnitude m_R ≈17.0

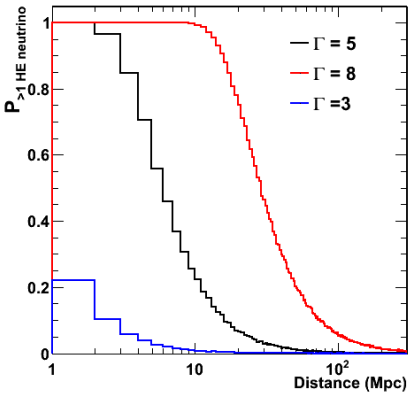

(b) Probability of observing 1 HE neutrino or more (after HE trigger) from a CCSN with Γ = 3, 5 and 8 as a function of its distance.

Figure 5.20: Optical and neutrino detection probabilities of a core collapse supernova with $E_{jet} = 10^{51.5}$ erg with 10 s jet duration.

In order to estimate the number of SNe detectable by a telescope, we need to use a rate and make a hypothesis on the distribution. For CCSNe, the rate can be approximated by a continuous distribution of 1 CCSN yr^{-1} (10 Mpc)$^{-3}$ [22], this rate could however be 3 times underestimated for nearby distances, as close-by galaxies are richer in SNe explosions. Using this rate and the limiting magnitude, the number of visible SNe by the telescopes is shown in figure 5.21(a) .

The number of detectable SNe relying on the neutrino signal and the optical signal together is shown on figure 5.21(b). For comparison, the expected detectable SNe using the neutrino information only is also shown on the figure. For SNe within 300 Mpc, requesting an optical detection in conjunction with 1 neutrino detection reduces the detection background rate by a factor 5 (Γ =3) to 10 (Γ =8) comparing to a neutrino detection only.

The significance of a correlated neutrino-optical detection, *i.e* the case where a SN is identified in coincidence with a HE neutrino can be derived. Assuming one year of data where N_{alerts} = 25 alerts are sent to the optical network, each alert leads to $\Delta\ \Omega = 1.85^\circ \times 1.85^\circ = 3.4$ square degree field. Hence, this would lead to a total sky coverage per year of $25 \times \frac{\Delta\Omega}{4\pi} = 2.1 \cdot 10^{-3}$ of the total sky area. Moreover, one has to account for the time window in which the SN explosion would be coincident with the neutrino event. Based on the optical light curve extrapolation, the coincidence time window is taken to be Δ t ≈1 day [48], this can further be reduced if the follow-up is prompt enough allowing a better

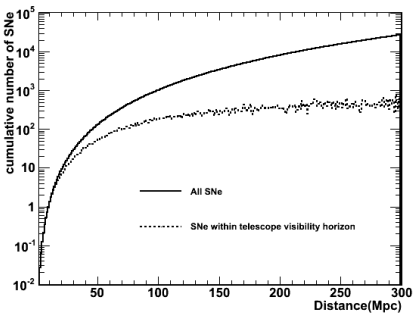

(a) Cumulated distribution of detectable SNe using a telescope with $m_R \approx 17.0$.

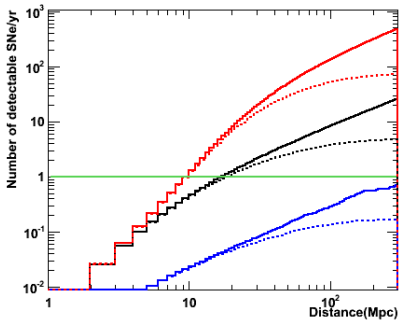

(b) Cumulated distribution of detectable SNe per year in neutrino only (solid line) and combining the optical detection (dashed line) for $\Gamma = 3$ (blue), 5(black) and 8 (red). The green line marks one detection /yr

Figure 5.21: Cumulated number of detectable SNe considering a distribution rate of 1 CCSN yr^{-1} $(10\ Mpc)^{-3}$ in optical only (left), in neutrino only and in neutrino and optical (right).

fit with a template LC. The number of random coincidences is proportional to the number of SNe that the telescopes would detect considering their limiting magnitude $N_{telescope} \approx 4.0\ 10^2$ as shown on figure 5.21(a).

Therefore, the number of random coincident detections is :

$$N_{random} = (N_{alerts}\frac{\Delta\Omega}{4\pi})N_{telescope}\frac{\Delta t}{yr} = 2.1 \cdot 10^{-3} \times 400 \times \frac{1}{365.25} = 2.2 \cdot 10^{-3}/yr \quad (5.5)$$

Thus, the probability to observe at least one random background event is p = 1-exp(-N_{random}) $\approx N_{random}$. Observing a SN in coincidence with a neutrino alert considering a visibility depth of 300 Mpc has a significance of $\sim 3\ \sigma$.

This number can be further improved by two means : (i) one can estimate the events energy and calculate the probability for an event to be higher than a certain threshold and include it in the significance calculation. (ii) If a candidate SN is found in coincidence with a neutrino, its distance would be known, then one can calculate the probability of a background detection at that distance. The first case can not be used as no adequate energy estimator is available yet. We will hence use the second solution, which is already efficient enough. Indeed, it is safe to assume that the trigger has a strong preference to closer SNe as shown in figure 5.20(b). Hence, the probability to detect a random SN at distance d can be expressed as p(d) = $N_{telescope}$(d)/ $N_{telescope}$. Thus, the total chance probability would be p = p(d) × N_{random}. This gives a p-value of 4.10^{-5} for a SN at 20 Mpc, which is almost significant. Figure 5.22 shows the p-value associated with a SN detection as a function of its distance.

Due to their rarity, and to their non-standard expected fluxes, a neutrino - optical GRB coincidence rate can be derived as a first order approximation by the following arguments. Assuming a rate of 500/yr/ hemisphere detected with SWIFT, 40% have an associated optical afterglow, leading to N_{sky}/yr = 500*0.4 = 200/yr. Taking into account the portion of visible sky by the telescopes, we get $N_{telescope}$ =$2.1 \cdot 10^{-3}$ × 200/yr = 0.4/ yr. The

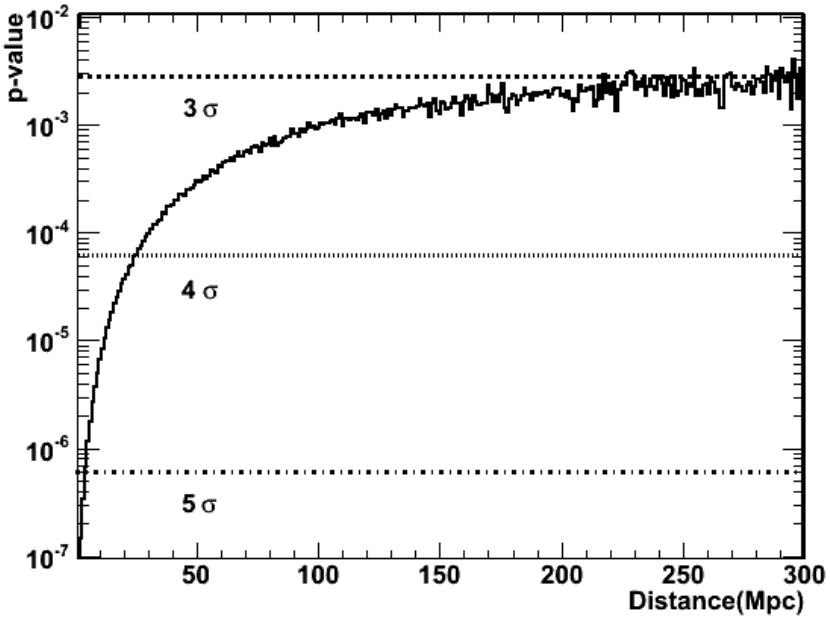

Figure 5.22: p-value distribution as a function of the SN distance.

time coincidence window is taken to be 1 hour around the neutrino trigger. The expected background in 1 year of operation based on equation 5.5 is $\approx 4.10^{-5}$ /yr.

Based on these calculations, the significance of a random coincidence between a transient source type GRB or CCSN is very promising. This calculation is however conservative as the optical data analysis strategy requires more drastic conditions on the light curve shape; which is not taken into account in this calculation.

5.4 Offline alerts : The coordinate refinement

Although the pointing accuracy of the online reconstruction algorithm is suitable for the field of view of the telescopes used for the follow-up, the use of the detailed knowledge of the detector geometry can further improve the determination of the neutrino direction. For this purpose, we use the standard ANTARES offline reconstruction algorithm. Since the ANTARES lines are not rigid structures, sea currents can move the top buoy by several meters, and distort the line positions from a vertical line geometry, thus affecting the direction of the reconstructed muon trajectory. In order to achieve the best track reconstruction performance, it is necessary to monitor the relative positions of all OMs with an accuracy of better than 20 cm, equivalent to 1 ns timing precision. In addition, a precise absolute orientation of the whole detector is necessary to point to individual neutrino sources in the sky. Two independent monitoring systems are used to attain the required accuracy:

- A high frequency long baseline acoustic system giving the 3D position of hydrophones placed along the line. These positions are obtained by triangulation from emitters anchored at the bases of the lines.

- A set of tiltmeter-compass sensors giving the local tilt angles of each OM storey with respect to the horizontal plane (pitch and roll) as well as its orientation with respect to the Earth's magnetic field (heading).

In order to obtain a quasi-online precise detector geometry (within a delay of typically few tens of minutes), the shape of the detector lines is derived from a model which estimates the mechanical behaviour under the influence of the sea water flow, obtained from online measurements of the sea current. The positions of the OMs are then calculated by combining the line shape with the measurements of the tilt and orientation angles of the storeys given by the tiltmeter-compass sensors. The offline reconstruction algorithm derives the muon track parameters that maximize a likelihood function built from the difference between the expected and the measured arrival time of the hits from the Cherenkov photons emitted along the muon track. This maximization takes into account the Cherenkov photons that scatter in the water and the additional photons that are generated by secondary particles (e.g. electromagnetic showers created along the muon trajectory). Figure 5.23(a) shows the median Monte Carlo computed angular resolution as a function of the neutrino energy for events selected by the high energy alert trigger, for both online and offline algorithms. The improvement obtained with the offline algorithm is clearly visible at low energies. The angular resolution for neutrino energies above 10 TeV is 0.4° for the online algorithm and 0.35° for the offline algorithm. Figure 5.23(b) shows the improvement on the fraction of signal events reconstructed within the telescopes FOV.

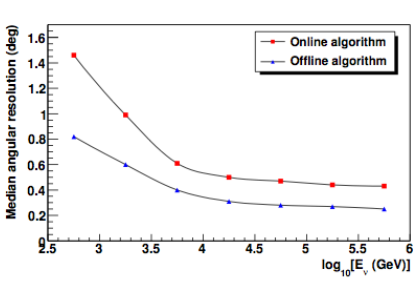

(a) Angular resolution obtained for both online and offline reconstructions as a function of the neutrino energy.

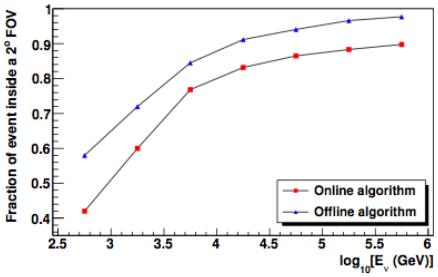

(b) Fraction of events inside a field of view of 2° × 2° as a function of the energy of the event.

Figure 5.23: Offline reconstruction algorithm performances

This offline step stands as a position refinement sent to the telescopes within $\sim$ 15 mn. If the reconstructed positions agree within 0.5° between the on-line and the off-line strategy, the alert is sent again to the telescopes and the follow-up of the first coordinates sent is suppressed. If the angular difference obtained is larger, the offline refinement is ignored. Tables A.1, A.2 and A.3, show the angular difference between the on-line and the offline strategy for the list of alerts. For some alerts, the difference in the position determination accuracy is important. These events are mostly due to electromagnetic showers. In this case, the event is investigated in details by visualizing the track fit on each detector line. An example is shown on figure 5.24.

Before this option became automatically available in Sept 2011, the offline position was sent if necessary, within a delay of 1 day to the telescopes.

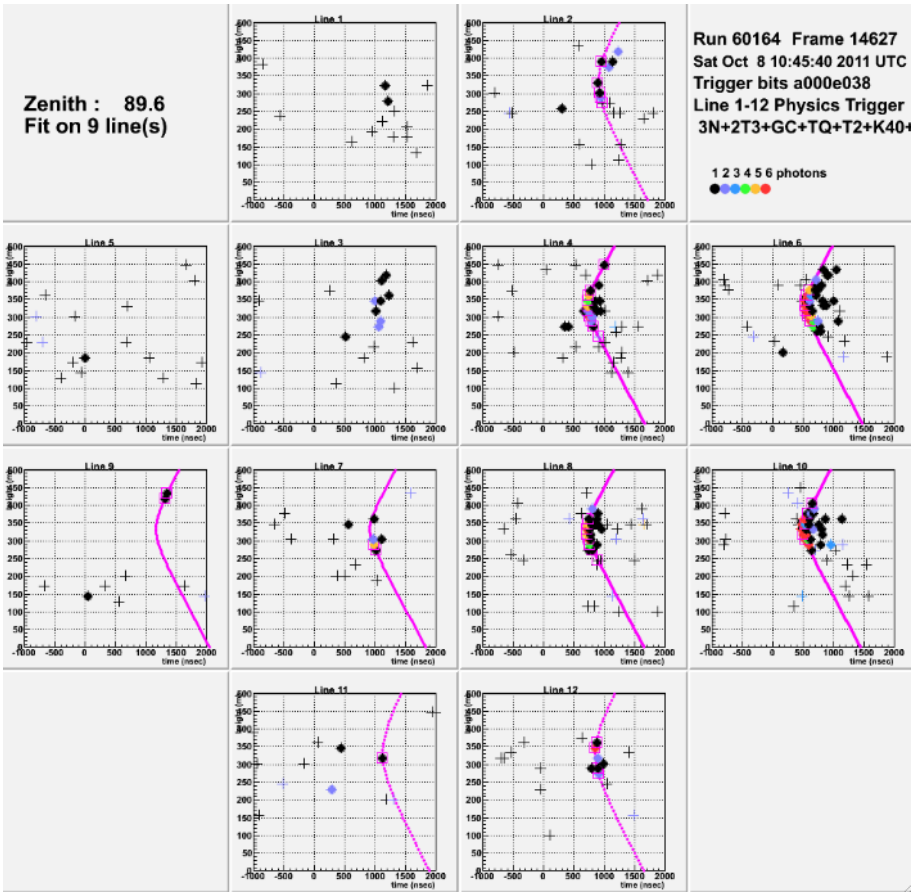

Figure 5.24: Example of the track fit on each line of an event assumed to originate from an electromagnetic shower.

5.5 The alert sending monitoring

The alert system relies on two major programs : The first one is BBAlert which includes `BBfit` described above, its main role is the reconstruction of the tracks and the trigger selection. The second program is the TAToO Run Control, which corresponds with `BBAlert` and insures the communication with the telescopes.

The TAToO Run Control (RC) is a stand-alone control application which channels the triggers generated by the alert application to the optical telescope network. Thus, it is the main interface between the neutrino detection and the optical follow-up. The connections to this network are checked periodically and automatic reconnection is performed resulting in a fully autonomous and stable system. A veto prevents an alert to be sent if the ANTARES event counting rate exceeds 50Hz in periods of high bioluminescence activity for instance.

In addition, if the alert criteria are fulfilled soon after a previous alert has already been issued, the new alert is stored in a FIFO and sent 1 hour later to avoid alert pileup in the telescope schedule. In some rare cases, the alert coordinates are wrongly decoded on the telescopes site. Manual alerts can also be generated and sent again to the telescope. All alerts are sent using the Gamma-ray bursts Coordinates Network (GCN) normalized for-

mat [1], allowing easy implementation of connections to additional telescopes. Information about the event that triggered the alert, i.e. a unique identifier, the time and the celestial coordinates, the number of hits used in the reconstruction and the track reconstruction quality are sent to the optical telescopes network at the time of the alert. Whenever an alert is sent, shifters are prevented by e-mail and SMS messages, allowing them to check if the telescopes have correctly received and decoded the alert coordinates, and in case of failure, resend the alert manually. Figure 5.25 shows a snapshot of the Run Control window. The left side of the panel displays on-line trigger rates and the connection status to the ligier. The right side shows the connection status to the telescope network and from top to bottom the list of the latest sent alerts and the list of pending alerts. The bottom part displays the blocking time and the rate threshold as well as the current trigger rate.

During 2010-2011, the blocked time which corresponds to trigger rates higher than 50 Hz threshold is negligible since it is equivalent to 1.5 %. Time periods with no triggering events because of the detector calibration or periods with OMs off are more frequent and represent a dead time fraction of 18% (not accounting for periods with high bioluminescence activity leading to operate in HV reduced mode).

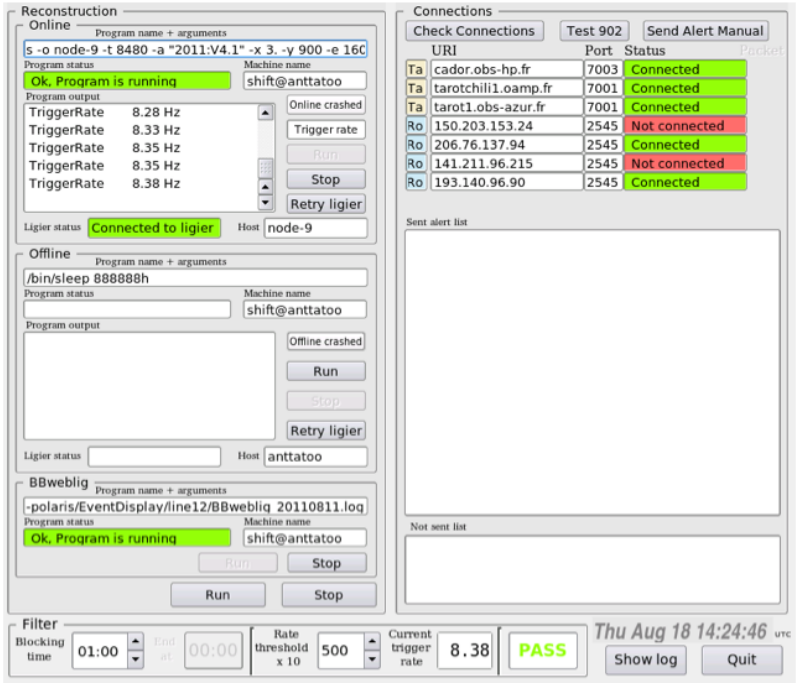

Figure 5.25: TAToO Run control.

[1] http://gcn.gsfc.nasa.gov/gcn_main.html

5.6 The optical follow-up

In this section, the optical follow-up of the neutrino alerts is presented. First, the telescopes characteristics are depicted. Second, the alert processing on the telescope sites and the follow-up strategy is described. Finally, the efficiency of the follow-up is presented from 2009 to 2011.

5.6.1 The telescopes

The follow-up of the alerts is done by a network of robotic telescopes : 2 TAROT telescopes of 0.25 m diameter and 2° ×2° FOV. The 4 ROTSE telescopes of 0.45 cm diameter joined the network in January 2010, they have comparable performances with TAROT. The telescopes have a Cassegrain design, their locations are listed in table 7.7.

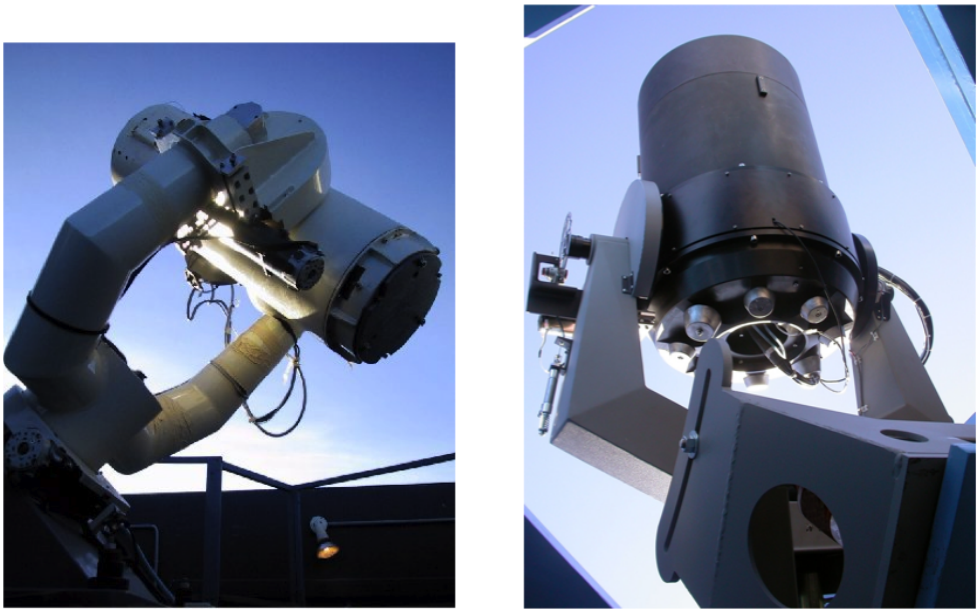

(a) TAROT-NORD telescope located at Calern, France.

(b) ROTSE 3b located at McDonald Observatory in Texas.

Figure 5.26: Robotic telescopes of TAToO network.

Telescope	location	Latitude	Altitude (m)
TAROT -SUD	La Silla (Chile)	-29 15 N -70 43 E	2420
TAROT -NORD	Calern (France)	43 43 N 6 54 E	1270
ROSTE 3a	Coonabarabran Naomi (Australia)	-31 16 N 149 4 E	1149
ROSTE 3b	Fort Davis (Texas, USA)	30 36 N -103 54 E	2075
ROSTE 3c	Windhoek (Namibia)	-22 36 N 17 6 E	1800
ROSTE 3d	Antalya (Turkey)	36 54 N 30 42 E	2550

Table 5.10: Telescopes characteritics

The telescopes have a big FOV (2° × 2°) and are therefore adequate to match the

angular resolution of the neutrino telescope. Each image is sampled using 2045 × 2048 pixels.

For ground-based telescopes, one expects the angular resolving power i.e the ability to discern two adjacent stars to be limited by the effect of atmospheric turbulence on the light trajectory from the source. This is a very important and deleterious process called seeing. Instead of the image of a point source being an Airy pattern caused by light interference from different parts of the mirror, it is a fuzzy blob with a quasi- Gaussian profile. Thus, the angular size of the blob is set by the atmosphere, and not by the telescope (except for very small telescopes which have Airy patterns comparable in angular extent to the seeing). Astronomers characterize the seeing by the angular FWHM (full width at half maximum), which is the angular size of the star image at a level of half the peak level. The best seeing is obtained for higher altitude telescopes, as there is less air to look through the higher one goes. Other effects such as the elevation or the temperature gradient between inside and outside the dome can affect the seeing value. For the given telescopes, a mean value of the seeing is around 2 pixels (8.35 arcsec) [1] under good conditions. The seeing has a fundamental impact on the image analysis process to extract the signal and derive an accurate photometry. This is shown more in detail in the next chapter.

To allow the detection of rapidly fading transients such as GRBs, the telescopes have a fast response time, it takes ∼ 4 s upon the reception of an alert to image a field when the telescope is in stand-by mode (pointed at zenith). The sensitivity to a flux emitted by a source is set by the limiting magnitude, which is defined as the faintest source detectable in the imaged field at a certain confidence level, usually set to 3 or 5 sigma from the sky background. Because the Signal to noise Ratio (SNR) is proportional to the exposure time, the limiting magnitude is also defined by specifying the exposure time. A value of R∼ 18 for a typical 60 s exposure is quoted for the telescopes when running in good conditions (moon is low, no clouds).

5.6.2 ANTARES alerts processing

The neutrino alerts are normally followed by 3 telescopes in each hemisphere. The telescopes in the northern hemisphere insure a better coverage in case of horizontal neutrino events. The connection status with the telescopes is checked via "I am alive" messages which ping the connection every 60 s. In order to check if ANTARES alert messages are properly received and decoded by the telescopes, a log file filled on-line can be checked in the case of TAROT telescopes [2]. The log file reports all useful informations about the telescope status and helps to identify reasons for which no follow-up was undertaken. ROTSE communicate a global status on each night via a webpage for each telescope[3].

The telescopes observations are based on a scheduler which orders the observations according to their priority. For both networks, GCN alerts of prompt bursts are the first in line followed by ANTARES prompt alerts. Burst Follow-up observations and ANTARES follow-up observations are respectively 3rd and 4th in the rank and finally, other observations such as specific target imaging or sky patrols are programmed with least priority. On one hand, if the neutrino alert is issued while the telescope is doing a prompt burst observation, the neutrino alert observation is postponed. On the other hand, if the telescope is treating an ANTARES alert and a prompt burst observation is demanded, the

[1] The pixel scale (arcsec/pix) is chosen to make a good signal sampling. It is usually set according to the seeing value. For ROTSE and TAROT telescopes, it is equivalent to ∼3.3 arcsec/pixel

[2] `http://tarotchili1.oamp.fr/ros/logs/majordome/majordome.log`

[3] `http://www.rotse.net/operation/`

ANTARES observation is stopped and restarted later. However, this latter case did not appear in almost 3 years of TAToO operation.

For each of the schedule items specified above, the imaging sequence is different as it is chosen by each client for his special use. Table 5.11 shows the images sequences specified for ANTARES prompt and late follow-up observations for each telescope network. TAROT sequences are the same for prompt and follow-up observations and consist of long exposures in order to enhance the limiting magnitude [1]. ROTSE sequences consist of shorter exposures but more numerous images, especially for the prompt observations where a GRB signal could be rapidly fading as shown on figure 5.27(a). This latter strategy is complemented by coadding (described in 6.5.1) the images to reach better limiting magnitudes.

Telescope network	Prompt observation	Follow-up observations	Total observations (nights)
TAROT	6 images of 180 s	6 images of 180s	12
ROSTE	30 images of 60 s	8 images of 60 s	13

Table 5.11: Real time (prompt) and delayed (follow-up) imaging sequences of ANTARES alerts by TAROT and ROTSE telescopes.

If the trigger location is above the horizon and the system is running in good weather, the mount is told immediately to slew to the trigger location, and system begins the preconfigured imaging sequence. Apart from the trigger location and the weather, other vetoes are applied in order to start an acquisition. For ROTSE telescopes, the sun elevation should be less than -15°. Moreover, when the moon is bright, the sky brightness can nearly saturate a long 60 s exposure. Therefore, when the moon is up (angular distance $< 30°$), the exposure lengths are automatically reduced down to 20 s.

The delayed observations are taken each night of the week following the trigger and at T0+9 days, T0+15 days, T0+16 days (ROTSE only), T0+27 days, T0+28 days (ROTSE only), T0+ 45 days (TAROT only),T0+ 60 days (TAROT only). The prompt acquisition is mainly used for GRB afterglow search as it fades very rapidly. The delayed observations are used for SNe search as the optical counterpart can last for several days after the explosion as shown on figure 5.27(b).

5.6.3 The telescopes efficiency

The robotic telescopes offer the advantage for an ease of use and rapid reaction. However, in case of technical problems, and due to their remote location, human intervention is difficult. Table 5.12 shows the the fraction of alerts with follow-up comparing to the total alerts sent for each year. In 2009, TAROT Chili had technical problems in addition to the commissioning phase of the alert sending system. The contribution of ROTSE telescopes in the follow-up in the beginning of 2010 enhanced the follow-up efficiency. In 2011, 2 ROTSE telescopes were permanently shut down while TAROT telescopes alert follow-up greatly enhanced.

Apart from technical maintenance periods which cause an entire follow-up to be cancelled, few conditions can influence the optical data taking. For alerts which transmission was successful, not all of them had a complete follow-up as specified in the strategy. The problems are well-known and are usually related to weather conditions; for example, in case

[1] The limiting magnitude evolves as $\sqrt{T_{exp}}$ considering a sky dominated image background.

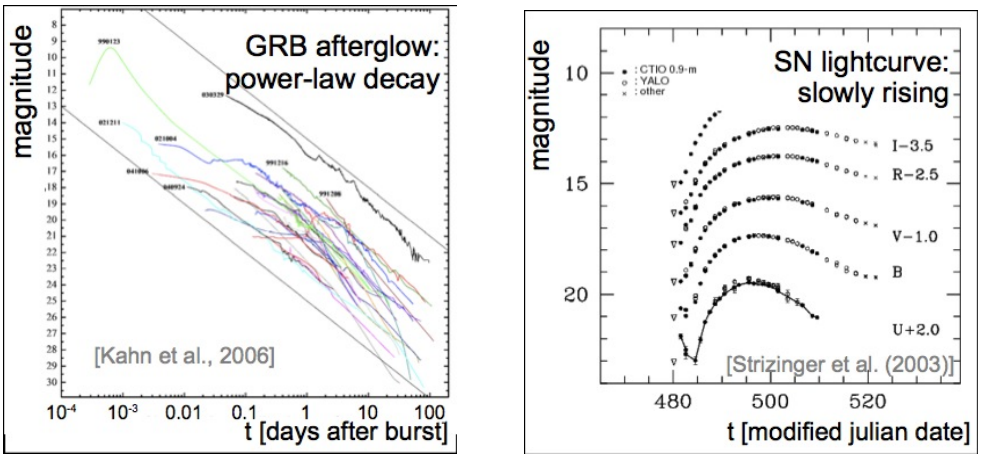

(a) GRB light curves examples

(b) Typical SN light curve using different filters.

Figure 5.27: Typical optical counterparts from GRBs and SNe. The image taking strategy is optimized for the detection of such signals.

Year	2009	2010	2011
Efficiency	30%	91%	91%

Table 5.12: Fraction of followed alerts comparing to total alerts sent.

of precipitations, the current exposure is aborted, the mount stops slewing or tracking, and the clamshell closes.

Figure 5.28 shows the fraction of observations comparing to the predefined strategy for successfully sent on-line alerts. Among these observations, some images have a poor quality and can not be used in the image analysis, so only the efficiency of data taking is quoted here independently from its quality. ROTSE telescopes show a good follow-up in 2010 but its efficiency decreased in 2011 due to technical problems. TAROT kept a stable follow-up. For most of our alerts, TAROT-SUD was taking data in 2011.

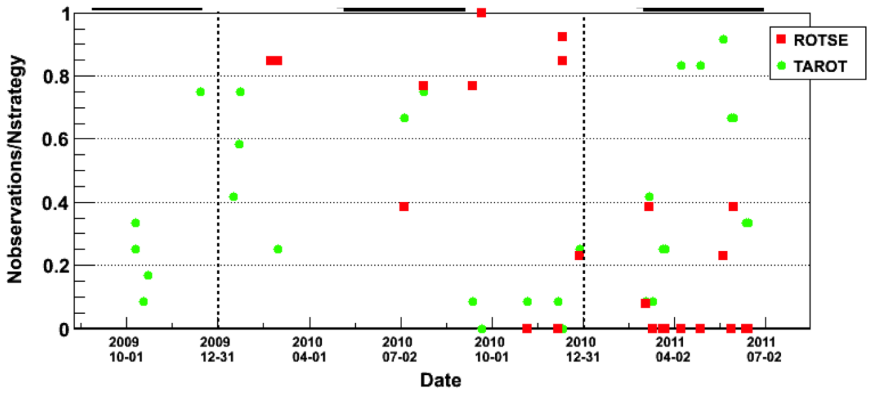

Figure 5.28: ROTSE and TAROT follow-up efficiency of successfully sent neutrino alerts .

Chapter 6

Optical data analysis

The optical follow-up of the neutrino alerts results in series of images taken at specific times defined by the observation strategy. Images are copied from the telescope sites, ordered by their observation time and processed off-line on the local TAToO machine. The images retrieved are in FITS format (Flexible Image Transport System) [1].

The image processing and analysis is dedicated to the search of a fading GRB afterglow or a rising SN optical counterpart in correlation with the neutrino alert. In this chapter, we will first discuss general features of CCD imaging, data reduction and photometry methods. Second, the analysis pipelines implemented in TAToO is described. A general diagram of the described steps is shown on figure 6.1.

Content

[1] A FITS file consists of one or more Header + Data Units (HDUs), where the first HDU is called the 'Primary HDU', or 'Primary Array'. The primary array contains an N-dimensional array of pixels, such as 2-D image in our case. Any number of additional HDUs may follow the primary array; these additional HDUs are called FITS "extensions" and consist in our case of a table extension containing different informations about the image features and observation conditions.

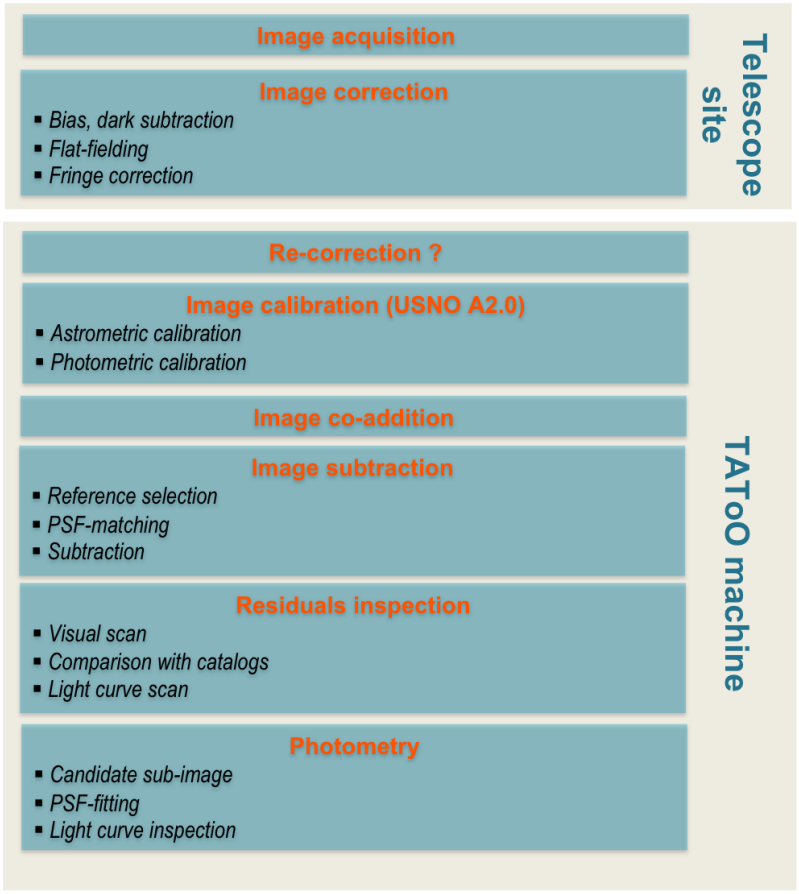

Figure 6.1: TAToO optical analysis diagram.

6.1 Image processing principle

The CCD sensor is a light sensitive silicon "chip" which is electrically divided into a large number of independent pieces called pixels (for "picture elements"). The output is a digital image, consisting of a matrix of numbers, one per pixel, each number being related to the amount of light falling on the pixel. However, part of the number is an electrical offset called the bias and part may be due to dark current. After bias and dark signals subtraction, the signal is related to the number of electrons liberated by photons in each pixel. The photon count is related to the characteristics of the CCD, namely the gain and the quantum efficiency QE as follows :

$$\text{Photons/pix} = \frac{\text{number of electrons/pix}}{\text{QE}} = \frac{\text{gain} \times \text{ADU/pix}}{\text{QE}} \tag{6.1}$$

Where ADU (Analog to Digital Units) is the output number from the CCD, also called DN (Data Numbers).

The CCD is an integrating device. The signal builds up with time. The integration time (or exposure time) is controlled by a mechanical shutter (like in a camera) or electrically (changing voltages in CCD). Except in the case of a very bright star, where the CCD response becomes non-linear before saturating, the signal from a star increases linearly

with time.

6.1.1 Noise sources

Before actually starting to process CCD images, some considerations specific to the CCD use have to be considered :

Read noise After a certain integration time (exposure), the CCD must be "read out" to find the signal value at each pixel - because the signal may be as low as a few electrons per pixel, this step involves some very sophisticated amplifiers that are part of the CCD itself ("on chip" amps). Inevitably, the read out process itself generates some electronic noise. The average noise per pixel is called the read noise. Modern CCDs typically have a read noise of 5 to 20 electrons per pixel per read out (read noise is independent from the exposure time).

Bias frame If we simply read out the CCD, without making an integration, there will be a signal called the bias signal. It can be thought of as an electrical offset or background. This bias signal must be measured and subtracted from the images. It is also related to the temperature, so it may change on a nightly basis. Since there is read noise associated with any readout of the CCD, even bias frames have read noise associated with them. To minimize the noise introduced when bias is subtracted, many bias frames are combined.

Dark frame If we allow the CCD to integrate for some amount of time, without any light falling on it, there will be a signal (and more importantly noise associated with that signal) caused by thermal excitation of electrons in the CCD. This is called the dark signal. The dark signal is very sensitive to temperature (lower temperature = lower dark signal), and that is why CCDs used in astronomy are cooled (often to liquid nitrogen temperature). Even with cooling, some CCDs have a non negligible dark current. This must be measured and subtracted from the image. As for the bias, we want to take many dark frames and combine them to beat down the noise.

Flat frame All CCDs have non-uniformities. That is, uniformly illuminating the CCD will not generate an equal signal in each pixel (even ignoring noise for the moment). Small scale (pixel to pixel) non-uniformities (typically a few percent from one pixel to next) are caused by slight differences in pixel sizes. Larger scale non-uniformities are caused by small variations in the silicon thickness across the chip, non-uniform illumination caused by telescope optics (vignetting), etc. These can be up to maybe 10% variations over the chip. To correct for these, we want to shine a uniform light on the entire CCD and see what the signal (image) looks like. This frame (called a flat) is taken at twilight [1]. The flat can then be used to correct for the non-uniformities by dividing the image by the flat.

6.1.2 Instrumental correction

The CCD image has to be corrected from the listed "instrumental" noise sources. After the raw image is subtracted from bias [2], one needs to subtract the dark frame. Usually, a median dark frame is built from a set of individual dark frames to reduce the associated

[1] or simply by using a screen in the dome, and illuminate the screen with artificial lights!

[2] Usually, the bias is uniform across the chip

noise. A dark-corrected image is obtained out of the subtraction of the median-dark image from the bias-subtracted image.

The next step is flat-fielding. Basically, it consists of dividing the resulting dark-corrected image by the twilight flat. A median twilight is also derived from a set of individual twilight images, when light is most uniform. The telescope is slightly moved at each twilight exposure, this would reduce the contribution of stars in case they appear in the twilight frames.

$$\text{Reduced image} = \frac{\text{Raw object frame} - \text{bias frame} - \text{Median(dark frames)}}{\text{Median(twilight frames)}} \tag{6.2}$$

A raw ROTSE image is shown on figure 6.2(a), the twilight flat (figure 6.2(b)) and the image after correction (figure 6.2(c)) are also shown. On the corrected image, patterns are still distinctly seen. Those are caused by distinct emission lines in the far red part of the light spectrum which interfere in the thinned substrate of back-illuminated CCDs (the substrate becomes transparent at these wavelengths). Usually, filterless optics enhance the fringe effect because of the large wavelength bandwidth admitted. The fringe effect, when important, influence the photometric accuracy by introducing non-uniformities in the sky background.

6.1.3 Sky brightness correction

In order to obtain accurate pixel counts issued from a celestial object and derive reliable flux measurements, the sky level must be subtracted. A common procedure to correct from the sky level is based on the assumption that the sky radiation is distributed normally around a typical sky value; *i.e* the most common value in the image. Thus, if the distribution of the image intensities is constructed, the sky pixels will practically form a Gaussian centered on the sky level. Other radiating sources in the frame, which represent additional photon contributions on top of the sky, will form a tail on the bright side of the sky distribution. Except for defective pixels, there should be no pixels significantly below the intensity level of the sky. This is illustrated in figure 6.3, where a typical image and the associated pixel values distribution are shown. The sky value can be taken as the mean value of a Gaussian fitted to the histogram in its peak region and then subtracted from the image. This method of background estimation is called "mode estimation". Other contributors are likely to be present if they are faint and close to the sky level *i.e* bad pixels, cosmic rays, which have to be discarded from the sky level calculation. In this case, it is usual to use some sort of clipping (or filtering) to remove the effects of such contamination. k-sigma clipping consists of rejecting pixel values deviating more than +/- k-sigma from the mean sky level. The sky level is then recalculated with the new clipped histogram and subtracted from the image.

6.2 Aperture photometry

In astronomical applications, the usual purpose of aperture photometry is to measure the brightness of an object without including possible contributions from contaminating sources such as sky levels, defects or other close-by stars or galaxies. Because the sky level is not homogenous over the image, it should be calculated using the same method as described above, but in a "local" mode i.e around every stellar object which magnitude

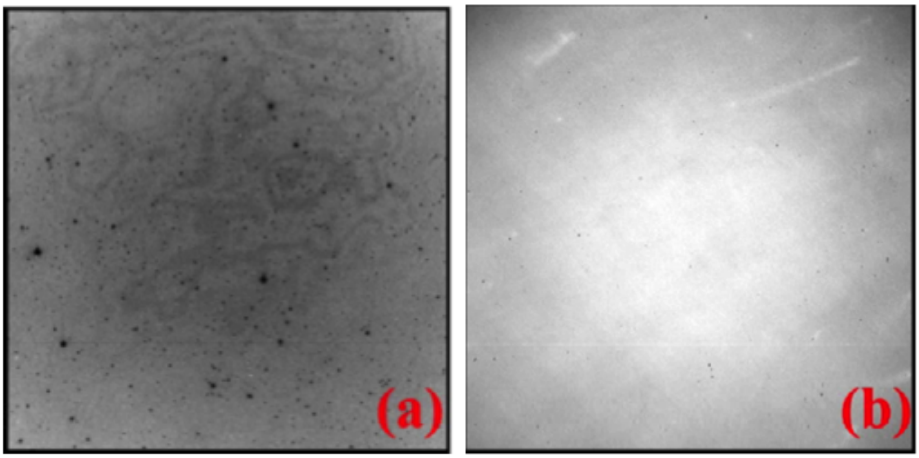

(a) Raw image. (b) Twilight flat.

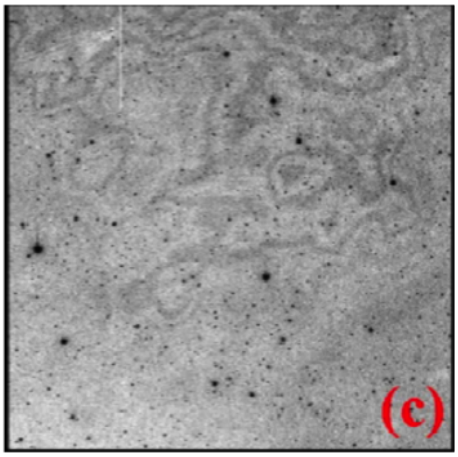

(c) Corrected image.

Figure 6.2: A raw ROTSE 2045 × 2048 pixels image. A twilight flat used to correct from CCD non-uniformities and the dark-subtracted, flat-fielded image.

needs to be precisely measured. This is done by defining a sky annulus around the object in which the sky level would be measured as shown in figure 6.4.

The size and the shape of a point-like source on an astronomical image is defined by the Point Spread Function (PSF). The driving factor which determines the shape of the PSF is the smearing caused by the seeing. The most common representation of the PSF involves a Gaussian core and exponential tails. The size of the PSF is normally measured by the Full Width at Half Maximum (FWHM) which is the size of the PSF where the flux is 50% of the maximum value.

Two crucial questions are how to determine the optimal sky annulus width, and how to determine the aperture radius in which the source flux would be calculated.

To answer the first question, one has to consider that if the sky annulus is too small, this would result in low statistics and a poor Gaussian fit of the sky level peak. Thus, it should be wide enough. In this case, the possible flux contamination from neighboring objects can be eliminated if one uses k-sigma clipping.

To answer the second question, one has to invoke the Signal-to-Noise Ratio (SNR). The

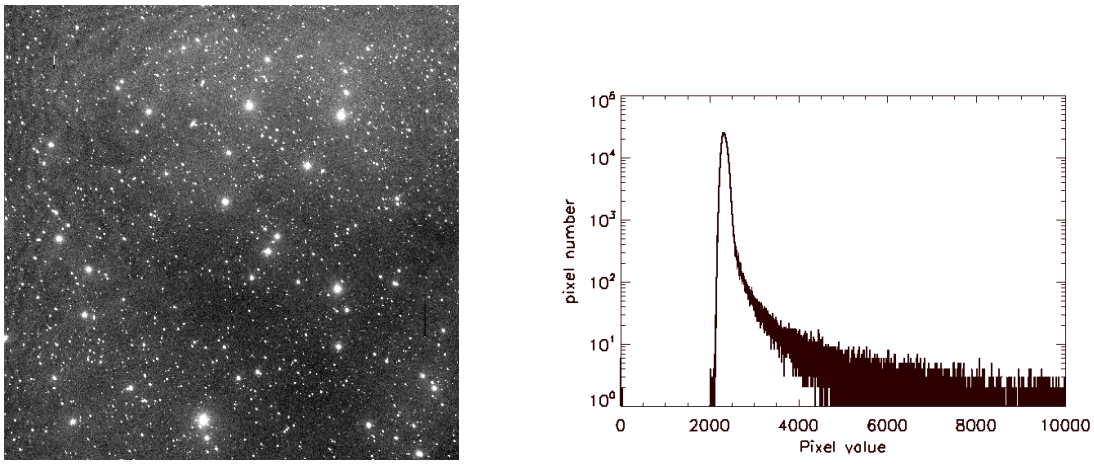

(a) Image from ROTSE telescope. (b) Image histogram.

Figure 6.3: Typical ROTSE image and its pixel value distribution. The peak represents the sky level, the tail is due to the brighter sources on the image.

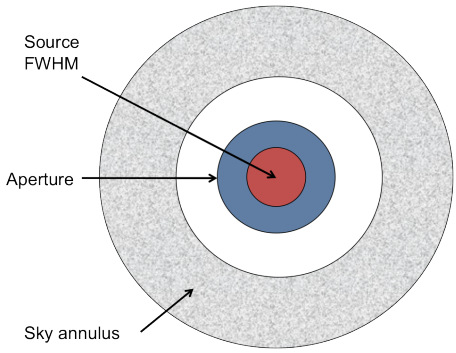

Figure 6.4: Aperture photometry principle.

optimum aperture size is the one that maximizes the SNR. It has been found empirically that the optimum aperture radius is $\sim$ FWHM [66]. Since the stars PSF can vary across the image due to seeing conditions, it is convenient to set it to a slightly larger value than the characteristic seeing FWHM.

After the determination of the sky level in the sky annulus, the instrumental flux F^{inst}_{source} measured from a source in ADU/s is obtained by summing over the n_{pix} pixels included in the aperture centered on the star. F^{inst}_{source} is expressed as :

$$F^{inst}_{source} = \sum_{j=1}^{n_{pix}} a_j \cdot f_j - \sum_{j=1}^{n_{pix}} a_j \cdot b \tag{6.3}$$

where a_j is the area of the j^{th} pixel, f_j is the ADU count/s in the j^{th} pixel (star+sky) and b is the sky background count per pixel/s.

The noise $\sigma_{\rm tot}$ associated to the flux when accounting for the exposure time $F^{inst}_{source} \cdot t$ considers the contribution of the Poisson noise of the source and sky flux [1] :

[1] In this expression, the readout noise per pixel R and the noise due to dark current D in

$$\begin{aligned} \sigma_{\rm tot} &= \sqrt{\sigma^2_{\rm photon} + \sigma^2_{\rm sky}} \\ &= \sqrt{(F^{inst}_{source} \cdot t) + (b \cdot n_{pix} \cdot t)} \end{aligned} \tag{6.4}$$

The signal to noise ratio expression is thus :

$$\begin{aligned} SNR &= \frac{(F^{inst}_{source} \cdot t)}{\sigma_{tot}} \\ &= \frac{F^{inst}_{source} \cdot t}{\sqrt{(F^{inst}_{source} \cdot t) + (b \cdot n_{pix} \cdot t)}} \end{aligned} \tag{6.5}$$

If the source is bright, the SNR is dominated by the photon noise, equation 6.5 gives SNR = $\sqrt{F^{inst}_{source} \cdot t}$. In case of a faint source, equation 6.5 gives :

$$\begin{aligned} SNR &= \frac{F^{inst}_{source} \cdot t}{\sqrt{b \cdot n_{pix} \cdot t}} \\ &= \frac{F^{inst}_{source} \cdot \sqrt{t}}{\sqrt{b \cdot n_{pix}}} \end{aligned} \tag{6.6}$$

The instrumental magnitude can be calculated with the following equation :

$$\begin{aligned} m^{inst}_{source} &= -2.5 \cdot \log(F^{inst}_{source}) \\ &= -2.5 \cdot \frac{\ln(F)}{\ln(10)} \end{aligned} \tag{6.7}$$

The photometric error Δ m$^{inst}_{source}$ can be expressed as a function of the measured SNR :

$$\begin{aligned} \Delta {\rm m}^{inst}_{source} &= \frac{-2.5}{\ln(10)} \cdot \frac{dF^{inst}_{source}}{F^{inst}_{source}} \\ &= 1.09 \cdot \frac{dF^{inst}_{source}}{F^{inst}_{source}} \\ &= 1.09 \cdot \frac{1}{\rm SNR} \\ &\sim \frac{1}{\rm SNR} \end{aligned} \tag{6.8}$$

counts/pix/s are negligible and were consequently neglected. Otherwise, the total noise would be equal to $\sqrt{(Ft) + (bn_{pix}t) + (Dn_{pix}t) + (R^2 n_{pix})}$

6.3 Source extraction with SExtractor

SExtractor (Source-Extractor) [38] is a program that builds a catalogue of objects from an astronomical image. It is widely used in the astronomy community. Its main tasks are :

- Background estimation and background subtraction
- Filtering and thresholding
- Deblending
- Photometry

Other options are also handled such as cross-identifications with catalogues. Only the steps used in the analysis pipelines are described :

6.3.1 Background estimation and background subtraction

To evaluate the sky background, SExtractor constructs a background map by making a first pass through the pixel data, computing an estimator for the local background in each mesh of a grid that covers the whole frame. The background estimator is a combination of clipping and mode estimation. Briefly, the local background histogram is clipped iteratively until convergence at $\pm$ 3 σ around its median; if σ is changed by less than 20% during that process, the field is considered as not crowded and the mean of the clipped histogram is taken as a value for the background.

The user has to configure the mesh size, namely BACK-SIZE parameter in the SExtractor configuration file. The sky mesh size has to be larger than few times the aperture used to calculate the source flux. It is similar to changing the size of the sky annulus as described in section 6.2. The effect on the background mesh size is clearly visible as shown on figure 6.5 representing the background map for 32 pixels and 64 pixels mesh width. With larger mesh sizes, the background is smoother and stars flux contribute less to the background. Once the background map is obtained, it is automatically subtracted from the image.

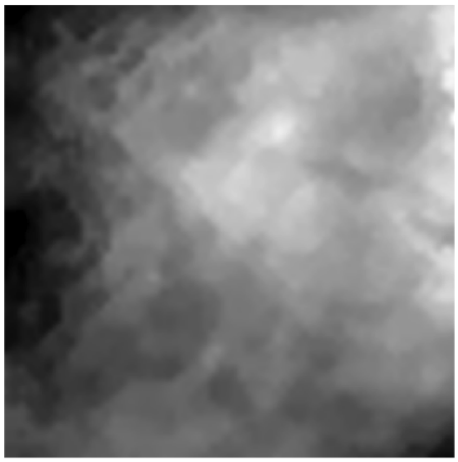

(a) Sky background obtained with 32 pixels mesh size.

(b) Sky background obtained with 64 pixels mesh size.

Figure 6.5

In parallel with the making of the background map, an "RMS-background-map", that is, a map of the background noise in the image is produced. `SExtractor` is able to handle images with variable noise, which is the case in our data due to the large FOV. It does it through weight maps, which are frames having the same size as the images where objects are detected or measured, and which describe the noise intensity at each pixel within the same background mesh. At this step, each pixel has its associated background value and background RMS.

6.3.2 Filtering and thresholding

After subtracting the sky level, and prior to the source extraction process, the detectability can be enhanced by convolving the image with a Gaussian filter. The Gaussian FWHM value is set to the typical PSF of the objects to be extracted. Thresholding is applied to the background-subtracted, filtered image to isolate connected groups of pixels. Each group defines the approximate position and shape of a basic `SExtractor` detection that will be processed further in the pipeline. Groups are made of pixels whose values exceed the local threshold. The detection threshold as well as the minimum number of pixels above threshold, namely, DETECT-THRESH and DETECT-MINAREA in the configuration file are specified by the user. The thresholding is based on how much the flux contribution of an astronomical source is believed to be dominant over that of the sky background, it is usually expressed in units of the background standard deviation or in SNR [1]. DETECT-MINAREA is the minimum area in pixels which flux has to be above the threshold to be detected.

6.3.3 Deblending

Within DETECT-MINAREA, the source can be blended to another object *i.e*, a single detection may include more than one celestial object. In this case, the maximum pixel value within DETECT-MINAREA is noted. Then it is lowered recursively over 32 sub-levels. At each step, the contrast is checked: if it is higher than 0.0001, a separate object is found. This operation is called "deblending". This can be helpful especially in crowded fields.

6.3.4 Photometry

Aperture photometry is used in `SExtractor` to calculate the magnitudes. The parameter PHOT-APERTURES is used to specify the pixel area in which the source flux is believed to be completely integrated, it is equivalent to the aperture size described in section 6.2. The associated errors are derived as explained in section 6.2. At this step, a list of extracted objects over the threshold along with their X, Y image positions, flux, magnitude and associated errors is obtained.

6.4 Magnitude calibration

In order to convert instrumental magnitudes to calibrated magnitudes, a photometric Zero-Point (ZP) needs to be specified. The ZP is a magnitude offset, it is obtained by measuring a set of primary standard stars with known magnitudes in a certain filter, this measurement

[1] The signal at threshold can be expressed as S = k.σ. The SNR is thus equivalent to S/N=k.σ/σ = k.

is then compared with the same stars magnitude using the same filter expressed in the standard photometric system (Landolt stars [82], Henden stars).

The magnitude difference between the measured and the standard magnitudes is the ZP value. One problem is that the filter used does not match the standard system identically, and there will be a color dependence of the ZP. To determine the dependence of the ZP on color, the standard stars are measured in 2 different filters (V and R for example) and a correction factor c is derived. The ZP will thus be expressed as ZP = ZP_0 + c (V-R), where ZP_0 is the zero-point for a star of color 0.0. The color correction is specific to each filter used.

A major problem is that photometric calibration using standard stars can only be carried out in completely photometric conditions. More importantly, if the telescope operates filterless, the images cannot be calibrated to a standard photometric band. USNO A2.0 [92] catalogue contains a large number of calibrated stars. The color corrected magnitudes of the stars are expressed in V and R filters.

ROTSE and TAROT do not use filters, however, their response peaks in the R-band, this would provide the most appropriate ZP for the data. Typically, in the telescopes FOV, thousands of stars have magnitudes in the USNO A2.0 catalogue. Stars from USNO A2.0 catalog can be used to calibrate observations even in poor conditions with cloud or bad seeing. Figure 6.6 [1]shows the distribution of some selected stars from USNO A2.0 measurements and their real magnitude in the standard system. In the R-band, the magnitudes show a quite good agreement. However, the RMS error in the USNO measurements is about 0.30 mag [92], this would contribute to the systematic errors on the magnitudes measured by the telescopes.

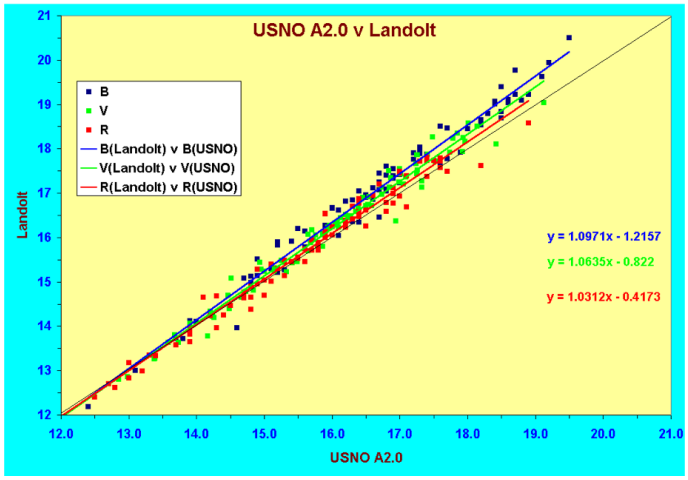

Figure 6.6: Comparison of the USNO A2.0 photometry with the scale defined by Landolt's standards

At the output of `SExtractor`, the objects are compiled into lists along with their positions in pixels and measured magnitudes. The pixel positions are first converted to equatorial coordinates based on the image center equatorial coordinates. The calibration process then uses the position and magnitude comparison with known stars retrieved from USNO A2.0 in the image field.

In order to bypass the optical distortions caused by the telescope mirrors or refractive

[1] `http://www.britastro.org/asteroids/USNO%20photometry.htm`

surfaces and obtain accurate source positions, the output source list celestial positions are matched with the catalog bright stars. For each pair of matched stars, a conversion matrix along x and y axis k_x and k_y is determined via least squares estimation. Mapping the extracted objects coordinates $\vec{X}$, $\vec{Y}$ to the catalog coordinates $\vec{X'}$, $\vec{Y'}$ is then applied by using axis geometrical transformations ($a(X_i,Y_i)$ and $b(X_i,Y_i)$) with 3-order polynomials. This operation is called "N-order polynomial warping". The conversion of every pixel i in the field using a polynomial of degree N is expressed as :

$$X'_i = a(X_i, Y_i) = \sum_{m,n=0}^{N} k_x(m,n) X_i^m Y_i^n \tag{6.9}$$

$$Y'_i = b(X_i, Y_i) = \sum_{m,n=0}^{N} k_y(m,n) X_i^m Y_i^n \tag{6.10}$$

For pairs of matched stars in each image, the magnitude difference is calculated. The magnitude zero-point for each image is taken as the median magnitude difference between the pairs formed by the extracted objects and the catalog R-band stars.

6.5 Operations on images

6.5.1 Image co-adding

Equation 6.6 show that the SNR enhances as the square root of the image exposure time. Another way to optimize the SNR is to take many short exposure images and stack them into one single frame. Because of optic distortions, the flux on each pixel of each frame has to be correctly distributed on the new stacked frame. Thus, the images need to be perfectly aligned to each other before the stacking operation. This process is called "co-adding". The input images are aligned to the same reference using geometrical transformations, so a process similar to that described in section 6.4 is used. But in this case, one has to worry about the flux projection or how does the flux would be distributed after the alignment on the same reference, as this latter process performs shifts or rotations on the original input image. In this case, the output image is resampled using a cubic convolution interpolation. The new pixel value in the output image is created by weighting the average of the 16 nearest input cell centers values, and is adjusted to account for their distance from the center of the input cell as illustrated on figure 6.7.

The images are then added to the reference image. A median filter is applied so each pixel on the result image is filled with the median of the stacked images. Using a median value reduces the cosmics hitting the CCD.

6.5.2 Image subtraction

The analysis pipeline in TAToO rely on the image subtraction method to detect transient sources. A source is identified as transient if its flux varies during the observation period. In order to see a flux variation, one has to choose a reference image (REF). The pipeline detects only positive signal variations. The REF image selection is based on the assumption that the signal we are looking for is fainter in REF than in the other images of the sequence (NEW) [1]. For both pipelines, the subtraction principle is based on Alard and Lupton

[1] In the case where REF probably contains a signal, the images are inverted (pixel values multiplied by -1 matrix).

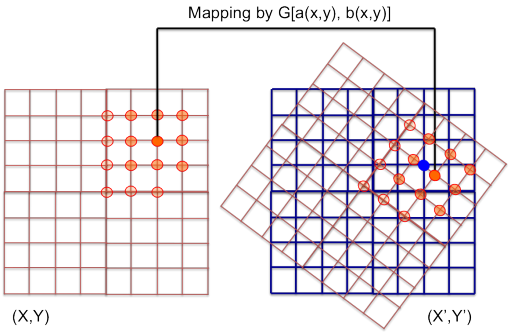

(a) Geometric transformations on the input image before alignment. The red source in the input image reference (X,Y) is remapped on the new image reference (X',Y') by using a cubic interpolation spline. The blue point is the new position in the new reference.

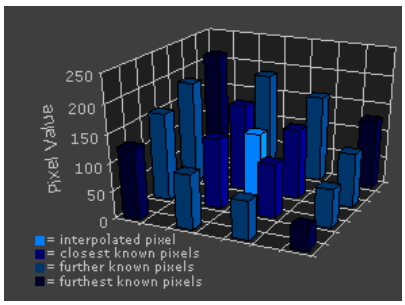

(b) Flux projection on the new reference coordinates using a bicubic spline interpolation.

Figure 6.7: Image alignment process.

subtraction method [14][1]. This method adds an additional constraint on the REF selection. For the method to work properly, the REF image must be the best quality image.

In order to perfectly subtract one image from another, again, they have to be aligned to the same reference using the procedure described in section 6.5.1. However, when looking for variable signals on long time scales, the nights of observations have different qualities (wind degrading the PSF, clouds degrading the SNR...), so the PSFs in each image can be different due only to atmospheric fluctuations responsible of enlarging the seeing [2]. Thus, the frames need to be matched to exactly the same seeing.

Prior to the subtraction, (REF(x,y)) is convolved with the seeing of each other frame before subtracting it from each frame. Since it is the best quality image, *i.e* with the best seeing (smallest FWHM), this process degrades its PSF. This implies finding a suitable convolution kernel K(u,v) that when convolved with the reference image , generates a transformed image REF′(x,y) which can be compared pixel by pixel to an image of less quality NEW(x,y). Thus, the transformed reference REF′(x,y) would be expressed as :

$$REF'(x,y) = REF(x,y) \otimes K(u,v) \tag{6.11}$$

In the original method by Alard and Lupton [14], the Kernel is decomposed into basis functions using Gaussians and a set of polynomials of order p of the form:

$$K(u,v) = \sum_i a_i B_i(u,v) = \sum_l e^{\frac{-(u^2+v^2)}{2\sigma_l^2}} \sum_{j=0}^{p_l} \sum_{k=0}^{p_l - j} a_{ljk} u^j v^k \tag{6.12}$$

In [14], the values of p and σ_l^2 are determined *ad hoc* directly by fitting the data points, so they should depend on the characteristic PSF of the telescope. A combination of three Gaussians (l respectively equal to 1, 2, 3) with σ (σ_l) in the 1-9 range width were suggested by the authors as well as associated polynomial degrees p_l in 2 to 6 range, which gives : $\sigma_1 = 1$, $p_1 = 6$

[1] ROTSE pipeline method is slightly different, it is explained later in this chapter.

[2] This case is different from co-adding the images, as we usually co-add fields imaged on the same night with comparable atmospheric conditions.

$\sigma_2 = 3$, $p_2 = 4$
$\sigma_3 = 9$, $p_3 = 2$

The amplitudes of the polynomials a_{ljk} are determined via least square functions which minimize the pixel to pixel variations between REF$'$ and NEW. NEW images are then subtracted from REF' image.

6.6 The analysis pipelines

Two independent image analysis pipelines are implemented in TAToO. ROTSE pipeline handles ROTSE images. In case of an interesting detection, SNLS pipeline is used as a second loop to cross-check ROTSE results. TAROT images are analyzed with the SNLS pipeline, as this latter is more easily configurable for different image conditions.

6.6.1 ROTSE pipeline

Image correction

Image correction is operated automatically in the telescope site. When corrected images are copied on TAToO machine, they can be corrected again using new flats or new darks. A Median dark from 6 dark frames with the same time exposure as the image is subtracted from the image. The flat-fielding uses the median of 15 twilights images. As seen in figure 6.2(c), usually after this operation, the fringe effect is visible. In ROTSE pipeline, an attempt to correct for this effect is automatically done.

It is interesting to notice that this fringe is most visible in quite good conditions. Cases where the fringe effect is less important are moonlight polluted observations or when clouds are present, because the light is diffuse along the CCD pixels. In other words, the fringe effect is mostly visible when we have generally a good SNR.

ROTSE operates an automatic fringe correction. To do this, it builds a fringe map to subtract from the corrected image. To obtain the fringe map, another type of flat is built : the night-sky flat; it is based on exactly the same principle as the twilight flat but operated at night with pointing offset between exposures to wash away the point sources contribution (Dithering). This frame has the particularity of having a strong fringe pattern as shown on figure 6.8(a). The fringe map as shown on figure 6.8(b) is built from the subtraction of the night-sky flat from the twilight flat. In photometric nights, the amplitude of the fringing pattern scales directly with the sky background in the individual images. The brightness scaling factor is obtained when plotting the pixel values of the image under correction as a function of the pixel values of the fringe map and fitting the slope by linear regression. If $\chi^2 < 3.0$, the fringe map is scaled and then subtracted from the individual image, as scattered light is of additive nature. In non-photometric nights, the fringe scaling factor varies in a difficult manner across the CCD, as the assumption that the fringing amplitude scales with the sky background does not hold any more. The fit is poor (i.e $\chi^2 > 3.0$) and the image is not corrected from fringe. The contribution of the fringe to the sky background and hence to the photometric errors in ROTSE data is at most 5% [106].

Source extraction : `sexpacman`

The source extraction from each image is done by calling `SExtractor`. The sky mesh size is fixed to 32 pixels. A Gaussian filter of 2 pixels FWHM in each 3×3 pixels is

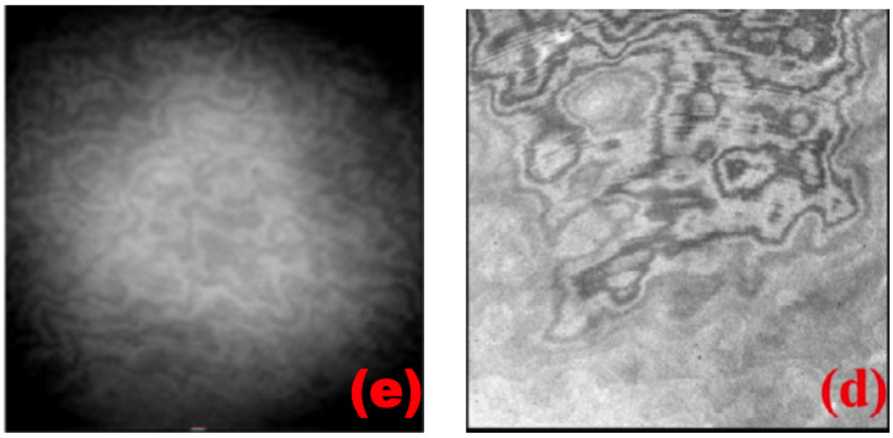

(a) Sky flat. (b) Fringe map.

Figure 6.8: Example of a sky flat and a fringe map from ROTSE telescopes.

convolved with the image to enhance the detectability of PSFs with FWHM $\sim$ 3 pixels. The detection threshold is set to 1 σ above the background. An arbitrary ZP is put in the configuration file to calculate the magnitudes. Aperture magnitudes are obtained assuming photometric apertures of 5 pixels. Typically, with such parameters, few thousands of sources are extracted and compiled into lists along with some diagnosis parameters, called "flags". Sources can be flagged if they happen to be saturated, originally blended, or with incomplete or truncated flux. Table 6.1 show the extraction parameters used in `SExtractor` :

Parameter name	Description	Value
BACK-SIZE	Sky mesh size	32 pix
FILTER-name	Image filtering	gauss-2.0-3×3.conv
DETECT-THRESH	Detection threshold	1 σ above the background
DETECT-MINAREA	Minimum area of a source	5 pix
PHOTO-APER	Photometric aperture	5 pix
MAG-ZP	Arbitrary ZP	23.0

Table 6.1: `SExtractor` parameters called in `sexpacman`

The outputs from sexpacman are fits files containing the extracted sources with image coordinates, approximate equatorial coordinates, aperture magnitudes using an approximate ZP, and associated photometric errors.

Image calibration : `idlpacman`

idlpacman performs an astrometric registration to stars brighter than 15 mag in the USNO A2.0 catalog. It first derives an initial coordinate solution for each source by triangle matching with the catalog. It then iterates 15 times the operation using 3^{rd} order polynomial warping between the catalog stars and USNO stars. The position resolution is better than 0.3 pixels (1 arcsec) provided that thousands of matched are found in a typical image. When the image is of poor position resolution, which may be caused by bad seeing con-

ditions, and not enough matches with the catalog, it is automatically rejected from the pipeline.

The calibrated magnitudes in each frame are obtained by calculating a ZP offset for each source matched with the catalog. The USNO catalog gives stars magnitudes in red and visual wavelengths. ROTSE operates with filterless optics but the optical bandpass sensitivity is closer to the R-band. Hence, it is convenient to calibrate the instrumental magnitudes with standard "redder" stars. R-band standard stars in the magnitude range of 13.5<V<20.0 with a color index of 0.4<V-R< 1.0 are selected for calibration. The ZP offset is the difference between the image sources magnitudes and the list of matched catalog stars. A ZP offset map is built for each image. The median value of the ZP offset is then added to each detected source, and the statistical error is noted. Good quality images have more matched objects, thus the statistical error on calibrated magnitudes is reduced. In a typical image, the ZP offset is around 2 mag, the associated RMS error is around 0.3 mag.

At the end on this procedure, a calibrated object list for each image is obtained.

Image co-adding and subtraction

Before the subtraction process, images are usually co-added to enhance their SNR. It is a common procedure to GRB or SN search that the reference image is made by the co-add of many images from the same night. The NEW image can be an individual image or a co-add of 2 or more frames taken in the same night depending on the analysis. An automatic check on the coadds quality is performed in order to reject bad quality images which may degrade the quality of the coadd. This is done by choosing the image of the set with the maximum number of matched stars with the catalog. Only images having sources at least equivalent to 75% of this number are considered for the co-add. At this step, a bad pixel map is supplied to the program to flag the bad pixels present in the image. Once the images are co-added, `SExtractor` is called again to perform source extraction. The new parameters take into account that the co-adding operation may enlarge the PSF.

Parameter name	Description	Value
BACK-SIZE	Sky mesh size	32 pix
FILTER-name	Image filtering	gauss-2.0-5×5.conv
DETECT-THRESH	Detection threshold	1 σ above the background
DETECT-MINAREA	Minimum area of a source	5 pix
PHOTO-APER	Photometric aperture	7 pix

Table 6.2: `SExtractor` parameters called in co-added images.

The extracted sources are calibrated again with the USNO catalog.

For the image subtraction process, ROTSE pipeline uses a more sophisticated method [127] than the standard Alard and Lupton method described in section 6.5.2. Alard and Lupton method works efficiently if the reference has a azimuth symmetric PSF along the axis, this is not always true as PSFs can be elliptical with axis oriented in different directions. In [127], a more symmetric method is used in order to reduce the dependency on the reference quality. Thus, 2 kernels are generated. They should meet the requirement

that :

$$REF(x,y) \otimes K_{REF}(u,v) \approx NEW(x,y) \otimes K_{NEW}(u,v) \tag{6.13}$$

The addition of a second convolution operator injects a new degree of freedom that must be constrained, this is solved by requesting that at least one kernel should satisfy :

$$\sum K(u,v) = 1 \tag{6.14}$$

The SNR in the image produced by the subtraction may be high and lead to large uncertainties on the photometry, this would be due to the PSF diffusion in the images. In analogy to the optimization technique for generating bicubic smoothing splines, the inclusion of an RMS width penalty term in the image constrains the diffusion of stellar images caused by the convolution with the kernels.

The penalty term is obtained by cross-validation [1]. It would constrain radially the diffusion of the PSF. Figure 6.9 shows the convolved reference image when thousands of sources are used (extracted at 1 sigma above background) to calculate the penalty term on stellar diffusion, and the result when few hundreds of sources are used (extracted at 3 sigma above background). The flux interpolation step fails at high thresholds. For low thresholds, the PSF is radially well constrained as the penalty term was efficiently estimated. It is thus important to keep a low detection threshold when using this method. Moreover, if not enough sources are extracted which could be simply due to a bad image quality, the subtraction fails. The procedure was tested so that the photometric error induced by the subtraction contributes less than the statistic errors on photometric calibration [127].

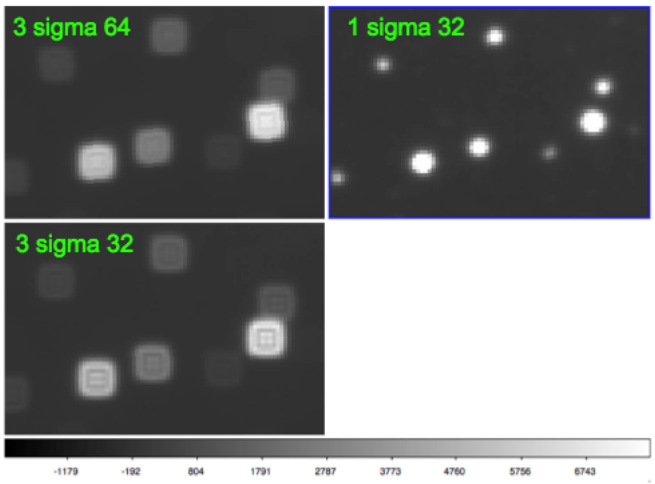

Figure 6.9: The convolved reference obtained by cross-convolution when using different detection thresholds. DETECT-THRESH sigma BACK-SIZE are marked in green.

Figure 6.10 shows an example of a NEW and REF images before an after convolution. The NEW image is shown before the alignment to the reference coordinates (upper left). After alignment + convolution with Kernel K_{NEW}, the resulting image NEW' is shown

[1] cross-validation involves partitioning a sample of data into complementary subsets, performing the analysis on one subset, and validating the analysis on the other subset. To reduce variability, multiple rounds of cross-validation are performed using different partitions, and the validation results are averaged over the rounds.

in the bottom left plot. The convoluted reference REF' shows a smoother background than the original REF, because of the flux interpolation of each pixel. The effect of the Kernel K_{NEW} is clearly visible on the NEW image. If the source flux has not varied (not transient), and in case that the PSF-matching and the subtraction are successful, no trace would be found on the resulting image after subtracting NEW convoluted from REF convoluted and only varying sources would be present. The image after subtraction is shown on figure 6.11.

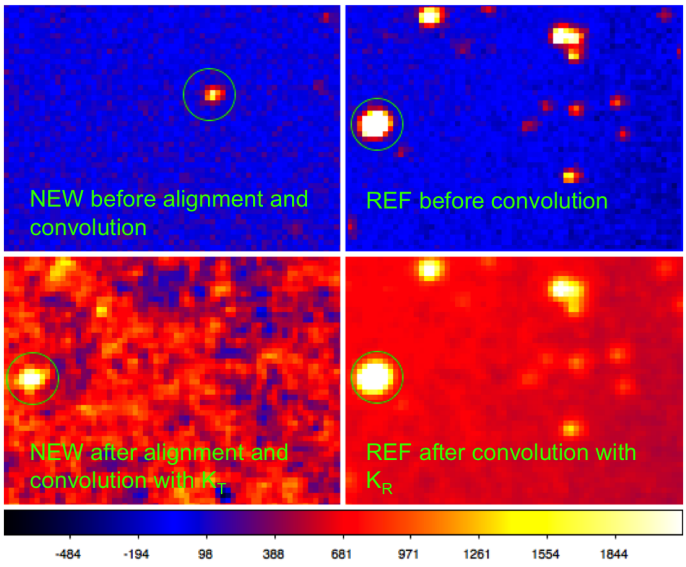

Figure 6.10: Upper Left) Image NEW before alignment and convolution. Bottom Left) NEW image after alignment and convolution. Upper Right) REF image before convolution. Bottom Right) REF image after convolution. The green circle delimits an area of 5 pixels around the centroid of the source.

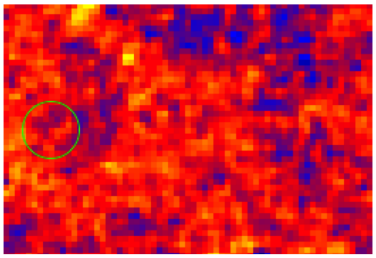

Figure 6.11: Result image from the subtraction of NEW convoluted with K_{NEW} from REF'. The contrast parameter and the circle size is the same as in figure 6.10. The stable source leaves no trace on the result image.

Once the residual image is obtained, `SExtractor` is called again to extract sources which flux has varied positively from REF to NEW. The extraction parameters are slightly different from those described in section 6.6.1. Mainly, they account for the PSF enlargement after convolution and set higher detection threshold because of the additional background.

A list of residual sources is obtained at the output of `SExtractor`. The major part

Parameter name	Description	Value
BACK-SIZE	Sky mesh size	32 pix
FILTER-name	Image filtering	gauss-2.0-5×5.conv
DETECT-THRESH	Detection threshold	1.5 σ above the background
DETECT-MINAREA	Minimum area of a source	5 pix
PHOTO-APER	Photometric aperture	9 pix

Table 6.3: `SExtractor` parameters called in the subtracted images.

of these sources are due to defective pixels [1], detections close to very bright or saturated sources [2], asteroids or cosmics. In order to reduce the background residuals in (NEW-REF) image, the candidate sources must have their SNR > 5. This rejects efficiently the background residuals due to strong fringe patterns or local variations of sky background.

To furthermore reduce the background, the pipeline divides the images used to build the coadd of NEW image into two groups and coadds each group forming NEW1 and NEW2 [3] subtracting the reference REF from each of them. The following cuts are then performed on each residual image (NEW1-REF) and (NEW2-REF):

- The candidate source SNR must be larger than 2.5 in both residual images.
- The position of the candidate source residual must match within 1 pixel if its SNR > 15 and 1.5 pixels otherwise.
- Candidates near to the image edges are eliminated (within 20 pixels from the image edge) to avoid abnormal PSF shapes usually lying at the image edges or truncated flux.

These cuts prevent from cosmics, satellites or asteroids. A low threshold on the flux change is applied, we require that the candidate flux has changed by at least 10% comparing to the reference.

After these cuts, lists of residual candidates for each set of (NEW$_i$-REF) is obtained, i being the number of individual or co-added images where a transient signal is investigated.

For each (NEW$_i$-REF), the associated candidate sources are shown on a html page to be visualized. Each candidate source is shown on the NEW image, the REF image and on the residual image. The residual shape is checked for symmetry and compared to its neighbors. The webpage contains different informations on the candidate sources:

- The SNR in the residual image.
- The magnitude in the residual image.
- The flux change comparing to the reference.
- The motion calculated from the candidate position comparison with the reference.

[1] A map of "bad pixels" for each telescope is used in order to flag the dead or hot pixels. However, some of them can still cause wrong detections.

[2] Most of very bright sources are masked prior to the detection process.

[3] For instance, for a NEW image formed by the coadd of 8 individual images from the same night, NEW1 and NEW2 will be the coadd of the first 4 images and the second 4 images respectively.

The pipeline offers the opportunity to do cross-checks with catalogs within the webpage. The candidate position is searched in SDSS seventh data release (The Sloan Digital Sky Survey) [1]. SDSS is a large database of stellar objects detected by 2.5 m diameter optical telescope located in Apache Point Observatory in New-Mexico [1]. If the candidate is present in the catalog, it is rejected, as stars are not candidates for neutrino sources. If it is a galaxy, it is kept for the next steps. Since the observation can be outside the SDSS footprint, a check in the 2MASS (The Two Micron All Sky Survey) [2] database is also performed. The 2MASS catalog[111] consists celestial objects detected in three near-infrared bands; J-band, H-band and K_s band. A database of minor planets (asteroids) is also available from the webpage [3], the database is searched for an asteroid in the candidate coordinates and detection date. An example of the webpage is shown in figure 6.12.

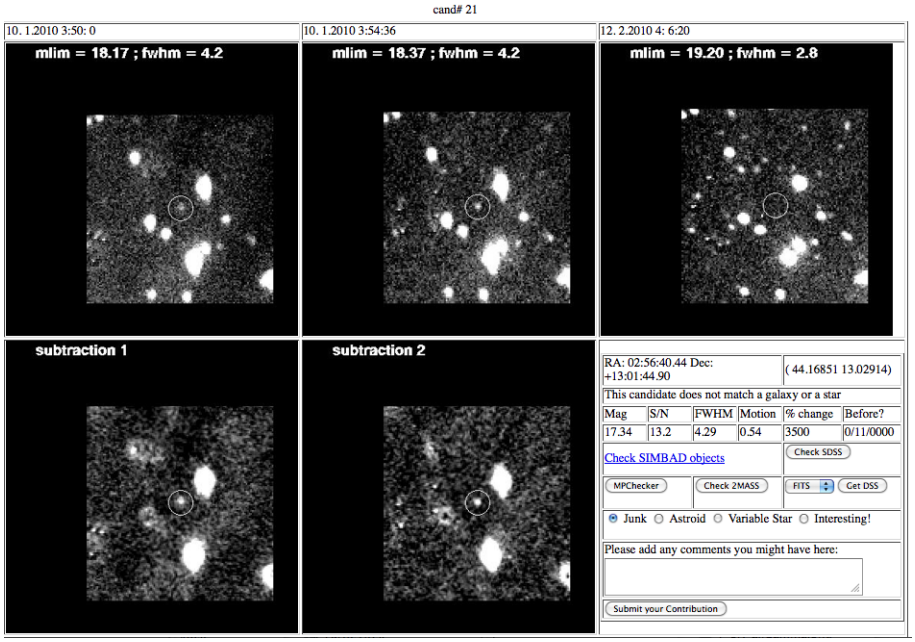

Figure 6.12: Webpage showing a residual and its characteristics.

6.6.2 Adapted SNLS pipeline

The SNLS pipeline was adapted for the image features of TAToO data. It relies on Poloka package for image reduction and photometry originally used for the SNLS program. The main steps explained above are common to both pipelines. However, this pipeline is still not optimized for an automatic use. The main difference is that it uses the original Alard and Lupton method to subtract the images. It is processed in case of an interesting candidate or for TAROT images analysis.

[1] `http://www.sdss.org`
[2] `http://www.ipac.caltech.edu/2mass/`
[3] `http://scully.cfa.harvard.edu/cgi-bin/checkmp.cgi`

6.7 Further photometry checks on the candidates

The default analysis pipelines use aperture photometry to extract magnitudes. Aperture photometry is speed and stable. However, by calculating the flux within a fixed circular aperture and not examining the flux profile, some information is lost. The PSF-fitting photometry is thus used as a post-processing step if an interesting residual is found. PSF-fitting is computationally expensive; while `SExtractor` calculates aperture magnitudes in $\sim$ 30 s for a typical frame of thousands of objects, PSF photometry takes several minutes. If an object is found with the processing pipeline, its light curve using the PSF-fitting photometry can be obtained with errors $\sim$30% smaller than aperture photometry.

The PSF-fitting package RPHOT [100] [99] are undertaken for every single remaining transient. RPHOT is a photometry console based on DAOPHOT [114] photometry package where the user can check step-by step all the photometry process and control it.

The reference (REFIM) image is cropped around the candidate centroid. A group of nearby stars (REFSTARS) is then automatically selected using `SExtractor` output list objects which were not flagged as saturated or blended and passing the following cuts:

- SNR $>$ 7 in at least 75 % of the images
- Successfully fitted by a Gaussian

The user can add/remove REFSTARS to make sure to avoid saturated objects, blends, etc. After the reference stars have been chosen, a procedure is called to calculate the PSF model. As the PSF does vary significantly across the ROTSE field of view, the REFSTARS used to construct the PSF fitting template should fall within 14 arcmin from the target, thus the image cropping radius is optimized in this sense. The radius represents a balance between an improved PSF template accuracy gained from an increase in the number of objects included, and deviations from the target PSF at larger separations that degrade the template. In crowded fields, close to the galactic plane, the candidate flux can enclose nearby stars fluxes, RPHOT provides a tool to remove the interfering source if a source overlaps with or is otherwise confused with the target before the psf-fitting photometry. A two-dimensional Gaussian profile with individual fits for each axis and fit residuals are obtained. All detected objects are fit with the PSF model. In some cases, the procedure fails for objects with a very bad seeing. If the target (the candidate) is not detected, a limiting magnitude is calculated at the target location[1]. This limiting magnitude is defined as the magnitude that the target must have to provide a 3σ detection.

Figure 6.13 shows the reduced image around a candidate. Objects extracted by `SExtractor` are shown in red. REFSTARS are shown in yellow. The target candidate is shown in green. The area around the target is 200 by 200 pixels.

RPHOT calculates the weighted average of flux ratios of the reference stars to the REFIM in each image in order to derive the relative magnitude offsets. These are then calibrated in an absolute sense by determining the flux zeropoint for the REFIM. The user must input a file listing coordinates and calibrated magnitudes for objects in the field, taken from the USNO-B1.0 catalog [93]. RPHOT matches this list against the REFSTARS and then computes the median zeropoint, which it adopts as the REFIM zeropoint.

ROTSE telescope can not resolve galaxies, in case our candidate is overlapped with a galaxy, RPHOT can not estimate the object magnitude alone but treats the galaxy and

[1]The ROTSE processing pipeline, the limiting magnitude is defined as the 90th percentile of objected detected with 1σ above the background.

the transient object as a single source. In this case, we build a list of good REFSTARS as output from RPHOT and do again the subtraction procedure described in section 6.5.2 on the reduced image centered at the galaxy. In this sense, assuming that a transient source appeared on top of a galaxy, this latter does not change its overall flux and only the transient contributes to the flux difference noticed. Since the galaxy is present on the reference, subtracting the new image from the reference would give the transient object flux alone. The transient object photometry is done using the PSF-fitting method.

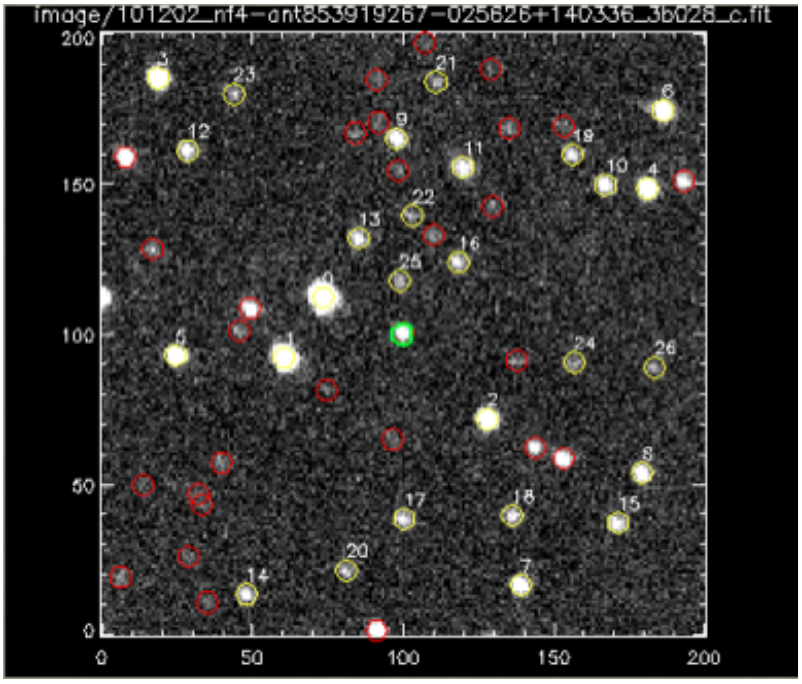

Figure 6.13: RPHOT photometry console. The target is in green. REFSTARS are in yellow. The total extracted objects are in red.

Chapter 7

Results

The implemented high energy filter described in chapter 5 was optimized to select the most energetic and best reconstructed events detected by ANTARES. Monte Carlo simulations show that an purity greater than 99% in selecting neutrinos is expected. In this chapter, we address the question whether the so selected neutrinos do have an associated optical counterpart indicating the presence of a transient astrophysical phenomenon related to the HE neutrino detection. This approach is complementary to the standard neutrino search from transient sources in ANTARES. It makes an *à priori* assumption that the neutrino is in fact of cosmic origin, independently from the nature of the source which have emitted it. If an optical counterpart is discovered in coincidence, it would confirm the emission of HE neutrinos from cosmic sources. Moreover, it would give the opportunity to identify these sources by means of their optical light curves analysis. The study of a possible serendipitous coincidence between the neutrino and candidate sources such as CCSNe or GRBs is detailed in chapter 5. Under the hypothesis of 25 HE alerts sent per year and a limiting magnitude of 17 mag, the detection of a SN or a GRB signal in coincidence with a neutrino passing the HE filter would lead as a first order approximation to 3 and 5 sigma significance respectively for each source.

The quest for an optical counterpart associated with a neutrino emission considers two scenarii; (i) the case where the optical emission is most important during the first seconds to minutes after the neutrino emission and rapidly fading afterwards and (ii) the case where the optical counterpart is expected to last for few days after the neutrino emission. GRBs are typical objects for case (i), while SNe are representative of case (ii). In this chapter, we will focus on case (i) by analyzing prompt observations taken within one day after the neutrino alert. Over 2010, ROTSE telescopes responded by a prompt observation to 5 neutrino alerts. TAROT telescopes were more efficient in 2011 by responding to 7 alerts in prompt mode, however, observation of only 3 alerts could be exploited[1]. No prompt observation was recorded from ROTSE in 2011. The optical analysis of 2010 data is presented.

Content

[1]The 4 other prompt observations did not contain any signal (black images).

7.1 The neutrino data quality

A total of 8 neutrino alerts have a prompt observation from 2010 and 2011 data. The characteristics of the analyzed events are shown in bold characters in the annex A.2. Alerts in 2010 were optically followed by ROTSE telescopes, while 2011 alerts led to prompt observations by TAROT telescopes. The alerts (denoted ANTyymmddA) are :

- 2010 (ROTSE telescopes) : ANT100123A, ANT100302A, ANT100725A, ANT100922A, ANT101211A.
- 2011 (TAROT telescopes) : ANT110409A, ANT110529A, ANT110613A.

Figure 7.1 shows the on-line event display of the neutrino event which triggered an alert on 11/06/13. This event was fitted on 9 ANTARES lines. Each plot presents the event track fit on a single line. The abscissa axis is the time in ns and the ordinate axis is the OM altitude above the seabed, denoted z. Each cross represents a single hit on an optical module. The colored points represent the amplitude of the hits. The same representation of the other triggering neutrinos is shown in annex B.1 for each alert. This representation is acquired automatically from the on-line reconstruction each time a neutrino passes the HE filter described in chapter 5. It is used as a fast diagnose tool to check the on-line reconstruction quality.

For each alert, the agreement between the on-line reconstruction (`BBfit`) and the off-line reconstruction (`AAfit`) was investigated. The space angular difference between the reconstructed neutrino directions delivered by each algorithm is shown on table 7.1. `AAfit` takes into account estimated positions of the OMs while `BBfit` considers the lines straight in space and merges the hits measured by each OM in a storey. The off-line angular accuracy is enhanced as shown on figure 5.23. Because `BBfit` is more robust and `AAfit` is more precise, the agreement between the two independent reconstruction strategies proves that the triggered event direction is well reconstructed. For 2010 (2011) alerts, the line-dependent fit quality cut (hit-dependent fit quality) was used in `BBfit`, with an expectation of 99.5%(99.7%) performance on discarding mis-reconstructed atmospheric muons as shown on table 5.5. While these events are unlikely to originate from an atmospheric muon background, three cases of important disagreement are found for alerts ANT100725, ANT101211 and ANT110613. In each case, the difference was investigated.

In the case of ANT100725, the detector was running in reduced HV gain configuration (nominal gain G divided by 4) because of high bioluminescence activity. The precise PMT calibrations in G/4 mode are not available[1]. The off-line reconstruction `AAfit` is much more dependent than the on-line reconstruction on the calibration precision, which explains the given discrepancy. Therefore, the coordinates given by `BBfit` were sent to the telescopes.

[1]The detector calibration file used in `BBfit` is available for nominal gain conditions G and for G/2 configuration. An interpolation of the time and charge calibration is used when the detector is running in G/4 mode.

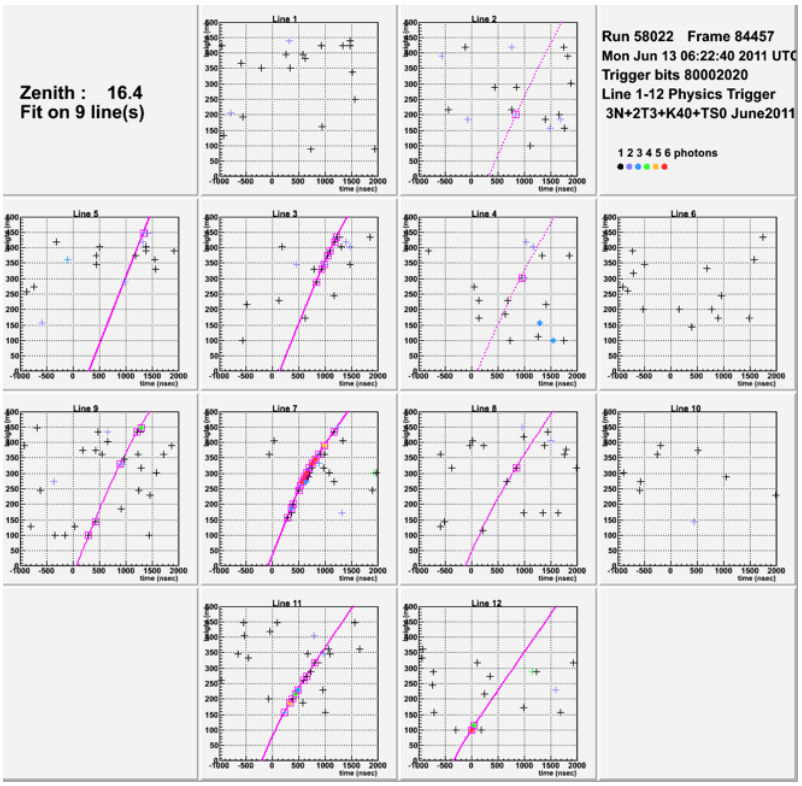

Figure 7.1: The event display of a triggering event in TAToO (see text for details).

Alert name	$\Delta_{online-offline}(^\circ)$
ANT100123	0.7
ANT100302	0.5
ANT100725	60
ANT100922	0.25
ANT101211	6.1
ANT110409	0.1
ANT110529	0.4
ANT110613	24

Table 7.1: Angular differences between the reconstructed triggering neutrino events directions using the on-line and the off-line track fit reconstructions.

The triggering event of alert ANT101211 was reconstructed on 4 lines. An ambiguity on the reconstructed azimuth angle due to the mirror symmetry is introduced when `BBfit` reconstructs a multi-line track using lines that lie approximately in the same vertical plane. This is always true when reconstructing on two lines but may happen for events fitted on 4 lines. The mirror track has the same zenith angle as the original track but rotated Φ. A check was operated off-line by running the `BBfit` reconstruction on the event and forcing it to consider hits from line 2 and 8 in the fit. The results were then compared to the off-line reconstruction and agreed within 0.37 degree. The reconstructed positions are given in table 7.2 for the coordinates obtained with a fit on 4 lines, those obtained with 6 lines by adding line 2 and 8 in the fit and those obtained with the off-line algorithm. The refined

position was sent again to the telescopes.

Alert name	Zenith	Azimuth	RA	DEC
BBfit	45.88	143.00	320.42	-50.91
Refit	46.35	150.94	322.69	-45.37
AAfit	46.2	151.42	323.07	-45.11

Table 7.2: Alert ANT101211 triggering neutrino event direction using the on-line reconstruction `BBfit`, the on-line reconstruction corrected from mirror solution Refit (added lines 2 and 8 in the fit) and the off-line reconstruction `AAfit`.

The implementation of a new version of `BBfit` at the beginning of year 2011 helped to resolve the problem of the mirror solution. The enhanced reconstruction consists of performing a temporary hit selection based on a very strict time residual cut of 20 ns for both mirrored tracks, selecting among the entire set of event hits. The track estimated as correct is the one with the highest weighted charge (the weight is dependent on the charge associated to the hit, the incident angle of the Cherenkov photon and the angular acceptance of the OM). No other mirrored track for our events has been noticed since this upgrade.

The last mismatch is found for alert ANT110613. Similar checks on the mirror solution in the on-line reconstruction have discarded the possibility of a mirrored track in the online track reconstruction. The two zenith angles agree well: (`BBfit` 16.4 degrees versus `AAfit` 16.6 degrees) but divergence exists for azimuth angles (93.5 degrees versus -2.65 degrees). However, the offline reconstruction `AAfit` gave a bad track fit quality, causing most probably this discrepancy. Thus, the on-line position was kept for the follow-up.

The on-line and off-line positions show a good agreement (less than 1 degree) for the rest of the alerts. The off-line reconstruction algorithm was basically a cross-check tool in 2010. In 2011, the refined neutrino position calculation became automatically available. Each event quality was checked in details, and the sanity of both reconstructions is investigated before deciding whether the refined coordinates should be sent again to the telescopes.

These neutrino events are part of the highest energy and best reconstructed ones detected by ANTARES. A particular effort was deployed to determine the most precise position to trigger optical observations in the direction of the detected neutrino. The use of two independent reconstruction algorithms running directly on data events reduces the dependency on each reconstruction intrinsic uncertainty. In TAToO, these reconstructions are used in a complementary way taking advantage of the inherent assets of each of them in terms of robustness and precision.

7.2 The optical data quality

As described in section 5.6, the robotic telescopes acquisitions are based on a scheduler, which orders the observations upon reception of the alert. It first verifies that the given position is instantaneously visible in order to start taking data, otherwise, the observation query is delayed until the asked position becomes visible. The network is composed of telescopes in the Southern hemisphere (TAROT-SUD, ROTSE 3a, ROTSE 3c) and telescopes in the Northern hemisphere (TAROT-NORD, ROTSE 3b, ROTSE 3d) for the follow-up of

neutrino events detected near the horizon. For instance, no southern telescope responded to the event which triggered ANT100302A alert (zenith = 83.6 °, dec = -28.16°), but data could be acquired from ROTSE 3b. The fact that the telescope network covers a full hemisphere is certainly an advantage, as we enhance the probability to observe in the neutrino direction, in addition to increasing the chance of a prompt response when the alert is issued at day time. The constraints on delayed observations are much less severe than prompt observations as there is always a chance that telescopes would react in the following nights when the source becomes visible, and acquire images according to the defined observation strategy (detailed in section 5.6).

As in the case of the neutrino data quality, the associated optical data quality is of capital importance. The quality of the optical data determines TAToO sensitivity to transient sources by setting a determinant limitation on the visibility horizon within which a transient signal would be investigated. This limit is constrained by atmospheric conditions at the telescope site. Figure 7.2 shows the first image from each alert. A zoom in the center of each image is shown. The effect of the scattered moonlight on the prompt image of alert ANT101211 is visible. Moreover, the signal-to-noise ratio of 2011 (only TAROT-sud responded for these alerts) observations is in average better than 2010 alerts response acquired by ROTSE telescopes, as for these responses, better atmospheric conditions were available.

As explained in chapter 6, the astrometric and photometric calibration is based on the matching of the extracted sources with the brightest USNO-A2 catalog stars. Using the 3-σ clipped-mean `SExtractor` function to estimate the background, the number of extracted sources using a threshold of 3σ above the background is shown in table 7.3. The associated number of matched sources is also shown. The first image quality of ANT100123 is very poor with only 17 matches over the entire field-of-view, followed by ANT101211(215 matches) and ANT100922 (280 matches) .

Alert name	Telescope	Number of extracted sources	Number of matched sources
ANT100123	3c	158	17
ANT100302	3b	2922	1975
ANT100725	3c	4309	3169
ANT100922	3a	421	280
ANT101211	3c	944	215
ANT100409	tarot-sud	16992	7217
ANT110529	tarot-sud	8284	8159
ANT110613	tarot-sud	25427	24529

Table 7.3: First image properties of each alert response. The extraction threshold is fixed to 3σ above the background. The calibration is done using USNO-A2 catalog stars.

The ROTSE pipeline is highly automatized. As described in section 6.6.1, at least thousand matched stars are required in the entire field-of-view to reach a good astrometric solution (mean value on the astrometric error should be less than 1"). If not enough matching stars are found in the field, the image is automatically rejected from the pipeline. Thus, when using ROTSE software, the first images of these alerts are not expected to get calibrated. This would lead to an additional data loss.

ROTSE pipeline modules for source extraction and calibration described in section 6.6.1 were used to analyze ROTSE data. The number of calibrated images is the effective number of images which can be used in the analysis. The other images were automatically

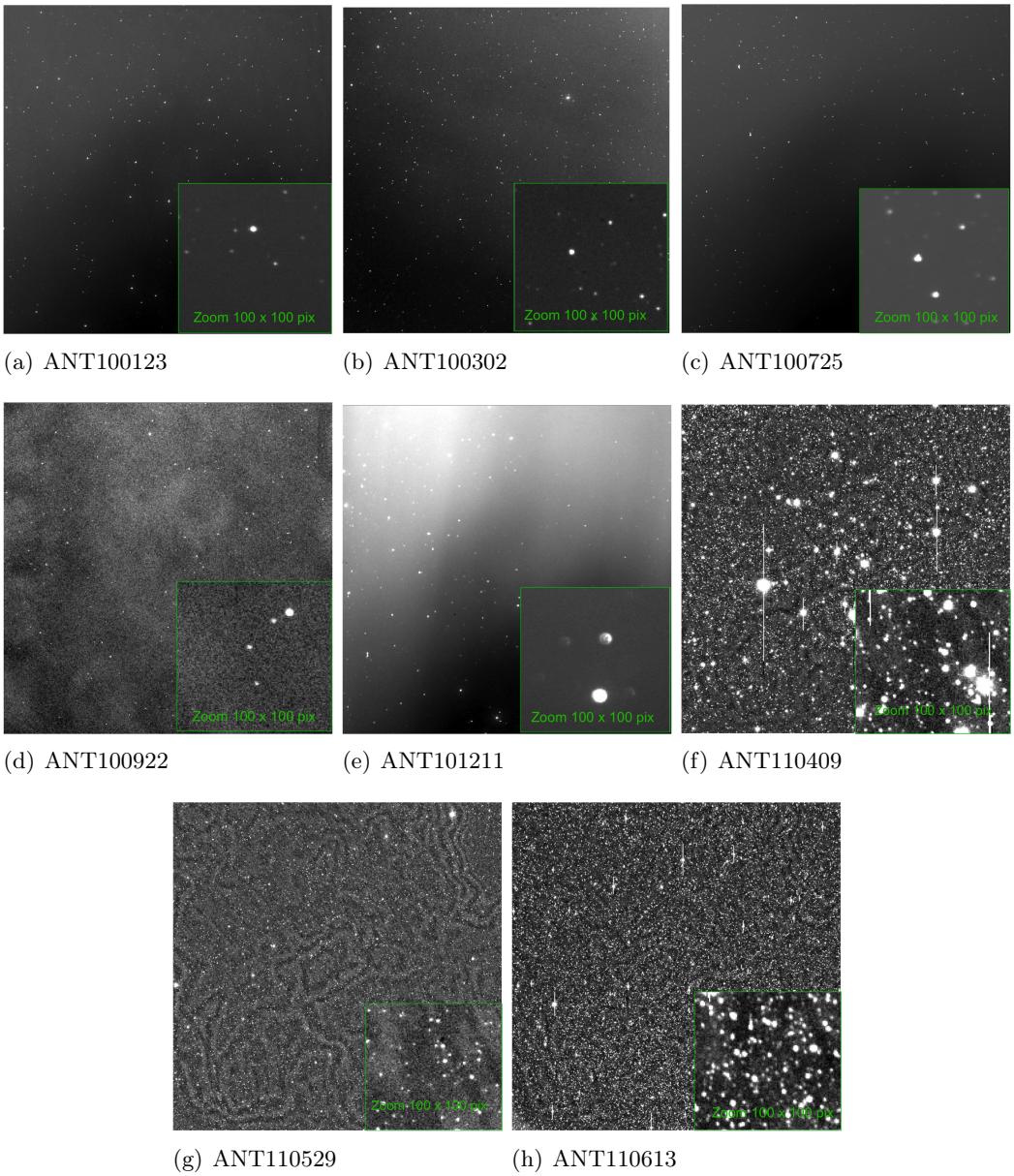

(a) ANT100123 (b) ANT100302 (c) ANT100725

(d) ANT100922 (e) ANT101211 (f) ANT110409

(g) ANT110529 (h) ANT110613

Figure 7.2: Typical prompt image quality for each alert.

rejected. TAROT optical data was processed with the adapted SNLS pipeline, regarding the overall good quality of the images. No case of optical data loss was encountered for these alerts[1]. Table 7.4 shows the effective number of images used in the analysis.

[1]No automatic rejection is implemented in the adapted SNLS pipeline in case of a bad quality image. Nevertheless, a bad astrometric calibration would always have visible effects in the subtraction process by leading to many background residuals in the resulting subtracted image.

Alert name	Images	Processing software	Calibrated images	T_{exp}(s)
ANT100123	23	ROTSE	15	60
ANT100302	30	ROTSE	11	20
ANT100725	30	ROTSE	30	20
ANT100922	24	ROTSE	24	20
ANT101211	8	ROTSE	6	60
ANT110409	6	adapted SNLS	6	180
ANT110529	6	adapted SNLS	6	180
ANT110613	6	adapted SNLS	6	180

Table 7.4: Number of useful (calibrated) images for the analysis and exposure time per image of the acquired sequence.

7.3 Prompt optical counterpart search

The follow-up program aims at the discovery of HE neutrino sources. One important principle is that no hypothesis is made on the nature of the source which would have emitted the neutrino. The only constraint on the source nature is dictated by the fact that it is expected to be responsible of the emission of the highest energy neutrino events detected by ANTARES. The analysis strategy is optimized to detect sources which would show a bright optical signal at early times (less than 1 day) after the neutrino emission.

As already discussed in chapter 6, the adapted SNLS pipeline is used to analyze TAROT data. If an interesting transient candidate is found in ROTSE data, further photometry checks based on PSF-fitting photometry are undertaken using RPHOT, described in section 6.7. If the candidate still shows a significant flux variation, the adapted SNLS pipeline is used as a last check step. Because each pipeline uses a slightly different subtraction algorithm, the presence of the same candidate in the adapted SNLS pipeline output would reject the hypothesis of the source being a subtraction artifact.

7.3.1 The reference frame

The subtraction first requires the choice of an appropriate reference frame to subtract from the images where the signal would be investigated. Since the adapted SNLS pipeline uses the original method of Alard and Lupton [14], the condition on the reference quality being better than the images to analyze is important (see section 6.5.2 for details). Because the ROTSE pipeline relies on the cross-convolution method, the requirement on the reference quality is suggested to be less strict. However, the pipeline has to be fed with an important number of extracted sources for the subtraction to work efficiently (see discussion in section 6.6.1). Thus, it generally fails when the images are of bad quality. For this reason, the requirement on the reference quality is also respected when using ROTSE pipeline. Among the delayed observations, the best quality image sequence where no optical counterpart is expected after the neutrino trigger is chosen. The reference can be made out of the co-add of these good images, to further enhance the SNR. The reference frame can also be the last image of the "prompt" sequence assuming that the signal has fainted comparing to the first images of the sequence. Table 7.5 shows the reference used for each analysis.

Alert name	Reference
ANT100123	100202
ANT100302	100312
ANT100725	Last image
ANT100922	101202
ANT101211	Last image
ANT110409	Last image
ANT110529	Last image
ANT110613	Last image

Table 7.5: The reference choice

7.3.2 Co-added frames or individual frames

As described in section 6.6.1, the images to analyze can be co-added into one single frame before subtracting the reference frame from it. Using co-added frames enhances the SNR and enables to detect fainter sources. Individual frames, however with poorer SNR, allow to have a more precise time sampling on the candidate source flux variation [1]. When enough images are available to allow for co-adding, both approaches were used. The analysis adopted for each alert are given in table 7.6.

Alert name	Number of co-adds
ANT100123	single
ANT100302	single
ANT100725	single / 4 images / 8 images
ANT100922	single / 4 images / 8 images
ANT101211	single
ANT110409	single
ANT110529	single
ANT110613	single

Table 7.6: The conducted analysis for each alert. ANT100725 and ANT100922 had enough images to allow for a co-added frame analysis of 4 and 8 images in addition to a single frame analysis.

7.3.3 Subtraction residuals

In the ROTSE pipeline, the residuals passing a certain number of cuts (detailed in section 6.6.1) are shown on a html webpage for eye scan. The adapted SNLS pipeline requires only a threshold on the flux variation comparing to the reference, and a threshold on the SNR of the candidate in the residual image. These thresholds are not fixed and the user can control it to reduce the number of background detections or to detect fainter sources. The number of transient candidates per alert can range from one hundred to tens of sources before eye inspection. Despite the fact that ANT110409 and ANT110613 imaging field was crowded due to the position near the galactic plane, the PSF of single sources could be successfully deblended and the adapted SNLS pipeline could perform the subtraction.

[1] The use of individual frames is sensitive to signals with time variation scales of $\sim T_{exp}$ comparing to variations on $n \times T_{exp}$ for n co-added frames.

As an illustration, figure 7.3 shows a residual example from the adapted SNLS pipeline, the image on the left is the image where the source appeared, the image in the middle is the reference frame in which the source is too dim to be detected and the image on the right is the resulting residual.

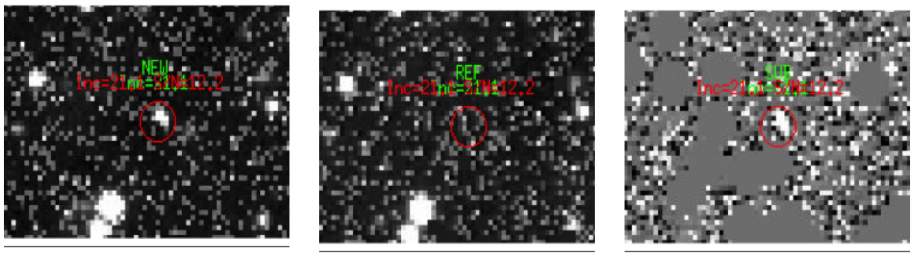

Figure 7.3: Example of a residual resulting from the adapted SNLS pipeline (see text for details) .

Background residuals

The background residuals in prompt images analysis comes mostly from defective, hot or cold pixels, cosmics or noise spikes as the one seen in figure 7.3. The number of residuals left by alert is still reasonable to be investigated by eye [1]. Most of these objects are rejected when using the co-added frames. The residual shape is checked for symmetry and compared to its neighbors. Failed subtractions when the PSF is too large or close to neighboring saturated stars which were partly masked are also a background source. The background due to these phenomena are easily distinguished by eye. Few examples extracted from the ROTSE pipeline are shown on figure 7.4. At least two persons examined the residuals independently for each alert.

An interesting candidate

For alert ANT100725, an interesting candidate was found after eye inspection. The candidate is shown in figure 7.5.

This candidate is overlaid over a galaxy. In order to extract the transient flux alone, we relied on the PSF photometry. The images were cropped around the candidate and subtracted from the reference. Seventy stars were used as reference stars from which a PSF model was derived. Figure 7.6 shows the light curve of the candidate. Red squares indicate the candidate magnitude in each image with a time bin of 20 s. Error bars represent the photometric error which is the sum of the contribution of the candidate photon noise and the contribution of the zero-point error [2]. This latter contribution is of the order of 0.05 mag for the faintest selected REFSTARS (14 mag). When the object is not detected in an image, the limiting magnitude indicate that the object must be dimmer than the magnitude indicated by the blue arrows in figure 7.6. The candidate light curve shows important fluctuations. This candidate has disappeared when doing the analysis using co-added frames. The residual is most probably due to a bad subtraction of the bright

[1] The number of residuals left in the SN counterpart search is considerably higher because all the nights of observation are used.

[2] The error on the zero-point is derived as the median value of the distribution of magnitude differences between the selected REFSTARS and their matched catalog magnitude in each image.

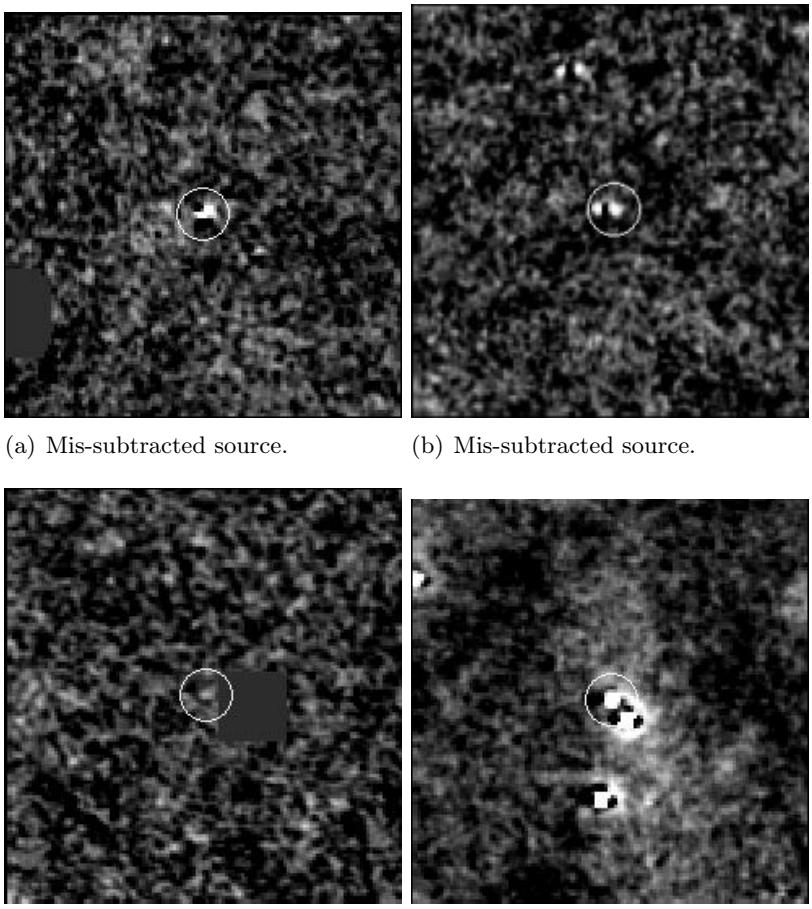

(a) Mis-subtracted source.

(b) Mis-subtracted source.

(c) Detection in a saturated star neighborhood.

(d) Detection in a saturated star neighborhood.

Figure 7.4: Prompt counterpart search background examples.

galaxy. For these reasons, the candidate was rejected. No other interesting candidate was found.

7.4 Upper limits

No transient candidate was found in the analyzed data. In this case, one can derive upper limits on the magnitude of transient sources which could have emitted a HE neutrino detected by ANTARES. As already discussed in the beginning of this chapter, we make the hypothesis that the detected neutrino is of cosmic origin, independently from the nature of the source. In this sense, TAToO is a discovery tool; a single HE neutrino associated to an optical counterpart would lead to a significant discovery regarding the very low serendipitous coincidences expected. In case of a non-detection, upper limits on the magnitude of the celestial objects within the neutrino-optical time delay are derived.

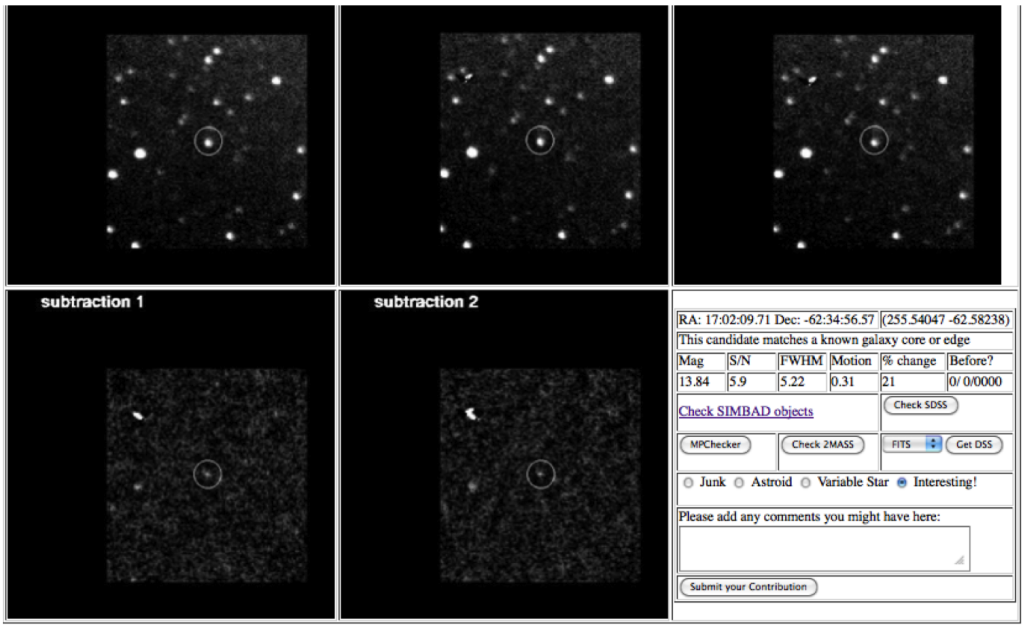

Figure 7.5: A transient candidate from alert ANT100725. The upper left image is NEW1, the upper middle image is NEW2 and the upper right image is REF. The bottom left image is (NEW1 -REF) and the bottom right image is (NEW2 - REF).

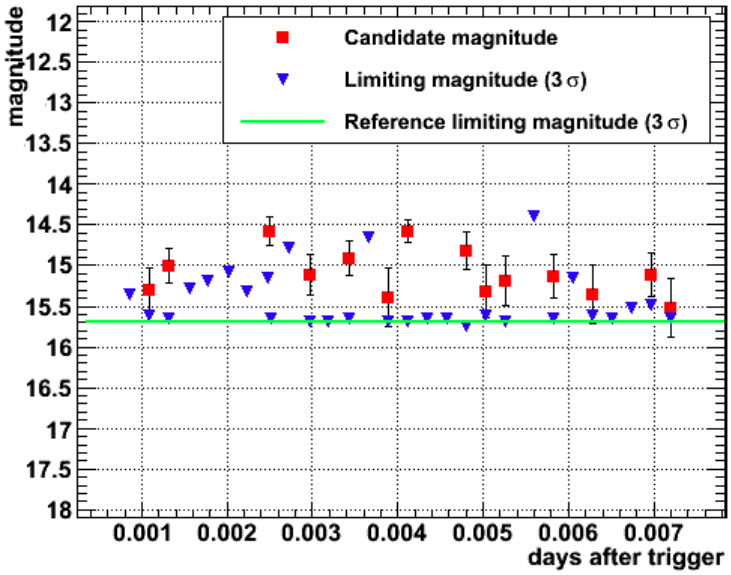

Figure 7.6: A candidate light curve using PSF-fit magnitudes.

7.4.1 Limiting magnitude definition

The ROTSE and adapted SNLS pipeline definition of the limiting magnitude is different. Basically, the ROTSE pipeline gives a limiting magnitude defined as the magnitude of the 90th percentile source extracted above 1 unit of background standard deviation, while the

adapted SNLS pipeline gives a limiting magnitude as the mean value of the magnitudes of sources extracted above a threshold of 3 units of background standard deviation.

When calculating the limiting magnitude on the same set of images, a difference up to one magnitude was noticed between the pipelines. In order to give coherent values of limiting magnitudes, two steps were verified :

- The source extraction parameters : the ROTSE pipeline convolves the image with a gaussian filter of 2×2 pixels in each 3×3 pixel area before extracting sources above SNR=1. The SNLS pipeline simply extracts sources above a threshold of SNR=3 without using a filter. The fact that these two methods give different sensitivities to the faintest sources, it may lead to an incoherence in the limiting magnitude value.

- Photometric calibration : Both pipelines use a calibration with USNO-A2 catalog as well as a 3^{rd}-order polynomial warping to convert image coordinates to celestial coordinates. However, the ROTSE pipeline makes a selection of the brightest and redder stars to use in the calibration step, because its operating clear filter is closer to the red passband. This "color correction" can induce a difference in the measured magnitudes.

The main difference may come from the first point, so a common definition was adopted. Sources are extracted without the use of a filter, and we require that the photometric error (aperture photometry error) of the extracted sources should be equivalent to 0.300 ± 0.015 mag [1]. Figure 7.7(a) shows the distribution of the extracted sources from a typical image in the Magnitude-Error on magnitude plane. The signal at threshold can be expressed as $S = k.\sigma$, where σ is the sky background standard deviation. The SNR is thus equivalent to $S/N = k.\sigma/\sigma = k$. From equation 6.8, requiring an error of 0.3 mag on the source magnitude is equivalent to a magnitude defined at 3σ level. In a typical image, this leads to few hundreds of sources. The mean value of the magnitude distribution of the selected sources at 3 sigma level is taken as the limiting magnitude of the image. An example is shown on figure 7.7(b).

To test the latter point, checks on the photometric calibration were undertaken by comparing the zero-point offset values for a set of images. The difference is found to be within the systematic error of 0.3 mag induced by the calibration using USNO stars (see discussion in section 6.4).

With this common definition, the discrepancy is reduced down to ~ 0.3 mag between the photometric results outputs from the pipelines.

7.4.2 Results

Upper limits on transient source magnitudes at early times after a HE neutrino detection in ANTARES

The results on the magnitude upper limits are calculated either using the first image analyzed in case of individual frames analysis or considering the first co-added frame in the corresponding analysis as described in table 7.6. When different analysis on the same alert data were conducted, the best limiting magnitude was chosen (limiting magnitudes of an 8 image co-add in the cases of ANT100725 and ANT100922 alerts).

The limiting magnitudes are further corrected from Galactic extinction causing magnitudes to be dimmer and redder by the effect of Galactic dust. Figure 7.8 shows the A_v

[1] The window was optimized to extract around one hundred sources from a typical image.

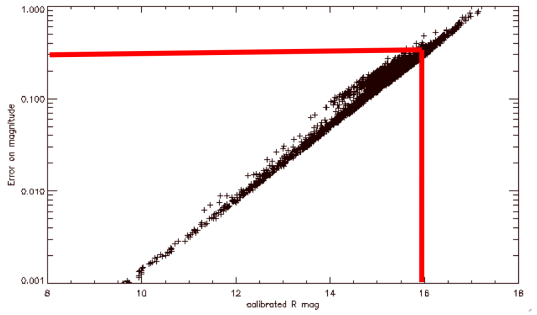

(a) Source distribution as a function of the magnitude and its associated error.

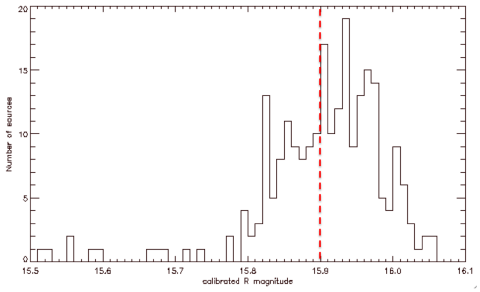

(b) Magnitude distribution of sources defined selected 3 σ level above the sky background. The red line represents the mean value of the distribution.

Figure 7.7: Illustration of the limiting magnitude calculation for alert ANT100922A.

extinction dependence on Galactic latitude[90]. We used the Schlegel et al. [108] maps to calculate the extinction from the NED database [1]. Alert ANT110409 image sequence highly suffered from galactic extinction since it is lying at a galactic latitude of 0.6 which reduced the limiting magnitude by $\sim$ 6 magnitudes.

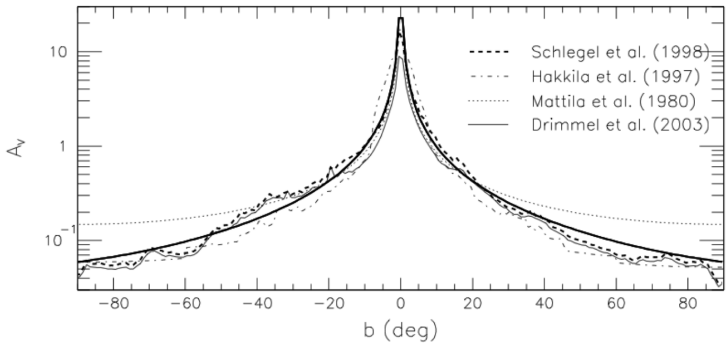

Figure 7.8: Extinction dependence on Galactic latitude.

The results for each alert are shown in table 7.7. The time since trigger is referred to as the time of the first image considered in the analysis. The limiting magnitudes shown are corrected from the Galactic extinctions A_v (mag).

An example case: GRB-like optical signal detection probability

As an example of a candidate source, the optical detection probability of a GRB -like signal which could be associated to the neutrino trigger is calculated. The detection probability would help to assess TAToO capabilities in detecting a GRB-like signal using the upper limits on magnitude found in the analysis. This upper limit probability on GRB detection is presented for each alert. Because no optical counterpart is found over the course of the program, the probability that the detected neutrinos have an origin different from GRB neutrinos is derived.

[1] `http://ned.ipac.caltech.edu/forms/calculator.html`

Alert name	time since trigger (days)	A_v (mag)	Corrected 3-σ M_{lim} (mag)
ANT100123	0.64	0.2	12.9 ±0.1
ANT100302	1.01	0.2	15.4 ±0.1
ANT100725	8.7 10^{-4}	0.3	15.2 ±0.3
ANT100922	4.7 10^{-2}	0.5	15.4 ±0.1
ANT101211	0.50	0.1	15.0 ±0.1
ANT110409	3.0 10^{-3}	5.9	13.0 ±0.3
ANT110529	5.2 10^{-3}	1.1	15.1 ±0.3
ANT110613	7.8 10^{-4}	1.4	16.2 ±0.3

Table 7.7: 3-σ upper limits on transient sources magnitude from early time optical follow-up of HE neutrino detected by ANTARES with its associated photometric errors. The Galactic extinction values have been taken into account in the final results.

Neutrino-photon timing considerations Models predict a neutrino emission expected in three phases of non-thermal processes; (i) Precursor neutrinos emitted at $\sim$ -10/-100 s before the gamma-burst [102], (ii) prompt neutrinos expected at the same time as the prompt gamma-ray emission[103], *i.e* in a time window of $\sim$0/T90, T90 being the duration of the gamma-ray burst[1], and (iii) Afterglow neutrinos which are emitted after the prompt gammas[103], *i.e* at times greater than T90. Figure 7.9 shows the different neutrino production scenarii during the three different phases of a GRB. The corresponding electromagnetic output is indicated schematically in the upper panels.

The optimized HE filter is around 90% efficient for the detection of prompt GRB neutrinos as found in chapter 5. As the filter selects events around 5 TeV mean energy, it is still adapted, however much less efficiently, to the detection of precursor neutrinos where the environment is still optically thick for gamma-ray emission. Afterglow neutrinos are very highly energetic and are unlikely to be detected by ANTARES due to the very low expected fluxes, so the two first scenarii are those which offer better detection prospects in ANTARES.

Upper limit probabilities on GRB afterglow detection per alert Since no optical counterpart was found, we want to derive the probability that GRB afterglow-like signals could be detected given our limits $p_{GRB}(M_{limit},T_{response})$, where M_{limit} is the limiting magnitude and $T_{response}$ is the neutrino-optical response delay.

Figure 7.10 shows 79 light curves from a large sample from *Swift* GRB afterglows up to September 2009, taken from Kann et al. 2010 [72]. This population includes fast decaying afterglows [2] ($\alpha \sim$ 1.5-2), slow decay afterglows ($\alpha \sim 1$) and plateau afterglows ($\alpha \sim$ 0-0.4) followed by a decay. The population also includes special afterglows like the prompt optical flash of the "naked-eye" GRB 080319B (z = 0.9371), which is the most luminous GRB ever detected at early times, it lies several magnitudes above all other afterglows. At late times, 030329 (z = 0.1685) remains brighter than any other afterglow discovered since. It is one of the closest GRB ever known which possibly explains the exceptional brightness of this afterglow.

The optical counterpart of these GRBs was detected upon a Gamma-ray satellite trigger [3]. The afterglows are corrected for galactic extinction using Schlegel et al. [108] maps.

[1] An average value of the burst duration T90 is $\sim$ 30s

[2] The GRB light curve is generally fitted by a power low; Flux $\propto t^{-\alpha}$. See discussion in section 4.1.2.

[3] Except for GRB 080319B where wide-field sky monitors were observing GRB 080319A which happened

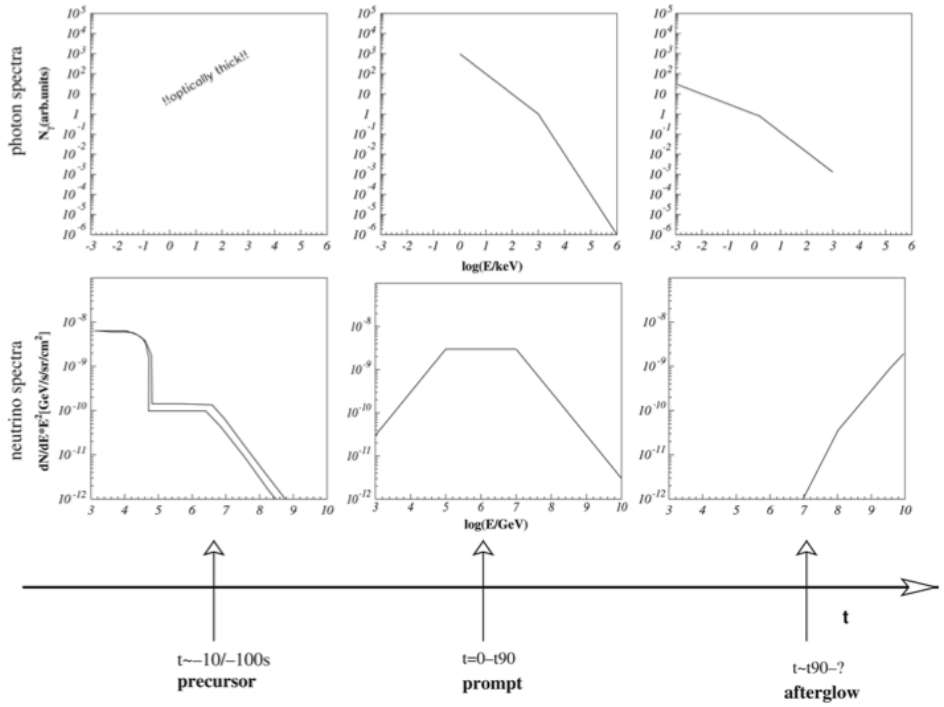

Figure 7.9: Overview of different neutrino production scenarios during the three different phases of a GRB. The corresponding electromagnetic output is indicated schematically as well, from [35].

In the scenario where the neutrino would be contemporaneous with Gamma rays, the detection probability of GRBs associated to a prompt neutrino emission can be derived. Considering a 20 mn time window in which the transient signal was actually investigated (typical image sequence length), we used the light curves from [72] to retrieve the number of GRBs lying above the telescope limiting magnitude for each response to a neutrino alert. The probability is calculated as the fraction of GRBs bright enough to be detected over all GRBs in the same time window.

GRB-like detection probability associated to each alert is reported in table 7.8

Alert name	GRB afterglow detection probability (%)
ANT100123	0
ANT100302	0
ANT100725	40
ANT100922	2
ANT101211	2
ANT110409	10
ANT110529	23
ANT110613	55

Table 7.8: Detection probability per alert of GRBs in the scenario where the gamma prompt emission is accompanied by a neutrino emission.

just 27 minutes earlier and 14° away on the sky, it was thus observed even before the gamma trigger.

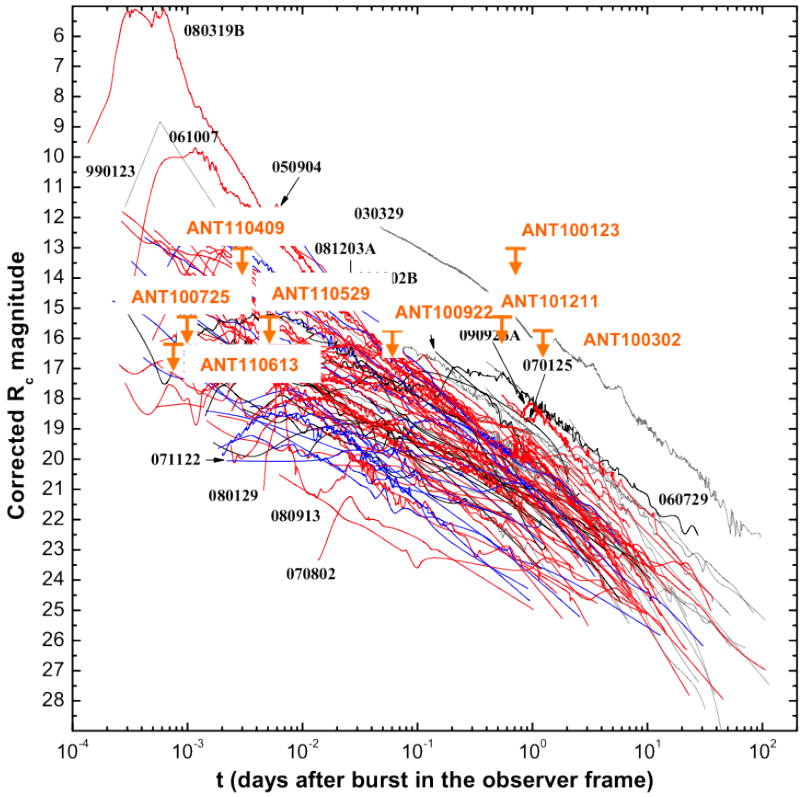

Figure 7.10: Optical light curves of 79 GRBs detected until 2010. The orange arrows indicate the limiting magnitudes of ROTSE and TAROT observations in response to the neutrino alerts. The time of the neutrino trigger is considered to be the same as the gamma ray trigger.

The following conclusions can be drawn :

- Time delays greater than 1 hour lead to a very low detection probability (2%-0%) with a magnitude upper limit of 15.4.
- Time delays within the minute give a maximal detection probability of 55% considering prompt neutrinos. Using the most precursor neutrinos in the models (t_{Gammas}-$t_{neutrino}$= 100 s), the corresponding detection probability remains unchanged. This suggests that with such time responses, in case of a positive optical counterpart detection, the follow-up program can test the neutrino emission from GRBs independently from the underlying model on neutrino timing. Because the time factor is satisfying for theses alerts (ANT110613A, ANT110409, ANT110529, ANT100725), the sensitivity to the GRB signal is constrained by the limiting magnitude only.

Are the detected neutrinos issued from GRBs ? We want to test the hypothesis that the neutrino is in fact a GRB neutrino. So far, we have assumed that the neutrino have a GRB origin *i.e* $p_{\nu_{GRB}} = 1$. Because no optical counterpart is discovered, the optical constraints would enable to exclude this hypothesis. The probability that the neutrinos detected by ANTARES over 1.5 year of data do not have a GRB origin would then be derived as $P_{1.5yr} = p_{\nu_{GRB}} \times p_{NoGRB}(M_{limit},T_{response}) = p_{\nu_{GRB}} \times (1 - p_{GRB}(M_{limit},T_{response}))$.

Minimized values of the latter term would exclude the hypothesis that the detected neutrinos were produced by GRBs. Using the values in table 7.8, the neutrinos detected by ANTARES are found not to be GRB products with 1.5 sigma confidence. This is not sufficient to reject the hypothesis with meaningful confidence.
The technical challenge of a rapid follow-up is fulfilled successfully for $\sim 50\%$ of the alerts by responding within the minute after the neutrino trigger. In the particular case of GRBs, the detection probabilities are maximized when the response is fast and conditions on the limiting magnitude are less strict than for later responses.

7.5 Future plans for early time observation enhancement in TAToO

With the same performances as achieved up to now, 4 years (9 years) are necessary to reject the hypothesis on the GRB neutrino origin with 3(5) sigma confidence. This is far too much from our needs within a reasonable time. If we had 8 ANT100613-like responses during this 1.5 yr data, we could already reach a 3-sigma rejection probability for GRB-like signals. It is therefore necessary to optimize the systematic time response quality for the future to reach at least ANT110613 quality. Since the telescopes are based on a priority system and the image acquisition is strongly dependent on the atmospheric conditions which can cancel a prompt observation, there is little hope that the time response would get any better from the telescope side. However, the sensitivity can be improved by redefining the observation strategy. Recently, the image sequence strategy for prompt observation with TAROT has been modified to acquire a first sequence of 6 images upon the alert reception, followed by a second sequence 30 mn later and a third sequence 1 h later with an exposure time of 180 s. ROTSE telescope have not responded to any alert in 2011 and the complete system will probably be stopped in September 2012. A solution would be adding other fast response telescopes in the network. Figure 7.11 shows the map of robotic telescopes in the world (in operation, being commissioned, under construction). The choice among the Southern hemisphere telescopes is reduced. Moreover, the 2-m telescope class can not be used in the follow-up because of the their small FOV (few arcminutes).

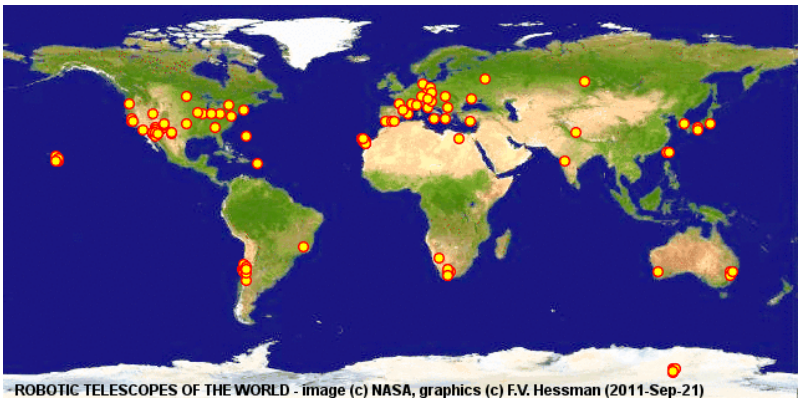

Figure 7.11: Robotic optical telescopes in the world, from `http://www.uni-sw.gwdg.de/~hessman/MONET/links.html`.

The 0.6 m robotic BOOTES-III telescope in New-Zealand (Burst Observer and Optical

Transient Exploring System) [1] can be an alternative.

If by multiplying the telescopes in TAToO network, a fast response could be acquired for 25 alerts with the quality of ANT110613, the hypothesis could already be rejected with 5 sigma confidence.

It is however ambitious to believe that prompt observations on minute time scale response to the neutrino trigger would systematically lead to the required sensitivity, even when increasing the number of acquired images. It can be seen on figure 7.10 that time delays of hours can still offer an opportunity for GRB detection (ANT100922) if the limiting magnitude is enhanced down to 20-22 mag. Small robotic telescopes can not offer such a sensitivity.

For this purpose, the 1-m class ZADKO [2] telescope recently joined the optical network. Because of its limited field-of-view comparing to the average error on the neutrino direction ($\sim 0.5^\circ$), tiling would be necessary.

Since a good limiting magnitude would however spare the requirement on the minute scale follow-up, bigger telescopes responding few hours after the neutrino trigger would be needed to reach sensitively better limiting magnitudes. Other 1-m class telescopes like PTF[83] or Sky Mapper [75] are also good candidates, but the availability of these telescopes is limited due to survey programs. In addition, it is planned to implement an X-ray follow-up of the 6 most interesting neutrino candidates of the year. The refined position of the events with high threshold on the amplitude and the number of hits used in the reconstruction would be sent to *SWIFT* satellite (XRT instrument). The detection of an X-ray counterpart is very promising since the rate of X-ray counterparts detected is 50% more important than optical counterparts.

[1] `http://www.laeff.cab.inta-csic.es/BOOTES/ing/index.html`

[2] `http://www.zt.science.uwa.edu.au/`

Summary and outlook

The work presented in this thesis is among the first attempts to ally an on-line neutrino information with a probable electromagnetic counterpart in ANTARES. As an introduction to the most debated questions in the astrophysics domain, the first chapter depicts the general context in which neutrino science evolves and what questions it is expected to resolve. The technical challenges of an implementation of a neutrino detector as well as the performances which it is expected to deliver are described in the second chapter.
The photomultipliers being the "eyes" of the neutrino detector, are a fundamental aspect in the neutrino detection success. Chapter 3 focuses on the development of a hybrid photomultiplier, based on a revisited concept of crystal-based photomultipliers. In this thesis, the realization and characterization of the first hemispherical hybrid photomultiplier were undertaken. The realization of the prototypes was done in Photonis factory where the prototypes manufacture was supervised step-by-step, first after the suggestion of a larger photocathode spread (60°) and second, with the test of a thinned LYSO crystal in the photomultiplier. A test bench was implemented in CPPM to test the prototypes. While Photonis photomultiplier activity has ceased in end of 2009, and the hybrid photomultiplier R&D activity was consequently abandoned, the test bench was used as a characterization facility in CPPM for other PMT tests and the hybrid concept can be exploited in the future by other PMT companies on industrial production scales.

The third part of the thesis focuses on the realization of an optical follow-up program in ANTARES. The first step in this work was to find the appropriate filter to send the highest energy events in ANTARES, described in chapter 5. The filter was optimized to reject the atmospheric muon background efficiently and resulted in more than 99% purity. The optimization from year to year took advantage of the updates on track reconstruction tools available in ANTARES. The performances on the HE filter for GRB signals and CCSNe in the frame of various models were tested. While the HE filter selects GRB events efficiently, the performances are poor assuming CCSNe signal. This is intended to be upgraded in the future with the implementation of the "directional" trigger. The second step in the follow-up program was the implementation of an appropriate image analysis method and strategy, depicted in chapter 6. The ROTSE pipeline was implemented and each step was explicated in a comprehensible analysis manual, made available for the TAToO group. The inclusion of an independent analysis pipeline adapted from the SNLS image subtraction program was also studied, and the pipelines were compared to give coherent results from TAROT and ROTSE images.

Finally, alerts over 1.5 year of data were analyzed. No optical counterpart was discovered, hence 3 σ upper limits on the magnitude of transient sources with an optical counterpart associated to the neutrino alert were obtained. When these upper limits are used to test the GRB-like signal detection prospects, it is found that a follow-up within a minute time scale can test the model of neutrinos precursor or contemporaneous to gamma-rays. This was realized with a good sensitivity for 4 alerts over a total of 8. The next

challenge is thus to make this fast response more systematic, inevitably by adding more fast-response telescopes in the network. Furthermore, it has been found that due to the lack of prompt observations, especially in 2011 from ROTSE telescopes, and that about half of the first acquired images lye at hours after the neutrino trigger, the hypothesis that the detected ANTARES neutrinos are from a GRB origin could only be excluded at 1.5 σ confidence. Future solutions to achieve better detection prospects are given at the end of chapter 7.

Multi-messenger astronomy with neutrinos is a young and a certainly promising detection alternative. Besides the neutrino-electromagnetic follow-up programs running efficiently in ANTARES and Ice Cube, which plan to further extend their field of research to the radio wavelengths, the coupling of a neutrino detection with gravitational waves would also give important constraints on the physics inside the most energetic sources in the Universe. In this sense, the project AMON (the Astrophysical Multimessenger Observatory Network) [1] is intended to gather all these messengers in a single framework by implementing a follow-up of most interesting events in Auger, Fermi, HAWC, IceCube, LIGO, Swift, ANTARES.. and trigger observations in X-ray, optical and radio wavelengths. Correlating high energy astrophysical signals across all known possible astronomical messengers would shed a new and unified vision on the most violent and powerful phenomena occurring in the Universe.

[1] `http://amon.gravity.psu.edu`

Appendices

Appendix A

Alert list

This annex presents the neutrino alerts successfully sent to the optical network since January 2009. The neutrino alert information is presented in a table format with the following information:

- Amplitude: The amplitude of an event is given in number of photoelectrons.
- Nhit: The number of hits used in the fit is the number of storeys touched by the photons emitted by the muon event.
- Nline: The number of lines used in the fit.
- Q: The reduced fit quality as described in section 5.1.2.
- $\Delta_{online-offline}(^{\circ})$: The angular difference in muon directions given by the on-line reconstruction and the off-line reconstruction algorithms.
- Number of observations: The number of nights with optical acquisitions. The symbol (T) is for TAROT telescopes observations and (R) for ROTSE telescopes observations.

The alerts written in bold characters are those which had a prompt observation (within 1 day from the neutrino alert) and were analyzed in search for a transient signal.

Date	Amplitude	Nhits	Nline	Q	$\Delta_{online-offline}(^\circ)$	Number of observations
13 Jan 09	91	14	3	0.8	0.6	0
16 Jan 09	260	36	7	1.2	0.3	0
19 Jan 09	167	33	4	1.2	0.4	0
27 Jun 09	170	33	4	1.0	0.3	0
18 Sep 09	80	21	3	1.1	7.1	0
07 Oct 09	122	31	4	1.4	7.2	0
10 Oct 09	168	16	3	1.4	34	3 (T)
10 Oct 09	96	22	5	2.7	25	4 (T)
23 Oct 09	78	18	3	1.3	1.5	1 (T)
23 Oct 09	83	17	3	1.5	9.2	1 (T)
06 Nov 09	113	22	3	1.6	14	0
09 Nov 09	151	27	4	2.5	1.7	0
09 Nov 09	121	19	3	0.6	0.3	0
08 Dec 09	207	23	5	3.2	NA	0
14 Dec 09	296	28	5	2.3	NA	9 (T)

Table A.1: 2009 HE alerts

Date	Amplitude	Nhits	Nline	Q	$\Delta_{online-offline}(^\circ)$	Number of observations
07 Jan 10	298	44	5	2.6	0.7	0
16 Jan 10	154	19	3	1.2	0.9	5 (T)
22 Jan 10	173	19	3	0.6	0.7	7 (T)
23 Jan 10	**340**	**34**	**4**	**1.4**	**0.7**	**9 (T)**
02 Mar 10	**200**	**26**	**4**	**1.0**	**0.5**	**3 (T), 11 (R)**
06 Jul 10	506	44	5	2.6	1.8	8 (T), 5 (R)
25 Jul 10	**66**	**12**	**3**	**1.3**	**60**	**9 (T), 10 (R)**
13 Sep 10	277	46	5	2.0	0.7	1 (T), 10 (R)
22 Sep 10	**158**	**19**	**3**	**1.2**	**0.25**	**13 (R)**
07 Dec 10	1080	114	9	14.6	88	0
11 Dec 10	**309**	**20**	**4**	**1.6**	**6.1**	**11 (R)**
29 Dec 10	205	48	10	2.9	0.1	3 (T)

Table A.2: 2010 HE alerts

Date	Amplitude	Nhits	Nline	Q	$\Delta_{online-offline}(^\circ)$	Number of observations
02 Feb 11	300	33	8	1.4	0.82	0
05 Mar 11	194	27	8	1.98	0.64	1 (T), 1(R)
08 Mar 11	77	20	7	1.14	0.1	5 (T), 5 (R)
11 Mar 11	453	46	10	3.7	4.5	1 (T)
22 Mar 11	93	20	7	0.6	0.2	3 (T)
24 Mar 11	116	31	9	2.3	0.1	3 (T)
09 Apr 11	**253**	**21**	**8**	**1.24**	**0.1**	**10 (T)**
28 Apr 11	114	24	4	1.40	0.3	10 (T)
21 May 11	134	27	4	1.59	1.5	10(T), 3 (R)
29 May 11	**165**	**20**	**3**	**0.57**	**0.4**	**8 (T)**
31 May 11	439	54	5	4.82	28	10(T), 6 (R)
13 Jun 11	**181**	**21**	**3**	**1.28**	**24**	**6(T)**
15 Jun 11	224	24	3	1.64	8.3	9(T), 13(R)

Table A.3: 2011 HE alerts

Appendix B

Neutrino data of the optically analyzed alerts

This annex shows the reconstruction of events which triggered a successful optical observation within one day from the neutrino alert. The following figures represent the fit of the event direction on each detector line. The abscissa axis represents the time and the ordinate axis represents the depth in meters. The upper right corner of each figure shows the run number of the event as well as the frame index. It also shows the trigger logic which was used during data taking.

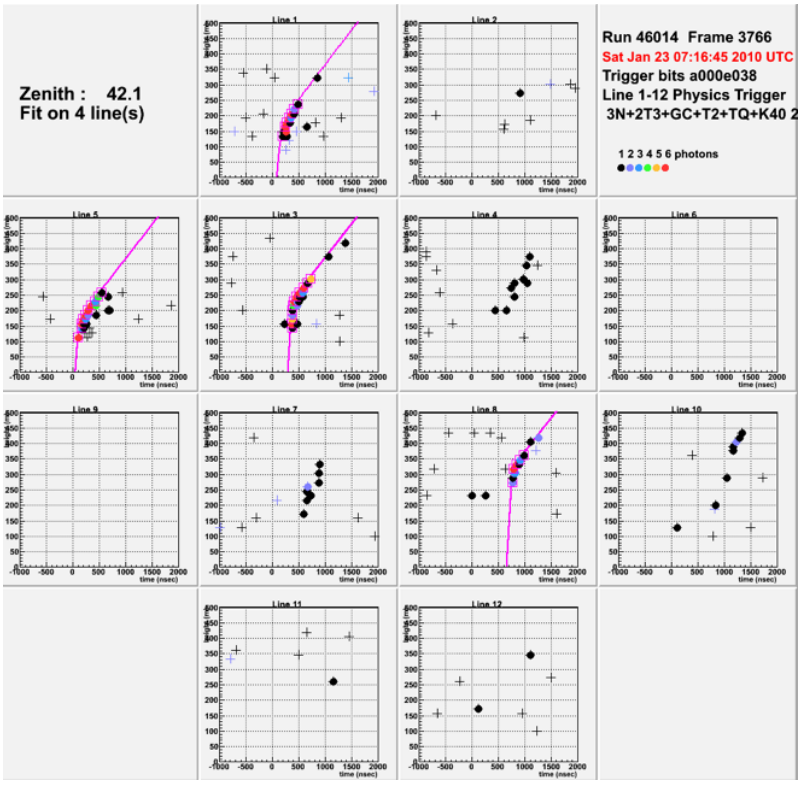

Figure B.1: Alert ANT100123

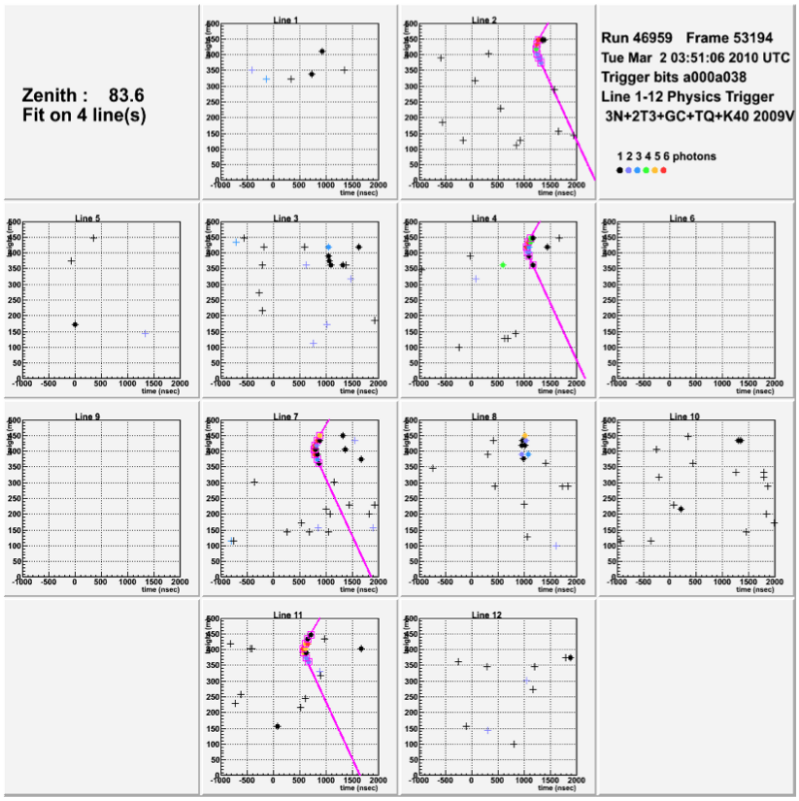

Figure B.2: Alert ANT100302

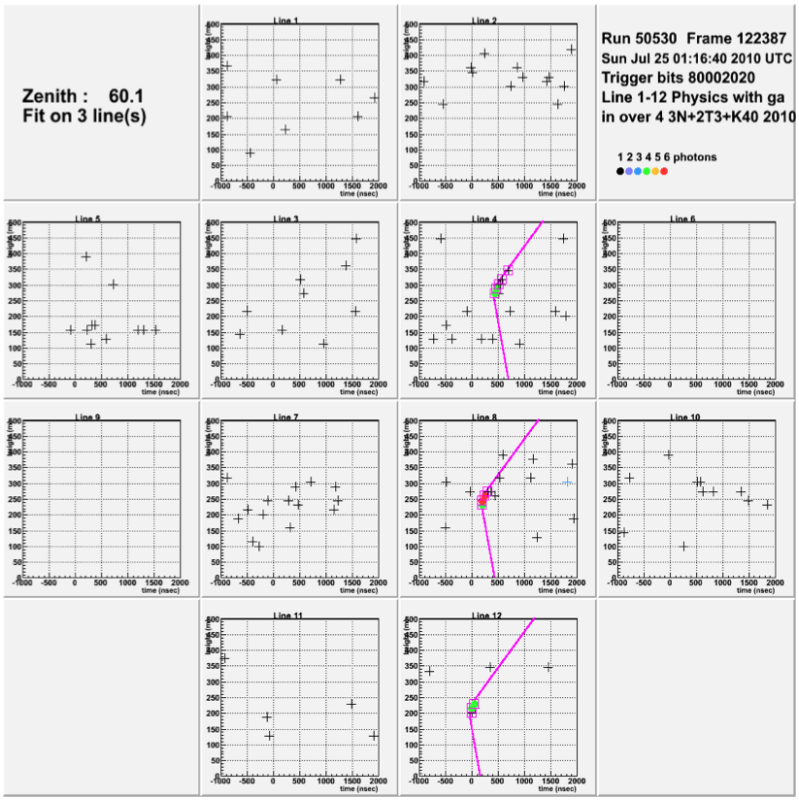

Figure B.3: Alert ANT100725

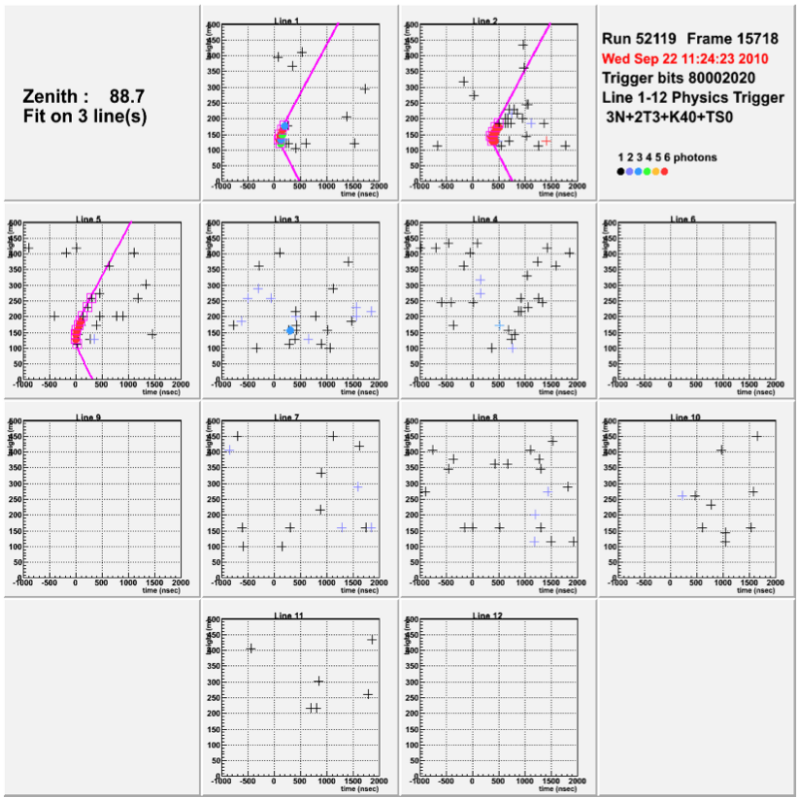

Figure B.4: Alert ANT100922

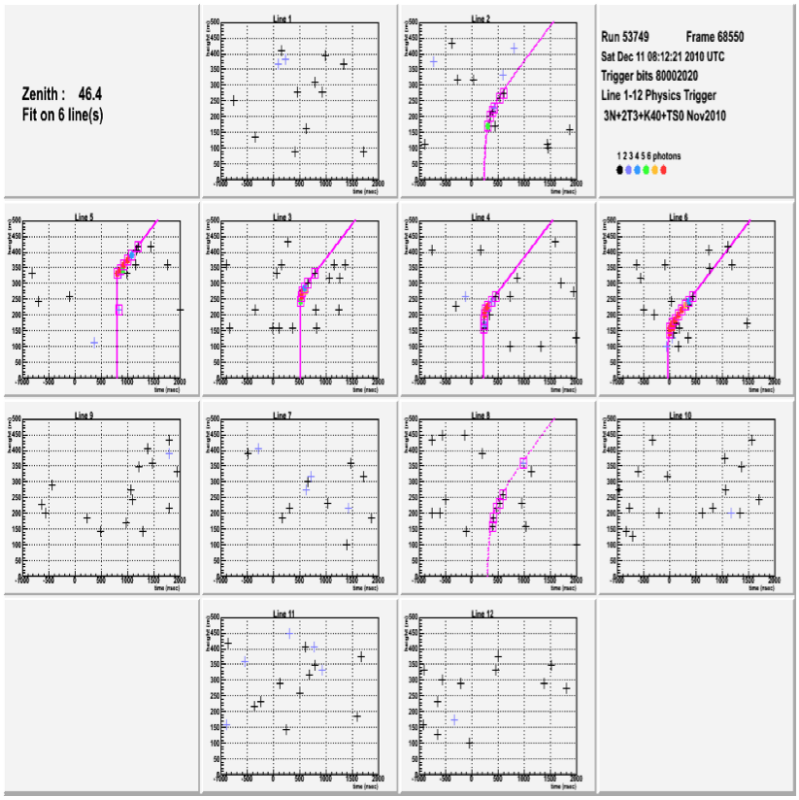

Figure B.5: Alert ANT101211

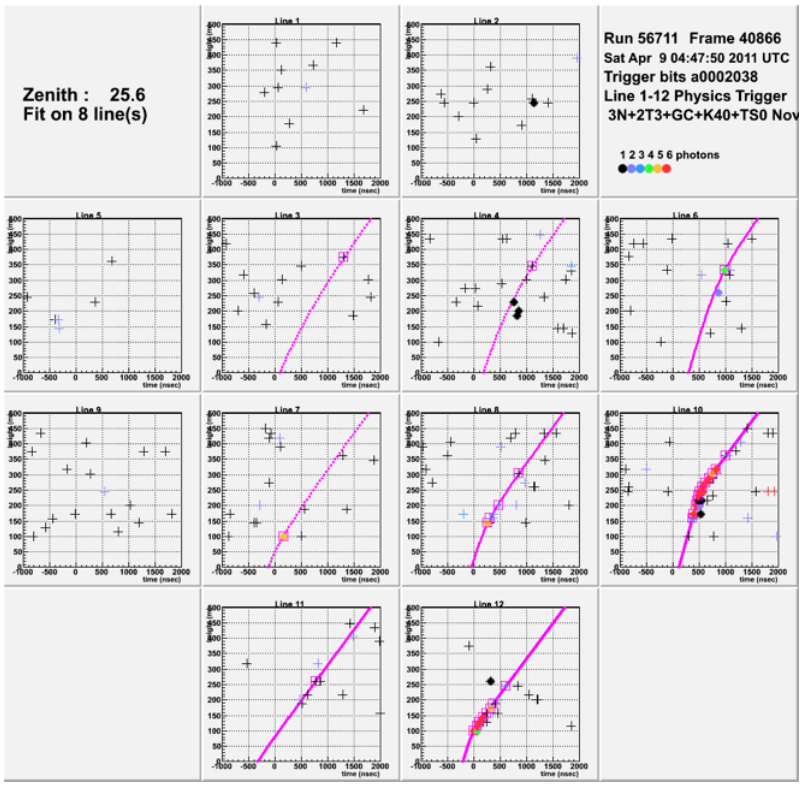

Figure B.6: Alert ANT110409

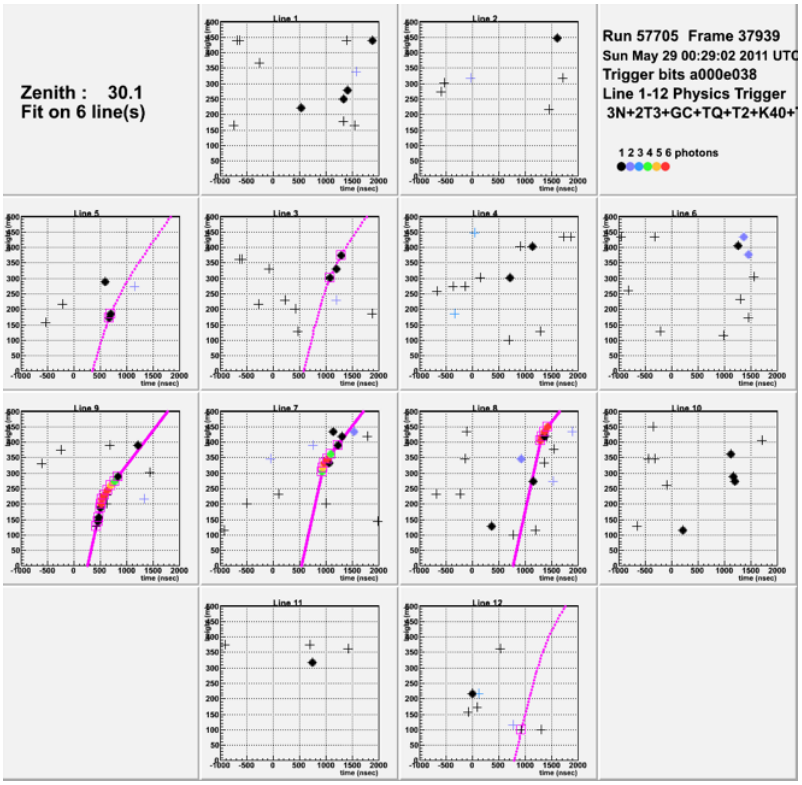

Figure B.7: Alert ANT110529

Bibliography

[1] K. N. Abazajian et al. (SDSS). «The Seventh Data Release of the Sloan Digital Sky Survey». *Astrophys J Suppl* 182:543–558, 2009. 0812.0649, URL http://arxiv.org/abs/0812.0649.

[2] A. A. Abdo and Fermi LAT Collaboration. «Observations of the young supernova remnant RX J1713.7- 3946 with the Fermi Large Area Telescope». *Astrophys J* 734:28, 2011. URL http://arxiv.org/pdf/1103.5727v1.

[3] A. A. Abdo, et al. «TeV gamma-ray sources from a survey of the Galactic plane with Milagro». *Astrophysical Journal* 664(2, Part 2):L91–L94, 2007.

[4] J. Abraham, et al. «Correlation of the highest-energy cosmic rays with the positions of nearby active galactic nuclei». *Astroparticle Physics* 29(3):188–204, 2008.

[5] M. Ageron, et al. «The ANTARES Telescope Neutrino Alert System» 2011. URL http://www.citebase.org/abstract?id=oai:arXiv.org:1103.4477.

[6] J. Aguilar, et al. «Study of large hemispherical photomultiplier tubes for the ANTARES neutrino telescope». *Nuclear Instruments and Methods in Physics Research Section A: Accelerators, Spectrometers, Detectors and Associated Equipment* 555(1-2):132 – 141, 2005. URL http://www.sciencedirect.com/science/article/pii/S016890020501836X.

[7] J. Aguilar, et al. «Transmission of light in deep sea water at the site of the ANTARES neutrino telescope». *Astroparticle Physics* 23(1):131–155, 2005.

[8] J. Aguilar, et al. «A fast algorithm for muon track reconstruction and its application to the ANTARES neutrino telescope». *Astroparticle Physics* 34(9):652 – 662, 2011. URL http://www.sciencedirect.com/science/article/pii/S0927650511000053.

[9] J. A. Aguilar, et al. «The data acquisition system for the ANTARES neutrino telescope». *Nuclear Instruments & Methods In Physics Research Section A-Accelerators Spectrometers Detectors And Associated Equipment* 570(1):107–116, 2007.

[10] C. Akerlof, et al. «The ROTSE-III robotic telescope system». *Publications Of The Astronomical Society Of The Pacific* 115(803):132–140, 2003.

[11] B. Al Ali, et al. «Luminous bacteria in the deep-sea waters near the ANTARES underwater neutrino telescope (Mediterranean Sea)». *Chemistry And Ecology* 26(1):57–72, 2010.

[12] I. Al Samarai, et al. «Development of scintillating crystal hybrid photon detectors for the KM3NeT (km^3-scale) deep-sea neutrino telescope». *Nuclear Instruments and Methods in Physics Research A* 610:262–266, 2009.

[13] I. Al Samarai, et al. «Scintillator-based hybrid photon detector development for the KM3NeT (km-scale) deep sea neutrino telescope». *Nuclear Instruments and Methods in Physics Research A* 602:197–200, 2009.

[14] C. Alard and R. H. Lupton. «A Method for Optimal Image Subtraction». *The Astrophysical Journal* 503(1):325, 1998. URL `http://stacks.iop.org/0004-637X/503/i=1/a=325`.

[15] D. Allard, E. Parizot, and A. Olinto. «On the transition from galactic to extragalactic cosmic-rays: Spectral and composition features from two opposite scenarios». *Astroparticle Physics* 27(1):61 – 75, 2007. URL `http://www.sciencedirect.com/science/article/B6TJ1-4M4TM03-1/2/3ecc3059fa8970d2230c9b5771e00be9`.

[16] R. Aloisio, V. Berezinsky, and S. Grigorieva. «Analytic calculations of the spectra of ultra-high energy cosmic ray nuclei. I. The case of CMB radiation», 2008. URL `http://www.citebase.org/abstract?id=oai:arXiv.org:0802.4452`.

[17] J. Alvarez-Muniz and F. Halzen. «Possible High-energy neutrinos from the cosmic accelerator RXJ1713.7-3946». *The Astrophysical Journal* 576:L33, 2002. URL `doi:10.1086/342978`.

[18] P. Amram, et al. «Background light in potential sites for the ANTARES undersea neutrino telescope». *Astroparticle Physics* 13(2-3):127–136, 2000.

[19] P. Amram, et al. «The ANTARES optical module». *Nuclear Instruments & Methods In Physics Research Section A-Accelerators Spectrometers Detectors And Associated Equipment* 484(1-3):369–383, 2002.

[20] P. Amram, et al. «Sedimentation and fouling of optical surfaces at the ANTARES site». *Astroparticle Physics* 19(2):253–267, 2003.

[21] C. Amsler and Particle Data Group. «Review of particle physics» 667:1, 2008. URL `http://www.citebase.org/abstract?id=oai:eprints.soton.ac.uk:56968`.

[22] S. Ando. «Detection of Neutrinos from Supernovae in Nearby Galaxies». *PhysRevLett* 95, 2005.

[23] S. Ando and J. Beacom. «Revealing the supernova-gamma-ray burst connection with TeV neutrinos». *Physical Review Letters* 95(6), 2005. URL `http://arxiv.org/pdf/astro-ph/0502521`.

[24] M. Anghinolfi. Tech. Rep., ANTARES-OPMO-2008-001, 2008.

[25] ANTARES collaboration. «A Deep Sea Telescope for High Energy Neutrinos» 1999. URL `http://www.citebase.org/abstract?id=oai:arXiv.org:astro-ph/9907432`.

[26] T. Antoni, et al. «KASCADE measurements of energy spectra for elemental groups of cosmic rays: Results and open problems». *Astroparticle Physics* 24(1-2):1–25, 2005.

[27] M. Ardid. «Positioning system of the ANTARES neutrino telescope». *Nuclear Instruments & Methods In Physics Research Section A-Accelerators Spectrometers Detectors And Associated Equipment* 602(1):174–176, 2009. 3rd International Workshop on a Very Large Volume Neutrino Telescope for the Mediterranean Sea, Toulon, FRANCE, APR 22-24, 2008.

[28] G. Askaryan. «Effects of the gradient of a strong electromagnetic beam on electrons and atoms». *Soviet Physics Jetp-Ussr* 15(6):1088–1090, 1962.

[29] R. I. Bagduev. «The optical module of the Baikal deep underwater neutrino telescope». *NUCLINSTRUMMETHA* 420:138, 1999. URL doi:10.1016/S0168-9002(98)01156-5.

[30] D. Band. «BATSE observations of gamma-ray burst spectra. I - Spectral diversity». *Astrophysical Journal* 413:281, 1993. URL http://articles.adsabs.harvard.edu//full/1993ApJ...413..281B/0000284.000.html.

[31] M. G. Baring, K. W. Ogilvie, D. C. Ellison, and R. Forsyth. «Acceleration of solar wind ions by oblique interplanetary shocks». *Advances in Space Research* 15(8-9):385 – 388, 1995. Proceedings of the D2.1 Symposium of COSPAR Scientific Commission D, URL http://www.sciencedirect.com/science/article/pii/027311779400121G.

[32] S. M. Barr. «Simple and predictive model for quark and lepton masses». *Phys Rev Lett* 64:353–356, 1990. URL http://link.aps.org/doi/10.1103/PhysRevLett.64.353.

[33] S. Basa. «Photomultipliers activity inside the ANTARES project». *Nuclear Instruments & Methods In Physics Research Section A-Accelerators Spectrometers Detectors And Associated Equipment* 442(1-3):91–98, 2000. 2nd International Conference on New Developments in Photodetection, BEAUNE, FRANCE, JUN 21-25, 1999.

[34] P. M. Bauleo and J. R. Martino. «The dawn of the particle astronomy era in ultra-high-energy cosmic rays». *NATURE* 458(7240):847–851, 2009.

[35] J. K. Becker. «High-energy neutrinos in the context of multimessenger physics», 2008. URL doi:10.1016/j.physrep.2007.10.006.

[36] V. Berezinsky. «Ultra High Energy Cosmic Rays». *NuclPhysProc* 70:419, 1999. URL http://www.citebase.org/abstract?id=oai:arXiv.org:hep-ph/9802351.

[37] A. Bersani. *Nucl Instr and Meth A* 602:213, 2009.

[38] E. Bertin and S. Arnouts. «SExtractor: Software for source extraction.» *aaps* 117:393–404, 1996.

[39] A. Bhadra. «Cosmic Rays from nearby Pulsars». In «29th International Cosmic Ray Conference Pune», 2005.

[40] P. Bhattacharjee and G. Sigl. «Origin and propagation of extremely high-energy cosmic rays». *Physics Reports-Review Section Of Physics Letters* 327(3-4):109–247, 2000.

[41] M. Bouwhuis and ANTARES Collaboration. «Increasing the detection efficiency for neutrinos from GRBs». *Nuovo Cimento Della Societa Italiana Di Fisica C-Geophysics And Space Physics* 28(4-5):805–808, 2005. 4th Workshop on Gamma-Ray Bursts in the Afterglow Era, Rome, ITALY, OCT 18-22, 2004.

[42] A. Braem, et al. «The X-HPD : conceptual study of a large spherical hybrid photodetector». *Nuclear Instruments and Methods in Physics Research A* 570:467–474, 2007.

[43] A. Braem, et al. «The X-HPD: Development of a large spherical hybrid photodetector». *Nuclear Instruments and Methods in Physics Research A* 581:469–472, 2007.

[44] A. Braem, et al. «Design, fabrication and characterization of an 8-in. X-HPD». *Nuclear Instruments and Methods in Physics Research A* 610:61–64, 2009.

[45] A. Braem, et al. «Design, fabrication and characterization of an 8-in. X-HPD». *Nuclear Instruments & Methods In Physics Research Section A-Accelerators Spectrometers Detectors And Associated Equipment* 610(1):61–64, 2009.

[46] J. Brunner. «The BBfit Reconstruction algorithm. ANTARES-SOFT-2009-003». Tech. Rep., ANTARES-SOFT-2009-003, 2009.

[47] E. Carmona and A. Collaboration. «Status report of the ANTARES neutrino telescope». *Nuclear Physics B-Proceedings Supplements* 95:161–164, 2001. 6th International Conference on Frontiers in Particle Astrophysics and Cosmology, SAN FELIU DE GUIXOLS, SPAIN, SEP 30-OCT 05, 2000.

[48] D. F. Cowen, A. Franckowiak, and M. Kowalski. «Estimating the explosion time of core-collapse supernovae from their optical light curves». *Astroparticle Physics* 33:19–23, 2010. 0901.4877.

[49] e. a. Dalal N. «The Difficulty in Using Orphan Afterglows to Measure Gamma-Ray Burst Beaming». *The Astrophysical Journal* 564:209–215, 2002.

[50] M. De Jong. Tech. Rep., ANTARES-SOFT-2009-001, 2009.

[51] D. Ellison, E. Berezhko, and M. Baring. «Nonlinear shock acceleration and photon emission in supernova remnants». *Astrophysical Journal* 540(1, Part 1):292–307, 2000.

[52] D. Fargion. «Air-shower spectroscopy at horizons». *Progress in Particle and Nuclear Physics* 57(1):384 – 393, 2006. International Workshop of Nuclear Physics 27th course - Neutrinos in Cosmology, in Astro, Particle and Nuclear Physics, URL http://www.sciencedirect.com/science/article/pii/S0146641005001262.

[53] E. Fermi. «On the Origin of the Cosmic Radiation». *Phys Rev* 75:1169–1174, 1949. URL http://link.aps.org/doi/10.1103/PhysRev.75.1169.

[54] S.-O. Flyckt and C. Marmonier. *Photomultiplier Tubes-Principles and Applications*. Photonis, 2002.

[55] A. Fukasawa. *Conference Record of IEEE Nuclear Science Symposium* 1:43, 2006.

[56] R. Gandhi. «Ultrahigh-energy neutrino interactions». *Astroparticle Physics* 5:81, 1996.

[57] A. P. W. Gorham, et al. «Observations of the Askaryan Effect in Ice». *PHYSREVLETT* 99:171101, 2007. URL doi:10.1103/PhysRevLett.99.171101.

[58] F. Halzen. «IceCube Science». *Journal of Physics: Conference Series* 171(1):012014, 2009. URL http://stacks.iop.org/1742-6596/171/i=1/a=012014.

[59] F. A. e. a. Harrison. «Optical and Radio Observations of the Afterglow from GRB 990510: Evidence for a Jet». *The Astrophysical Journal* 523:L121–L124, 1999.

[60] B. Hartmann. *Reconstruction of neutrino-induced hadronic and electromagnetic showers with the ANTARES experiment*. Ph.D. thesis, Erlangen University Germany, 2006.

[61] D. Heck. «Report FZKA 6019». Tech. Rep., Forschungszentrum Karlsruh, 1998.

[62] A. M. Hillas. «Cosmic rays: Recent progress and some current questions», 2006. astro-ph/0607109.

[63] J. Hinton. «The status of the HESS project». vol. 48, 331–337. 2004. 2nd VERITAS Symposium on TeV Astrophysics from Extragalactic Sources, Adler Planetarium & AStron Museum, Chicago, IL, APR 24-26, 2003.

[64] J. Hjorth. *Nature* 423:847, 2003.

[65] J. Horandel. *Astropart Phys* 19:193, 2003.

[66] S. B. Howell. «Two-dimensional aperture photometry - Signal-to-noise ratio of point-source observations and optimal data-extraction techniques». *Astronomical Society of the Pacific* 101, 1989. URL http://articles.adsabs.harvard.edu//full/1989PASP..101..616H/0000616.000.html.

[67] H. E. Iams and B. Salzberg. «The secondary emission phototube». *Proc IRE* Vol. 23:pp. 55–64.

[68] F. James and M. Roos. *Comput Phys Commun* 10:343, 1975.

[69] F. C. Jones and D. C. Ellison. «The plasma physics of shock acceleration». *Space Science Reviews* 58:259–346, 1991. 10.1007/BF01206003, URL http://dx.doi.org/10.1007/BF01206003.

[70] O. Kalekin. «Optical modules for the neutrino telescope KM3NeT». *Nuclear Instruments and Methods in Physics Research Section A: Accelerators, Spectrometers, Detectors and Associated Equipment* 623(1):312 – 315, 2010. 1st International Conference on Technology and Instrumentation in Particle Physics, URL http://www.sciencedirect.com/science/article/pii/S0168900210005176.

[71] N. Kalmykov and S. S. Ostapchenko. *Yad Fiz* 56:105, 1993.

[72] D. A. Kann. «The afterglows of swift-era gamma-ray bursts. i. comparing pre-swift and swift-era long/soft (type ii) grb optical afterglows». *The Astrophysical Journal* 720:1513 – 1558, 2010. URL http://iopscience.iop.org/0004-637X/720/2/1513/fulltext.

[73] A. Kappes and M. Kowalski. «Detecting GRBs with IceCube and follow-up observations». In «Proc. 30th Int. Cosmic Ray Conference», 2007. URL http://arxiv.org/pdf/0711.0353v1.

[74] I. D. Karachentsev, V. E. Karachentseva, W. K. Huchtmeier, and D. I. Makarov. «A Catalog of Neighboring Galaxies». *The Astronomical Journal* 127(4):2031, 2004. URL http://stacks.iop.org/1538-3881/127/i=4/a=2031.

[75] S. C. Keller, et al. «SkyMapper and the Southern Sky Survey» 2007. URL http://www.citebase.org/abstract?id=oai:arXiv.org:astro-ph/0702511.

[76] R. W. Klebesadel, I. B. Strong, and R. A. Olson. «Observations of Gamma-Ray Bursts of Cosmic Origin». *Astrophysical Journal* 182:L85, 1973.

[77] A. Klotz, F. Vachier, and M. Boer. «TAROT: Robotic observatories for gamma-ray bursts and other sources». *Astronomische Nachrichten* 329(3):275–277, 2008. Workshop on Hot-Wiring the Transient Universe, Tucson, AZ, JUN 04-07, 2007.

[78] G. F. Knoll. *Radiation Detection and Measurement 3rd ed.* P270, 1999.

[79] C. Kouveliotou. «BATSE results on observational properties of gamma-ray bursts». *The Astrophysical Journal Supplement Series* 92:637, 1994.

[80] M. Kowalski and A. Mohr. «Detecting neutrino transients with optical follow-up observations». *Astroparticle Physics* 27(6):533–538, 2007.

[81] R. Lahmann. «Status and first results of the acoustic detection test system AMADEUS». *Nuclear Instruments & Methods In Physics Research Section A-Accelerators Spectrometers Detectors And Associated Equipment* 604(1-2):S158–S163, 2009. 3rd International Workshop on Acoustic and Radio EeV Neutrino Detection Activities, Rome, ITALY, JUN 25-27, 2007-2008.

[82] A. U. Landolt. «UBVRI photometric standard stars in the magnitude range 11.5-16.0 around the celestial equator». *Astronomical Journal* 104:340–371, 1992.

[83] N. M. Law, et al. «The Palomar Transient Factory: System Overview, Performance, and First Results». *Publications of the Astronomical Society of the Pacific* 121:1395–1408, 2009. 0906.5350.

[84] J. G. Learned and K. Mannheim. *High-Energy Neutrino Astrophysics Annu Rev Part Sci* 50:679, 2000.

[85] M. Lemoine-Goumard, et al. «Morphological and spectral studies of the shell-type supernova remnants RX¬†J1713.7,Äì3946 and RX¬†J0852.0,Äì4622 with H.E.S.S.» *Astrophysics and Space Science* 309:379–384, 2007. 10.1007/s10509-007-9446-3, URL http://dx.doi.org/10.1007/s10509-007-9446-3.

[86] H. Lohner. *Nucl Instr and Meth A* 602:209, 2009.

[87] K. Mannheim. «Possible Production of High-Energy Gamma Rays from Proton Acceleration in the Extragalactic Radio Source Markarian 501». *Science* 279:684, 1998. URL doi:10.1126/science.279.5351.684.

[88] D. Manura and D. Dahl. *Simion 8 3-D electrostatic and charged particle trajectory simulation program*. Idaho National Laboratory, distributed by Scientific Instrument Services Inc., Ringoes, NJ, USA.

[89] C. Meegan, et al. «The spatial distribution of gamma-ray bursts observed by BATSE». *AIP Conference Proceedings* 280(1):681–685, 1993. URL `http://link.aip.org/link/?APC/280/681/1`.

[90] A.-L. Melchior, F. Combes, and A. Gould. «The surface brightness of the Galaxy at the solar neighbourhood». *Astronomy and Astrophysics* 462:965–976, 2007. `arXiv:astro-ph/0610884`.

[91] C. D. Mobley. «Light and Water (Radiation Transfer in Natural Water)». *Academic Press* 1994.

[92] D. Monet. «USNO-A2.0» 1998.

[93] D. G. Monet, et al. «The USNO-B Catalog». *The Astronomical Journal* 125(2):984, 2003. URL `http://stacks.iop.org/1538-3881/125/i=2/a=984`.

[94] T. Montaruli. Tech. Rep., ANTARES-SOFT-2004-010, 2004.

[95] W. Paciesas. «The fourth BATSE gamma-ray burst catalog (revised)». *Astrophysical Journal Supplement Series* 122:465, 1999. URL `http://arxiv.org/abs/astro-ph/9903205`.

[96] N. Palanque-Delabrouille. Tech. Rep., ANTARES-SITE-2004-001, 2004.

[97] T. Pradier. «Coincidences between gravitational wave interferometers and high energy neutrino telescopes». *Nuclear Instruments & Methods In Physics Research Section A-Accelerators Spectrometers Detectors And Associated Equipment* 602(1):268–274, 2009. 3rd International Workshop on a Very Large Volume Neutrino Telescope for the Mediterranean Sea, Toulon, FRANCE, APR 22-24, 2008.

[98] E. Presani. «Search for neutrinos from Gamma-Ray Bursts with ANTARES». *To appear in GRB 2010 Proceedings (AIP Publishing)* 2011.

[99] R. M. Quimby. *The Texas Supernova Search*. Ph.D. thesis, The University of Texas at Austin, 2006.

[100] R. M. Quimby, et al. «Early-Time Observations of the GRB 050319 Optical Transient». *The Astrophysical Journal* 640:402–406, 2006. `arXiv:astro-ph/0511421`.

[101] J. Rajchman and E. Pike. «Electrostatic Focusing in Secondary Emission Multipliers». *CA Technical Report TR-362* 1937.

[102] S. Razzaque, P. Meszaros, and E. Waxman. «High energy neutrinos from gamma-ray bursts with precursor supernovae». *Physical Review Letters* 90(24), 2003. URL `http://arxiv.org/pdf/astro-ph/0212536v3`.

[103] S. Razzaque, P. Meszaros, and E. Waxman. «Neutrino tomography of gamma ray bursts and massive stellar collapses». *Physical Review D* 68(8), 2003. URL `http://arxiv.org/abs/astro-ph/0303505`.

[104] S. Razzaque, P. Mészáros, and E. Waxman. «Erratum: TeV Neutrinos from Core Collapse Supernovae and Hypernovae [Phys. Rev. Lett. 93, 181101 (2004)]». *Phys Rev Lett* 94(10):109903, 2005. URL http://prl.aps.org/pdf/PRL/v94/i10/e109903.

[105] D. Richardson. «A comparative study of the absolute magnitude distributions of supernovae». *The Astronomical Journal* 123:745–752, 2002.

[106] E. S. Rykoff, et al. «A Search for Untriggered GRB Afterglows with ROTSE-III». *The Astrophysical Journal* 631(2):1032, 2005. URL http://stacks.iop.org/0004-637X/631/i=2/a=1032.

[107] R. SARI and T. PIRAN. «Hydrodynamic timescales and temporal structure of gamma-ray bursts». *Astrophysical Journal* 455(2, Part 2):L143–L146, 1995. URL http://arxiv.org/abs/astro-ph/9512125.

[108] D. J. Schlegel, D. P. Finkbeiner, and M. Davis. «Maps of Dust Infrared Emission for Use in Estimation of Reddening and Cosmic Microwave Background Radiation Foregrounds». *Astrophysical Journal* 500:525, 1998. arXiv:astro-ph/9710327.

[109] J. Schuller. «ANTARES: status report». *Nuclear Physics B - Proceedings Supplements* 150:177 – 180, 2006. Proceedings of the 9th Topical Seminar on Innovative Particle and Radiation Detectors, URL http://www.sciencedirect.com/science/article/pii/S0920563205008364.

[110] J. A. Simpson. «Elemental and Isotopic Composition of the Galactic Cosmic Rays». *Annual Review of Nuclear and Particle Science* 33(1):323–382, 1983. http://www.annualreviews.org/doi/pdf/10.1146/annurev.ns.33.120183.001543, URL http://www.annualreviews.org/doi/abs/10.1146/annurev.ns.33.120183.001543.

[111] M. F. Skrutskie, et al. «The Two Micron All Sky Survey (2MASS)». *Astrophysical Journal* 131:1163–1183, 2006.

[112] J. Slepian. *US Patent* 1:265,450, 1923(Filed 1919).

[113] K. Z. Stanek. *Astrophys J* 591:L17, 2003.

[114] P. STETSON. «Daophot - a computer-program for crowded-field stellar photometry». *Publications Of The Astronomical Society Of The Pacific* 99(613):191–222, 1987. URL http://articles.adsabs.harvard.edu/full/1987PASP...99..191S.

[115] N. R. Tanvir, et al. «A gamma-ray burst at a redshift of z approximate to 8.2». *Nature* 461(7268):1254–1257, 2009. URL http://dx.doi.org/10.1038/nature08459.

[116] The Fermi-LAT Collaboration. «Fermi Large Area Telescope First Source Catalog». *Astrophysical Journal Supplement Series* 2010.

[117] R. B. Tully. «Nearby Galaxies Catalogue (NBG) (Tully 1988)». *VizieR Online Data Catalog* 7145:0–+, 1994.

[118] M. Unger and for the Pierre Auger Collaboration. «Study of the Cosmic Ray Composition above 0.4 EeV using the Longitudinal Profiles of Showers observed at the Pierre Auger Observatory», 2007. URL http://www.citebase.org/abstract?id=oai:arXiv.org:0706.1495.

[119] Update of localized GRBs URL http://www.mpe.mpg.de/~jcg/grbgen.html.

[120] G. van Aller. *Helv Phys Acta 59* 1119, 1986.

[121] V. Van Elewyck and A. Collaboration. «Multi-messenger programs in ANTARES: Status and prospects». *Nuclear Instruments & Methods In Physics Research Section A-Accelerators Spectrometers Detectors And Associated Equipment* 626(S):S180–S182, 2011.

[122] D. Volpi, L. Del Zanna, E. Amato, and N. Bucciantini. «Non-thermal emission from relativistic MHD simulations of pulsar wind nebulae: from synchrotron to inverse Compton». *Astronomy & Astrophysics* 485(2):337–349, 2008.

[123] E. Waxman. «COSMOLOGICAL GAMMA RAY BURSTS AND THE HIGHEST ENERGY COSMIC RAYS». *PHYSREVLETT* 75:386, 1995. URL doi:10.1103/PhysRevLett.75.386.

[124] E. Waxman and J. Bahcall. «High energy neutrinos from astrophysical sources: An upper bound». *Physical Review D* 59(2), 1999. URL http://arxiv.org/pdf/hep-ph/9807282.

[125] T. Wibig and A. W. Wolfendale. «At what particle energy do extragalactic cosmic rays start to predominate?» *Journal of Physics G: Nuclear and Particle Physics* 31:255, 2005. URL http://stacks.iop.org/0954-3899/31/i=3/a=005.

[126] R. J. Wilkes. «DUMAND and AMANDA: High Energy Neutrino Astrophysics». *ECONFC940808* 017, 1994. URL http://www.citebase.org/abstract?id=oai:arXiv.org:astro-ph/9412019.

[127] F. Yuan and C. W. Akerlof. «Astronomical Image Subtraction by Cross-Convolution». *The Astrophysical Journal* 677:808–812, 2008. 0801.0336, URL http://adsabs.harvard.edu/abs/2008ApJ...677..808Y.

[128] V. Zworykin and J. Rajchman. «The electrostatic electron multiplier». *Proc IRE* Vol. 27:558–566, 1939.

[129] V. Zworykin and E. Ramberg. *Photoelectricity and its Application.* John Wiley and Sons, 1949.